Estimating the radiation environment in the Great Barrier Reef

by

Itsara Masiri
M.Sc. (Physics)

Submitted in fulfilment of the requirements for
the Degree of Doctor of Philosophy

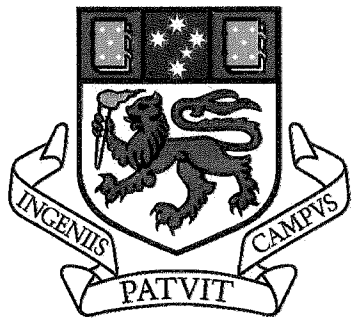

University of Tasmania

December 2008

Declaration

This thesis contains no material which has been accepted for the award of any other degree or diploma by the University of Tasmania or any other institute, except by way of background information that is duly acknowledged. To the best of my knowledge and belief this thesis contains no material previously published or written by another person, except where due reference is made in the text.

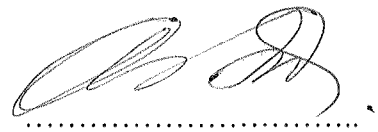

(Itsara Masiri)

Authority of Access

This Thesis may be available for loan and limited copying in accordance with the *Copyright Act 1968*.

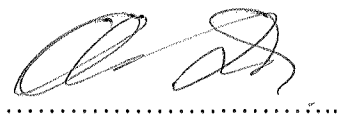

(Itsara Masiri)

Abstract

There are a number of studies that have examined solar irradiance in the environment above and below the ocean surface. Unlike other previous studies, this thesis maps both surface and underwater irradiances using a combination of geostationary and SeaWiFS satellite data and surface measurements. Detailed estimates of broadband, PAR and UVB solar radiation, both above and below water, is obtained for the Great Barrier Reef region in northeast Australia. The study area covers the Coral Sea including the Great Barrier Reef (GBR), northeast of Queensland (10° S - 26° S, 142° E - 155° E). Geostationary meteorological satellite (GMS) data collected for periods between 1995 and 2005 are combined with the models to obtain broadband solar radiation at the surface. PAR and UVB underwater irradiance are estimated from the attenuation coefficients K_d derived from the SeaWiFS instrument for the period of 1998-2005.

In developing algorithms, a look-up table (LUT), which contains series of broadband surface solar radiation and the Earth-atmosphere reflectivity, is created from the Streamer radiative transfer model. The broadband Earth-atmosphere reflectivity α_{EA} derived from the GMS data is used to estimate the surface solar radiation from the LUT algorithms. The attenuation coefficients K_d for PAR, UVB and SeaWiFS wavebands are obtained from Monte Carlo models, and relationships between these K_d values are derived as a result. Using SeaWiFS-derived K_d data, PAR and UVB underwater irradiance are estimated across the regions from the K_d relationships.

Comparisons between the satellite-derived surface solar radiation and the measurements at Rockhampton and Cairns give good agreement with root-mean-square

difference (RMSD) of 2.26 MJ-m^{-2}-day^{-1} and 2.85 MJ-m^{-2}-day^{-1}, respectively. The SeaWiFS-derived K_d at six different wavebands obtained from Monte Carlo models are compared to the measurements at Heron Island, with a smallest RMSD value of 0.075 m^{-1}.

Maps of solar radiation both above and below the water surface are provided for the study area. On average, strong solar radiation is exhibited in summer and autumn periods at latitude bands between 18° S and 26° S. The temporal information suggests there is a small increase in solar radiation of about 1 percent per decade. The underwater PAR and UVB irradiances along the GBR coastline at 2.5 m depth were in magnitude of ~300 W-m^{-2} and ~120 mW-m^{-2}, respectively. Monthly distribution at 2.5 m depth underwater for PAR shows an outstanding feature throughout between September and February. There are patterns of high PAR irradiance throughout the summer months of 2001/2002 and 2002/2003. Results of the satellite-derived solar radiation are used to examine the 2002 coral bleaching events. A correlation between maximum solar radiation and the bleaching data are seen in summer months of 2001/2002.

Acknowledgements

The completion of this thesis would not be possible without valuable guidance and support from my supervisors, Dr. Manuel Nunez and Dr. Kelvin Michael. I would like to thank both of them. Without these two people, I could not have overcome so many difficult tasks that I encountered during this study.

Thanks to my fellow student, Evan Weller, for all the discussions that we had during my study. Also, the investigation involving the SST data would not have been completed without his help.

Thanks to Cameron Veal who contributed to the underwater solar irradiances at Heron Island.

Sincere thanks go to Dr. Peter Gies, who provided me the UVB measurement data, which were used for model validation.

I am most grateful to Dr. Carol Freeman for reviewing my thesis, also providing such very useful advice about writing to me, thank you.

Finally, I would like to thank my family and friends for their encouragement and care. Their continued support was a driving force pushing me to arrive at this success.

Contents

List of Figures

List of Tables

List of Acronyms and Abbreviations

5S	Simulation of the Satellite Signal in the Solar Spectrum
AOPs	Apparent Optical Properties
ARPANSA	Australian Radiation Protection and Nuclear Safety Agency
ASTM	American Society for Testing and Materials
AU	Astronomical Unit
AVHRR	Advanced Very High Resolution Radiometer
BRDF	Bidirectional Reflectance Distribution Function
BOM	The Australian Bureau of Meteorology
CZCS	Coastal Zone Color Scanner
DISORT	Discrete Ordinates Radiative Transfer model
DOM	Dissolved organic matter
DU	Dobson Unit
EAC	East Australian Current
ERBE	Earth Radiation Budget Experiment
GAC	Global Area Coverage
GBR	The Great Barrier Reef
GBRMPA	The Great Barrier Reef Marine Park Authority
GMS	Geostationary Meteorological Satellite
GOES	Geostationary Operational Environmental Satellites
HDF	Hierarchical Data Format
IDL	Interactive Data Language
IOPs	Inherent Optical Properties

ISCCP	International Satellite Cloud Climatology Project
JMA	Japanese Meteorology Agency
LOWTRAN	Low Resolution Atmospheric Transmission
LUT	Look-Up Table
LWC	Liquid Water Content
MBE	Mean bias error
MODIS	Moderate Resolution Imaging Spectroradiometer
MODTRAN	Moderate resolution atmospheric Transmission
MTSAT	A Japanese Geostationary Meteorological Satellite
N	Number of variables used in regression analysis
NASA	National Aeronautics and Space Administration, USA
PAR	Photosynthetically active radiation
PUV	Profiling Ultraviolet
QSA	Quasi-Scattering Approximation
RMS	Root mean square
SBDART	Santa Barbara DISORT Atmospheric Radiative Transfer
S.E.	Standard error
SeaWiFS	Sea-viewing Wide Field-of-view Sensor
SMART	The Spectral Mapping Atmospheric Radiative Transfer
SMM	Solar Maximum Mission
SOHO	Solar and Heliospheric Observatory
SST	Sea Surface Temperature
Streamer	A radiative transfer code for calculation of radiances (intensities) or irradiances in the atmosphere.
TOA	Top of the atmosphere

TOMS	Total Ozone Mapping Spectrometer
TOVS	TIROS Operational Vertical Sounder
UVB	Ultraviolet-B
UVSPEC	A numerical code for calculating the radiation field in the Earth's atmosphere for a given set of input parameters
WEFAX	Weather Facsimile
WRC	World Radiation Center

List of Symbols

a_w	Total absorption coefficient of water [m^{-1}]
a_{wp}	Absorption coefficient of pure water [m^{-1}]
a_{wtr}	Absorption coefficient due to tripton [m^{-1}]
a_{wph}	Absorption coefficient due to phytoplankton [m^{-1}]
a_{wy}	Absorption coefficient due to yellow substance [m^{-1}]
a_{wde}	Absorption coefficient due to detritus [m^{-1}]
a_{wc}	Absorption coefficient due to chlorophyll [m^{-1}]
$a_{wp\lambda}$	Spectral absorption coefficient of pure water [m^{-1}]
a^*_{wc}	Normalized chlorophyll specific coefficient [m^{-1}]
b_w	Total scattering coefficient of water [m^{-1}]
b_{ws}	Beam scattering coefficient [m^{-1}]
b_{wb}	Back-scattering coefficient [m^{-1}]
b_{wp}	Scattering coefficient of pure water [m^{-1}]
$b_{wp\lambda}$	Spectral scattering coefficient of pure water [m^{-1}]
b_{wph}	Scattering coefficient due to phytoplankton [m^{-1}]
b_{wtr}	Scattering coefficient due to tripton [m^{-1}]
BFp	Backscatter fraction of particle [-]
B	The visible clear brightness of satellite pixels [-]
B_{clo}	Brightness threshold to cloud pixels [-]
B_m	Mean target (surface) brightness [-]

B_0	The normalized clear brightness of satellite pixels [-]
c_w	Total attenuation coefficient of water [m^{-1}]
$c_{w\lambda}$	Spectral attenuation coefficient of water [m^{-1}]
c_{wtr}	Attenuation coefficient due to tripton [m^{-1}]
$chlo$	Chlorophyll-*a* concentration [mg-m^{-3}]
C	Cloud fraction [-]
C_n	Cloud index [-]
$\overline{C}_{eff}$	Mean effective cloudiness factor [-]
$\widetilde{C}$	Speed of light [m-s^{-1}]
d	Distance [m]
$\vec{d}$	Radius vector [-]
$D_d(z)$	Distribution function of downwelling irradiance at depth z [-]
E_λ	Action spectrum of erythemal ultraviolet irradiance [-]
F	Forward scattering probability [-]
F_{CDOM}	CDOM absorption factor [-]
g	Asymmetry factor [-]
h	Planck's constant [J-s^{-1}]
I_{sc}	Solar constant [W-m^{-2}]
I_o	extraterrestrial solar irradiance [W-m^{-2}]
I_{net}	Net solar radiation incident at the surface [W-m^{-2}]
I_{abs}	Irradiance that is attenuated in the atmosphere [W-m^{-2}]
I_G	Irradiance absorbed by the Earth's surface [W-m^{-2}]
$I_{sat}^{\uparrow}$	Upward irradiance observed by satellite [W-m^{-2}]
$I_\lambda^{\uparrow}$	Monochromatic upwelling solar irradiance [W-m^{-2}]

$I_o^{\uparrow}$	Upwelling irradiance at the top of the atmosphere [W-m^{-2}]
$I_{l\lambda}^{\downarrow}$	Monochromatic solar irradiance received at the surface [W-m^{-2}]
$I_{o\lambda}^{\downarrow}$	Monochromatic solar irradiance at the beginning point or at the top of the atmosphere [W-m^{-2}]
$I_o'^{\downarrow}$	Downwelling irradiance arriving at the top of the atmosphere, determined for the satellite channels [W-m^{-2}]
$I_{s\lambda}^{\downarrow}$	Direct beam monochromatic solar irradiance [W-m^{-2}]
$I_g^{\downarrow}$	Global solar irradiance [W-m^{-2}]
$I_s^{\downarrow}$	Direct solar irradiance [W-m^{-2}]
$I_d^{\downarrow}$	Diffuse solar irradiance [W-m^{-2}]
$I_{da}^{\downarrow}$	Diffuse solar irradiance due to aerosol attenuation [W-m^{-2}]
$I_{dR}^{\downarrow}$	Diffuse solar irradiance due to Rayleigh scattering [W-m^{-2}]
$I_{dm}^{\downarrow}$	Diffuse solar irradiance due to multiple reflections between the Earth's surface and atmosphere [W-m^{-2}]
$I_{atm}^{\downarrow}$	The irradiance that is attenuated in the atmosphere [W-m^{-2}]
$I_{gw+}^{\downarrow}$	Downwelling solar irradiance just above the water surface [W-m^{-2}]
$I_{gw+}^{\uparrow}$	Upwelling irradiance just above the water surface [W-m^{-2}]
$I_{gw-}^{\downarrow}$	Downwelling solar irradiance received just below the water surface [W-m^{-2}]
$[I_g]$	Solar radiation [MJ-m^{-2}-day^{-1}]
$[I_o]$	Solar radiation at the top of the atmosphere [MJ-m^{-2}-day^{-1}]
K_d	Vertical attenuation coefficient of waters [m^{-1}]

K_d(PAR)	Vertical attenuation coefficient for PAR [m^{-1}]
K_d(UVB)	Vertical attenuation coefficient for UVB [m^{-1}]
K_d(490)	Vertical attenuation coefficient for the SeaWiFS waveband (480-500 nm) [m^{-1}]
K_c	Chlorophyll-*a* specific vertical attenuation of underwater irradiance [m^{-1}]
K_w	Vertical attenuation coefficient of underwater irradiance due to pure water [m^{-1}]
K_g	Vertical attenuation of underwater irradiance due to non-algal material
$L_o^{\uparrow}$	Upwelling radiance observed by satellite [W-m^{-2}-sr^{-1}]
$L_{w+}^{\uparrow}$	Upwelling radiance measured just above water's surface [W-m^{-2}-sr^{-1}]
$L_{0w}^{\uparrow}$	Water leaving radiance [W-m^{-2}-sr^{-1}]
$L_d^{\downarrow}$	Sky radiance [W-m^{-2}-sr^{-1}]
$L(z,\theta,\varphi)$	Radiance per unit distance [W-m^{-2}-sr^{-1}]
$L_o^{\uparrow}(\theta,\varphi)$	Upwelling Radiance at the top of the atmosphere [W-m^{-2}-sr^{-1}]
LF	Non-Lambertian correction factors [-]
m_r	Optical airmass [-]
n_a	Refractive index of air [-]
n_w	Refractive index of water [-]
N_o	The number of streams [-]
p	Refraction of global radiation that is diffuse [-]
P_b	Backscattering probability [-]
$P(\theta',\varphi';\theta,\varphi)$	Scattering matrix [-]

$P(\mu', \mu)$	Scattering function [-]
PAR	PAR radiation [Ei m^{-2} s^{-1}]
$r_{\perp}$	Reflectance of perpendicular incident radiation fluxes [-]
$r_{\Downarrow}$	Reflectance of polarised incident radiation fluxes [-]
r	Reflectance [-]
$\widetilde{r}$	The spherical reflectivity [-]
$r^{\circ}(\theta_0)$	The reflectivity of the atmosphere for a non-reflecting surface [-]
r_n	Narrowband bidirectional reflectance [-]
r_b	Broadband bidirectional reflectance [-]
r_{cle}	Clear sky atmospheric reflectance [-]
r_o'	Pseudo-reflectivity observed by satellite [-]
r_w	Surface reflectance of water [-]
r_G	Surface reflectance of the ground [-]
r_{rs}	Remote-sensing reflectance [-]
r_n	Narrowband bidirectional reflectance [-]
r_b	Broadband bidirectional reflectance [-]
RN	Random number [-]
T_{λ}	Monochromatic transmission [-]
T	Transmission of the atmosphere [-]
T_o	Transmission of the atmosphere due to ozone [-]
T_w	Transmission of the atmosphere due to water vapour [-]
T_a	Transmission of the atmosphere due to aerosols [-]
T_R	Transmission of the atmosphere due to Rayleigh scattering [-]
T_g	Transmission of the atmosphere gases [-]

T_A	Transmission of a clear atmosphere [-]
T_C	Transmission of cloud [-]
$\hat{T}_C$	Effective daily cloud transmission [-]
T_{wR}	Transmittance of a clear atmosphere accounting for water vapour and Rayleigh scattering and water vapour absorption [-]
$\widetilde{T}$	The spherical transmissivity [-]
T°	The transmissivity of the atmosphere for a non-reflecting surface [-]
u	Path length [m]
w	Precipitable water vapour [g-m^{-3}]
X_o	The component of the direct beam irradiance [-]
z	height or depth [m]
ε_λ	Spectral attenuation coefficient [-]
κ_λ	Spectral extinction coefficient [-]
α	Single scattering albedo [-]
α_g	Surface albedo [-]
α_c	Cloud albedo [-]
α_A	Broadband atmospheric albedo [-]
α'_A	Atmospheric albedo observed by satellite [-]
α'_c	Cloud albedo observed by satellite [-]
α'_g	Ground surface albedo observed by satellite [-]
α_w	Ocean surface albedo [-]
α_{TOA}	Planetary albedo [-]
α_{sw}	Ocean albedo for direct solar irradiance [-]

α_{dw}	Ocean albedo for diffuse solar irradiance [-]
α_P	Normalized albedo [-]
α_s	Surface albedo for direct solar irradiance [-]
α_d	Surface albedo for diffuse solar irradiance [-]
$\widetilde{\alpha}$	Spherical albedo [-]
α_{EA}	Broadband Earth-atmosphere reflectivity [-]
α'_{EA}	Satellite-derived Earth-atmosphere reflectivity [-]
α'_{sat}	Pseudo-reflectivity retrieved from GMS satellite [-]
$\alpha'_{EA(\min)}$	Minimum Earth-atmosphere reflectivity observed by satellite [-]
$\alpha'_{EA(\max)}$	Maximum Earth-atmosphere reflectivity observed by satellite [-]
α_{clear}	The top of the atmosphere albedo for clear sky [-]
$\alpha_{overcast}$	The top of the atmosphere albedo for overcast sky [-]
α_{EC}	The albedo of the cloud-layer-surface system [-]
β	Volume scattering function [-]
$\widetilde{\beta}$	Scattering function [-]
ρ	Single scattering [-]
ρ_λ	Monochromatic scattering [-]
$\delta\rho_a$	Extra scattering due to aerosols [-]
ϕ	Absorption coefficient [-]
$\delta\phi_a$	Extra absorption function due to aerosols [-]
γ	Proportionality factors [-]
θ_z	Solar zenith angle [degree]
θ	Zenith angle [degree]

θ_{w+}	Angles between the incident direct radiance and normal to the air-water interface [degree]
θ_{w-}	Angles between the refracted direct radiance and normal to the air-water interface [degree]
θ_i	Angles of incident beams [degree]
θ_r	Angles of reflected beams [degree]
φ	Azimuth angle [degree]
Ω	Solid angle [sr]
$\phi(u_1)_t$	Absorption of downward solar radiation above the cloud [-]
$\phi(u_1)_b$	Absorption of downward solar radiation below the cloud [-]
ϕ_{clo}	Cloud absorption [-]
τ	Optical thickness [-]
μ	The cosine of zenith angle, $\cos(\theta_i)$ [-]
μ_o	The cosine of solar zenith angle, $\cos(\theta_z)$ [-]

Chapter 1

Introduction

This study examines the solar radiation environment in the Australian Great Barrier Reef (GBR). Solar radiation plays a central role in reef function and development. It is possible to consider a coral reef as a living system involving a symbiosis between the coral polyp, the host organism and the zooanthella, the single-celled alga which carries out photosynthesis and provides the polyp with excess nutrients (Gateno *et al.*, 1998; Anderson, 2001). This symbiotic relationship can only function effectively at high levels of solar radiation, essentially defining the geographic range of coral reefs. They are confined to ocean depths within the euphotic zone of within 50 m depths, where light levels are sufficiently high for photosynthesis to occur. On a large scale, coral reefs are confined to tropical regions and occur at shallow depths in the continental shelf. In Australia, the GBR extends from New Guinea at its northern edge to a latitude of 24° S and from the Australian coast to the edge of the continental shelf, some 250 km eastward.

Despite its obvious importance, there are no studies that have examined the climatology of solar radiation above coral reefs. Most of the previous solar radiation studies have been only designed to support their specific needs (Gautier, 1980; Pinker and Ewing, 1985; Dedieu, 1987; Darnell *et al.*, 1988; Pinker and Laszlo, 1992; Schmetz, 1991; Islam and Exell, 1996; Tovar and Baldasano, 2001; Hansen *et al.*, 2002; Kandirmaz *et al.*, 2004). The reason is very likely the difficulty in conducting radiation measurements in a marine environment (Lough, 1998), which requires a recording system that can withstand storms and long-term weathering. Salt encrustation on the sensing surface is a major problem which requires daily maintenance, a task which is difficult and costly.

A major motivation for this study deals with the phenomenon of coral bleaching, a process in which the polyp host rejects the zooanthella. As a result, the photosynthesis pathway is disrupted, the coral loses its colour and eventually dies if not colonized by other zooanthella (Brown, 1997; Fitt *et al.*, 2001; Mumby *et al.*, 2001). In recent years, coral bleaching has become more frequent and widespread, and a number of studies have reported bleaching events in many regions across the globe (Glynn and D'Croz, 1990; Jokiel and Coles, 1990; Brown, 1997; Wilkinson *et al.*, 1999; Berkelmans and Oliver, 1999; Hoegh-Guldberg, 1999; Dunne and Brown, 2001; Berkelmans *et al.*, 2004; Barton and Casey, 2005). In the Great Barrier Reef, major coral bleaching events occurred during the summer months of 1997/1998 and 2001/2002 (Berkelmans and Oliver, 1999; Berkelmans *et al.*, 2004).

Several variables such as water temperatures, solar radiation, nutrient concentrations, sedimentation, salinity, currents, and hurricane impacts have been suggested as major factors causing coral bleaching (Dollar and Grigg, 1981, Jokiel and Coles, 1990, Brown *et al.*, 1994, Brown, 1997). Despite the links between rising sea surface temperature (SST) and bleaching events, cited as a primary effect by many studies, solar radiation is also important to the bleaching process (Brown, 1997; Jones *et al.*, 1998; Dunne and Brown, 2001; Fitt *et al.*, 2001; Barton and Casey, 2005). In shallow reef environments, high solar irradiance is dominant in the bleaching process as it heats the shallow water and modifies the temperature variability (Jones *et al.*, 1998; Fitt *et al.*, 2001; Mumby *et al.*, 2001). A direct solar radiation effect has been argued in some studies which found that very high levels of photosynthetically active radiation (PAR) and ultraviolet-B (UVB) irradiances could inhibit photosynthesis by producing free oxygen radicals and reducing chlorophyll concentration produced by corals (Warner *et al.*, 1996; Brown *et al.*, 1999; Hoegh-Guldberg, 1999; Fitt *et al.*, 2001). However, these effects are

not applicable to all species of corals as the investigations were performed at specific locations or in laboratories.

An important step in studying bleaching events is to characterise the solar radiation climate both above and within the water environment. To overcome the scarcity of solar radiation data in the Great Barrier Reef, this study develops techniques which use satellite data to provide a long-term climatology of surface broadband solar radiation, and underwater UVB/PAR irradiance. Statistics including seasonal and inter-annual trends of surface and underwater solar radiation at the surface and underwater are also produced as a result. This study also presents relationships between solar radiation, SST and bleaching events which hopefully will help in understanding the role of light in recent mass coral bleaching that occurred in the Great Barrier Reef.

1.1 Aims of the study

The primary objective of this study is to provide statistics of solar radiation above and within the Great Barrier Reef (10°S-26°S, 142°E-155°E). This is to be accomplished using satellite data that characterises firstly the cloud regime in the region, and secondly the turbidity of the shallow water of the GBR. Both of these data are used in radiation models which are then validated with the *in situ* measurements.

The second objective is to provide insight into the role of solar radiation in recent bleaching events. This objective is to be accomplished by a detailed examination of solar radiation and bleaching during recent mass bleaching episodes.

In summary, most studies have examined the environment above and below the water surfaces, but not jointly. In addition, there are no accurate estimates of solar radiation measurement in the GBR regions either above or below the water surface. In deed, the measurements of underwater solar irradiance are very limited or non-existent

and yet, this data is crucial to understand the phenomenon and the role of sunlight in coral bleaching. This consideration shapes the aims of the study:

1) To developed techniques for estimating above and below solar irradiances using the geostationary meteorological satellite and SeaWiFS data.
2) To provide spatial and temporal statistics of broadband, PAR and UVB radiation above the Great Barrier Reef region over a long 10-year periods.
3) To provide underwater statistics of UVB/PAR radiation concurrent with the above surface estimates.
4) To examine the character of the depletion of solar radiation both above and below the water surface. While depletion of solar radiation above the surface is expected to be quite conservative, below water irradiance will strongly depend on local turbidity and therefore it is expected that there will be large spatial variability.
5) To examine the influence of solar radiation in explaining the pattern and intensity of coral bleaching events.

1.2 Thesis structure

Chapter 2 provides a background to the physical concepts of radiation theory. Chapter 3 describes how these physical concepts are used in the remote sensing literature to estimate solar irradiance incident on and below the water surface. The specific remote sensing approaches used in this study are described in Chapter 4, the methodology chapter. The remote sensing data is validated with ground truth measurements in Chapter 5. The results of estimating irradiance above and below the water surface, including their statistics, are presented in Chapter 6, and in Chapter 7 they are examined within the perspective of recent coral bleaching events. Finally, Chapter 8 presents the main conclusions of this study.

Chapter 2

Background Theory

2.1 Solar radiation

2.1.1 Spectral distribution of solar radiation

The Sun is a star at the centre of our solar system. Its mass comprises hydrogen (74%), helium (25%) and some other heavier elements (1%). It releases enormous energy from nuclear fusion reactions inside its central core (Stix, 1989). Solar radiation encompasses a broad spectrum of wavelengths ranging from gamma rays to radio waves. The spectral distribution of solar radiation features a continuous curve with 95% of its radiant energy with wavelengths between 0.29 μm and 3.0 μm (Iqbal, 1983; Liou, 2002). The curve has a distinctive shape, increasing sharply from the shorter wavelengths to reach a peak at 0.555 μm and decreasing slowly at longer wavelengths (Figure 2.1). The energy spectrum is a close fit to black body radiation at 5,777 K, which is believed to be the surface temperature of the Sun (Iqbal, 1983). The spectrum may be divided into several intervals, generally they are: gamma-rays (λ<0.00001 μm), X-rays (0.00001 μm <λ<0.01 μm), ultraviolet radiation (0.01 μm <λ<0.39 μm), visible radiation (0.39 μm<λ<0.74 μm), infrared radiation (0.74 μm<λ<3000 μm) and microwave or radio wave (λ>3000 μm) (Bukata *et al*, 1995). Radiation from the Sun has a crucial influence on our planet, directly affecting global climate and all life forms.

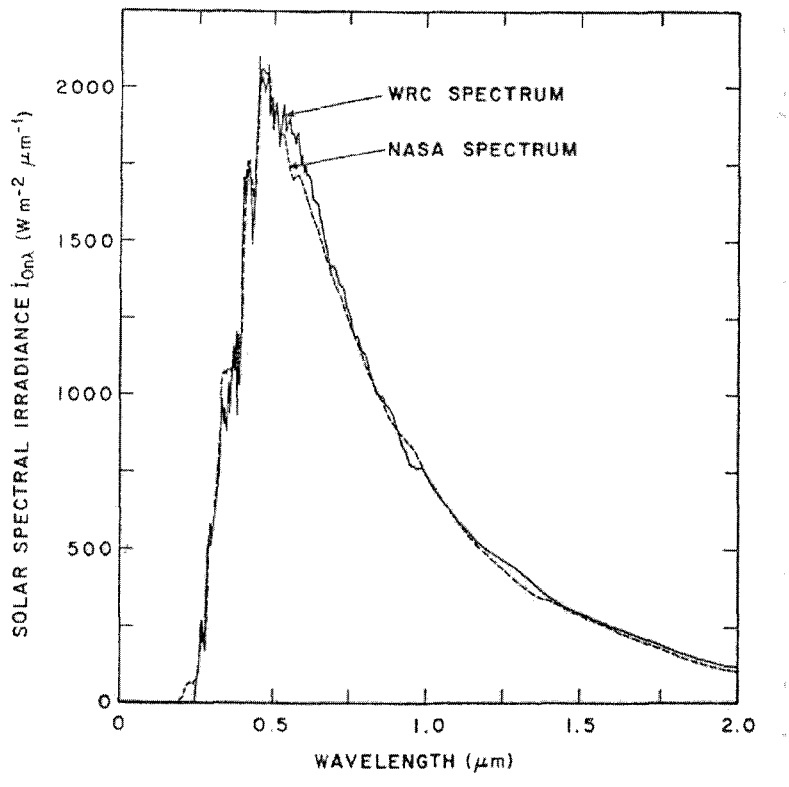

Figure 2.1 Spectral distribution of extraterrestrial solar radiation (Iqbal, 1983).

2.1.2 Ultraviolet radiation and PAR

The region between 0.28 μm and 0.70 μm occupies the shorter end of the solar spectrum and contains most of the solar energy (Stix, 1989). The wavelength interval is separable into ultraviolet (UV) and visible light. Ultraviolet radiation has some negative impacts on living organisms such as germs, bacteria and cell tissues, and it is also known as an important agent in causing skin cancer (Bukata *et al*, 1995; Verdebout, 2000). The spectrum of UV radiation may be partitioned into three intervals: UV-A (0.32-0.39 μm), UV-B (0.28-0.32 μm) and UV-C (0.10-0.28 μm) (Zerefos and Bais, 1997; Bukata *et al*, 1995; Madronich and Flocke, 1997). UV-C is extremely harmful to all life on Earth but does not reach the Earth's surface, as UV-C is completely absorbed by ozone and oxygen in the stratospheric layer at altitudes of 25 km to 50 km (Bukata *et al*, 1995; DeLuisi, 1997; Madronich and Flocke, 1997). By contrast, UV-A and UV-B can penetrate further into the atmosphere and reach the Earth's surface (DeLuisi, 1997;

Simon, 1997). In the clear atmosphere, stratospheric ozone plays an important role in the attenuation of UV-B and some UV-A radiation.

The biological effects of UV-B radiation on living organisms are determined by the *action spectra*. These response curves represent the biological effects of UV-B radiation at different wavelengths on organic materials. In the cases of the redness, sunburn and skin cancer (erythema), the action spectrum E_λ proposed by McKinlay and Diffey (1987) is expressed as the following equation (McKinlay and Diffey, 1987; Madronich and Flocke, 1997; McKenzie *et al.*, 2004):

$$\begin{aligned} E_\lambda &= 1 && \text{for } \lambda < 0.298\ \mu\text{m} \\ &= 10^{94(0.298-\lambda)} && \text{for } 0.298\ \mu\text{m} \le \lambda < 0.328\ \mu\text{m} \\ &= 10^{15(0.139-\lambda)} && \text{for } 0.328\ \mu\text{m} \le \lambda < 0.4\ \mu\text{m} \\ &= 0 && \text{for } \lambda < 0.4\ \mu\text{m} \end{aligned} \qquad (2.1)$$

therefore

$$UVB = \int_{0.28\,\mu m}^{0.32\,\mu m} UV \cdot E(\lambda)\ d\lambda \qquad (2.2)$$

where *UVB* is the erythemally-weighted UV irradiance. Figure 2.2 illustrates various action spectra between 0.28 μm and 0.4 μm. All the action spectra display an increase in biological damage on living cells as the wavelength decreases.

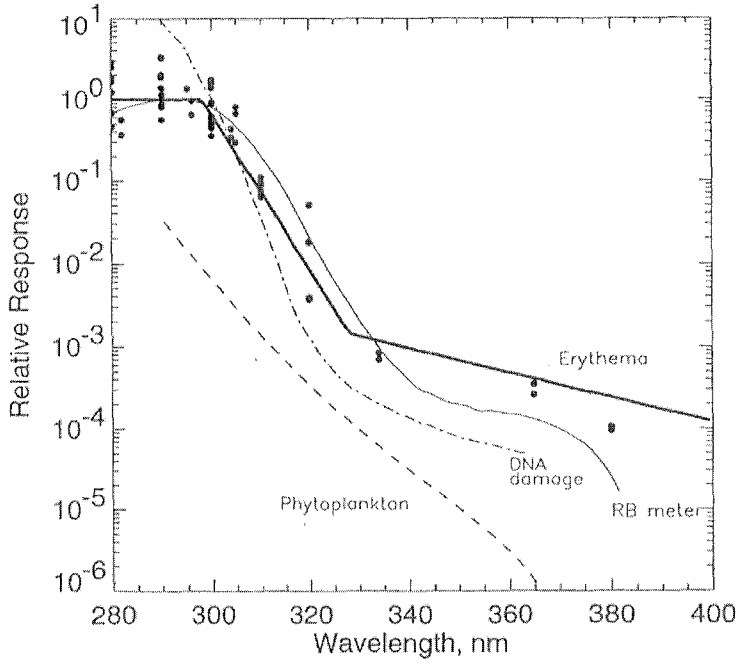

Figure 2.2 Biological action spectra for erythema, DNA damage, RB meter and phytoplankton productivity (taken from Madronich and Flocke, 1997).

Solar radiation between 0.4 μm and 0.7 μm is technically called *visible light* and is also referred to as photosynthetically active radiation (PAR). This radiation is important for plants, planktons, corals and some bacteria. It is used in photosynthesis, whereby plants absorb light and carbon to produce living matter (Kirk, 1994). The PAR at the Earth's surface is the dominant part of the solar spectrum. For all atmospheric conditions, it constitutes about 45-50% of the total radiation that reaches the Earth's surface at solar elevations between 40° and 90° (Stix, 1989; Kirk, 1994). Downwelling PAR at the Earth's surface is mainly attenuated by ozone, aerosols and atmospheric molecules (Iqbal, 1983; Kirk, 1994). According to Rayleigh scattering theory, the attenuation in this region is chiefly due to scattering. Blue light between 0.425 μm and 0.450 μm is scattered strongly by the air molecules to dominate the skylight (diffuse

radiation). In the PAR region, absorption by oxygen and ozone is present but quite weak (Paltridge and Platt, 1976; Bukata *et al.*, 1995; Liou, 2002).

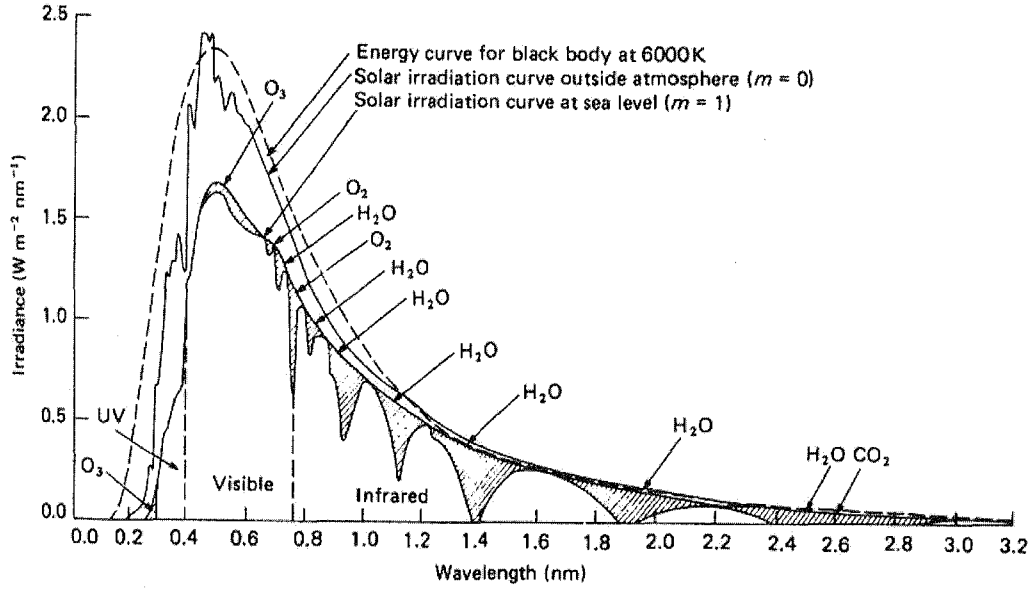

Figure 2.3 Spectral distribution of solar radiation showing the ranges of UV, visible and infrared radiation (Kirk, 1994).

2.1.3 Solar and longwave infrared radiation

Solar radiation of wavelengths greater than 0.7 μm is called *infrared radiation*. The absorption of emitted thermal infrared radiation (Figure 2.4) is mainly caused by carbon dioxide (CO_2), water vapour (H_2O), ozone (O_3) and some other gases, such as carbon monoxide (CO), nitric oxide (N_2O) and methane (CH_4) (Iqbal, 1983; Liou, 2002). Carbon dioxide dominates the absorption in regions of around 15 μm, while ozone accounts for narrow regions centered ~ 9.7 μm. At wavelengths shorter than 8 μm, the prime absorption is caused by water vapour. On the other hand, the 'atmospheric window' region between 8 μm and 13 μm is almost free from atmospheric absorptions, with only weak absorptions caused by water vapour. This provides for very

effective transmission of infrared radiation through the atmosphere. Details of spectral absorptions in infrared regions are illustrated in Figure 2.4.

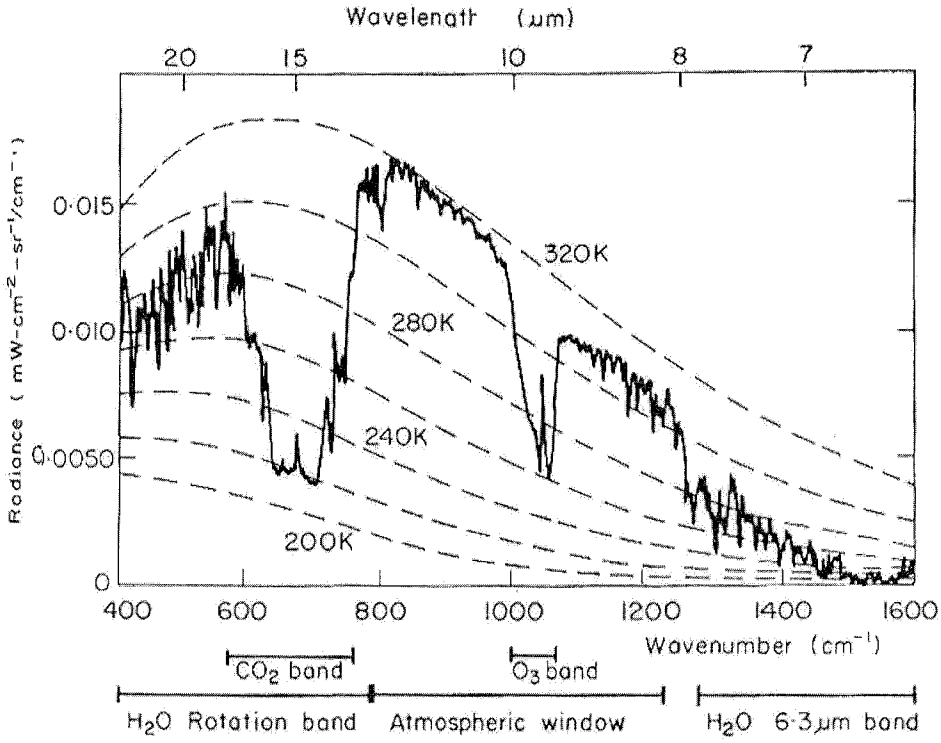

Figure 2.4 Spectral distribution of solar infrared radiations absorbed by various atmospheric gases (Liou, 2002).

2.2 Solar radiation at the top of atmosphere and solar constant

Solar irradiance outside the Earth's atmosphere fluctuates due to the occurrence of sunspots and faculae in the Sun. On a monthly basis, the irradiance presents small variations within a range of 4 W-m^{-2} (Kyle *et al.*, 1994; Solanki and Krivova, 2005). Since 1978, there have been a series of space programs measuring solar irradiance at the top of atmosphere (Table 2.1). These include the Earth Radiation Budget (ERB), the Solar Maximum Mission (SMM), Earth Radiation Budget Experiment (ERBE) and Solar and Heliospheric Observatory (SOHO) (Frohlich, 2000; Dewitte *et al.*, 2005; Solanki and Krivova, 2005). The complete spectrum of solar irradiance was established in 1976 by American Society for Testing and Materials (ASTM), and it is called the

NASA standard reference spectrum. In 1981, the World Radiation Center (WRC) reexamined the data and proposed a new standard spectrum, which is known as the WRC spectrum (Thekaekara, 1976; Iqbal, 1983; Liou, 2002). The comparison between the NASA standard and WRC spectrum shows a slight difference, as illustrated in Figure 2.1. The latest standard of extraterrestrial solar irradiance was announced by ASTM in 2000. The curve was provided over a very broad range of wavelengths from 0.1195 μm to 1000 μm (Thullier *et al.*, 2003).

Table 2.1 Summary of the satellite equipped radiometers measuring the extraterrestrial solar radiation (Dewitte *et al.*, 2005).

Periods	Instrument	Satellite
1978 – 1993	ERB	Nimbus 7
1980 – 1989	ACRIM 1	SMM
1984		ERBS
1991 – 2001	ACRIM 2	UARS
1992 – 2003	SOLCON	Space Shuttle
1992 – 1993	SOVA 1,2	EURECA
1996 – current	DIARAD/VIRGO	SOHO
1996 – current	PMO06/VIRGO	SOHO
2000 – current	ACRIM 3	ACRIMSAT
2003 – current	TIM	SORCE

The solar constant is defined as the integrated spectrum of solar irradiance incident perpendicularly upon a unit area at a distance of one astronomical unit (1 AU = 150×10^6 km) from the Sun outside the Earth's atmosphere (Iqbal, 1983; Liou, 2002). Since the beginning of this century, the solar constant has been estimated using a number of instruments such as ground observations, high-altitude aircraft, balloons and space-borne radiometers. A value used during 1975 and 1977 was 1368 W-m^{-2} (Liou, 2002). Later, Frohlich *et al.* (1981) proposed the value of 1367 W-m^{-2} which was extracted from eight different solar constants that were measured between 1969 and 1980 (Iqbal, 1983). In 2000, ASTM adopted a solar constant of 1366.1 W-m^{-2} (Thullier *et al.*, 2003).

2.3 Solar radiation at the ground

2.3.1 The atmosphere

The change of solar radiation at the Earth's surface on the global scale is simply described in terms of revolution and rotation periods of the Earth. The rotation axis is tilted by 23.5° to the plane of the Earth's orbit around the Sun, which takes 365 days to complete (Iqbal, 1983). It is convenient to consider an instantaneous solar irradiance arriving at the Earth's surface which changes as a function of extraterrestrial irradiance and the Earth's atmospheric composition (Liou, 2002). The Earth's atmosphere comprises several gases whose concentrations vary with height, time and location. Clean air may be separated into permanent and variable constituents (Lenoble, 1985). Some atmospheric constituents such as ozone, aerosols and water vapour have direct effects on the transmission of solar flux, and act selectively on various wavelengths (Iqbal, 1983). The attenuation processes due to these constituents is discussed in the next section.

2.3.2 Attenuation of solar irradiance in the atmosphere

The attenuation of incoming solar irradiance by the Earth's atmosphere is separated into scattering and absorption (Liou, 2002). Both processes are caused by molecules of gases in the atmosphere, mainly, carbon dioxide, water vapor, ozone, oxygen, nitrogen and methane. The attenuation, either absorption, scattering or both, occurs selectively in varying amounts due to their atomic structures, concentrations and particle diameter in the case of aerosols. For short (visible and ultraviolet) wavelengths and a cloudless atmosphere, depletion is by scattering and absorption for molecular oxygen and ozone, and scattering by the other gases. Scattering occurs at wavelengths less than 0.7 μm, with Rayleigh and Mie scattering being the dominant scattering mechanisms. At longer wavelengths, carbon dioxide, oxygen and water vapor are the

better absorbers, especially in the infrared part of the spectrum (Iqbal, 1983; Bukata *et al*, 1995; Liou, 2002).

2.3.3 Solar radiation at the Earth surface and its transmission

The depletion of direct irradiance in its passage through the atmosphere may be expressed by Lambert's equation which is written as (Iqbal, 1983):

$$I_\lambda = I_{\lambda o} \exp(-\varepsilon_\lambda d) \tag{2.3}$$

where I_λ is the monochromatic irradiance flux received after travelling through a distance d, $I_{\lambda o}$ is the monochromatic irradiance flux at the beginning point and ε_λ is the spectral attenuation coefficient. The $\varepsilon_\lambda d$ term is called the monochromatic optical depth of the medium. From equation (2.3), the monochromatic transmission T_λ of the medium can be defined as the ratio of the emerging flux to the original incident flux at the beginning point, which is written as:

$$T_\lambda = \frac{I_\lambda}{I_{\lambda o}} = \exp(-\varepsilon_\lambda d) \tag{2.4}$$

Despite the difficulty in their estimation, there are a number of studies that have provided spectral attenuation coefficients ε_λ and developed empirical formulas, such as those by Ångström (1930), Leckner (1978) and Vigroux (1953). Alternatively, using Equation (2.4), the total transmission can be derived from solar irradiance measurements. The spectral transmission of direct solar irradiance as measured at the Earth's surface may be written as follows:

$$T_\lambda = T_o T_w T_a T_R T_g \tag{2.5}$$

where T_o, T_w, T_a, T_R and T_g are the total transmission due to ozone, water vapour, aerosols, Rayleigh scattering and gases, respectively.

The irradiance scattered by the air molecules is dispersed widely into the atmosphere. The monochromatic scattering ρ_λ can be written as a function of the spectral atmospheric transmission:

$$\rho_\lambda = 1 - T_\lambda \tag{2.6}$$

The scattered irradiance is known as diffuse irradiance or skylight. In physical terms, the irradiance flux reflects continuously in backward and forward directions between sky and ground, and is termed multiple reflections (Iqbal, 1983).

In cloudless conditions, the global irradiance at the ground is dominated by direct rather than diffuse radiation. By contrast, there is no direct radiation in overcast skies due to the scattering properties of clouds. Direct radiation in clear sky conditions is diminished by the air molecules in a process described by the radiative transfer equation. Using Equations (2.3) and (2.5), the total downwelling direct beam irradiance in clear skies, I_{bn}, can be expressed as:

$$\begin{aligned} I_s^\downarrow &= \int_{\lambda=0}^{\lambda=\infty} I_{o\lambda}^\downarrow \exp[-(\varepsilon_{o\lambda} + \varepsilon_{w\lambda} + \varepsilon_{a\lambda} + \varepsilon_{R\lambda} + \varepsilon_{g\lambda}) m_r] d\lambda \\ &= I_o^\downarrow T_o T_w T_a T_R T_g \end{aligned} \tag{2.7}$$

where $I_{o\lambda}^\downarrow$ is the direct beam monochromatic solar irradiance at the top of the atmosphere, m_r is the optical airmass, ε is the extinction coefficient and the subscripts

o, w, a, r and g refer to ozone absorption, water vapor absorption, aerosols, Rayleigh scattering and absorption by other gases, respectively. Changes in solar elevation affect the optical airmass. When refraction effects are included, m_r may be expressed as a function of solar zenith angle, θ_z, as follows (Iqbal, 1983):

$$m_r = [\cos(\theta_z) + 0.15(93.885 - \theta_z)^{-1.253}]^{-1} \tag{2.8}$$

Diffuse irradiance is an important component of total radiation. It can be estimated by subtracting a measured or estimated direct component from the measured global radiation. In order to accurately obtain the diffuse component, the atmospheric transmission becomes a crucial variable. Ideally, the diffuse irradiance may be separated into three components. That is (Iqbal, 1983):

$$I_d^{\downarrow} = I_{da}^{\downarrow} + I_{dR}^{\downarrow} + I_{dm}^{\downarrow} \tag{2.9}$$

where $I_{da}^{\downarrow}$ is the diffuse irradiance due to aerosol scattering, $I_{dR}^{\downarrow}$ is the diffuse irradiance due to Rayleigh scattering and $I_{dm}^{\downarrow}$ is the diffuse irradiance due to multiple reflections between the Earth's surface and atmosphere.

2.4 The description of radiative transfer theory

In order to estimate the attenuation of solar radiation at a specific level in the atmosphere (or water), a number of basic variables such as the extraterrestrial solar radiation, atmospheric (or aquatic) composition, optical properties and local geographic profiles are required. Radiative transfer theory is a fundamental method for deriving the complexity of attenuated solar irradiance in any medium. The theory considers the

physics of changing electromagnetic flux that propagates through the atmospheric (or aquatic) medium (Spinrad *et al.*, 1994; Liou, 2002).

The spectral radiance flux at any height, z, above the Earth's surface or below the water surface is described by $L_\lambda(z,\theta,\varphi)$ where θ and φ are zenith and azimuth angles respectively. An incremental change in $L_\lambda(z,\theta,\varphi)$ over an arbitrary path length dr may be described as:

$$dL_\lambda(z,\theta,\varphi) = -cL_\lambda(z,\theta,\varphi)dr + L'_\lambda(z,\theta,\varphi)dr \qquad (2.10)$$

where the first term on the right denotes an incremental depletion of radiance from absorption, scattering or both; and the second term represents an increase in the radiance field resulting from scattering into the polar direction (θ,φ). Note that the above expression assumes the radiance field is homogeneous at any height or depth z.

The second term in the right hand side of Equation (2.10) depends on the scattering matrix $P(\theta',\varphi';\theta,\varphi)$ defining the fraction of the radiance from direction (θ',φ') that is scattered into direction (θ,φ), integrating over all angles (Thomas and Stamnes, 1999)

$$L'_\lambda(z,\theta,\varphi) = \frac{\alpha}{4\pi}\int_{\phi=0}^{2\pi}\int_{\theta=0}^{\pi} L_\lambda(\theta',\varphi')\sin\theta\, P(\theta',\varphi';\theta,\varphi)d\theta d\varphi \qquad (2.11)$$

where α is the single scattering albedo and 4π is a normalisation constant. For a purely scattering medium, α equals unity. Equation (2.11) is a general form describing changes in the radiance field as it travels upward or downward in a horizontally-stratified medium. At any level z the downward irradiance $I_\lambda^{\downarrow}$ may be described as:

$$I_{\lambda}^{\downarrow}(z,\theta) = I_{o\lambda}^{\downarrow}(0,\theta)\cos\theta_z . e^{-\int_{M}^{z}\frac{cdz}{\cos\theta_z}} + \int_{\phi=0}^{2\pi}\int_{\theta=0}^{\pi} S_{\lambda}^{'}(z,\theta,\varphi)(1-\delta(\theta-\theta_0)\delta(\varphi-\varphi_0))\cos\theta d\theta d\varphi \quad (2.12)$$

where $I_{o\lambda}^{\downarrow}$ is the direct beam intensity at the top of the atmosphere, $S_{\lambda}'(z,\theta,\varphi)$ is the radiance scattered from point (z, θ, φ) and the delta terms, $\delta(\theta-\theta_0)$ and $\delta(\varphi-\varphi_0)$, are dirac-delta functions which are zero everywhere except $\theta=\theta_0$ and $\varphi=\varphi_0$ where they reach a value of 1. This formulation makes the double integral valid over the entire hemisphere except when $\theta=\theta_0$ and $\varphi=\varphi_0$. The first term in the right of Equation (2.12) denotes the depletion of direct beam radiation, originally $I_{o\lambda}^{\downarrow}(\theta,\varphi)$ upon entering the medium, but depleted by the exponential term which describes how the extinction coefficient changes from the top of the medium to level z. The expression follows directly from Beer's law (Thomas and Stamnes, 1999) and must be multiplied by $\cos\theta_z$ to obtain irradiance. The second term is the diffuse irradiance which must be estimated by integrating the radiance field at level z over all polar angles (θ,φ) in the upward-facing hemisphere. This procedure ensures that the integral term in Equation (2.12) only contains diffuse radiation and not direct. A similar relationship applies for upwelling irradiance $I_{\lambda}^{\uparrow}$. The upward and downward diffuse irradiances are complicated due to multiple scattering in the atmosphere.

There are several common techniques used in the literatures to estimate downward global and diffuse irradiances, for example Two-Stream Approximation, Discrete Ordinate, Eddington Approximation and Quasi-Scattering Approximation (Chandrasekhar 1950; Lenoble, 1985; Spinrad, 1994; Nakajima *et* al., 2000; Liou 2002; Lu *et al.*, 2008). These mathematical procedures were transformed into a set of computing codes and an early routine called 5S was published by Tanre *et al.* (1990).

Since then, a number of routines such as 6S, UVSPEC, DISORT, LOWTRAN, MODTRAN, Streamer, Hydrolight, SMART and SBDART have been developed. These techniques bring more flexibility and reliability in estimating solar radiation at large scales. Systematic errors in the codes were found to generally lie within a range of 2-3%. (Key and Schweiger, 1988; Stamnes *et al.*, 1988; Mayer *et al.*, 1997; Kylling *et al.*, 1998; Mobley, 2001; Wendisch, 2003; Crisp, 2006).

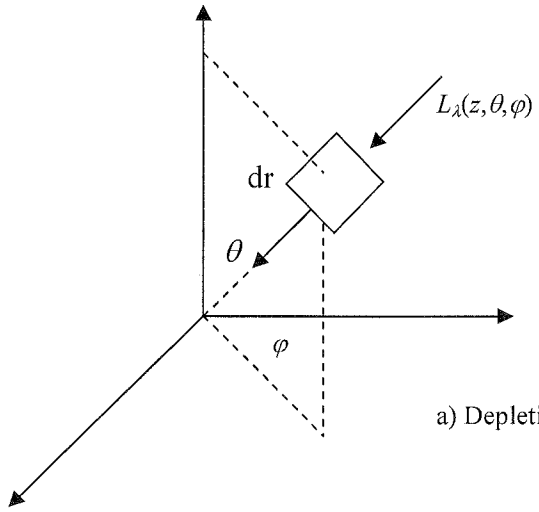

a) Depletion of direct radiance.

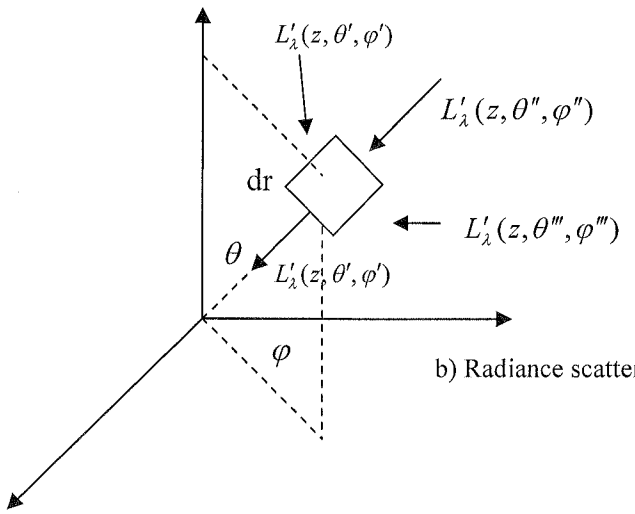

b) Radiance scattered into the direct beam direction.

Figure 2.5 The geometry of solar radiance in coordinates z,θ,φ, presenting a) direct and b) diffuse components, (Thomas and Stamnes, 1999).

2.5 Solar radiation in the water body

Solar radiation is just as important at the Earth's surface as in the aquatic environment. However, the excessive amount of shortwave radiation is an issue of concern as it is believed to cause some dramatic changes to aquatic biota (Ronald and Zaneveld, 1989; Spinrad, 1994; Neale *et al.*, 1998; Conde *et al*, 2000; Liu *et al.*, 2006). A recent study reported that UV radiation has a potential to affect concentrations of dissolved organic matter and chlorophyll (Conde *et al*, 2000), which argued the importance of understanding how the radiation behaves within a water medium. Several studies have successfully used radiative transfer and Monte Carlo methods to investigate the roles of underwater light field and optical property (Plass and Kattawar, 1972; Mobley, 1999; Mobley, 2001; Jiang and Stamnes, 2002; Carder *et* al., 2003; Mobley and Sundman, 2003; Zhang *et al.*, 2003; Lu *et al.*, 2008).

In order to understand the distribution of light, information such as the angular distribution, transmission and water properties is needed. However, measurements of these parameters are still limited. Thus, a number of techniques have been developed to provide aquatic information over local or global areas (Smith and Baker, 1981; Ronald and Zaneveld, 1989; Kirk, 1994; Hoge and Lyon, 1996; Bukata *et al.*, 1995; Ammenberg *et al.*, 2002; Liu *et al.*, 2006).

2.5.1 Boundary condition of solar radiation in water bodies

2.5.1.1) *Refraction and Reflection at air-water interface*

The interaction of radiation with the air-water interface is fundamentally described by laws of physics, and includes processes such as refraction and reflection. Refraction at the air-water interface depends on the densities of air and water. Ideally, the refraction angles of solar flux just below a flat air-water interface are calculated by Snell's Law:

$$\frac{n_a}{n_w} = \frac{\sin\theta_{w-}}{\sin\theta_{w+}} \qquad (2.13)$$

where n_a and n_w are the refractive indexes of air and water; n_w is usually defined as 1.333. θ_{w+} and θ_{w-} are the angles between the incident fluxes and normal to the air-water interface (Figure 2.6).

In terms of reflections, the incident angles of solar irradiances are identical to the reflected angles. The variations of surface reflectance depend on the incident angle of the solar beam. The reflectance at the water surfaces is computed by using the Fresnel-Reflectance formula:

$$r_{\perp} = \frac{\sin^2(\theta_i - \theta_r)}{\sin^2(\theta_i + \theta_r)} \qquad (2.14)$$

and

$$r_{\Downarrow} = \frac{\tan^2(\theta_i - \theta_r)}{\tan^2(\theta_i + \theta_r)} \qquad (2.15)$$

where $r_{\perp}$ and $r_{\Downarrow}$ are the reflectance of perpendicular and polarised incident radiation fluxes, respectively, θ_i and θ_r are the angles of incident and reflected beams, respectively (Bukata *et al.*, 1995). Moderate to high wind will reduce the reflectance of water surface particularly at high solar zenith angles (greater than 75°). An estimation suggested by Spillane and Doyle (1983) showed that strong winds can effectively decrease the surface reflectance of water (Figure 2.7). In actual events, the surface reflectance of water r_w can be estimated from solar irradiance measurements. The relation is simply defined as:

$$r_w = \frac{I_{w+}^{\uparrow}}{I_{w+}^{\downarrow}} \tag{2.16}$$

where $I_{w+}^{\uparrow}$ is the upwelling solar irradiance measured just above the water surface and $I_{w+}^{\downarrow}$ is the downwelling solar irradiance received just above the water surface. A downwelling beam irradiance measured just below the water surface $I_{w-}^{\downarrow}$ may be written as:

$$I_{w-}^{\downarrow} = I_{w+}^{\downarrow} \cdot (1 - r_w) \tag{2.17}$$

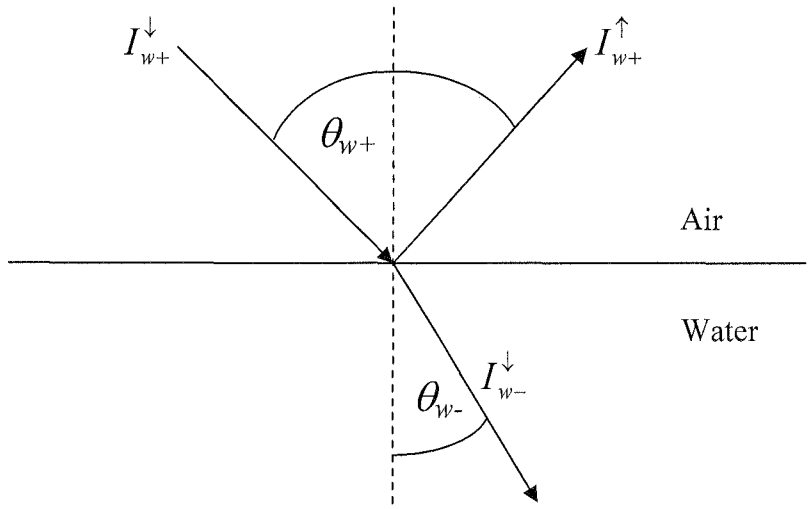

Figure 2.6 The refraction and reflection of an incident beam irradiance at the air-water interface.

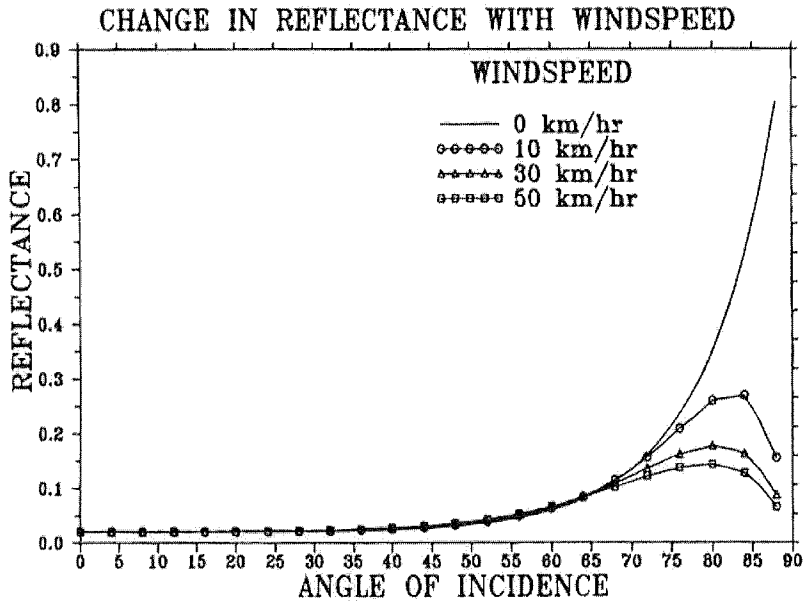

Figure 2.7 Changes in reflectance caused by wind speeds and solar zenith angles (Kirk, 1994).

In shallow water, upwelling radiance is complex and many ocean reflection estimates are treated as a Lambertian (Maritorena *et* al., 1994; Zhang *et al.*, 2003). Mobley (1999) presented various radiative transfer based techniques for estimating the reflectance from above-surface measurements. The study used the Hydrolight radiative transfer numerical model to compute remote-sensing reflectance of water surfaces. A variable, called the proportionality factors γ was introduced as a fraction of the downwelling sky radiance viewed by detector to the reflected sky radiance observed over the water surfaces. The remote-sensing reflectance, r_{rs}, may be defined as:

$$r_{rs} = (L_{w+}^{\uparrow} - \gamma L_d^{\downarrow}) / \left(\frac{\pi}{r_w} L_{0w}^{\uparrow} \right) \qquad (2.18)$$

where $L_{w+}^{\uparrow}$ is the upwelling underwater radiance received just above surface of water, $L_d^{\downarrow}$ is the sky radiance, $L_{0w}^{\uparrow}$ is the water leaving radiance and r_w is the surface reflectance of water (Mobley, 1999).

The technique appears to be accurate, but errors in evaluating the factor γ are still considerable, as γ depends on sky condition, surface wind speed and the viewing geometry of detectors, and these parameters are not easily obtained without surface observations, especially for longterm and large scale estimates. As a result, the surface reflected sky radiance is still difficult to determine from the total upwelling radiance measurements or remote-sensing data (Mobley, 1999).

2.5.1.2) *Effect of shallow bottom*

In many numerical models, the bottom boundary is an important factor to the reflected and upwelling radiance estimates (Carder *et al.*, 2003; Mobley *et al.*, 2003; Voss *et* al., 2003; Zaneveld and Boss, 2003). Angular distribution of the bottom-reflected radiance is defined as a function of incident and reflected nadir angles and azimuthal angle between the incident and reflected radiances (Figure 2.8).

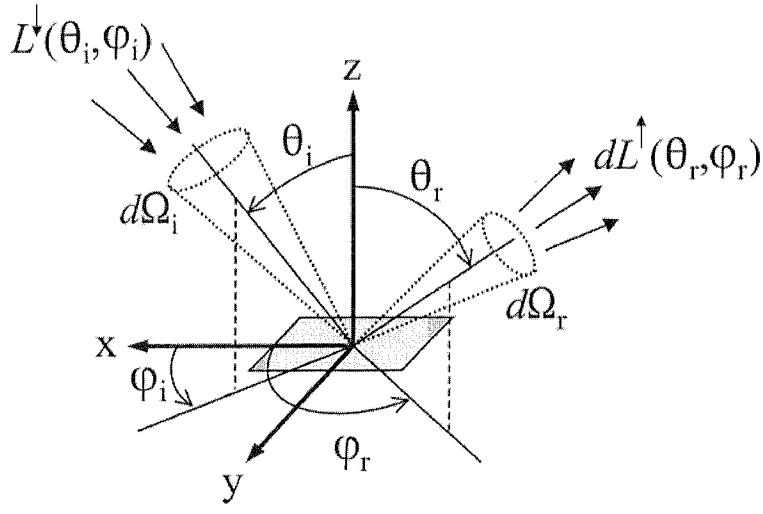

Figure 2.8. Viewing geometry of upwelling radiance reflected from a bottom surface, (taken from Mobley *et al.*, 2003).

Mobley *et al.* (2003) defines the radiance reflected from a shallow bottom as the bidirectional reflectance distribution function (BRDF), written as:

$$BRDF(\theta_i,\varphi_i,\theta_r,\varphi_r)=\frac{dL^{\uparrow}(\theta_r,\varphi_r)}{L^{\downarrow}(\theta_i,\varphi_i)\cos\theta_i d\Omega_i(\theta_i,\varphi_i)} \qquad (2.19)$$

where $dL^{\uparrow}(\theta_r,\varphi_r)$ is the radiance reflected from the surface in θ_r and φ_r directions. $d\Omega_i(\theta_i,\varphi_i)$ is the solid angle of the considered radiance. For a Lambertian surface the BRDF may be written as a function of the bottom reflectivity, *r*:

$$BRDF(\theta_i,\varphi_i,\theta_r,\varphi_r)=\frac{r}{\pi} \qquad (2.20)$$

A number if studies such as Mobley (1999), Mobley *et al.* (2003), Mobley and Sundman (2003) and Zhang *et al.* (2003) have used radiative transfer numerical models to examine the effects of bottom reflectance on underwater light distribution. Mobley *et al.*, (2003) argued that if the bottom feature is inhomogeneous, patchy and not level, the underwater light distribution estimated with Monte Carlo simulation must be computed in a three-dimensional scheme. In this hypothesis, Mobley *et al.* (2003) has developed a new bottom boundary model, called a backward Monte Carlo (BMC) 3-dimension model (BMC3D). Errors obtained from the uses of the BMC3D and 1D Hydrolight models showed a small difference of 10% (Mobley *et al.*, 2003).

2.5.1.3) *Optical property of water*

Water properties can be divided into two types called *inherent optical properties* (IOPs) and *apparent optical properties* (AOPs) (Kirk, 1994; Spinrad, 1994). IOPs

involve properties of the water medium that are independent of light sources. These are essentially the absorption coefficient a_w and scattering coefficient b_w and the volume scattering function β. On the other hand, the AOPs represent the optical properties of waters as a function of cloud cover, solar zenith angle and sea surface, which include the vertical attenuation coefficient K_d and volume reflectance r, both of which can be obtained by using direct measurements (Kirk, 1994; Spinrad, 1994).

In principle, the vertical attenuation coefficient K_d can be calculated from irradiance measurements taken at two different depths z. The equation is derived from Lambert's equation, that is:

$$I_2(z) = I_1(z)\exp(-K_d \cdot d) \tag{2.21}$$

where z is the depth and d is the distance between the two irradiances I_1 and I_2 ($d = z_2 - z_1$), hence we obtain:

$$K_d(z) = \frac{-1}{z_2 - z_1}\ln\left(\frac{I_2(z)}{I_1(z)}\right) \tag{2.22}$$

A study by Smith and Baker (1981) showed a collection of spectral K_d values derived from different sources. It shows lower K_d in the visible bands compared to the UV and infrared regions (Figure 2.9), particularly for the shorter visible wavelengths (Smith and Baker, 1981).

The second AOP, the volume reflectance $r(z)$, is defined as a ratio of upwelling and downwelling underwater irradiances ($I_w^{\uparrow}(z)$ and $I_w^{\downarrow}(z)$, respectively) (Kirk, 1994; Bukata *et al.*, 1995):

$$r(z) = \frac{I_{w+}^{\uparrow}(z)}{I_{w+}^{\downarrow}(z)} \tag{2.23}$$

The AOPs and IOPs may be estimated using empirical relationships, as presented in studies such as Prieur and Morel (1971), Smith and Baker (1981), Kirk (1984), Gordon *et al.* (1988), Lee *et al.* (1998), Ershova *et al.* (2002), Liu *et al.* (2002) and Højerslev (2004). These empirical parameterisations provide some advantages in larger-scale mapping applications where direct estimates of these optical properties are unavailable. Furthermore, oceanic remote sensing data from platforms such as Sea-viewing Wide Field-of-view Sensor (SeaWiFS) and MODIS, where the estimates of AOPs and IOPs can be made, provide a good opportunity for the study of solar radiation underwater anywhere on the globe.

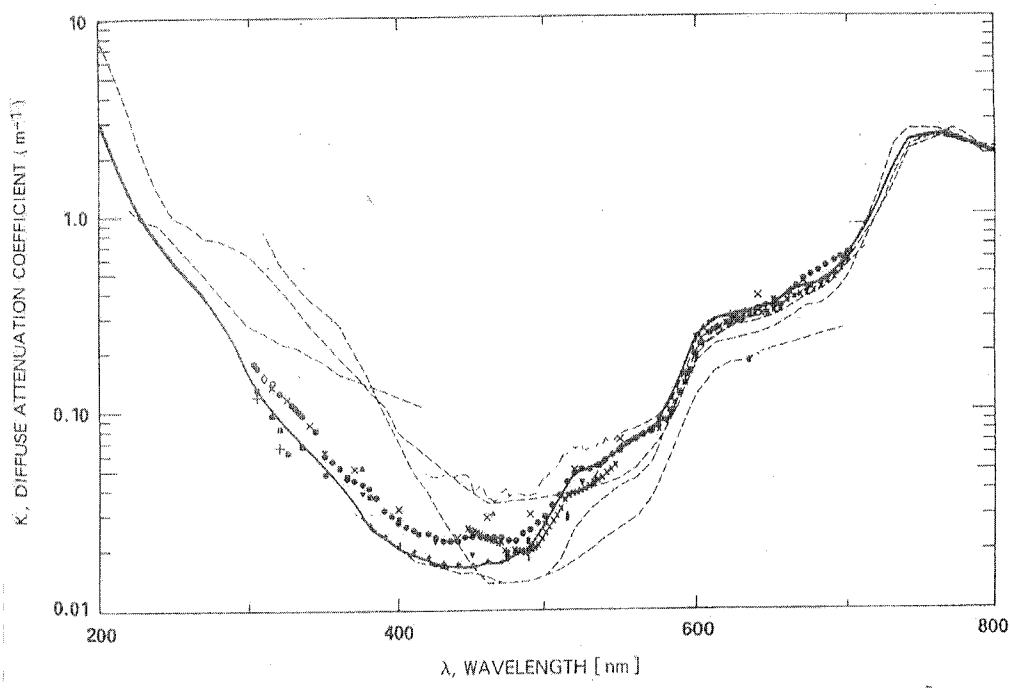

Figure 2.9 The spectral distribution of diffuse attenuation coefficient K_d collected from various locations (taken from Smith and Baker, 1981).

In most parameterisations, the attenuation coefficient K_d is used as a key parameter in the estimations. K_d can be derived by using either approximation or Monte Carlo techniques. In the cases of ocean waters, the scattering is very strong in forward directions (Plass and Kattawar, 1972; Spinrad *et al.*, 1994; Kirk, 1994) and therefore an approximation is applied to the radiative transfer equation in order to derive the K_d values, which is called Quasi-Scattering Approximation (QSA). Ideally, the QSA technique assumes that the scattering angles of photons in water are small and the total attenuation coefficient K_d becomes the beam attenuation: $a_w + b_{ws}$, where b_{ws} is the beam scattering coefficient. Therefore, the total irradiance at any depth z is approximated as the direct beam irradiance. Both a_w and b_w are strongly dependent on chlorophyll concentrations, *chlo* (Kirk, 1994). Near the water surface, this approximation can provide reliable estimates of K_d and r and it is sufficient to estimate solar irradiance in shallow waters (Gordon *et al.*, 1975; Spinrad, 1994; Liu *et al.*, 2002).

2.5.2 Underwater radiation field

Considering the solar irradiance flux within a water body, the vertical attenuation of the irradiance is most simply described as an exponential function. The variation of underwater solar irradiance is also wavelength-dependent (Kirk, 1994; Spinrad, 1994; Bukata *et al.*, 1995; Ershova *et al.*, 2002). Due to the low values of K_d in these spectral regions (Figure 2.8), PAR and UVB progressively dominate at greater depths. The values of K_d change spatially and spectrally due to dissolved organic matter in water, and are still very limited in their application to global areas.

In order to estimate underwater solar irradiance, some studies derived the empirical K_d models by using measurements collected from *in situ* and the results of these models are very specific to the local environments (Tilzer *et al.*, 1995; Schanz *et al.*, 1997; Lee *et al.*, 1998). On the other hand, the uses of radiative transfer and Monte

Carlo methods have been presented and the models can provide accurate outputs for spatial and temporal frameworks (Plass and Kattawar, 1972; Mobley *et al.*, 1993; Spinrad, 1994; Bukata *et al.*, 1995; Mobley 1999). For atmospheric-ocean system, discrete ordinate methods are a feasible way for underwater light field estimates as well as the Monte Carlo models (Thomas and Stamnes, 1999; Yan and Stamnes, 2002; Gjerstad *et al.*, 2003). Although, these techniques are well accepted in many studies, but the solutions are still difficult to derive for a large computational scheme. Therefore, the approximation techniques, such as Quasi-scattering approximation (QSA), or sometimes called as Quasi-analytical algorithm (QAA), and Two-Stream Approximation, have been used to provide a fast estimation for underwater irradiance and optical parameters in several remote-sensing studies (Aas 1987; Kirk, 1994; Aas and Højerslev, 1999; Højerslev 2001; Ammenberg *et* al., 2002; Ershova *et al.*, 2002; Liu *et al.*, 2006).

Details of the Monte Carlo, DISORT and other numerical techniques used for underwater radiation estimates are summarised in the following sections.

2.5.2.1) *Monte Carlo Method*

In physical environments typified by complex boundary conditions, or spatially-varying absorption coefficients a Monte Carlo approach might be warranted. This approach traces the exact behaviour of a stream of photons subject to the scattering and absorption properties of the medium and the complexities of the boundary conditions. The photons are injected into the complex medium and all obey the same scattering and absorption laws, but their particular path is subject to a random fluctuation within the constraints of the absorption and phase function. Eventually, an exact representation of the radiation field is obtained after a great number of photons are injected.

Monte Carlo methods consider the physical interactions between many photons and medium in a statistical manner (Plass and Kattawar, 1969; Kirk, 1981). The collisions between photons and the molecules of water can be considered as either scattering or absorption. In absorption processes, the photons lose some energy but continue in the same direction. In scattering processes, photons keep going in new directions as determined by their phase function. The process continues with many photons until a statistically reliable pattern is obtained (Bukata *et al.*, 1995).

In the past century, Monte Carlo simulations were developed by various groups of scientists to perform simulation of radiance distribution in atmospheric (or aquatic) medium (Plass and Kattawar, 1972; Gordon *et al.* 1975; DiToro, 1978; Jerome *et al.*, 1988; Kirk, 1994). The techniques used in these studies are similar in that they generate a set of random numbers in a range between 0 and 1 to simulate the attenuation events of photons that propagate along a distance l in a three-dimensional volume of an attenuating medium (Lenoble, 1985). The distance l of any scattering/absorption interaction is determined as (Bukata *et al.*, 1995):

$$l = \frac{-1}{c_w} \ln RN \qquad (2.24)$$

where c_w is the attenuation coefficient of water (a_w+b_w) and RN is a random number in the range [0, 1]. Monte Carlo techniques are time-consuming, as they require very large numbers of photons to be followed to derive the instantaneous irradiance beginning at the water surface. For example, estimation of a light flux arriving on a 1 m^2 horizontal surface in high summer requires approximately 10^{21} photons (Kirk, 1994). The calculation time for a Monte Carlo model depends on the amount of photons, wavelengths and optical properties of the water. However, the precision of Monte Carlo simulations is directly related to the number of photons (Bukata *et al.*, 1995).

2.5.2.2) *Monte Carlo approximation based on measurements*

Monte Carlo simulations are useful in providing estimates of K_d. To derive the relationships, a Monte Carlo model is first employed to simulate the trajectories of photons for given water. Once the results are obtained, regression estimates of absorption and scattering coefficients (a_w and b_w) linked to the K_d values are then derived (Bukata *et al.*, 1995). An early Monte Carlo simulation by Kirk (1981) presented an empirical K_d model based on volume scattering measurements taken at San Diego:

$$K_d = (a_w^2 + 0.256 a_w b_w)^{1/2} \tag{2.25}$$

Gordon *et al.*, (1975) proposed a simple K_d model based for a flat ocean which assumes the single scattering albedo (α_o) did not exceed 0.8. The model was written as:

$$\begin{aligned} K_d &= \{a_w + b_w \cdot [1 - F(\mu_o)]\} / \mu_o \\ &= c_w \cdot [1 - \alpha_o F(\mu_o)] / \mu_o \end{aligned} \tag{2.26}$$

where $F(\mu_o)$ is the forward scattering probability, α_o is the scattering albedo and μ_o is cosine of . Equation (2.26) derived at α_o = 0 may be written as (Gordon *et al.*, 1975; Spinrad *et al.*, 1994):

$$\frac{K_d}{c_w D_0} = 1 - \alpha_o F \tag{2.27}$$

or

$$K_d = D_0 (a_w + b_{wb}) \tag{2.28}$$

where

$$D_0 = \frac{1}{\cos\theta_{w+}} \tag{2.29}$$

and θ_{w+} are the angles between the incident fluxes and normal to the air-water interface.

In conclusion, Monte Carlo method can be vary accurate and provide exact data in complex environment. On the negative side, they are time consuming requiring much considerable computer power. Approximation techniques are much more practical and faster to run but are limited to the layer near the surface eventually, the choices of the approach to be followed (Monte Carlo approximation or Discrete Ordinate) depend very much on specific set that has been studied.

2.5.2.3) *Other numerical models*

a) Discrete-ordinate radiative transfer method

In principle, discrete-ordinate radiative transfer (DISORT) was originally developed by Chandrasekha (1950). The technique is useful for computing transfer of radiation in a plane-parallel atmospheric medium (or aquatic medium). In principle, the technique considers the discretization of the basic radiative transfer. In case of underwater irradiance estimate, DISORT was employed to compute optical properties of water. Because solution of DISORT is analytic, thus computational speed is fast and can be applied into any scale of the system without losing efficiency (Mobley, 1999; Liou, 2002).

The DISORT model is used to solve the radiative transfer equations using multiple stream. For azimuthally average condition, the radiative transfer equation for downward fluxes can be written as:

$$-\mu\frac{dI^{+}(z,\mu)}{dz} = I^{+}(z,\mu) - \frac{\alpha}{2}\int_{0}^{1} P(\mu',-\mu)I^{+}(z,\mu')d\mu' - \frac{\alpha}{2}\int_{0}^{1} P(-\mu',-\mu)I^{+}(z,\mu')d\mu' - I_{s}(z) \tag{2.30}$$

where I^{+} is diffuse intensity defined as optical depth z and angle μ $(\mu = \cos\theta_i)$, α is the single scattering albedo, $P(\mu',\mu)$ is the scattering function defined by the relative angle μ', μ and X_o is the component of the direct beam irradiance. $I_s(z)$ is the direct beam irradiance at a particular depth that travels into the direction of μ_o. Solution of this differential/integral equation is simplified by the discrete ordinate method.

Since 1988, DISORT has been transformed into numerical computing software (Stamnes *et al.*, 1988; Thomas and Stamnes, 1999). A number of studies have shown the use of DISORT program to compute distribution of underwater irradiance and optical properties of waters (Stamnes *et al.*, 2000; Ershova *et al.*, 2002; Yan and Stamnes, 2002; Lu *et al.*, 2008). At present, the DISORT program is widely applied in radiative transfer schemes, although they have been used mostly over the atmosphere. Lately, this technique has been used in coupled ocean-atmosphere models (Jin and Stamnes, 1994; Thomas and Stamnes, 1999; Jiang *et al.*, 2005).

b) N-stream approximation

Solution of radiative transfer models is solved analytically and the integral functions of DISORT can be replaced with summation of a polynomial of different degrees over a finite number of points in a considered medium. From this model, stream approximation techniques are developed for irradiance calculation. For two-stream approximation, there are only two components for the polynomial (I^{+}, I^{-}). In the four-

stream approximation, I now has four components two downwelling $(I^+(z_1,\mu_1), I^+(z_1,\mu_2))$ and two upwelling $(I^-(z_1,\mu_1), I^-(z_1,\mu_2))$.

Solution of this differential/integral equation is simplified in the discrete ordinate method (DISORT). The two integrals in the right hand side of Equation 2.30 are replaced by a polynomial sum with components:

$$W_1P(\mu',\mu)I^+(z,\mu_1)+W_2P(\mu',\mu)I^+(z,\mu_2)+W_3P(\mu',\mu)I^+(z,\mu_3)+...W_nP(\mu',\mu)I^+(z,\mu_n)$$

and

$$W_1P(-\mu',\mu)I^-(z,\mu_1)+W_2P(-\mu',\mu)I^-(z,\mu_2)+W_3P(-\mu',\mu)I^-(z,\mu_3)+...W_nP(-\mu',\mu)I^-(z,\mu_n)$$

The length of the summation depends on the number of streams, N_o. If N=1, there is only one component. For N=2, there are four components and so on. The solution reduces to a system of coupled differential equation. Commonly six or eight streams may be used.

c) Hydrolight

Hydrolight is a radiative transfer based numerical model, which was developed by Mobley and Sundman, (1999). Inputs of Hydrolight program consist of absorption and scattering libraries, the incident sky radiance, the water bottom boundary and surface wind profile. Condition of waters used in Hydrolight program can be varied from pure natural water to a variety of turbid waters that involve features of suspended CDOM, chlorophyll and mineral particle substances. The reflectance and bottom surface models of Hydrolight can be set as a simple Lambertian with input of BRDF function. In order to define the direct and diffuse downwelling irradiances above water, two semi-empirical models developed by Gregg and Carder, 1990 and Harrison and

Coombes (1988) were used as an optional choice of the Hydrolight program (Mobley and Sundman, 2001).

The application of Hydrolight radiative transfer model is versatile. Many studies used Hydrolight model to examine spectral relationship of the inherent and apparent optical properties (Liu *et al.*, 1999; Liu *et al.*, 2006) and present the effects of the bottom boundary and variation of BRDF (Mobley, 2003; Mobley and Sundman, 2003). Other studies, such as Lee *et al.* (1998) and Tozzi *et al.* (2004), used Hydrolight to estimate remote-sensing reflectance over large regions. However, these built-in models of the Hydrolight program are limited without ground-based measurements. In remote-sensing application, sky irradiance and bottom boundary models are still difficult to determine in real situations.

Overall, the techniques used for estimating underwater light field share the same physics that depends on boundary condition and optical properties of the medium. These detailed input data can be detailed and demanding, often providing results that are very specific to local environments. So far, the link of above to underwater solar radiation has not been addressed well and several estimations only focus on a specific state. For large scale predictions, Monte Carlo approximation seems to be the only choice to help reduce the computational time.

Chapter 3

Literature review

Solar radiation data has been widely used for agricultural, meteorological and biological applications worldwide (Gautier, 1980; Hansen *et al.*, 2002; Wloczyk and Richter, 2006). In remote areas, data can not be provided due to the lack of observations, and mathematical models are therefore used instead to fill the gap. In general terms, radiative transfer theory is a basic concept used to describe solar radiation fluxes as they travel through a medium. Chandrasekhar (1950) documented a classic model which used radiative transfer theory to estimate the depletion of solar radiation in the atmosphere. However, the model requires local atmospheric profiles to parameterize the attenuation coefficients of solar radiation, and this task is difficult in many areas due to the need for comprehensive atmospheric corrections. Techniques for deriving solar radiation data on a global scale have been developed by many groups over the past twenty-five years (Gautier, 1980; Dedieu *et al.*, 1986; Pinker and Laszlo, 1992; Frouin and Chertock, 1992; Meerkoetter *et al.*, 1997; Verdebout, 2000; Hensen *et al.*, 2002; Wloczyk and Richter, 2006).

The above studies rely on the satellite approach, and in particular, geostationary satellite data as a primary source of high-frequency atmospheric information (typically providing data at a frequency of 9 images to 13 images per day). Satellite data consists of arrays of digital numbers of the Earth-atmosphere reflectance, featuring scenes of clouds and the Earth's surface. In principle, a satellite sensor observes radiance that is reflected from the atmosphere, clouds and the Earth's surface (Gautier, 1980). Therefore, solar radiation reaching the ground can be solved as a residual if atmospheric properties are known. This radiation balance may be illustrated by a simple relationship

developed by Nunez and Kalma (1996), who described the extraterrestrial solar irradiance ($I_o^{\downarrow}$) as equal to the sum of the backscattered upward irradiance potentially observed by the satellite ($I_o'^{\uparrow}$), the irradiance that is attenuated in the atmosphere ($I_{atm}^{\downarrow}$) and that absorbed by the Earth's surface (I_G):

$$I_o^{\downarrow} = I_o'^{\uparrow} + I_{atm}^{\downarrow} + I_G \qquad (3.1)$$

The downwelling solar irradiance ($I^{\downarrow}$) may be derived using the relationship:

$$I_G = (1-\rho_g)I^{\downarrow} = I_o^{\downarrow} - I_o^{\uparrow} - I_{atm}^{\downarrow} \qquad (3.2)$$

where ρ_g is the surface albedo.

Most of the developed techniques rely on processing the satellite-derived reflectance data into an equivalent surface irradiance. Generally, the validation of satellite models show errors that range between 5% and 20%, depending strongly on the model parameterisation and the input satellite data (Nunez and Kalma, 1995; Laine *et al.*, 1999; Tovar and Baldasano, 2001; Kandirmaz *et al.*, 2004). Although the use of high spatial resolution satellite data has increased over the past 25 years (Laine *et al.*, 1999; Wang *et al.*, 2000; Hansen *et al.*, 2002; Wang *et al.*, 2005), there has not been any accompanying significant improvement in the accuracy of the estimations.

Both physical and statistical approaches are used in satellite models which estimate solar radiation (Gautier, 1980; Nunez and Kalma, 1995; Laine *et al.*, 1999; Flores Tovar and Baldasano, 2001). Physical models employ satellite reflectivity and atmospheric data in radiative transfer schemes such as the Two-Stream Approximation, Discrete Ordinate Radiative Transfer (DISORT), Delta-Eddington to estimate solar

irradiance. In general terms, the analyses also provide atmospheric transmission, surface albedo and cloud distribution, (Gautier, 1980; Dedieu, 1986; Pinker and Laszlo, 1992). An advantage of using a physical approach is that the model can be further applied anywhere on the globe. One disadvantage is that estimation is not possible without atmospheric data. Statistical methods, by contrast, are site-dependent and rely on accurate records of solar radiation measurements to parameterize the linear relationship between measurements of solar radiation and satellite data. The parameterization expresses the empirical relationship as a set of coefficients based on satellite reflectivity data, and is therefore applicable anywhere in the satellite domain. However, the regression coefficients can only be used in regions where the statistical regression is valid.

3.1 Cloud algorithms

Clouds play an important role in the attenuation processes (Iqbal, 1983). For both statistical and physical approaches, a number of techniques used for determining models of clouds were developed. Some approaches treat clouds by discriminating sky conditions into clear, partly cloudy and overcast (Gautier, 1980; Dedieu, 1986; Darnell *et al.*, 1988; Schmetz, 1991; Robert *et al.*, 1991; Laine *et al.*, 1999). Other approaches use satellite data to determine the amount of clouds, commonly expressed as a fraction called *cloud index* or *cloud fraction* (Tarpley, 1979; Darnell *et al.*, 1988; Tovar and Baldasano, 2001; Kandirmaz *et al.*, 2004). Basically, the cloud fraction (n) is determined as a ratio between the relative minimum and maximum reflectivity (Cano *et al.*, 1986; Tarpley, 1979). This fraction represents the opacity of the overhead sky. A well-known equation for estimating cloud index (C_n) from satellite data was presented by Cano *et al.* (1986):

$$C_n = \frac{r_i - r_{\min}}{r_{\max} - r_{\min}} \qquad (3.3)$$

where r_i is the current satellite reflectance, r_{min} and r_{max} are the minimum and maximum reflectance representing surface and cloud, respectively. A study by Tarpley (1979) divided the cloud index into three intervals, those pixels that are clear: C_n <0.4, partly cloudy: 0.4≤ C_n <1.0 and overcast: C_n =1.0, and these were subsequently used for estimating solar irradiance, (Tarpley, 1979).

Other studies, such as Gautier (1980), Pinker and Ewing (1985) and Koelemeijer and Stamnes (1999), have developed models for estimating surface solar irradiance by simulating layers of the atmosphere. Clouds are treated as an isotropic and homogeneous simple layer, although sometimes separated into two layers (Frouin and Chertock, 1992; Koelemeijer and Stamnes, 1999), or three layers (Pinker and Ewing, 1985). Radiative transfer models are used to provide cloud transmission values. Some further details of these models will be discussed in this chapter. The following section outlines studies which used the satellite approach during the period 1980 to 2005.

3.2 Statistical models

The statistical model is a linear combination of regression parameters which are derived from a relationship between satellite data and pyranometer measurements. The model may be written as functions of solar zenith angle, cloud index, precipitable water, amongst others, that is:

$$I = a_0 + a_1\theta_z + a_2\alpha_{EA} + a_3 w + \ldots \qquad (3.4)$$

where, I is the solar irradiance, θ_z is the solar zenith angle, α_{EA} is the Earth-atmosphere albedo, which is influenced by clouds, w is the precipitable water vapour and $a_0,...a_n$ are the regression coefficients.

Techniques for obtaining a set of the regression coefficients have been documented in many studies, such as those of Schmetz (1991), Islam and Exell (1996), Tovar and Baldasano (2001) and Kandirmaz *et al.* (2004). These methods derive on an empirical relationship between cloud index (C_n) and the corresponding atmospheric transmission (T) which is defined as the ratio of solar radiation measured at the ground to the top of the atmosphere. A simple formula for the relationship may be written as (Tovar and Baldasano, 2001):

$$T = a_1 \cdot C_n + a_0 \tag{3.5}$$

where a_0 and a_1 are the coefficients derived from regression techniques. The cloud index can take different forms. Many approaches derive the values from satellite data using a ratio between measured reflectance and its maximum in the scene.

In early studies, the models were simplified by discriminating the sky appearances for clear, intermediate and overcast conditions (Tarpley, 1979; Gautier, 1980; Schmetz, 1991).

Tarpley (1979) separated the sky conditions into three categories denoted by three intervals of cloud fraction C, which was computed as follows:

$$C = \frac{0.5N_2 + N_3}{N_1 + N_2 + N_3} = \frac{N_2 + 2N_3}{2N} \tag{3.6}$$

where N_1, N_2 and N_3 are the numbers of pixels in the clear, partly cloudy and cloudy cases, respectively, and N is the total number of pixels in the region of interest (Tarpley, 1979). The study used relative brightness threshold to define the characteristics of clouds and cloud-free pixels. The hourly solar irradiance model was partitioned into three groups:

$$I = a + b\cos\theta_z + cT_{wR} + dC + e\left(\frac{\overline{B}_m}{B}\right)^2, \qquad C<0.4 \qquad (3.7)$$

$$I = a + b\cos\theta_z + cC\left(\frac{\overline{B}_{cld}}{B_0}\right)^2, \qquad 0.4\leq C<1.0 \qquad (3.8)$$

$$I = a + b\cos\theta_z + c\left(\frac{\overline{B}_{cld}}{B_0}\right)^2, \qquad C=1.0 \qquad (3.9)$$

where I is the hourly solar irradiance, θ_z is the solar zenith angle, T_{wR} is the transmittance of a clear atmosphere accounting for water vapour and Rayleigh scattering and water vapour absorption, C is the cloud fraction, B is the visible clear brightness of satellite pixels, B_0 is the normalized clear brightness of satellite pixels, $\overline{B}_m$ is the mean target (surface) brightness, $\overline{B}_{cld}$ is the mean cloud brightness and a, b, c, d and e are regression coefficients.

The estimated hourly and daily sum of hourly radiation was compared against pyranometer measurements. The clear-sky case showed standard errors of less than 10% and an overestimation occurred for various reasons; for example, the appearance of cloud shadows and the excessive illumination of cloud scenes by the morning sun. However, there were considerably larger errors for the estimation of solar radiation for cloudy (standard error 30%) and partly cloudy sky (standard error 50%) when compared to the mean values.

Schmetz (1991) proposed a simple technique which differentiated between three clear-sky and two cloudy cases. The equation estimating the solar flux was written in a form relating the balance of solar net flux measured at the top of atmosphere and the balance at the surface. The model uses a simple concept of energy conservation simulating the physical processes of the atmosphere:

$$I_{sc}\cos\theta_z(1-\alpha_{TOA}) = I^{\downarrow}(1-\alpha_g) + I^{\downarrow}_{atm} \qquad (3.10)$$

where I_{sc} is the solar constant, $I^{\downarrow}$ is downward solar irradiance, θ_z is the solar zenith angle, α_{TOA} is the planetary albedo, α_g is the surface albedo and $I^{\downarrow}_{atm}$ is the solar irradiance absorbed in the atmosphere. The solar flux at the surface and the top of atmosphere were examined to obtain empirical regression parameters for each sky case. For a given condition the model was given as:

$$I^{\downarrow}_{atm} \approx a_1\, I_{sc} + a_0 \qquad (3.11)$$

where a_1 and a_0 are the constant coefficients. The validation gave good agreement with a monthly mean standard error of 5%.

Although the techniques of Tarpley (1979) and Schmetz (1991) may be applicable globally, the coefficients are strongly linked to the narrow set of cloud conditions experienced in these two studies. To overcome this problem, the coefficients should be parameterised from all sky conditions recorded over longer periods.

Another approach is to link a satellite-derived reflectivity (α'_{EA}) with an atmospheric transmissivity T derived from pyranometer measurements (Nunez, 1987;

Nunez *et al.*, 1990). Here T is defined as the fraction of the extra-terrestrial solar radiation flux (I_o) that reaches the Earth's surface, written as:

$$T = \frac{1-\phi-\alpha_{EA}}{1-\alpha_g} \approx a_0 + a_1\alpha'_{EA} \tag{3.12}$$

where a_0 and a_1 are related to properties of the atmosphere and surface in a conservative fashion, ϕ is direct beam absorption. Note that α_{EA} is a broadband estimate and is different from the satellite reflectivity α'_{EA}, which is constrained to the satellite window channel. In its simplest form, a plot of T vs α'_{EA} should give the regression constants a_0 and a_1, therefore allowing T to be estimated anywhere in the scene. However specific values of these coefficients are far from universally applicable as they depend on many other factors such as narrowband-broadband spectral differences, Lambertian characteristics of clouds and Earth surfaces as well as aerosol effects.

To provide a more universal relationship for Equation (3.12), Nunez (1993) derived expressions for both T and α'_{EA} in terms of the main radiation components of the atmosphere. These had the form:

$$T = [I_c]/[I_o] = (1-r_a-\delta r)(1-\phi_W-\delta\phi)/[1-(r_A+\delta r)r_g] \tag{3.13}$$

$$\alpha'_{EA} = \alpha'_a + \delta\alpha' + (1-\alpha'_a-\delta\alpha')^2(1-\phi_0-\delta\phi')\alpha'_g \tag{3.14}$$

where primes denote values in the satellite band and no primes refer to broadband values. As previously, r denotes an atmospheric reflection, ϕ is absorption, the subscripts o and w stand for ozone and water vapour respectively, and δ terms denote

extra scattering and absorption due to local aerosol sources. It is possible to solve the above two equations in terms of albedo α_a and α'_a. These may be related to each other, provided measurements of T and α'_{EA} are concurrent. Nunez (1993) showed that α_a and α'_a are strongly related to each other in many geographic locations in the western Pacific Ocean, largely independent of aerosols, water vapour and cloud reflection properties.

In the mapping scheme, the satellite estimate is transformed into α'_a and then into α_a. The surface irradiance may then be estimated in terms of broadband quantities:

$$[I_c] = [I_o] \cdot (1 - \alpha_A - \delta\alpha)(1 - \phi_w - \delta\phi) / (1 - (\alpha_a + \delta\alpha)\alpha_w) \qquad (3.15)$$

The validation of the model against the independent data measurements gave low errors. On monthly scale, RMS errors were around 14 W-m^{-2}.

Islam and Exell (1996) demonstrated a low-cost technique to derive solar radiation maps over a region of Thailand. They acquired satellite data with a low-cost operational system established in 1993 at the Asia Institute of Technology (AIT), Thailand. The Weather Facsimile (WEFAX) images were collected using a simple instrument comprising an HF receiver with a parabolic antenna that was processed via a personal computer.

However, there were only three images a day from WEFAX data. The study improved the process by first determining a mean effective cloudiness factor $\overline{C}_{eff}$ from satellite images, as a combination of instantaneous cloudiness collected at morning, afternoon and evening scans:

$$\overline{C}_{eff} = W_m C_m + W_a C_a + W_e C_e \qquad (3.16)$$

where C_m C_a, and C_e are cloudiness values, W_m, W_a and W_e and are the respective weights for each cloudiness value, there were separated into morning (m), afternoon (a) and evening (e) (note that $W_m + W_a + W_e = 1$). On the other hand, the averaged atmospheric transmission $\overline{T}$ was calculated as the ratio between the measured and the top of the atmosphere radiation. A number of linear statistical relationships between $\overline{C}$ and $\overline{T}$ were obtained with a number of coefficients. Three relationships were used, as the regression coefficients varied with zenith angle:

Case 1) Only afternoon $$\overline{T} = a + bC_a \quad (3.17)$$

Case 2) Afternoon and morning $$\overline{T} = a + b_a C_a + b_m C_m \quad (3.18)$$

Case 3) Afternoon, evening and morning $$\overline{T} = a + b_a C_a + b_e C_e + b_m C_m \quad (3.19)$$

The coefficients a and b for each case were obtained by using multiple regression analysis. The mean RMS-error presented in this study was obtained as 14% compared to the measured mean values. The standard error yielded 12.9% compared against mean daily global radiation measurements.

In the past ten years satellite data have been available over longer periods of record and at higher diurnal frequency. Statistical models were later applied mainly to estimate solar radiation for specific regions. With improved data sets came more reliable estimates, but without much difference in methods and data collection.

Tovar and Baldasano (2001) employed the statistical technique to estimate solar radiation for Catalonia, Spain. Similar to the study by Nunez (1993), the methodology was not concerned in sky classification, but instead, the model recognized cloud opacity using a cloud index. This study obtained the regression coefficients by deriving an empirical relationship between atmospheric transmission, T and the corresponding

cloud index, C_n from 11 months of satellite reflectance records. The cloud index at any location $C_n(i,j)$ with coordinate (i, j) was estimated by using a formula proposed by Cano *et al.* (1986):

$$C_n(i,j) = \frac{\alpha(i,j) - \alpha_{\min}(i,j)}{\alpha_{\max}(i,j) - \alpha_{\min}(i,j)} \tag{3.20}$$

So that, the empirical relationship at a given location (i,j) was written as:

$$T(i,j) = a \cdot C_n(i,j) + b \tag{3.21}$$

Once the coefficients, a and b, were obtained, the hourly global solar radiation at any location $[I(i,j)]$ was computed by using the product of the transmission $T(i,j)$ and the extraterrestrial solar radiation $[I_o(i,j)]$:

$$[I(i,j)] = [I_o(i,j)] \cdot T(i,j)\,. \tag{3.22}$$

RMS errors of the estimated hourly global solar radiation ranging between 3% and 16% were obtained for all sky conditions.

A similar approach was followed by Kandirmaz *et al.* (2004) to map solar radiation over Turkey. METEOSAT data for the period July 1997 to December 1998 was used, along with pyranometer data for seven stations from the Turkish Meteorological Service. Regression analysis between pyranometer transmission and satellite-derived cloud index was performed. The transmission relationship was applied to maps of monthly averages of daily solar radiation. The accuracy of the predicted

monthly-mean daily solar radiation compared with the measurements yielded 5% for cloudless conditions, but errors increased to 40% for overcast days.

3.3 Physical Models

Physical models rely on the processes of atmospheric scattering and absorption. Generally, the approach uses albedo information derived from satellite data to evaluate atmospheric properties and cloud (Gautier *et al.*, 1980). Surface irradiance may be described as:

$$I = f(\theta_z, O_3, aer, vis, w, cl) \qquad (3.23)$$

where I is the solar irradiance, θ_z is the solar zenith, O_3 is the total column ozone amount [Dobson units], cl is the cloud parameter, aer is the aerosol amount and w is precipitable water vapour.

In the past twenty-five years, many physical models have developed to estimate solar radiation at the surface (Gautier *et al.*, 1980; Diak and Gautier, 1983; Pinker and Ewing, 1985; Dedieu, 1987; Darnell *et al.*, 1988; Gautier, 1988; Pinker and Laszlo, 1991; Robert *et al.*, 1991; Frouin and Chertock, 1991; Laine *et al.*, 1999; Wang *et al.*, 2000; Hansen *et al.*, 2002; Wang *et al.*, 2005; Wloczyk and Richter, 2006). A few of these studies have applied physical models at the continental or global scale (Dedieu, 1987; Pinker and Laszlo, 1991; Hansen *et al.*, 2002).

In early studies, the approaches concentrated on simulation and algorithm development. Gautier (1980) used simple energy conservation to show that incoming solar radiation at the surface is primarily reduced by scattering and absorption processes (Figure 3.1). Pinker and Ewing (1985) developed a three-layer atmospheric model describing the attenuation of solar radiation in the atmosphere. It features a cloud layer

bounded by two clear atmosphere layers (Figure 3.2). A similar approach was taken by Frouin and Chertock (1992). Most of these models assume that attenuation is homogeneous and isotropic. These studies solve the radiative transfer equation based on atmospheric properties derived from tables or measured at the surface. Pinker and Ewing (1985) and Pinker and Laszlo (1992) used look-up tables to determine the net solar flux at the ground. Details of these investigations are described in the following section.

Gautier *et al.* (1980) employed the reflectance data obtained from the Visible Infrared Spin Scan Radiometer (VISSR) on the GOES-2 satellite to evaluate cloud distributions. The satellite data were analysed by modeling the reflectance properties as seen by the satellite. Incident solar radiation and net energy were estimated for cloudless and cloudy sky conditions, with sky conditions determined from satellite brightness data.

The clear sky model considers the energy balance of the attenuated downwelling radiation and the upwelling radiation that is reflected from the atmosphere and the surface. To solve the model, a net solar radiation incident at the surface I_{net} is written as:

$$I_{net} = I_o^{\downarrow}(1-r)(1-\phi(u_1)) \times [1 - r_g(1-r_1) - r_g{}^2 r_1] \qquad (3.24)$$

where $I_o^{\downarrow}$ is the downwelling extraterrestrial solar radiation, r is the atmospheric reflection coefficient for direct radiation, r_1 is the atmospheric reflection coefficient for diffuse radiation, $\phi(u_1)$ is the absorption coefficient for water vapour path u_1 and r_g is the surface albedo.

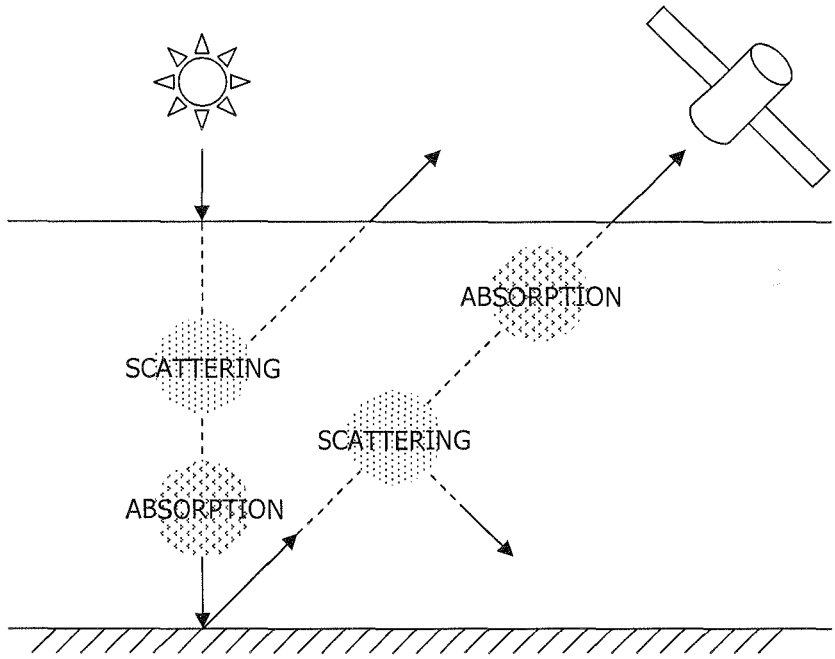

Figure 3.1 The atmospheric model proposed by Gautier (1980).

The model included water vapour absorption, and cloud absorption in cloudy conditions. These quantities were calculated on the assumption that narrowband variables derived from satellite data are the same as broadband variables used in the estimation of surface irradiance. Using the brightness values obtained from the satellite, the values of surface albedo, cloud threshold and cloud thickness were derived and precipitable water was assigned as a fraction to obtain the water vapour absorption above and below the cloud. The net downwelling radiation under a cloudy sky is given as:

$$\begin{aligned} I_{net} &= I_o^{\downarrow}(1-\alpha)[1-\phi(u_1)_t](1-\alpha_c)\times(1-\phi_{clo})[1-\phi(u_1)_b](1-\alpha_g) \\ &= I^{\downarrow}(1-\alpha_g) \end{aligned} \tag{3.25}$$

where

$\phi(u_1)_t$ and $\phi(u_1)_b$	absorption of downward solar radiation above and below the cloud, respectively
$\phi(u_2)_t$ and $\phi(u_2)_b$	absorption of upward solar radiation above and below the cloud, respectively
ϕ_{clo}	cloud absorption
α_c	cloud albedo.

The models were tested against pyranometer measurements in Canada. Over-estimation occurred for two conditions: 1) at low solar elevation angle and 2) during appearances of very thick cloud cover. Overall, the comparison of daily solar radiation made on a number of separate days between the satellite-estimation and ground measurements yielded a statistical error of less than 9%.

The model was improved in a later study (Diak and Gautier, 1983). Firstly, the modification included ozone absorption, which previously was neglected. Secondly, the physical processes of surface albedo, cloud threshold and cloud albedo were modified to account for the VISSR bandwidth. The comparison between pyranometer measurements and the new model achieved a better prediction of 5.3% of standard error.

Pinker and Ewing (1985) presented a three-layer atmospheric model which used a satellite-derived cloud optical thickness. The study examined two years (1981-1982) of surface measurements and satellite data collected from five specific locations in Canada which were utilized for the calculation and validation processes. The atmospheric structure was separated into three layers, bounded at 2 km and 5.5 km (Figure 3.2). The attenuation occurred within each layer was estimated as a function of albedo, single scattering ρ, asymmetry factor g and optical thickness τ. A set of ρ, g and

τ were evaluated by employing the Delta-Eddington technique, at four spectral bands (0.3-0.4 μm, 0.4-0.5 μm, 0.6-0.7 μm and more than 0.7 μm). The variables used in the parameterisations were generated as a data library within finite ranges:

Single scattering	$0.1 < \rho < 0.99$,
Asymmetry factor	$0 < g < 0.95$,
Optical thickness	$0.01 < \tau < 100$,
Surface albedo	$0 < \alpha_g < 0.8$.

The final step involved identifying cloud optical depth. Surface irradiance and planetary albedo were then estimated with these data sets and plots were done of various parameters including solar zenith angle, single scattering and optical thickness (Figures 3.3 and Figure 3.4). Comparison were made in two experiments, the first one used GOES-E VISSR data to predict daily solar radiation at the surface, while the second used cloud observations to estimate daily surface solar radiation. The standard error from both estimations compared to mean daily solar radiation values was 16% and 18%, respectively.

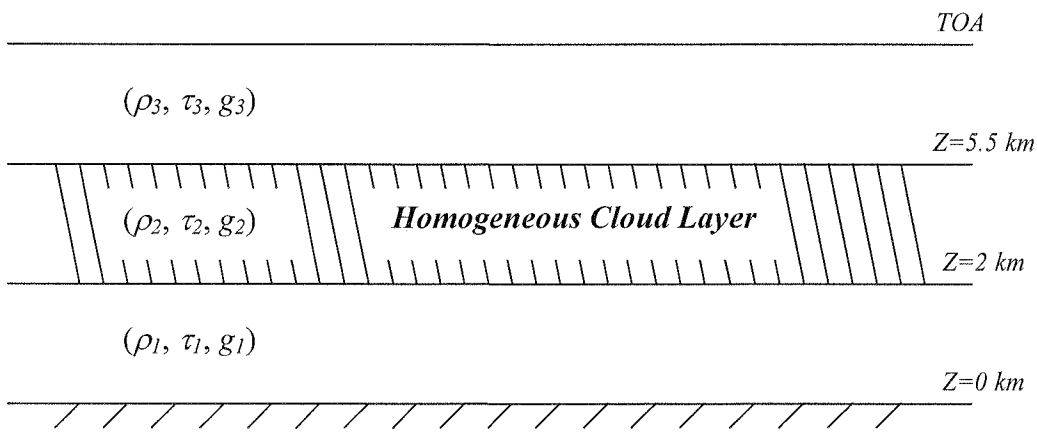

Figure 3.2 The three-layer atmospheric model used in the study of Pinker and Ewing (1985).

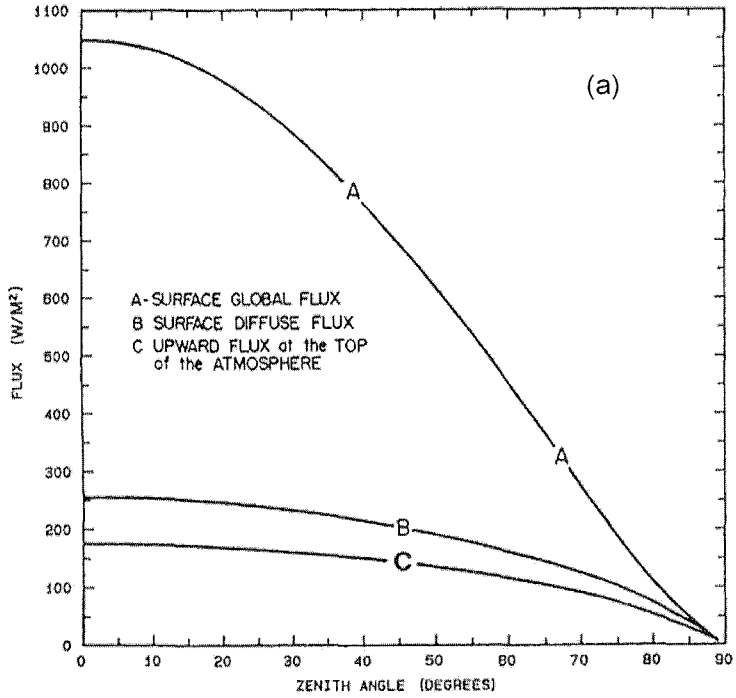

Figure 3.3 (a) The dependence of the solar fluxes and solar zenith angle (Pinker and Ewing, 1985).

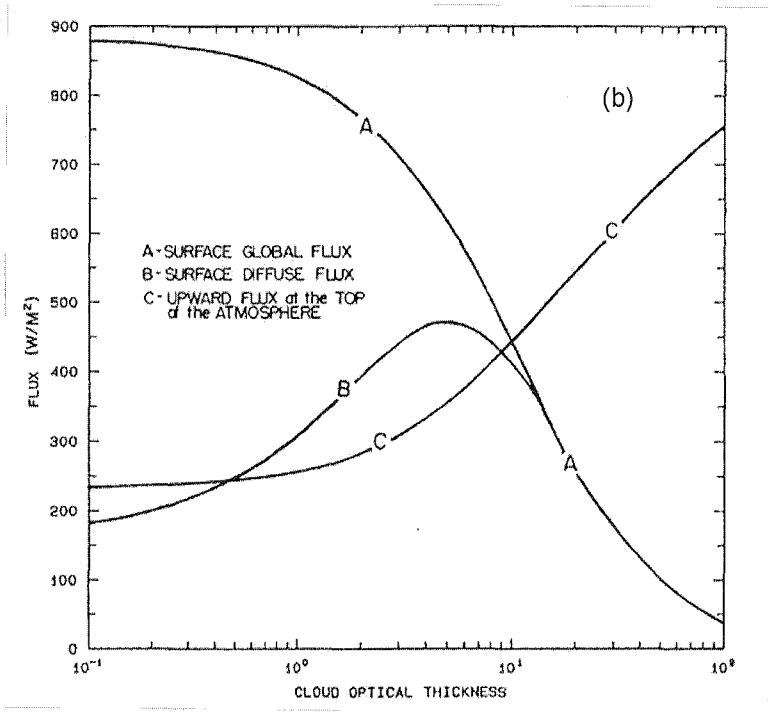

Figure 3.3 (b) The dependence of the solar fluxes and the cloud optical thickness (Pinker and Ewing, 1985).

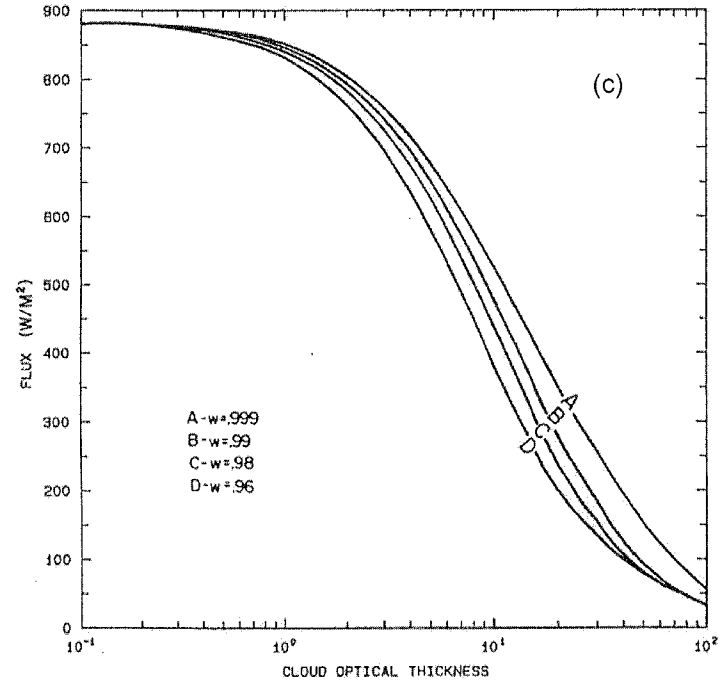

Figure 3.3 (c) The dependence of the solar fluxes and cloud optical thickness, presenting for various single scattering values (Pinker and Ewing, 1985).

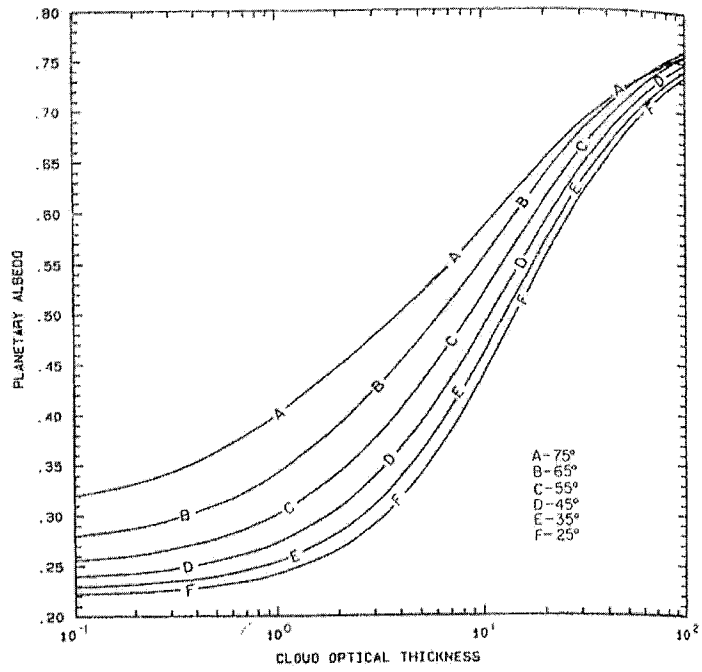

Figure 3.4 The relationship between satellite albedo and cloud optical thickness, presenting various degrees of solar zenith angles (Pinker and Ewing, 1985).

Dedieu *et al.* (1987) presented a physical model to estimate downward solar irradiance at the Earth's surface based on a similar technique to that of Gautier (1980). The approach used in the Dedieu *et al.* (1987) study employs a radiative transfer theory to derive the model, written as a simple function containing surface and Earth-atmosphere albedo. The planetary albedo data was obtained from visible imagery of the METEOSAT-1 satellite (2.5 km × 2.5 km resolution). The cloud transmission properties assumed isotropy of reflected radiance for the cloud layer and the surface. For clear sky conditions, the irradiance is written as:

$$I = I_{sc}\vec{d}^{-2}\cos(\theta_z)T(\theta_z) \tag{3.26}$$

I_{sc} is the solar constant, $T(\theta_z)$ is the transmittance factor due to gas absorption, Rayleigh and Mie scattering, $\vec{d}$ is the radius vector and θ_z is the solar zenith angle.

For the cloudy case, the Earth-atmosphere albedo (α_{EA}) viewed by the satellite is written as:

$$\alpha_{EA} = \alpha_c + (1-\alpha_c)^2\alpha_g/(1-\alpha_c\alpha_g) \tag{3.27}$$

where α_c and α_g are cloud and surface albedo, respectively. The attenuation properties of clouds and surfaces were assumed to be invariant for different wavebands. The solar irradiance for cloudy sky condition is given as:

$$I = I_{sc}d^{-2}\cos(\theta_z)T(\theta_z)(1-\alpha_{EA})/(1-\alpha_g) \tag{3.28}$$

The best prediction result was achieved for the clear-sky case, with RMS errors of noontime hourly solar irradiance of 10%, while the estimation for partly cloudy and overcast conditions gave 30% and 50% RMS errors, respectively.

Darnell *et al.* (1988) presented a technique for estimating solar irradiance using sun-synchronous satellite data. Satellite data were obtained from the TIROS Operational Vertical Sounder (TOVS) which provided surface temperature, precipitable water vapour cloud cover, cloud-top pressure, total ozone column, and channel radiances. The TOA albedo data were extracted from the Heat Budget Product (HBP), and these data were used to determine the cloud transmittance ($\hat{T}_C$).

The model was based on radiative transfer theory and assumed that the solar irradiance at the surface (I) is the product of extraterrestrial solar irradiance I_o and transmission of clear-atmosphere and cloud T_A and T_C, respectively. Surface irradiance is given as a simple formula:

$$I = I_o T_A T_C \tag{3.29}$$

For the clear-sky case, T_C is 1, and Equation (3.29) may be written as:

$$I = I_o \cos(\theta_z) T_A = I_o \cos(\theta_z) \exp(-\tau(\theta_z)) \tag{3.30}$$

where $\tau(\theta_z)$ is broadband atmospheric optical depth and θ_z is solar zenith angle. The study employed hourly data measured by TOVS to compute the values of $\tau(\theta_z)$. For the all-sky case, the estimated effective daily cloud transmission ($\hat{T}_C$) was given by:

$$\hat{T}_C = 1 - \alpha_p \tag{3.31}$$

where α_p is normalized albedo, defined as the following ratio:

$$\alpha_P = (\alpha_{EA} - \alpha_{clear})/(\alpha_{overcast} - \alpha_{clear}) \qquad (3.32)$$

In Equation (3.32), α_{EA} is the TOA albedo, while α_{clear} and $\alpha_{overcast}$ are the values of TOA albedo for clear and overcast skies, respectively. Comparison against pyranometer measurements gave very small RMS errors of 2.3% and 2.7% for hourly and monthly estimates, respectively.

Frouin *et al.*, (1992) carried out a study using Nimbus-7 Earth Radiation Budget (ERB) data to derive net solar irradiance at the ocean surface, with the eventual aim of providing a global data set. The model formulation used plane-parallel theory, and surface irradiance was given as a product of clear sky irradiance and a vertical cloud transmission. Sky conditions were classified into clear and cloudy cases, which were obtained from satellite brightness data. The clear sky model was written in terms of a clear sky TOA solar irradiance ($I_o^{\downarrow}$) incident at an angle (θ_z) and the atmospheric extinction load:

$$I(\theta_z) = I_o^{\downarrow} \cos(\theta_z) T_a T_g (1 - \tilde{\alpha}\alpha_{EC})^{-1} \qquad (3.33)$$

where α_{EC} is the albedo of the cloud-layer-surface system, which was defined as:

$$\alpha_{EC} = C\alpha_c + (1 - C)\alpha_g \qquad (3.34)$$

C is cloud fraction, α_g is surface albedo, $\tilde{\alpha}$ is spherical albedo, which determined when the incident irradiance on the surface is isotropic, T_a and T_g are the atmospheric

transmission due to aerosol scattering and gaseous absorption processes, respectively. The term $(1-\tilde{\alpha}\alpha_{EC})^{-1}$ represents multiple reflections from the cloud-surface layer, assumed to be isotropic and homogeneous. The general expression for net solar radiation in cloudy condition also included a cloud absorption term and is written as:

$$I(\theta_z) = I_o^{\downarrow} \cos(\theta_z) T_a T_g \times (1-\alpha-\phi_{clo})(1-\tilde{\alpha}\alpha_{EC})^{-1} \qquad (3.35)$$

where ϕ_{clo} is cloud absorption. The albedo α_{EC} was parameterised as function of planetary albedo (α'_{EA}), observed by the satellite and given as:

$$\alpha'_{EA} = A_a + \alpha T_a (1-\tilde{\alpha}\alpha_{EC})^{-1} \qquad (3.36)$$

A_a and T_a were defined as integral functions of atmospheric parameters accounting for scattering and absorption of various gases and aerosols of the atmosphere. They were computed using the 5S code with input climatology values for ozone and water vapour. The model was tested with a study of Gautier *et al.* (1980), and the comparison of monthly averages of hourly solar irradiance yielded RMS errors within 10-20 W-m^{-2}.

Pinker and Laszlo (1992) showed how a physical model and a satellite dataset could be used to compute direct and diffuse solar irradiance on a global scale. The satellite data were provided by the International Satellite Cloud Climatology Project (ISCCP). The study estimated solar irradiance by using a data library of computed radiative transfer parameters and the satellite broadband albedo. The structure of the models was based on a concept used in the previous study by Pinker and Ewing (1985), which examined the variation of solar irradiance on the various atmospheric parameters.

In Pinker and Laszlo (1992), the study constructed a data library which contained data pairs of broadband transmission T and broadband reflectivity r:

$$T = f(r) \tag{3.37}$$

The study assigns values of T to different range of values for r. At any solar zenith angle θ_z, the relationships may be written as:

$$r(\theta_z) = r^\circ(\theta_z) + \eta\widetilde{T} \tag{3.38}$$

$$T(\theta_z) = T^\circ(\theta_z) + \eta\widetilde{r} \tag{3.39}$$

where $\widetilde{r}$ and $\widetilde{T}$ are the spherical reflectivity and transmissivity, $r^\circ(\theta_z)$ and $T^\circ(\theta_z)$ are the reflectivity and the transmissivity of the atmosphere for a non-reflecting surface and η is determined as:

$$\eta = [1 - \alpha_d(\theta_z)\widetilde{r}]^{-1}[\alpha_s(\theta_z)T_s^\circ(\theta_z) + \alpha_d(\theta_z)T_d^\circ(\theta_z)] \tag{3.40}$$

where $\alpha_s(\theta_z)$ and $\alpha_d(\theta_z)$ are ocean albedo for direct and diffuse solar irradiance, and $T_s^\circ(\theta_z)$ and $T_d^\circ(\theta_z)$ are the direct and diffuse components of $T^\circ(\theta_z)$, respectively. The data libraries of $r^\circ(\theta_z)$, $\widetilde{r}$, $\widetilde{T}$, $T_s^\circ(\theta_z)$ and $T_d^\circ(\theta_z)$ were created using a radiative transfer model corresponding to various combinations of solar zenith angle, ozone amount, water vapour and the surface albedo, all defined at specific intervals.

In order to obtain the satellite-derived broadband Earth-atmosphere albedo α_{EA}, linear relationships between narrowband bidirectional reflectance r_n and broadband bidirectional reflectance r_b were introduced, resulting in a set of coefficients,

representing various satellite scenes (Table 3.1). A set of conversion factors were then applied in the spectral transformation between r_n and r_b, that is:

$$r_b(\theta,\theta_z,\varphi) = M_1 r_n(\theta,\theta_z,\varphi) + M_2 \qquad (3.41)$$

where

$$r_n(\theta,\theta_z,\varphi) = \frac{\pi L(\theta,\theta_z,\varphi)}{\cos(\theta_z) I_o} \qquad (3.42)$$

Table 3.1 Conversion factors

Scene type	M_1	M_2
Ocean	0.902	0.01426
Vegetation	0.779	0.06831
Desert	0.804	0.02819
Cloud	0.780	0.05004

Once r_b is known, the broadband albedo seen by satellite r_{sat} can be estimated with the anisotropic correction factors X, given as:

$$r_{sat} = r_b(\theta,\theta_z,\phi) / X(\theta,\theta_z,\phi) \qquad (3.43)$$

In order to estimate surface solar irradiance, the satellite albedo was used to select scene types associated with a subsets of r°, $\widetilde{r}$, $\widetilde{T}$, T_s° and T_d°. Further partitioning occurred within each subset, depending on solar zenith angle θ_z, ozone amount, water vapour and optical depth τ. The spectral transmission values of direct and diffuse components ($T_{s\lambda}$ and $T_{d\lambda}$) were estimated by matching the values of r_{sat} to the values of r that computed from the data library. In addition to this step, the spectral values of T_λ were obtained individually by linear interpolation of a reflectance function based on satellite data. The direct and diffuse irradiances were computed from the transfer equations:

$$I_{s\lambda}^{\downarrow} = I_{o\lambda}^{\downarrow} \cos(\theta_z) T_{s\lambda} \tag{3.44}$$

and

$$I_{d\lambda}^{\downarrow} = I_{o\lambda}^{\downarrow} \cos(\theta_z) T_{d\lambda} \tag{3.45}$$

Using a combination of equations (3.44) and (3.45), total solar irradiance was obtained by integrating the spectral global irradiance. The validation against surface measurements of daily solar irradiance averages averaged over 28 days from 7 stations yielded good agreements varying between 10-23% RMSD.

It is seen that Pinker and Ewing (1985) was an early version of deriving global, direct and diffuse components of solar radiation from analytical-based models and the relationships of various parameters, including solar zenith angle, water vapour, aerosol, cloud and surface albedo, were computed as a data library. The section that presents the variations of solar radiation with various solar zenith angles and cloud optical depths is very interesting, and the method could be improved to provide a clear picture of how solar radiation varies with each atmospheric parameter. However, the parameterisation steps presented in the study of Pinker and Ewing (1985) were substantially coarse as each of the data pairs was only examined in one dimension and did not composite well to each other. On the other hand, the model parameterizations and methods used in Pinker and Laszlo (1992) were very much sophisticated and they could be applied to the global estimation scheme. It is obvious that the use of data libraries, which incorporate such parameters of transmittance and reflectance, helps to improve computing times for a large scale estimate.

Most studies that map solar radiation have used geostationary satellites due to their high frequency, continuous observations and their homogeneous coverage. In recent years, global sets such as ISSCP and TOVS have also been popular as they

provide gridded satellite data with some degree of quality control. There is, however, one application where the use of geostationary satellite data is questionable. In high-latitude regions the pixel size and image quality is poor, so that polar-orbiting satellites must be used. While the image frequency is inferior, this is offset to a degree as the overlap of polar-orbiting passes increases at high latitudes, therefore increasing the number of cloud-related observations.

Laine *et al.* (1999) used this approach, employing NOAA–AVHRR data to map solar radiation in high latitude boreal forest regions as described below. Following the model of Iqbal (1983), the parameterization was treated separately for clear and overcast sky conditions. The clear-sky global solar radiation I_g was computed traditionally as a combination of direct and diffuse radiation at the ground, with diffuse radiation being partitioned into Rayleigh, aerosol and multiple reflection components I_{dr}, I_{da} and I_{dm}, respectively.

$$I_l^{\downarrow} = I_s^{\downarrow} + I_d^{\downarrow} = I_s^{\downarrow} + I_{dR}^{\downarrow} + I_{da}^{\downarrow} + I_{dm}^{\downarrow} \tag{3.46}$$

where

$$I_s^{\downarrow} = 0.9751 \times I_o^{\downarrow} \mu_0 T_R T_g T_w T_o T_a \tag{3.47}$$

$$I_{dR}^{\downarrow} = 0.79 \times I_o^{\downarrow} \mu_0 T_g T_w T_o T_{aa} 0.51(1 - T_R)/(1 - m_r + m_r^{1.02}) \tag{3.48}$$

$$I_{da}^{\downarrow} = 0.79 \times I_o^{\downarrow} \mu_0 T_g T_w T_o T_{aa} F_c (1 - T_{as})/(1 - m_r + m_r^{1.02}) \tag{3.49}$$

$$I_{dm}^{\downarrow} = (I_s^{\downarrow} + I_{dR}^{\downarrow} + I_{dm}^{\downarrow})[\alpha r_{cle}/(1 - \alpha r_{cle})] \tag{3.50}$$

where I_o is the solar constant, μ_0 is the cosine of solar zenith angle, T_R is the broadband transmittance due to Rayleigh scattering, T_g is the transmittance for uniformly mixed gases, T_w is the transmittance by water vapour absorption, T_o is the transmittance for ozone, T_{as} is the transmittance due to scattering by aerosols, T_{aa} is the transmittance due to aerosol absorption, m_r is the optical airmass, F_c is the forward scattering function and r_{cle} is the clear sky atmospheric reflectance.

For cloudy sky conditions, solar radiation was estimated by adding the cloud transmittance T_{clo} to the clear sky model. The T_{clo} was derived from the reflectance at the top of the atmosphere r_{atm}, which was empirically estimated from the channel 1 and 2 AVHRR satellite reflectivities. Further details are shown in Figure (3.5).

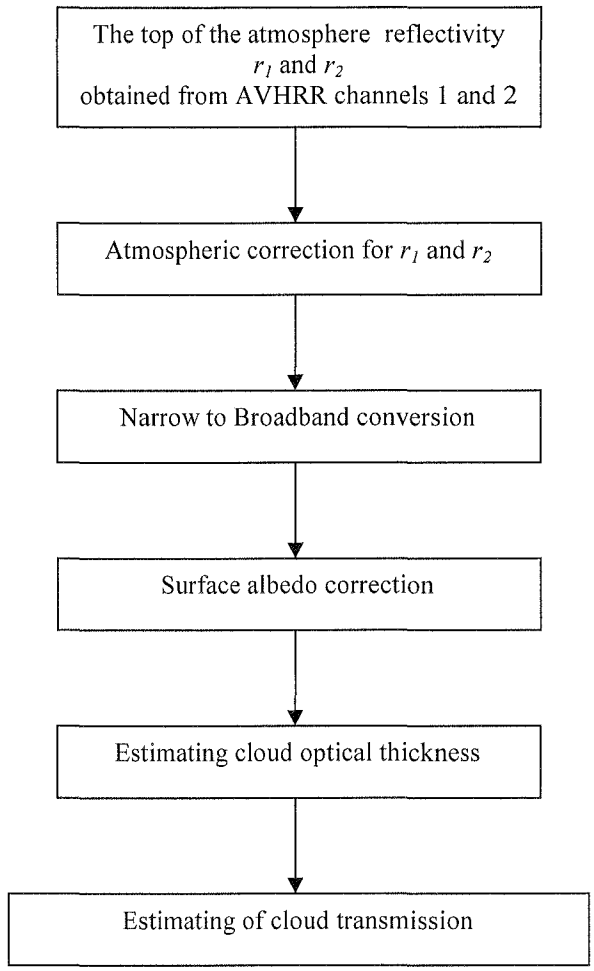

Figure 3.5 Flowchart detail of deriving cloud transmission T_{clo} (Laine *et al.*, 1999).

A cloud detection scheme was developed in Laine *et al.* (1999) using reflectance data from AVHRR and brightness temperatures from 2 AVHRR infrared channels. This step defined whether pixels were treated as cloudy or clear in the model. The validation of the model against pyranometer measurements gave high standard errors for cloudy conditons (from 11% to 39%), but smaller errors for the clear sky case, varying between 5% and 7%.

3.4 Conclusions for solar radiation mapping from satellites

Overall, these techniques show that it is feasible to use satellite data for estimating and mapping solar radiation when surface observations are scarce. Despite their successful outcome, most of the studies face some common difficulties such as unreliable geo-locations and systematic errors caused by the instruments. However clouds and aerosols are still the most dominant source of error. In particular, errors in the estimation are a strong function of the averaging period and not so dependent on the particular technique used, with relatively low errors of 5 to 10 % for the RMSE at the monthly scale (Nunez and Kalma, 1996). Nunez *et al.* (2005) argued that the fractal nature of low clouds requires a high frequency of satellite passes for an acceptable accuracy at the hourly scale, typically every 10 minutes. These data sets are unavailable with our present technology.

Statistical techniques provide distinct advantages for regional-scale mapping. The empirical regression coefficients can implicitly take into account processes such as aerosol depletion or non-Lambertian cloud reflection. Nevertheless the applicability of the coefficients to a wider set of conditions is, by its very nature, uncertain. Physical models do not have this uncertainty, but they have not been thoroughly validated at the global scale. They are also limited in their input data, mainly the frequency of satellite

passes (1/2 hourly for geostationary satellites) and in lack of information on aerosol properties such as optical depth and single scattering albedo. While the new generation of EOS satellites such as MODIS provide detailed solar irradiance with full parameterisation of aerosol and gaseous constituents of the atmosphere, their limited frequency of coverage make them impractical as a mapping tool. Alternatively, ISCCP provides high quality long-term global observations, but their coarse spatial resolution make them unsuitable for regional mapping.

The most useful approach, and the one adopted in this thesis, is to use a finite-dimension look-up table based on a radiative transfer model that incorporates all the different factors affecting the satellite reflectance (Pinker and Laszlo, 1992). Use of a look-up table saves computing time while at the same time producing rigorous results of the model based on a radiative transfer algorithm such as DISORT. This approach has been adopter in several studies (Verdebout, 2000; Gobron *et al*, 2006). And will be followed in this thesis using the Streamer radiative transfer model. A thorough validation of the model at the regional scale will assess its reliability and applicability to the region. This validation should include not only different geographic locations, but different averaging time scales as well. This approach will be developed further and applied to the Great Barrier Reef area so as to derive a solar radiation climatology.

3.5 Previous studies on underwater solar radiation

Solar irradiance entering a water body is partially reflected at the surface and then attenuated across a distance in the water column. A number of studies have stated that the extinction of solar irradiance while traveling through water varies as a function of depth and optical properties (Kirk, 1981; Tilzer *et al.*, 1995; Buiteveld, 1995; Schanz *et al.*, 1997; Ershova *et al.*, 2002; Liu *et al.*, 2006). In a similar fashion to atmospheric

attenuation processes, the absorption and scattering coefficients of the water medium are used as common variables to evaluate the light environment.

The optical properties of water can be described in terms of apparent and inherent optical properties. The apparent optical properties (AOPs), easily obtained from irradiance measurement, change as a function of solar zenith angle, cloud cover, wind velocity and water depth, as they are not intrinsic properties of the water medium (Kirk, 1983; Spinrad *et al.*; 1994; Bukata *et al.*, 1995; O'Reilly *et al.*, 1998). By contrast, inherent optical properties (IOPs) are unique to the water body and depend on such water features such as salinity, chlorophyll concentration, phytoplankton, yellow substance and other suspended materials such as detritus, tripton and gilvin (Tilzer *et al.*, 1995; Buiteveld, 1995). These variables can be used by model algorithms that estimate reflectance or solar irradiance values. The models are sometimes called *bio-optical models* (Roesler and Perry, 1995; O'Reilly *et al.*, 1998; Ammenberg *et al.*, 2002; Højerslev, 2004). However, most of these models operate only in specific bands, such as the PAR region.

Since the 1970s, there have been a number of studies that used either subsurface irradiance measurement and/or remote-sensing techniques to derive the relationships between IOPs and AOPs (Gordon *et al.*, 1975; Kirk, 1983; Spinrad *et al.*, 1994; Bukata *et al.*, 1995; Roesler and Perry, 1995; Højerslev, 2004; Liu *et al.*, 2006). It is well understood that the attenuation coefficient K_d is a key variable to express the amount of light underwater as a function of depth (Tilzer *et al.* 1995, Schanz *et al.* 1997, Ershova *et al.* 2002; Liu *et al.* 2006). Chlorophyll-*a* has a significant influence on the transmission of light, especially in the visible region (400 – 700 nm). It absorbs most of radiation in the blue and red bands, but transmits most of the green light (Kirk, 1983; Tilzer *et al.*, 1995; O'Reilly *et al.*, 1998). Some studies used spectral solar radiation and PAR measurements to derive empirical relationships between K_d and phytoplankton

concentration (Smith and Baker, 1981; Roesler and Perry, 1995; Tilzer *et al.*, 1995; Schanz *et al.*, 1997; Lee *et al.*, 1998). In addition, a number of remotely-sensed techniques were developed to obtain the K_d coefficients for large areas (O'Reilly *et al.*, 1998; Lee *et al.*, 1998; Ammenberg *et al.*, 2002, Ershova *et al.*, 2002; Liu *et al.*, 2006).

Values of IOPs and AOPs can be related using Monte Carlo approximation methods (Gordon *et al.*, 1975; Kirk, 1984; Jerome *et al.*, 1988). An early study by Gordon *et al.* (1975) used a Monte Carlo method to derive empirical relationships between volume reflectance r, vertical attenuation K_d, total attenuation coefficient c_w, scattering albedo $\rho = a_w/b_w$, forward scattering probability F and backscattering probability P_b. The relations are:

$$\frac{K(z)}{c_w D_d(z)} = \sum_{n=0}^{N} k_n(z)[\rho F]^n \tag{3.51}$$

and

$$r(z) = \sum_{n=0}^{N} \sigma_n(z)\left[\frac{\rho P_b}{1-\rho F}\right]^n \tag{3.52}$$

where $k_n(z)$ and $\sigma_n(z)$ are sets of expansion coefficients, $D_d(z)$ is distribution function of downwelling irradiance at depth z.

3.5.1 Studies based on surface measurements

Buiteveld (1995) obtained some interesting results with a Monte Carlo model originally developed by Kirk (1984) to estimate underwater PAR. Total absorption and scattering were estimated as a spectral sum of various aquatic substances including yellow substance, phytoplankton, tripton and detritus. Each of these IOPs was calculated using the following formulae (Buiteveld, 1995):

- Pure water

$$a_{wp}(\lambda) = a_{wy}(380)\exp[-k_{wy}(\lambda - 380)] \tag{3.53}$$

- Phytoplankton

$$a_{wph}(\lambda) = (0.058 + 0.018 \cdot chlo)a_{wc}(\lambda)k_{wph} \tag{3.54}$$

$$b_{wph}(\lambda) = a_{wph}(550) + 0.12 \cdot chlo^{0.63}k_{wph} - a_{wph}(\lambda) \tag{3.55}$$

- Tripton

$$c_{wtr}(\lambda) = k_{w1}tripton^{k_{w2}}\frac{400}{\lambda} \tag{3.56}$$

$$a_{wtr}(\lambda) = k_{w3}Detritus^{k_{w2}}\frac{400}{\lambda} \tag{3.57}$$

$$b_{wtr}(\lambda) = c_{wtr}(\lambda) - a_{wde}(\lambda) \tag{3.58}$$

where a_w is the absorption coefficient and b_w is the scattering coefficient. The subscripts *ph*, *tr*, *de*, *y* and *c* refer to phytoplankton, tripton, detritus yellow substance and chlorophyll, respectively. k_{w1}, k_{w2} and k_{w3} are the optimization values for tripton beam attenuation and phytoplankton. k_{wy} is the constant of yellow substance, 6.6262 J-s-nm^{-1}. PAR radiation, *PAR*, was obtained from integration of the Lambert-Beer equation in a region between 400 and 700 nm. The model is expressed in Ei m^{-2} s^{-1}, that is:

$$PAR(z) = \int_{400}^{700} I_{o\lambda}^{\downarrow} \exp(-K(\lambda) \cdot z \cdot f(\lambda))d\lambda \tag{3.59}$$

where $f(\lambda) = \frac{\lambda \cdot 10^9}{h \cdot \widetilde{C} \cdot 6.02 \cdot 10^{23}}$, $\widetilde{C}$ is speed of light and h is Planck's constant, 6.6262×10^{-34} J-s. Once PAR was obtained, K_d(PAR) values were then estimated by using the Lambert-Beer equation taken at two different depths at z_1 = 1 m and z_2 = 2 m. The relative errors for K_d(PAR) were shown to be between 5% and 15%.

Tilzer *et al.* (1995) used measurements of scalar, downwelling and upwelling spectral irradiance and PAR to analyse the relation between attenuation coefficient K_d and phytoplankton contribution by a regression technique. The study obtained some interesting relationships between the vertical attenuation of PAR and monochromatic irradiance and chlorophyll concentration. A linear relationship between the vertical attenuation of downwelling PAR and chlorophyll concentration, *chlo*, was obtained:

$$K_d(PAR) = 0.019 \cdot chlo + 0.26; \quad R^2 = 0.74; \quad N = 57 \tag{3.60}$$

The total attenuation coefficient $K_d(\lambda)$ was described as:

$$K_d(\lambda) = K_c(\lambda) \cdot chlo + [K_w(\lambda) + K_g(\lambda)] \tag{3.61}$$

where K_c is the chlorophyll-*a* specific vertical light attenuation, K_w is the light attenuation coefficient due to pure water and K_g is the vertical attenuation of light underwater due to non-algal material (Tilzer *et al.*, 1995).

Schanz *et al.* (1997) used a similar approach but applied to the PAR regions. The attenuation coefficient for PAR, is written as:

$$K_d(\text{PAR}) = K_c(\text{PAR}) \cdot chlo + K_w \tag{3.62}$$

where K_c(PAR) is the chlorophyll-*a* specific vertical light attenuation in the PAR region and K_w is the attenuation coefficient of water without phytoplankton. However, the parameters could only be applied to the study area where the measurements were conducted. Despite the progress being made in the above studies, they cannot provide systematic and large-scale estimates of ocean optical properties due to the high cost of instrumentation and field program. A more useful procedure, which is discussed in the next section, is to combine remote sensing data with field measurements and modelling schemes.

3.5.2 Previous studies based on remote sensing algorithms

Ocean colour data, such as from the Coastal Zone Color Scanner (CZCS) and Sea-Viewing Wide Field-of-view Sensor (SeaWiFS), provides a global estimate to the oceanographic community. The SeaWiFS project contributes global estimation of water-leaving radiance, Angstrom coefficient, chlorophyll-*a* concentration and diffuse attenuation coefficient at 490 nm (Hooker *et al.*, 1992). So far, the usefulness of SeaWiFS data has been well recognised in many studies across the globe (Lee *et al.*, 1998; O'Reilly *et al.*, 1998; Ershova *et al.*, 2002; Liu *et al.*, 2006).

Lee *et al.* (1998) developed an empirical algorithm for estimating total absorption coefficients and spectral absorption coefficients at 440 nm, *a*(440). The study examined linear relationships between *a*(440) and various spectral ratios of upwelling radiance determined from remote sensing data in the 410 nm, 490 nm, 510 nm and 555 nm wavelength bands. Validations against total absorption coefficient measurements resulted in a relatively low RMSD of 15.3%, while the spectral absorption comparison yielded a higher RMSD of 29.1%.

Ershova *et al.* (2002) illustrated a technique of using SeaWiFS satellite data to estimate the penetration of solar radiation. The method evaluates K_d from an empirical

relation written as a function of the vertical absorption and back-scattering coefficients, a_w and b_{wb}, respectively. That is:

$$K_d = 1.04 D_0 (a_w + b_{wb}) \tag{3.63}$$

and

$$D_0 = (1-p)/\cos\theta_{w-} + 1.197p \tag{3.64}$$

where θ_{w-} is the refraction angle at the air-water interface, and p is the fraction of incident solar radiation at the surface that is diffuse. Finally, underwater solar radiation at various depths was estimated by using the Lambert-Beer equation. The RMSD for K_d estimation was 1.2%.

Liu *et al.* (2006) presented a new method for estimating light distribution in water bodies. The technique used a series of analytical, semi-analytical and empirical algorithms to estimate various IOP*s* and the PAR flux. Using a look-up table, the IOPs retrieved from SeaWiFS are used to estimate the absorption and scattering coefficients. Initially the satellite provides the chlorophyll concentrations, the CDOM absorption factor F_{CDOM} and backscatter fraction of particle (BF_p). The spectral IOPs are separated into absorption, scattering and phase scattering functions using the following steps:

1) the spectral absorption coefficient $a_w(\lambda)$ was parameterised via a model proposed by Morel (1991) and Prieur and Sathyendranath (1981), written as functions of the absorption coefficient of pure water $a_{wp}(\lambda)$, chlorophyll concentration *chlo*, normalized chlorophyll specific coefficient $a^*_{wc}(\lambda)$ and CDOM absorption factor F_{CDOM}:

$$a_w(\lambda) = a_{wp}(\lambda) + 0.06a^*_{wc}(\lambda)chlo^{0.65} + F_{CDOM} \cdot 0.06 \cdot a^*_{wc}(440)chlo^{0.65} \exp(-0.014(\lambda - 440)) \quad (3.65)$$

2) using a model proposed by Gordon and Morel (1983), the scattering coefficient $b_w(\lambda)$ is estimated:

$$b_w(\lambda) = b_{wp}(\lambda) + 0.30\left(\frac{550}{\lambda}\right)chlo^{0.62} \quad (3.66)$$

where $b_w(\lambda)$ is the spectral scattering coefficient of pure water.

3) the phase scattering function $\tilde{\beta}$ was expressed with the following equation proposed by Mobley (1994):

$$\tilde{\beta}(\eta,\lambda) \equiv \frac{b_{wp}(\lambda)}{b_w(\lambda)}\tilde{\beta}_w(\eta) + \frac{b_{wb}(\lambda)}{b_w(\lambda)}\tilde{\beta}_b(\eta,\lambda) \quad (3.67)$$

where η is the scattering angle and $\tilde{\beta}_w(\eta)$ and $\tilde{\beta}_b(\eta)$ are the scattering functions for pure (w) and turbid (b) water respectively, were estimated from analytic functions. The LUT was constructed and then examined against the simulation of *chlo*, BF_p and F_{CDOM} provided by the Hydrolight program and linear regression coefficients were obtained. The relative errors of *chlo*, F_{CDOM} and BF_p were 5.19%, 1.73% and 6.78%, respectively. The PAR for a vertical homogeneous water column was computed using the constructed LUT based on radiative transfer theory. When checked against Hydrolight, a maximum error of 17% was obtained for *PAR*.

Most of the above studies have been conducted in deep water where the effect of bottom topography may be neglected. Unfortunately, this is not the case in this study

area since there are reef areas characterised by very shallow water. Carder *et al.*, (2003) has analysed aircraft images near Lee Stocking Island in Bahamas (Carder *et al.*, 2003) characterised by large sand bottom and large solar zenith angles. They found images contrast of 10-15% as a result of topography or algae accumulation in the trough. A Monte Carlo model was developed which estimated upwelling radiance in sandy facets of different exposure angles. Large errors (~15%) were associated with albedo retrievals in short facets. However, errors decreased with increasing water turbidity. Mobley *et al.*, (2003) used a Monte Carlo model in shallow water with a spatially inhomogeneous bottom. Results showed that the under water radiance is inherently three dimensional, but if the spatial scale of the bottom is much smaller than the bottom area seen by a radiometer the homogeneous bottom will be replaced with a spatial averaged reflectance (Mobley *et al.*, 2003). Clearly, these studies argued that there could be potentially inherent errors in parts of our study area, especially near shallow water reef regions. It is impractical to assign errors of these effects in our measurements. Nevertheless, we note that our measurements were taken in respectively that bottom surfaces with mixture and sands. Our results were consistence spatially and did not show large changes with solar zenith angle. In this study, SeaWiFS radiances were used, but bottom topography and bottom inhomogeneously is unlikely to produce errors due to the spatial involved.

3.5.3 Need for further development

This chapter has provided a review of progress made in mapping solar radiation above and below the water surface. However, there has been with attempt to date of linking above water to below water irradiance. To accomplish this, there is need to use published data on absorption, scattering and total depletion coefficients, and to merge this information with that provided from satellite. This approach will be discussed further in the result section, Chapter 6.

Chapter 4

Methodology

This study develops mapping techniques using geostationary meteorological satellite data to provide long-term statistics of surface solar radiation over the Great Barrier Reef (GBR) and Coral Sea regions. The method makes use of radiative transfer models, called Streamer and UVSPEC, to create look-up tables containing values of surface solar irradiance and Earth-atmosphere reflectivity as they vary in response to various parameters. Using the satellite-derived reflectivity, solar irradiance at the surface can be estimated from the look-up tables.

A technique for estimating underwater solar irradiance is also presented. Spectral distributions of the attenuation coefficient K_d are examined with various Monte Carlo models. The empirical relationships among three wavebands — UVB, PAR and the 480-500 nm SeaWiFS channel — are developed. Mapping of underwater solar irradiance is accomplished via parameterisations of the satellite-derived K_d and the models. Details of both surface and underwater solar radiation mapping are discussed in this chapter.

4.1 Study area

This study focuses on providing long-term statistics of solar radiation for the Great Barrier Reef (GBR). The study area covers the Coral Sea and the north-east coastline of Queensland (10° S - 26° S, 142° E - 155° E, Figure 4.1). Satellite data covering an 11-year period from January 1995 to December 2005 were acquired for this study area.

The Great Barrier Reef is one of the largest habitats of coral reefs on Earth. It is vast in biodiversity and ecosystems, supplying nutrients for the food chain. The growth in reef communities is mainly governed by climate, sediments and water circulation that depends on the reef structure and bathymetry (Lough, 1994). The topography is shaped by continental islands, coral reefs and some volcanic islands extending up to 200 km from the Queensland coastline. Due to environmental concerns, the area is protected and managed by the Great Barrier Reef Marine Park Authority (GBRMPA), Queensland. Details on morphology, climate and physical oceanography of the GBR are discussed in the following sections.

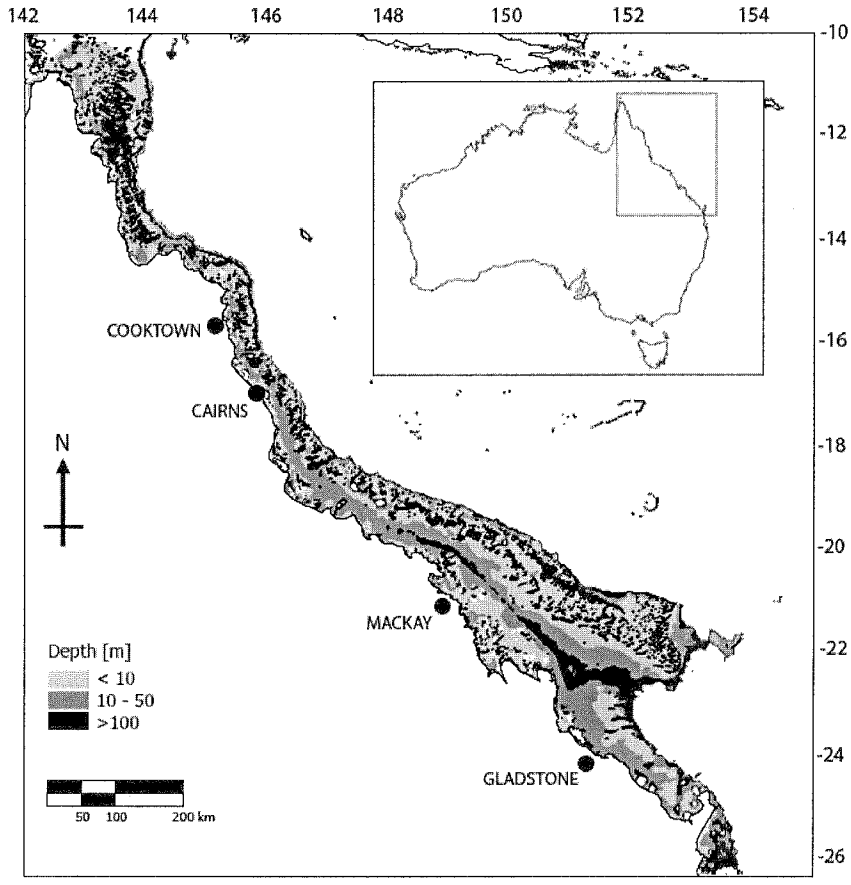

Figure 4.1 Study area covers Coral Sea and the Great Barrier Reef.

4.1.1 Morphology

The Great Barrier Reef is a complex geographical feature on the continental shelf. It is composed of about 2900 reefs and 900 islands stretching for nearly 2000 km along the east coast of Queensland (Lough, 1994; Hopley *et al.*, 2007). As illustrated in Figure 4.1, the northern boundary of the Great Barrier Reef is close to Papua New Guinea. The region features very dense habitats of coral reefs extending along the coastline from ~10° S to 24° 30′ S, covering about 2600 km^2. The width throughout the GBR belt is approximately 60-120 km. The maximum distance of the reef strip from the coast is roughly 200 km at 26° S and the minimum is about 30 km at 14° S.

Most of the reefs are located in shallow water, in depths ranging between 5 m to 130 m. Near-shore areas are characterized by shallow depths of about 10-20 m which increase sharply at the edge of the GBR offshore (Wolanski and Pickard, 1985). According to a study by Wolanski (1994), the GBR can be divided into four main regions — Torres Strait, Northern region, Central region and Southern region. The environment of Torres Strait region is shallow and dense. Most of the reefs in this region are located in water depths of less than 15 m. The reefs in the Northern, Central and Southern regions exhibit increasing depth with latitude, with average depths of around 30 m, 40-100 m and 140 m, respectively.

4.1.2 Climate

The climate of the Great Barrier Reef is tropical. Generally, south-east trade winds dominate most of the year. In the summer period, the monsoons bring rain and highly-humid air masses move across the northern region. Moderate north-westerly winds of about 11 to 20 km/hr blow over the northern region (Lough 1994; Hopley *et al.*, 2007). The winter months, from June to August, are characterised by dry conditions with low relative humidity and low rainfall amounts, especially in the southern part of

the GBR. South-easterly trade winds tend to be more pronounced during the winter months.

The sea surface temperature (SST) in the GBR region varies with latitude and season. Lough (1994) examined the SST data for the period 1958 – 1987 and suggested that the variation of SST is minimal in winter and mid-summer (Figure 4.2). For the summer, the mean SST ranges from 29 °C in the northern regions to 21 °C at the south. In winter, the SST shows a small decrease with latitude, ranging from 26 °C in the north to 22 °C in the south (Wolanski, 2001).

Each year, the GBR region experiences tropical cyclones, which impact approximately twice a year on average (Puotinen *et al.*, 1997; Lough 1994). There were a total of 92 cyclones over the GBR between 1969 and 2005. Most of these cyclones were category 1 and 2, which produced wind speeds of about 17-33 $m\text{-}s^{-1}$, causing high waves, sediment disturbance and heavy rainfall over the GBR (Puotinen *et al.*, 1997). It is believed that El Niño-Southern Oscillation events play a significant role in generating cyclone activity in the Great Barrier Reef region (Lough 1994; Puotinen *et al.*, 1997).

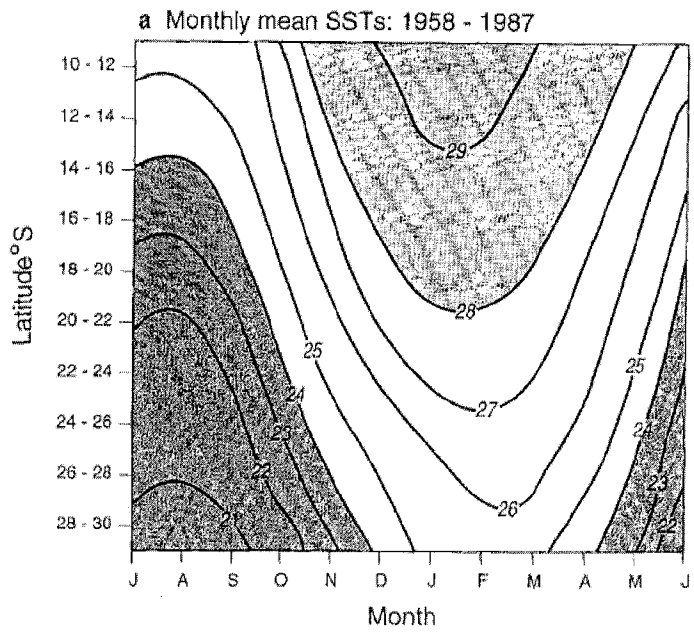

Figure 4.2 Temporal variation of monthly mean sea surface temperature, taken from Lough (1994).

4.1.3 Current

The water circulation over the GBR region depends on the geometry and density of the reefs, as well as other factors such as tidal movements and the Trade Wind Drift. Large-scale water movements are controlled by the poleward East Australian Current (EAC), which also drives circulation between surface and deep waters (Wolanski and Pickard, 1985). In areas of high reef density, strong currents can occur, with velocities exceeding 4 $m\text{-}s^{-1}$.

4.2 *In situ* measurements

4.2.1 Measurements of surface broadband solar radiation

Surface measurements of solar radiation are important to allow validation of the satellite-derived estimates. The Australian Bureau of Meteorology (BOM) maintains two surface radiation stations in the study, Rockhampton (23.3° S, 150.4° E) and Cairns (16.5° S, 145.3° E). The data was collected by Kipp & Zonen CM-11 pyranometers, located in the regional BOM offices. The spectral response of CM-11 pyranometer encompasses a broad range between 0.34-2.2 μm, with an error of detection less than 1% (Kipp & Zonen Instruction Manual).

Solar radiation measurements at Rockhampton were available between January 1995 and December 2005, while those for Cairns were available from January 1997 to December 2004. Solar irradiance obtained from these measurements was provided every 15 minutes. This study extracted the surface solar radiation data at the satellite operating times from sunrise to sunset at 30 minute intervals (Figure 4.3).

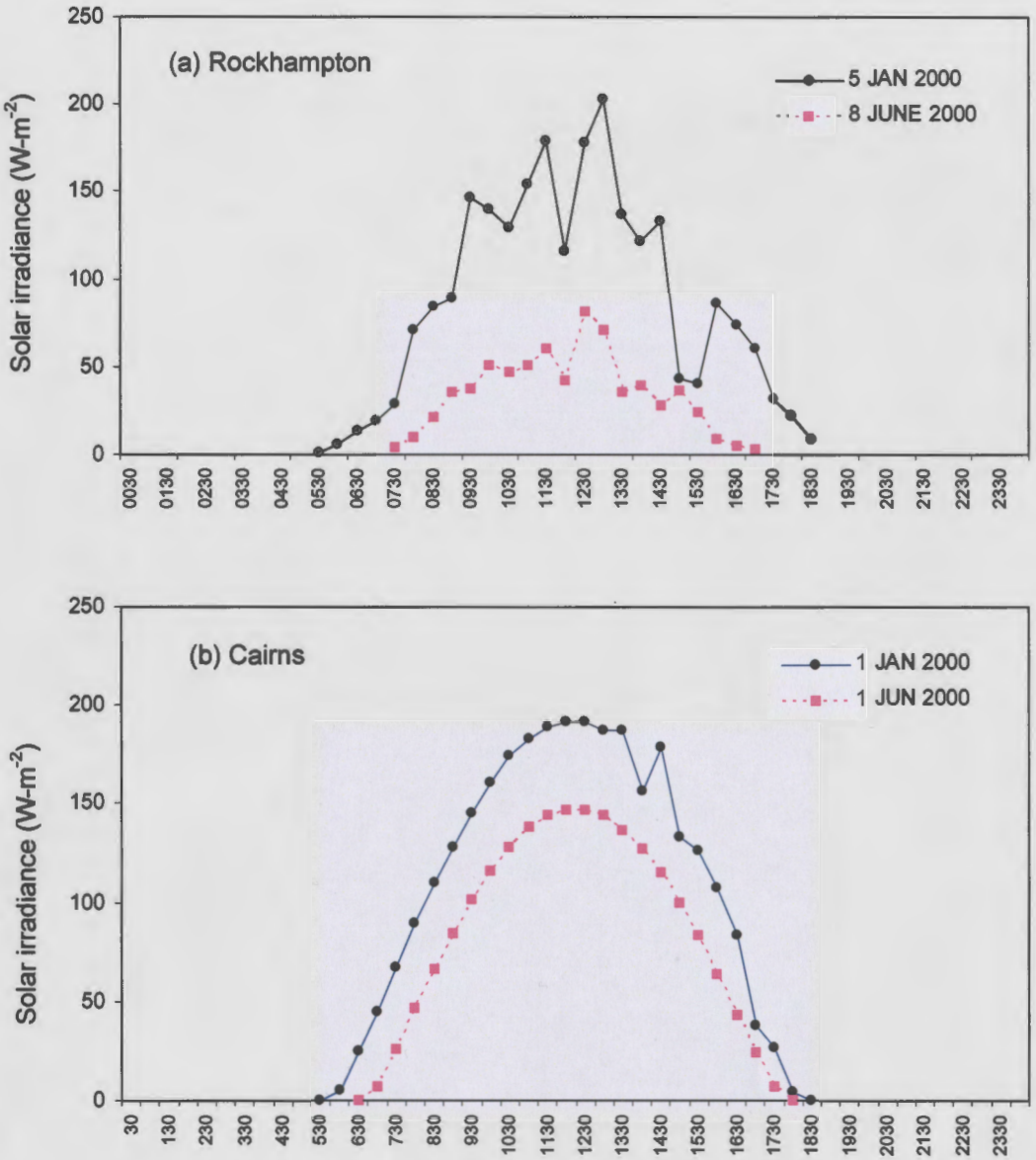

Figure 4.3 Examples of measured surface broadband solar radiation:

(a) Rockhampton, (b) Cairns.

4.2.2 Measurements of surface UVB irradiance

The Australian Radiation Protection and Nuclear Safety Agency (ARPANSA) maintains a network of UVB measurements across Australia (Figure 4.4). The UV-Biometer Model 501 used for these *in situ* measurements senses radiation between 0.28-0.32 μm, with a weighting which approximates the erythemal action spectrum (Figure 4.5). This study used the UVB data collected at Townsville (19.3° S, 146.8° E) to compare with satellite-derived UVB irradiances at the surface. The data was provided

every 15 minutes for a period between January 1997 and December 2001. A diurnal distribution of the UVB measurements is shown in Figure 4.6.

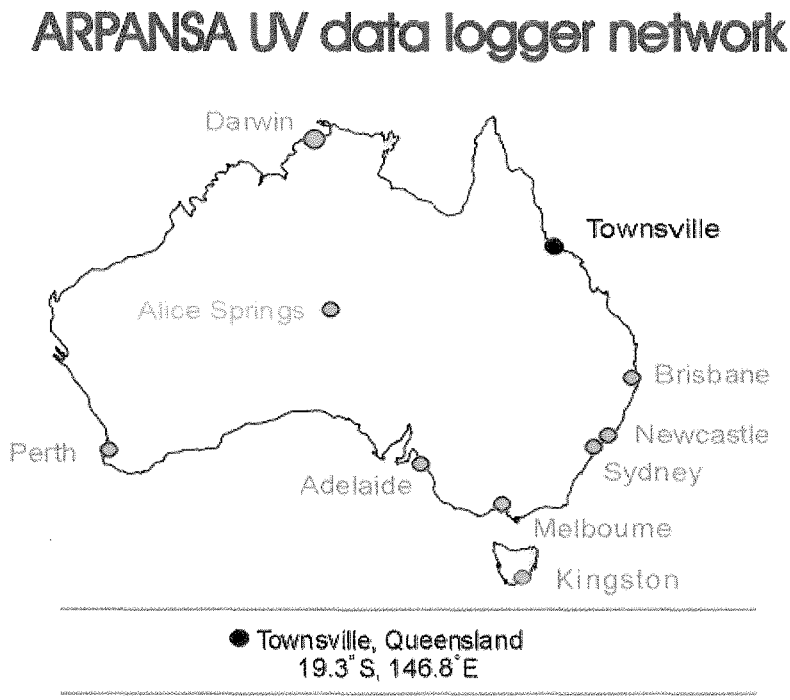

Figure 4.4 The ARPANSA UV measurement network (source from www.arpansa.gov.au).

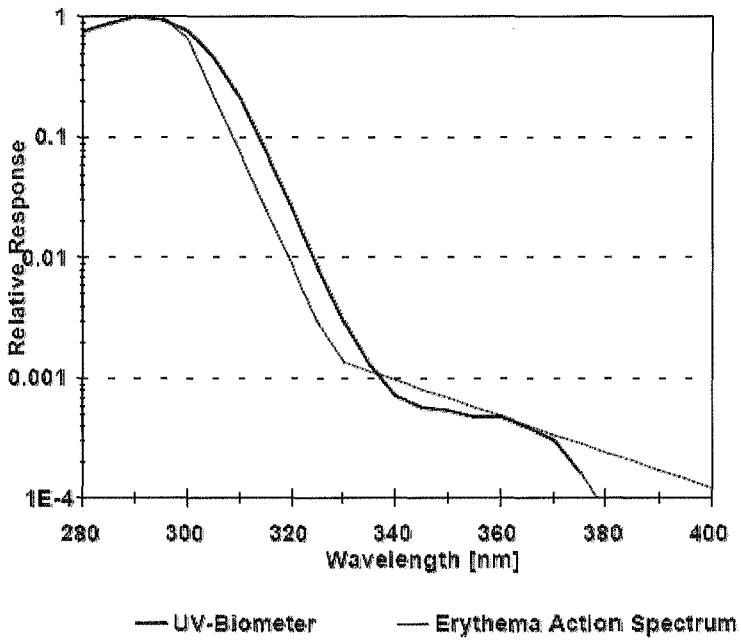

Figure 4.5 Action spectra and the sensitivity curve of UV-Biometer model 501.

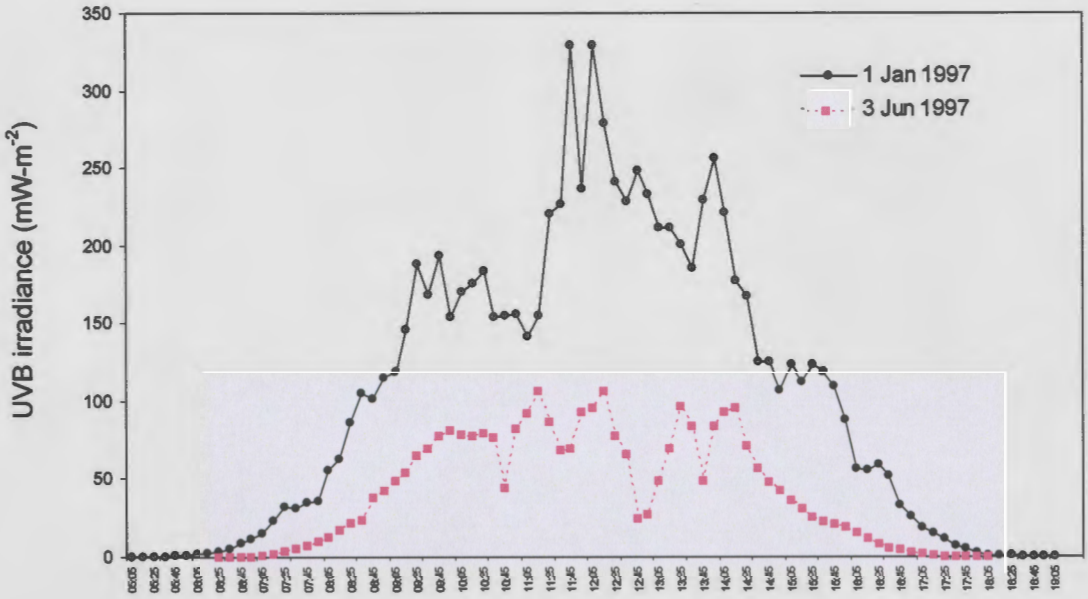

Figure 4.6 An example of UVB diurnal distribution collected by UV-Biometer Model 501.

4.2.3 Measurements of underwater PAR and spectral UV irradiances

Ancillary data for this study was collected using a Biospherical Instrument Profilling Ultraviolet radiometer (PUV) at Heron Island, Queensland. The purpose of this study was to collect K_d values in situ with which to validate the model's results. Heron Reef (23.27° S, 151.55° E) is a platform reef with a coral cay, Heron Island. The reef is located in the Capricorn-Bunker Group (CBG), about 70 km north-east of Gladstone, Queensland (Figure 4.7). Heron Reef covers an area of about 11 km (East/West) × 5 km (North/South) (Figure 4.8). The lagoon is shallow with depth, decreasing from ~1 m at the boundary to 6 m in the middle region (Veal, 2006). The measurements of PAR and spectral UV underwater irradiance were conducted both inside and outside the lagoon of Heron Reef on a number of separate days in June 2004 and December 2004. Details of the measurement locations are illlustrated in Figure 4.8.

Figure 4.7 Map shows location of Heron Island Reef (source from Google Earth).

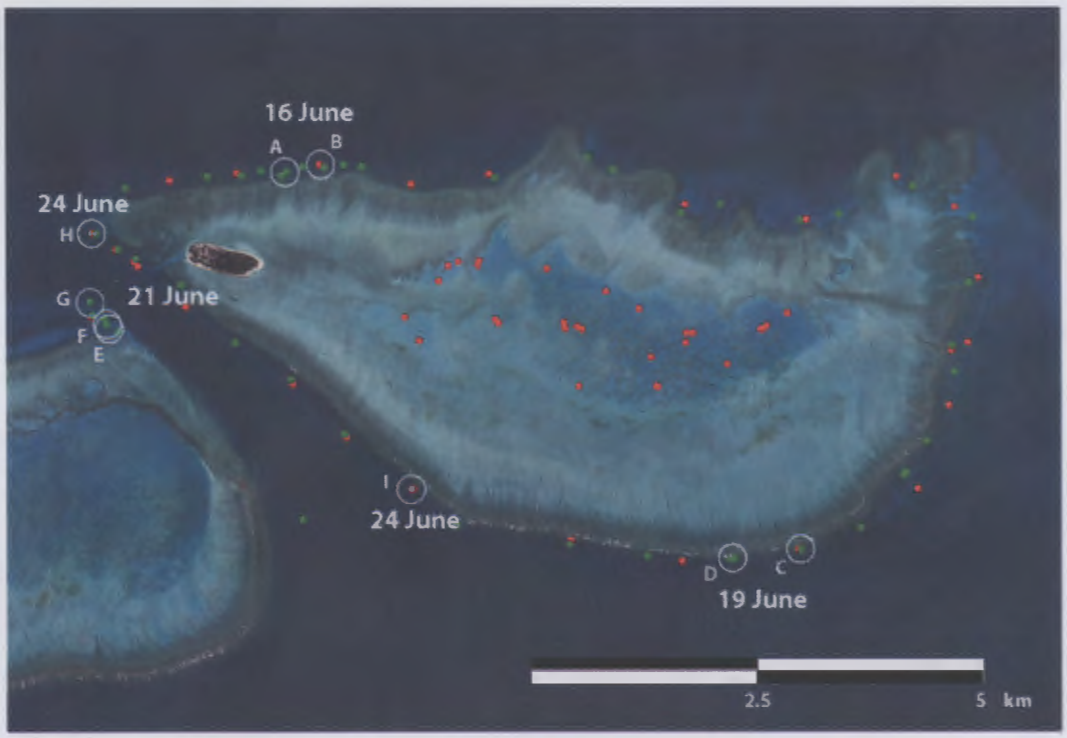

Figure 4.8 Map shows details of locations where the PUV measurements were conducted.

The measurements were collected with a small boat equipped with a stern deployment frame and PUV instrument (Figure 4.9 and 4.10). The measurements of spectral UV irradiances at 305 nm, 315 nm, 320 nm, 340 nm, 380 nm, 395 nm and PAR (400 nm – 700 nm) were collected by vertically moving the sensor through the water column. Figure 4.11 shows an example of the UV irradiances obtained from the measurements.

The underwater irradiance values obtained from PUV measurements can be compared with SeaWiFS-derived solar irradiance. However, there are two restrictions on the SeaWiFS satellite data: SeaWiFS scenes scan only one image per day, and no data are available if there is cloud present. As a result, only four days were available for the comparison, which are June 16th, 19th, 21st and 24th, 2004 (Figure 4.8). Details of the measurements including wind speed, ocean and sky observations are provided for each location in Table 4.1.

Table 4.1 Details of on boat measurements conducted across Heron Island. Notations A - I refer to the map of Heron Reef shown in Figure 4.8.

Locations on the map / Cast	Date	Local time	Cloud cover (tenths)	Wind speed (m-s^{-1})	Depth (m)	Wave height (m)	Swell (m)
A	16 June 2004	11.46	1-2	7.8 (South)	16.0	0.3	1.0
B	16 June 2004	12.54	1	6.6 (South)	12.0	0.2	0.8
C	19 June 2004	11.55	0	7.3 (West)	7.2	0.2	0.5
D	19 June 2004	12.22	0	6.4 (West)	6.5	0.2	0.5
E	21 June 2004	11.52	0	8.5 (South)	8.5	0.7	0.0
F	21 June 2004	12.10	0	6.9 (South)	10.0	0.7	0.0
G	21 June 2004	12.43	0	5.3 (South)	15.0	0.7	0.0
H	24 June 2004	11.34	1	6.6 (South)	11.0	0.4	1.0
I	24 June 2004	12.03	1	6.9 (South)	11.0	0.5	1.5

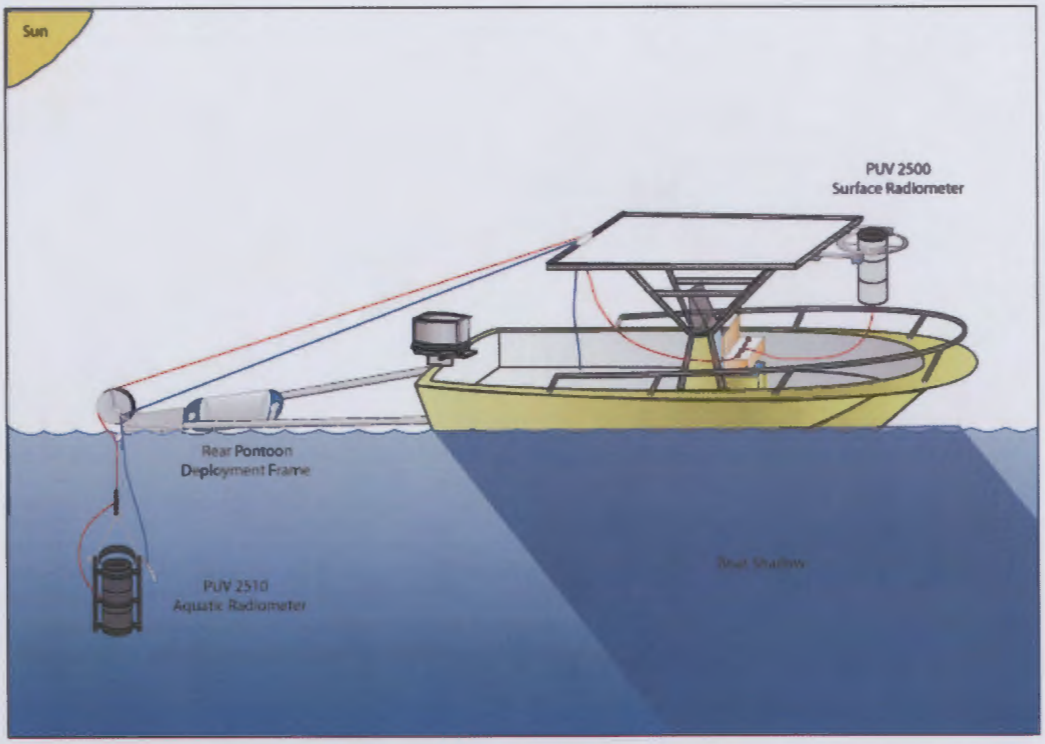

Figure 4.9 Configuration of PUV instrument and vessel (taken from Veal, 2006).

Figure 4.10 A deployment of PUV sensor into water at Heron Reef.

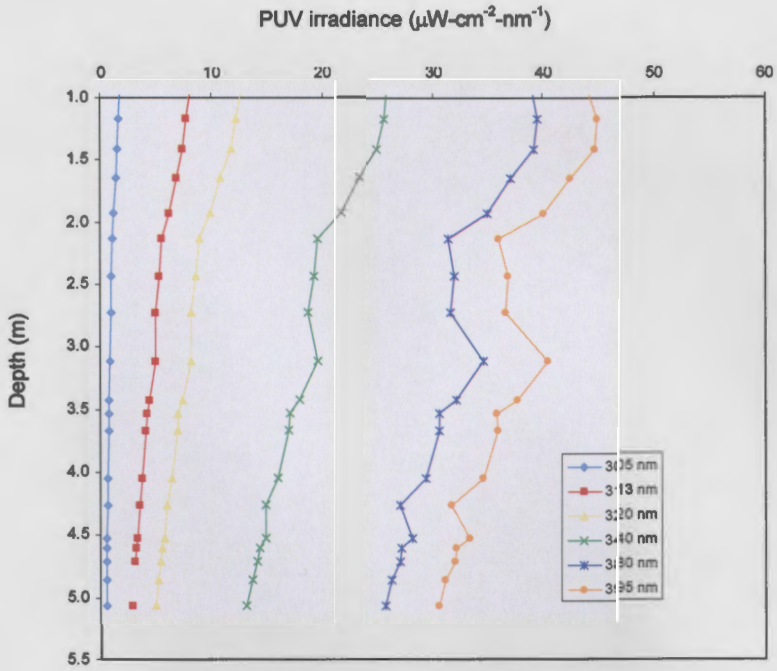

Figure 4.11 Spectral distribution of UV irradiance collected at local noon time on 17 June 2004.

Irradiance values obtained from PUV measurements can be transformed into the vertical attenuation coefficient K_d. This study describes the measured K_d values by following the studies of Kirk (1994), Spinrad (1994) and Ershova *et al.* (2002):

$$K_d(z) = \frac{-1}{z_2 - z_1} \ln\left(\frac{I(z_2)}{I(z_1)}\right) \qquad (4.1)$$

where $K_d(z)$ is the diffuse attenuation coefficient and $I(z_1)$ and $I(z_2)$ are the measured downwelling irradiances at depth z_1 and z_2, respectively. The relationship between $\ln\left(\frac{I_w(z_i)}{I_w(0)}\right)$ and the depth $(z_i - z_0)$ is shown in Figure 4.12. Note that errors of the K_d values estimated from PUV measurements fell within a range between ±0.15 and ±0.1 m^{-1} (Figure 4.13).

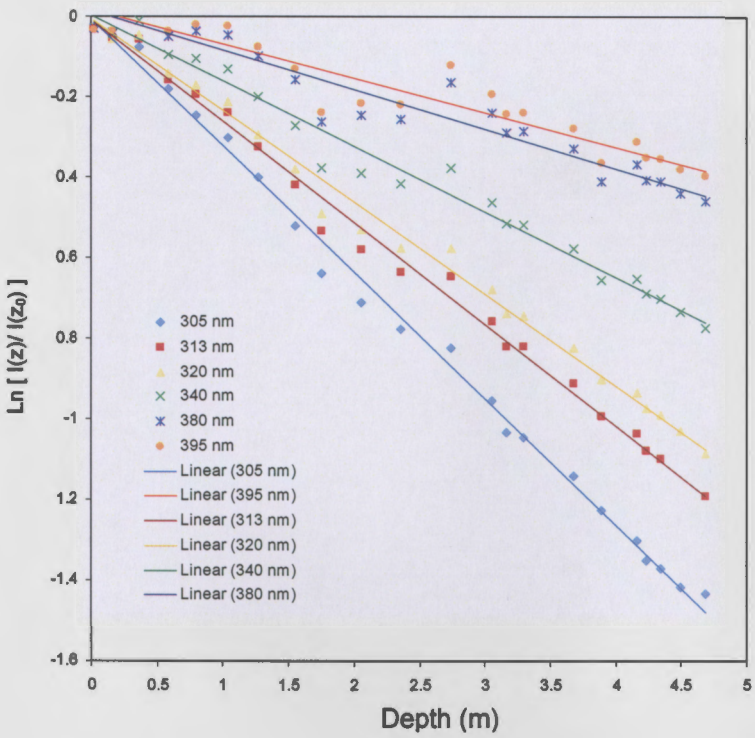

Figure 4.12 The relationship of $\ln\left(\frac{I_w(z_i)}{I_w(0)}\right)$ and the depth $(z_i - z_0)$ estimated from irradiance measurements on 17 June 2000.

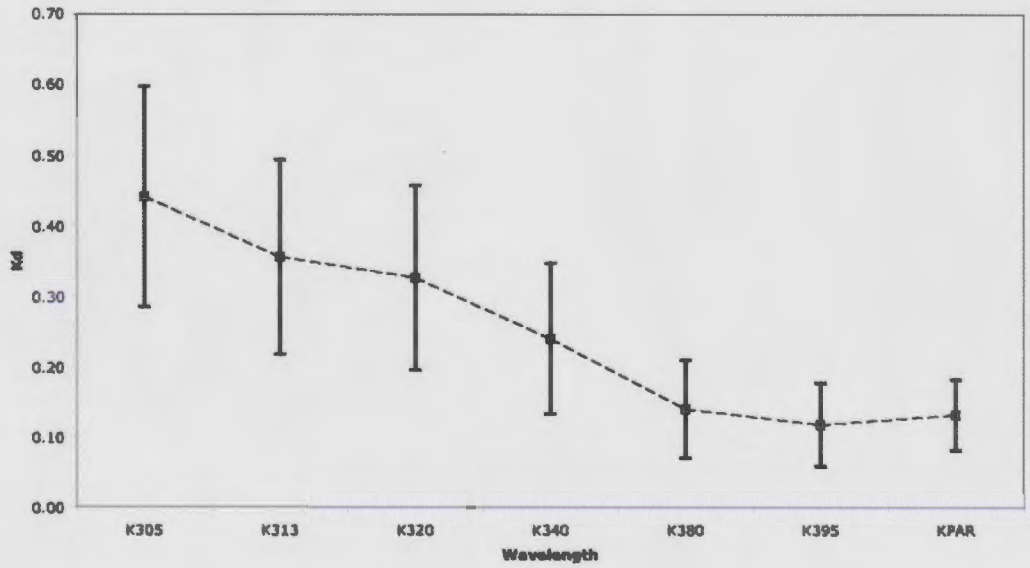

Figure 4.13 Typical errors of K_d estimates, derived from PUV irradiance measurements (K. Michael, private communication 2008).

4.3 Method for estimating solar radiation at the surface

4.3.1 Satellite Data

The Visible Infrared Spin Scan Radiometer (VISSR) on board the GMS-5 satellite is designed for monitoring cloud activities and other meteorological phenomena on Earth. The radiometer observes upwelling radiance $L_o^{\uparrow}$ from the atmosphere, clouds and the Earth's surface. It is common practice to define a pseudo-reflectivity term α'_{sat} defined as:

$$\alpha'_{sat} = \frac{\pi L_o^{\uparrow}}{I_o'^{\downarrow}} \tag{4.2}$$

where $I_o'^{\downarrow}$ is the downwelling irradiance arriving at the top of the atmosphere, determined for the satellite channels. The Earth-atmosphere system is treated as Lambertian surface for purpose of the satellite data analysis. With this assumption, a reflectivity can be derived as a ratio between upwelling and downwelling irradiance. That is:

$$\alpha'_{EA} = \frac{\pi L_o^{\uparrow}}{I_o'^{\downarrow} \cos\theta_z} = \frac{\alpha'_{sat}}{\cos\theta_z} \tag{4.3}$$

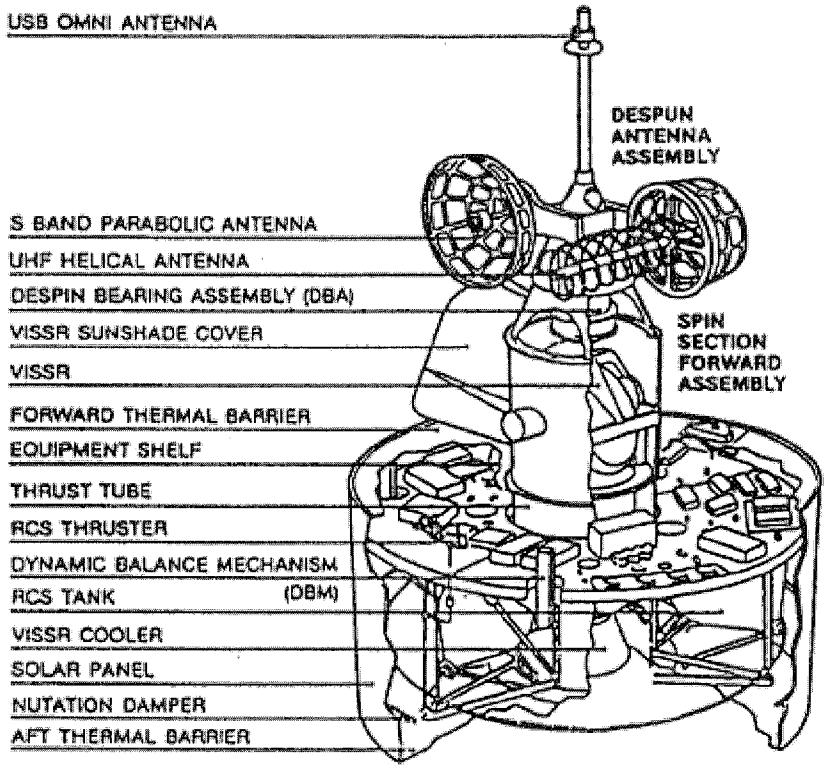

Figure 4.14 The GMS-5 satellite assembly details, showing the VISSR.

The configuration details of the GMS-5 satellite are shown in Figure 4.14. The VISSR instrument works with five different channels encompassing the visible, infrared, shortwave-infrared and water vapour absorption regions. This study uses the visible images to derive broadband Earth-atmosphere reflectivity. The images for this study were provided by the Australian Bureau of Meteorology, already sectorised for the GBR area and mapped into cylindrical projection. This study has obtained more than 36,000 images from three geostationary meteorological satellites covering an eleven-year period from January 1995 to December 2005. In particular, the data were from GMS-5 (January 1995 - May 2003), GOES-9 (June 2003 – July 2005) and MTSAT-R1 (August 2005 - December 2005). The raw images were provided every day for each hour from 2030 GMT – 1130 GMT.

The resolutions of GMS-5, GOES-9 and MTSAT-R1 at the sub-satellite point are 1.25 km × 1.25 km, 4.0 km × 4.0 km and 1.1 km × 1.1 km, respectively (Table 4.2). Due to the differences in spatial resolutions, all satellite images are first re-mapped into 600 pixels (East/West) × 650 pixels (North/South), then transformed into a final product with resolution of approximately 2.3 km (East/West) × 2.7 km (North/South). To improve the mapping processes, an algorithm has been developed which uses the pattern of the coastline to help adjust the image alignment.

The data from the VISSR instruments consists of digital counts (or gray values) that range between 0 and 255 - referred to as 8-bit data. Each digital count could correspond to reflection of radiation from the surface of the Earth (either ocean or land), or from cloud (Figure 4.15). In addition, the scattering and absorption effects of the atmosphere will also influence the value of digital count detected. To obtain the Earth-atmosphere reflectivity, digital counts for the various sensors are first converted into pseudo-reflectivity α'_{sat} via a look-up table provided by the Japanese Meteorology Agency (JMA) (see Appendix I). Figure 4.16 shows non-linear relationships between pseudo-reflectivity and satellite digital counts.

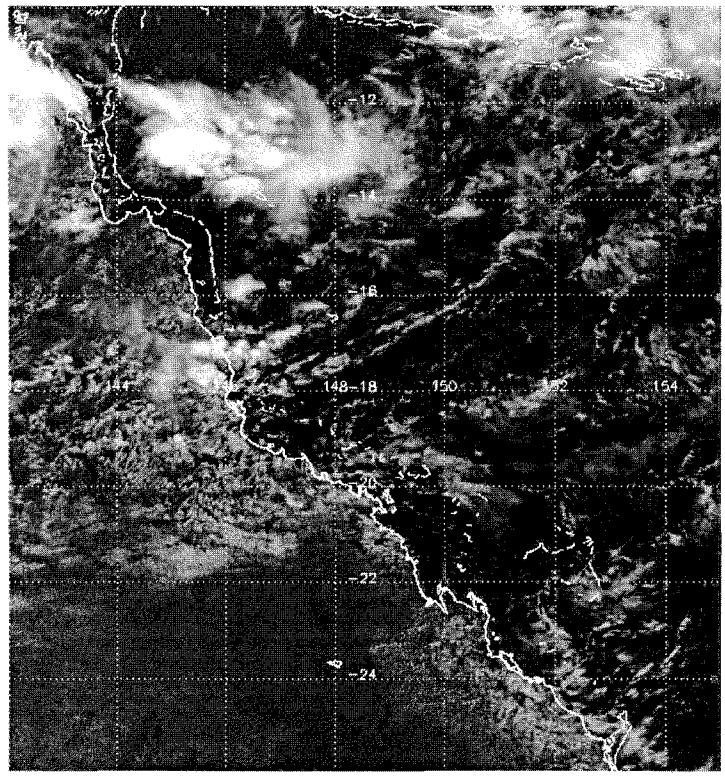

Figure 4.15 An original GOES-9 satellite image collected at 0230 GMT (1230 AEST) on 6 January 1995 shown in cylindrical projection, with 650 lines each of 600 pixels. The ocean, land and cloud portions of the image are apparent.

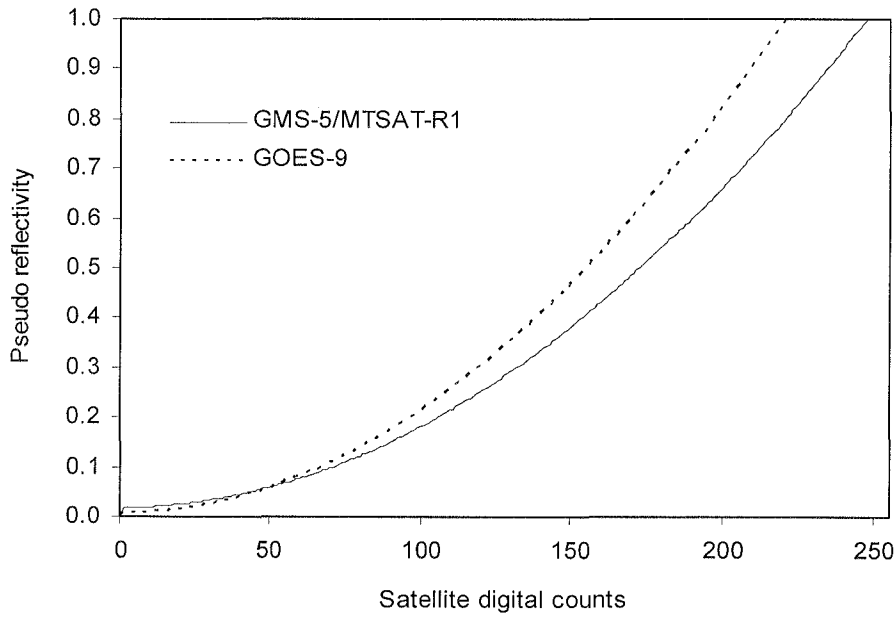

Figure 4.16 Calibration curves of GMS-5/MTSAT-R1 and GOES-9 satellites illustrating relationship between satellite pseudo-reflectivity and grey values.

Table 4.2 Details of the VISSR sensors on the GMS-5, GOES-9 and MTSAT-R1 satellites.

	GMS-5	GOES-9	MTSAT-R1
Operating periods for this study	January 1995 - May 2003	June 2003 – July 2005	August – December 2005
Spatial resolution	1.25 km × 1.25 km	4.0 km × 4.0 km	1.1 km × 1.1 km
Spectral response (visible channel)	0.44 - 0.99 μm	0.55-0.75 μm	0.44 - 0.99 μm

However, the spectral sensitivities of GMS-5 and MTSAT sensors are considerably different than that of GOES-9, as GMS-5 and MTSAT-R1 satellites accept a broad range of the visible and near-infrared regions, 0.44 - 0.99 μm, while GOES-9 senses a narrower region between 0.55-0.75 μm (Figure 4.17 and Table 4.2). This study corrects for the different sensitivities by developing a linear relationship between GOES-9 and GMS-5 pseudo reflectivity. An empirical solution obtained from a regression of the 256 data pairs of the 8-bit (0-255) digital counts is written as:

$$\alpha'_{sat(GMS)} = 0.7608\alpha'_{sat(GOES)} - 0.0088;\ R^2 = 0.99;\ SE=0.0018;\ N=256 \qquad (4.4)$$

Therefore all GOES-9 data were transformed to an equivalent GMS-5 signal. This procedure standardised all data to the spectral channels of GMS-5.

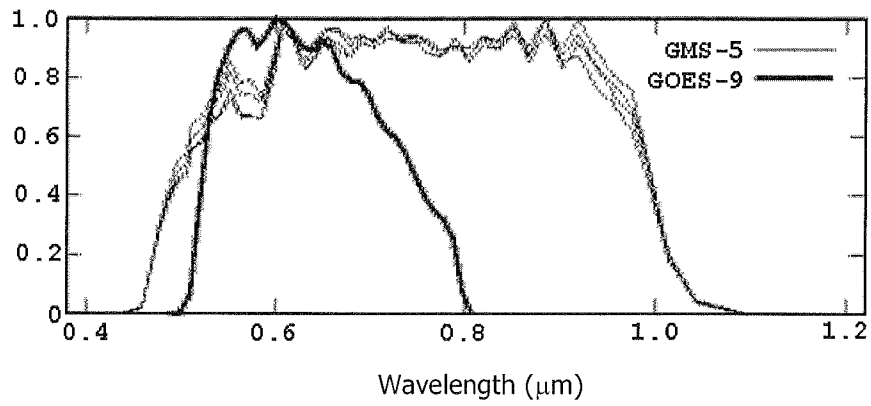

Figure 4.17 Spectral responses of the VISSR instruments on GMS-5 (thin lines) and GOES-9 (thick-line). The four thin lines represent sensitivities of the 4 visible detectors of GMS-5.

To obtain the Earth-atmosphere reflectivity (α'_{EA}), the pseudo-reflectivity values are divided by the cosine of solar zenith angle ($\cos\theta_z$). That is:

$$\alpha'_{EA} = \frac{\alpha'_{sat}}{\cos\theta_z} \tag{4.5}$$

where α'_{EA} is the earth-atmosphere reflectivity observed by the satellite, α'_{sat} is the pseudo-reflectivity and θ_z is solar zenith angle. High-reflectance objects such as cloud and snow can reach α'_{EA} values of more than 0.6. By contrast, vegetation and ocean have much lower α'_{EA}, ranging between 0.3 and 0.5.

The values of α'_{EA} are then adjusted for non-Lambertian surface factors, estimated as a function of solar zenith angle (Figure 4.18).

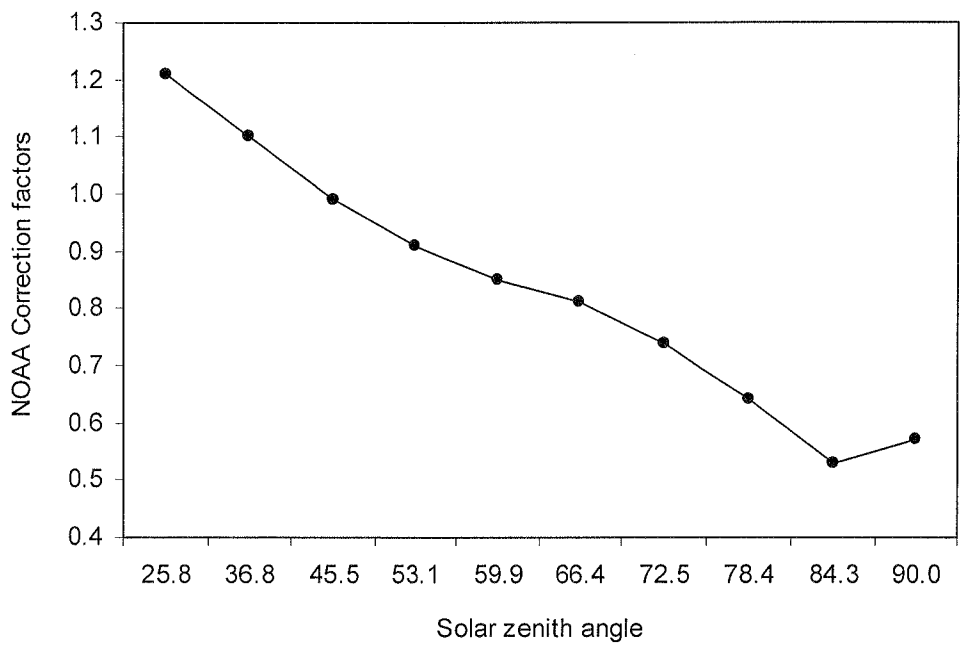

Figure 4.18 Non-Lambertian correction factors of a could surface obtained from NOAA (Taylor and Stowe, 1984).

The values of α'_{EA} are then adjusted for non-lambertian surface factors. The total upwelling irradiance at TOA may be written as:

$$I_o^{\uparrow} = \int_0^{2\pi} \int_0^{\pi/2} L_o^{\uparrow}(\theta,\varphi) \cos\theta \sin\theta d\theta d\varphi \tag{4.6}$$

assuming that $L_o^{\uparrow}(\theta,\varphi)$ is everywhere known. In most satellite work, this term is not known or the satellite only sees a radiance $L_o^{\uparrow}(\theta,\varphi)$. However, it is possible to turn this radiance into an upwelling irradiance by assuming a lambertian surface.

$$I_o^{\uparrow} = \pi L_o^{\uparrow}(\theta,\varphi) \tag{4.7}$$

The non-Lambertian correction factor (*LF*) to apply depends on satellite nadir and azimuth angle, as well as surface type. Explicitly, it can be written as:

$$LF = \frac{I_o^{\uparrow}}{\pi \cdot L_o^{\uparrow}(\theta,\varphi)} \tag{4.8}$$

Figure 4.18 describes *LF* for a could surface in the visible band. This correction was used for all images including clear images. To use separate correction factors for each pixel is impractical and inconsequential if the pixel is cloudless due to the much smaller surface albedos compared to cloud albedos. However, use of *LF* improves substantially the prediction of the satellite radiation model for cloudy conditions.

4.3.2 Relationship between satellite and broadband reflectivity

The last required process involves transformation of the α'_{EA} values into broadband Earth-atmosphere reflectivity, α_{EA}. This study establishes a linear relationship between satellite and broadband reflectivity estimated from a Streamer routine. The spectral reflectance $\alpha_{EA\lambda}$ is defined as a ratio between spectral upwelling and downwelling solar irradiance observed at the top of atmosphere:

$$\alpha_{EA\lambda} = \frac{I^{\uparrow}_{o\lambda}}{I^{\downarrow}_{o\lambda}} \tag{4.9}$$

where $I^{\uparrow}_{o\lambda}$ and $I^{\downarrow}_{o\lambda}$ are the spectral upwelling and downwelling solar irradiance observed at the top of atmosphere. To obtain the satellite to broadband conversion, a wide set of solar zenith angle, surface types and cloud properties are simulated and used to calculate sets of spectral $\alpha_{EA}(\lambda)$ values, which are then integrated for the regions of 0.44 μm - 0.99 μm and 0.3 μm - 3.0 μm to become satellite and broadband solar irradiance, respectively. For all the conditions, a regression analysis was derived from the satellite and broadband reflectivity:

$$\alpha_{EA} = 0.9069 \cdot \alpha'_{EA} + 0.0212 \tag{4.10}$$

$$R^2 = 0.9964; \text{ SE} = 0.012; \text{ N} = 11268$$

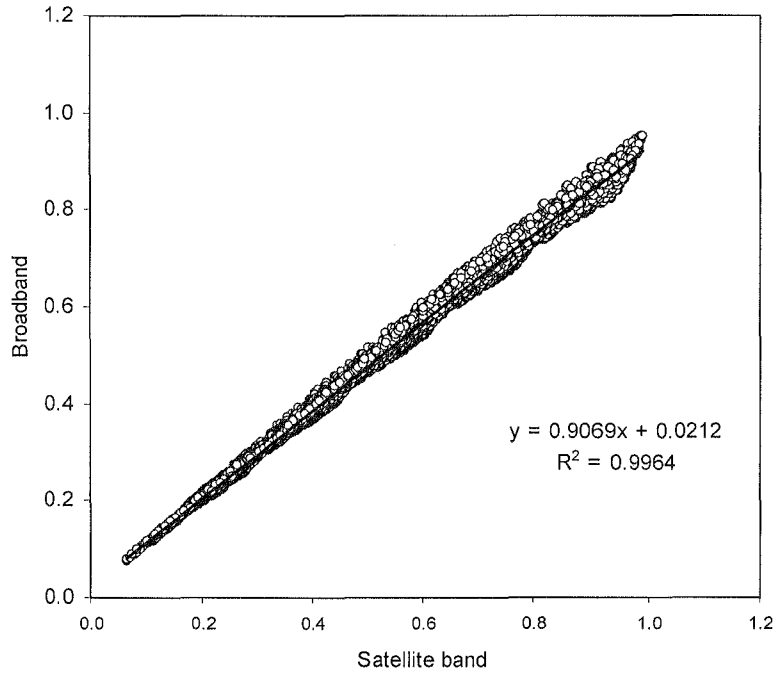

Figure 4.19 Linear relationship of Streamer-derived Earth-atmosphere reflectivity between satellite band and broadband solar radiation.

4.3.3 Cloud fraction

Following a study by Koelemeijer and Stammes (1999), α_{EA} can be written in terms of a cloud fraction. That is:

$$\alpha_{EA} = (1-C)T\alpha_g + CT\alpha_c \tag{4.11}$$

where C is the cloud fraction, T is the atmospheric transmission for direct radiation and α_g and α_c are the surface and cloud top albedo. Cloud fraction can be obtained by assuming a clear atmosphere (T = 1) to give:

$$C = \frac{(\alpha_{EA} - \alpha_g)}{(\alpha_c - \alpha_g)} \approx \frac{(\alpha'_{EA} - \alpha'_{EA(\min)})}{(\alpha'_{EA(\max)} - \alpha'_{EA(\min)})}. \tag{4.12}$$

In this study, images of $\alpha'_{EA(\min)}$ were compiled for each hour across a month. Each pixel of the image was searched for a minimum digital count. Images of $\alpha'_{EA(\min)}$ represent the reflectivity of the ocean or land surface under cloud-free conditions. The nine hourly minimum images produced for a month were also further averaged to a monthly minimum image. In a similar fashion, hourly images of $\alpha'_{EA(\max)}$ were obtained, corresponding to the reflectivity of cloud across the study region.

This estimation of cloud cover will vary smoothly with the surface albedo approximated as $\alpha'_{EA(\min)}$. However, the error expected is due to be small because $\alpha'_{EA(\min)}$ is contained both in the nominator and denominator. It is unlikely that the pixel can be confused as clouds because it is the minimum reflectivity pixel in a month. In addition, we have a cloud threshold, so that it is unlikely that cloud cover will be confused with $\alpha'_{EA(\min)}$.

4.3.4 Ozone data

This study collected daily global ozone data from the TOMS website (http://toms.gsfc.nasa.gov/ozone/ozone_v8.html) for the period 1995 to 2005. The data were mapped in a cylindrical projection at a resolution of 1° (North/South) $\times$ 1.25° (East/West) (Figure 4.21). This study sectorised the data and used an interpolation technique to fill gaps in the data over the study region (Figure 4.22). The daily data were then averaged over the 12 months of each year to provide monthly averages of ozone for the study region.

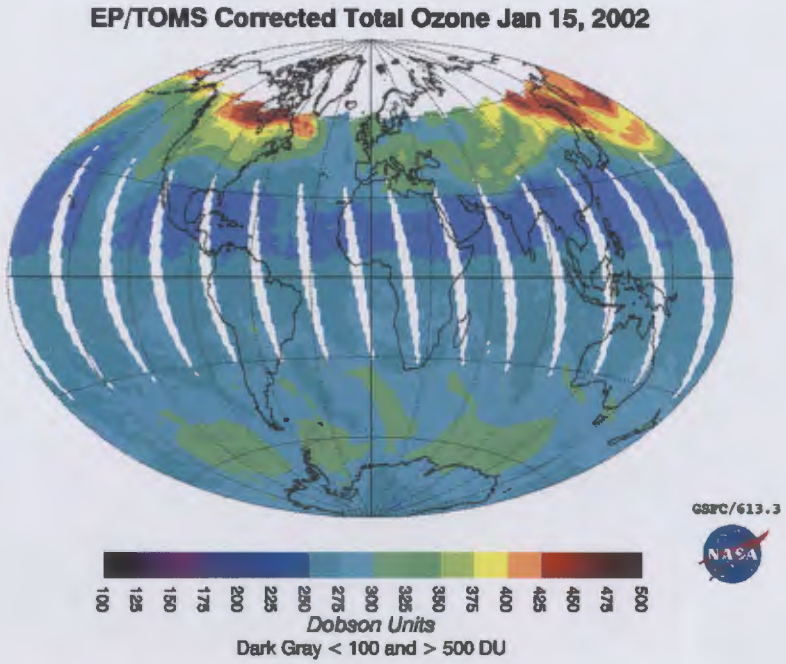

Figure 4.20 A global ozone image retrieved from TOMS website.

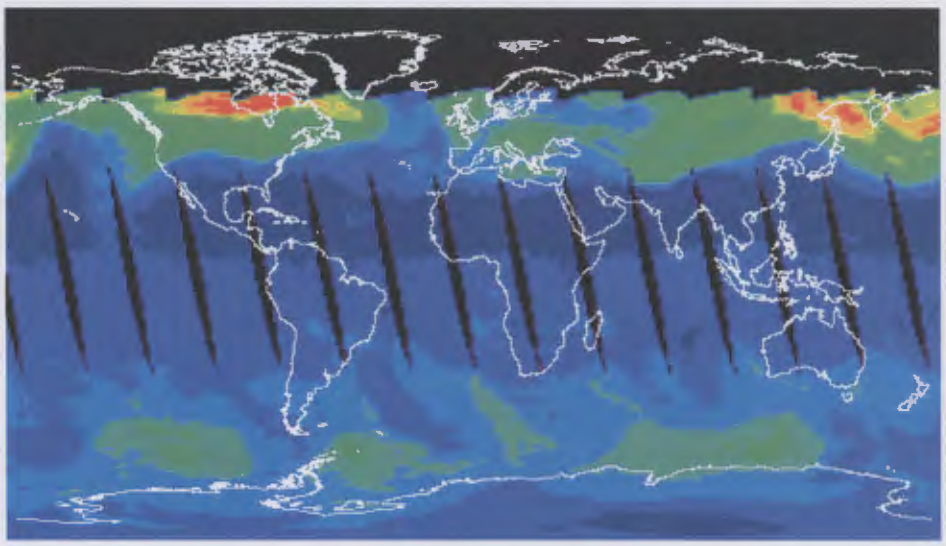

Figure 4.21 A TOMS global ozone image shown on a cylindrical projection.

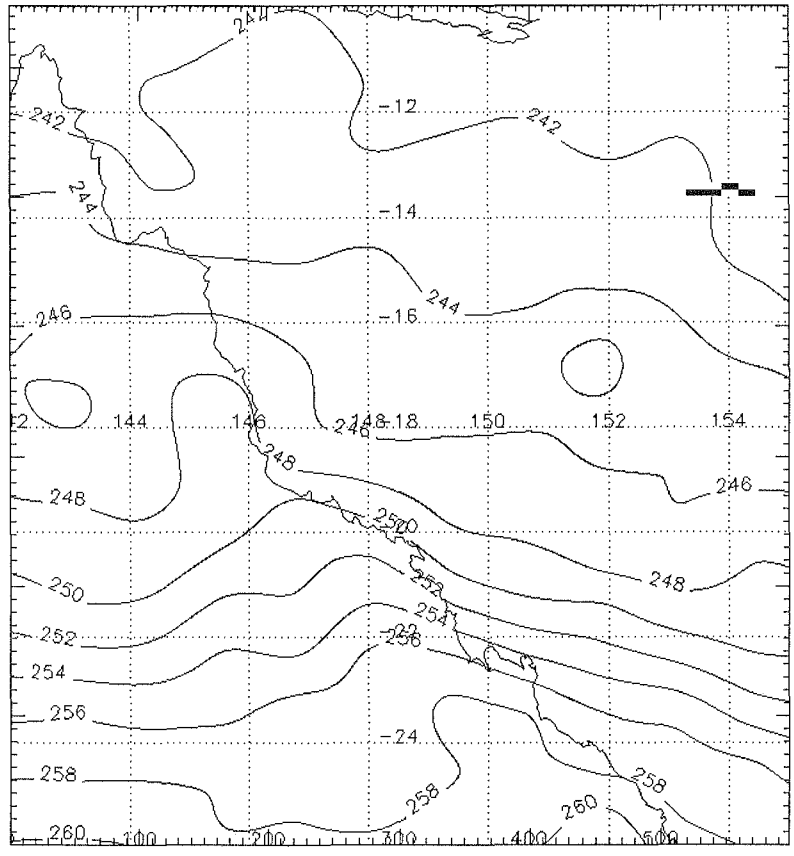

Figure 4.22 A map of monthly ozone data that was sectorised and mapped for the study area. The values are in Dobson units.

4.3.5 Model for estimating surface broadband solar radiation

This study has selected the Streamer radiative transfer model for the calculation of surface irradiance (Key and Schweiger, 1988; Key, 2001). The Streamer comprises of several radiative-based models such as DISORT and Two-stream Approximation that provide flexibility in radiance and irradiance computing. The model has options of atmosphere and surface conditions provided with spectrally-integrated of wavebands between 0.3 – 4.0 μm. Input variables involved cloud optical properties, such as, optical depth, liquid water content, droplet radius, and profiles of cloud based/top height and thickness, can be set into the program. The model can compute direct and diffuse irradiance using multiple streams and the Discrete Ordinate Solver (DISORT) algorithms, covering both the solar and thermal infrared regions in 24 and 105

wavelength bands, respectively. Use of discrete wavelength bands makes the model rapid to execute without scarifying accuracy.

It is grossly time consuming to repeat all the Streamer radiative transfer calculations on 390,000 pixels (600 pixels × 650 pixels) for all satellite images. This study uses an approach similar to that pioneered by Pinker and Laszlo (1992). They used a delta-Eddington approximation to simulate surface broadband irradiance as a function of various parameters including solar zenith angle, precipitable water vapour, aerosol profiles and cloud amount.

The user has given a choice of atmospheric models and liquid and ice cloud properties, which can be set with a wide variety of atmospheric and surface conditions. It is possible to use overlapping cloud at the same time with different cloud micro and macro properties: droplet radius, liquid water content, optical depth, thickness, based height, scattering function and many others. Similarly, surface albedo can be chosen from a switch of five different types or a specific user provided surface type. An additional feature is the user command language that allows looping structure such as time of day or surface, type water vapour etc. This makes a very efficient output which is well suited to the Look-Up Table approach that will be followed in this thesis. Given above advantages, this model was chosen over several candidates such as 5S, MODTRAN, DISORT and SBDART.

4.3.5.1) *Creating a Look-up Table*

This study develops a technique using Streamer routines to create a series of Look-up Tables (LUT) containing downwelling irradiance I_g and atmospheric reflectivity α_{EA}. Streamer contains two standard radiative models: a two-stream approximation model and a discrete ordinate solver (DISORT). Streamer can compute any specific ranges of solar radiance or irradiance that travel through the atmosphere.

The model calculation in this study uses the six stream approximation with discrete ordinate solver. To obtain as output total broadband, default options set for inputs in the Streamer routines involve a six-stream approximation and a discrete ordinary solver. Input data cover a range of solar zenith angle, cloud fraction, surface albedo, cloud based height, cloud thickness, liquid water content and droplet radius as Look-Up table as described below. Total broadband downwelling irradiance at the surface I_g and simulated Earth-atmosphere albedo α_{EA}, defined as a ratio between upwelling and downwelling irradiance at the top of atmosphere (Equation 4.6), are estimated.

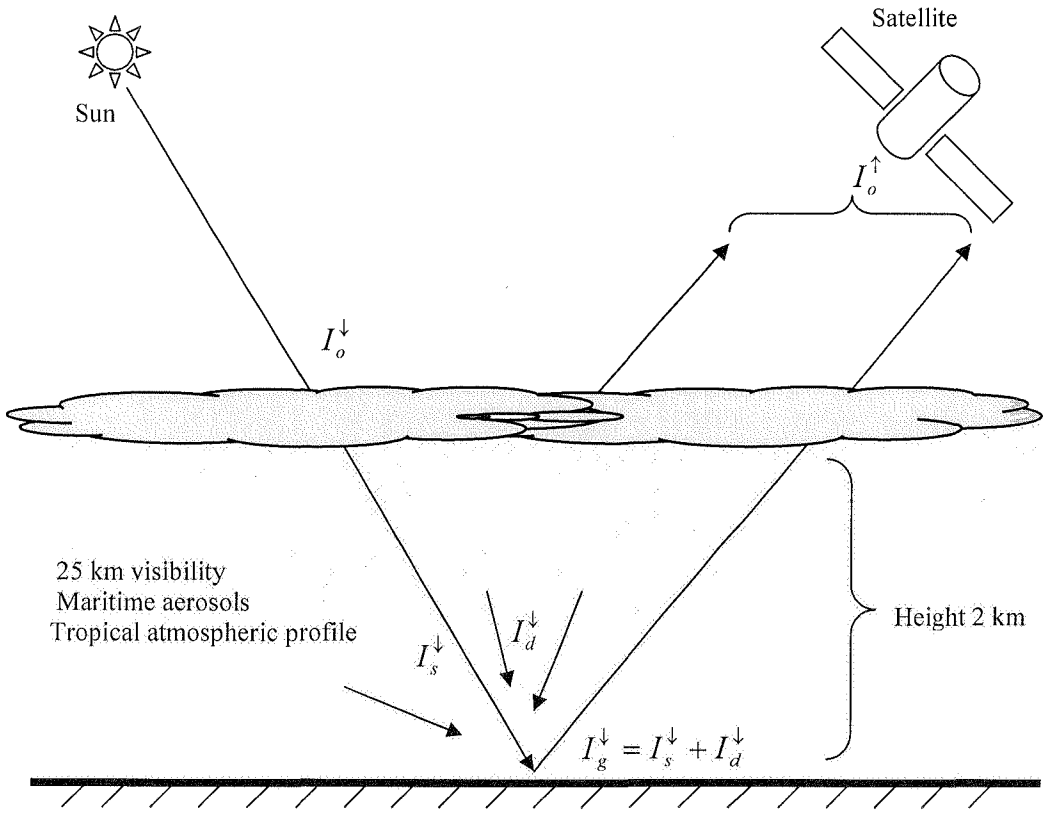

Figure 4.23 Atmosphere simulation used in Streamer routine.

As mentioned earlier, use of look-up table saves a computing time, while at the same time provides vigorous of solar radiation fluxes. To cover a full range of atmospheric conditions, the Streamer routine is programmed to compute I_g and α_{EA} values for a wide range of variable parameters including: solar zenith angle, surface albedo, cloud fraction, cloud height, cloud thickness, cloud droplet radius and cloud liquid water content (LWC). All routines are parameterised with one default condition, which is set for tropical atmospheric profile, summer season, maritime aerosols and 25 km visibility. Details of each input variable are listed in Table 4.3.

Table 4.3 Data used in Streamer input.

Parameters	Degree of Freedom	Variables
Solar zenith angle	9	0°, 10°, 20°, 30°, 40°, 50°, 60°, 70° and 80°
Cloud fraction	6	0, 20, 40, 60, 80 and 100 %
Surface albedo	2	5% Ocean, 10% Land
Cloud base height	1	2 km
Cloud thickness	5	0.1, 0.6, 1.1, 1.6 and 2.1 km
Cloud LWC.	5	0.05, 0.15, 0.25, 0.35 and 0.50 g/m^3
Cloud droplet radius	5	2.5, 4.0, 5.5, 7.0 and 8.5 μm

The data sets for solar zenith angle and cloud fraction obtained from the Streamer routines are considerably coarse in their resolution. An interpolation technique is therefore applied to define the output at 1° and 1% steps for solar zenith angle and cloud fraction, respectively. Results contain data sets of 90 solar zenith angles, 100 cloud fractions, 2 surface types, 5 cloud optical thickness, 5 droplet radius and 5 LWC, which provide a total of 2,250,000 degrees of freedom. Figure 4.24 shows a 3D plot of I_g after interpolation.

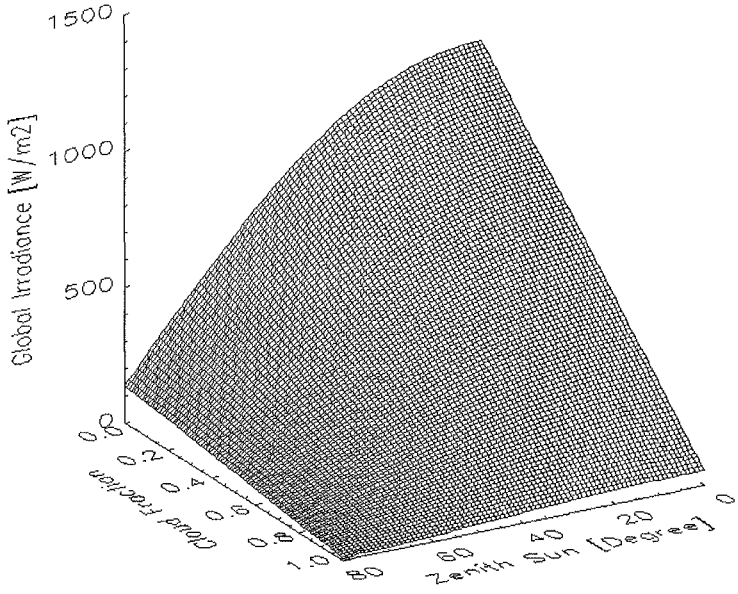

Figure 4.24 Interpolated plot of solar irradiance showing changes for steps of 1° of solar zenith angle and 1% in cloud fraction.

4.3.5.2) *LUT algorithm*

The first step in estimating solar irradiance from the LUT involves determining the cloud fraction using the Earth-atmosphere albedo and surface albedo at given pixel (Equation 4.8). Solar zenith angle at that pixel is also obtained, as the time of the satellite scene is also known. The next step involves estimating the cloud properties — liquid water concentration, cloud thickness and mean droplet radius — by observing which combination of the satellite-derived broadband reflectivity α_{EA} is closest to that computed by Streamer. Once all the parameters of the albedo LUT are obtained, they are then applied in a new LUT to determine surface irradiance (Figure 4.25). There are some cases in which more than one set of liquid water content, thickness and droplet radius satisfy α_{EA}. In this case, an average surface irradiance is calculated using these different possible consideration of parameters. In actual fact the variability of I_g is small for these conditions, typically within 50 W-m^2.

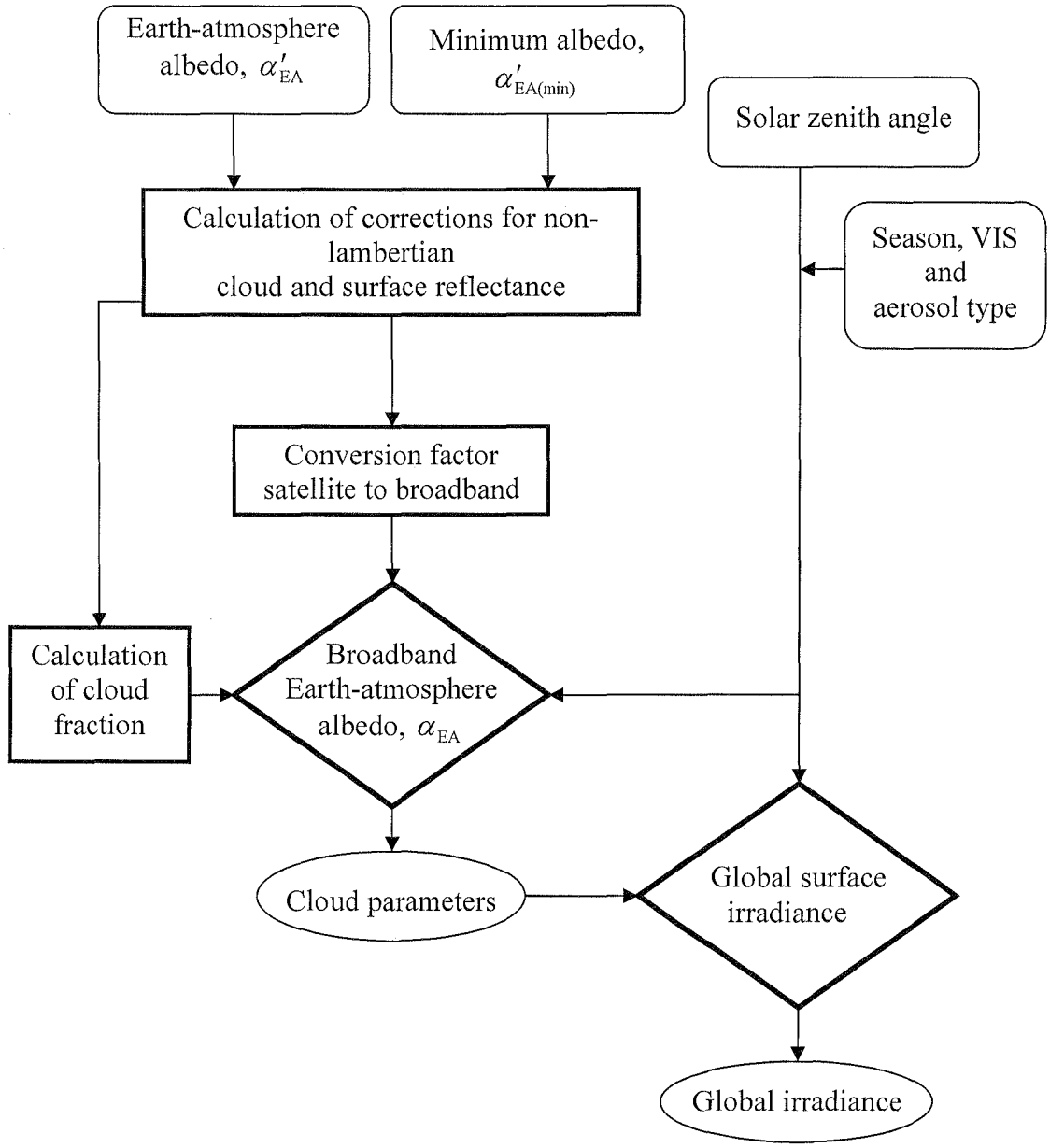

Figure 4.25 Approach used to estimate incident solar irradiance at the surface. The diamonds represent the two look-up tables used for estimating broadband Earth-atmosphere albedo and global surface irradiance.

4.3.6 Method for estimating UVB irradiance at the surface

Following the technique developed to construct LUTs for the broadband solar irradiance I_g estimation, this study uses the UVSPEC radiative transfer routine to create UVB irradiances. The parameters that vary in the UVSPEC calculation involve cloud base height, solar zenith angle, cloud fraction, surface albedo, ozone and cloud properties (Table 4.4). An interpolation approach is also applied to fill every 1° of solar zenith angle and 1% cloud fraction parameters.

The parameters of solar zenith angle, cloud fraction, surface type, cloud droplet radius, LWC and 11 ozone values (240, 250, 260, ... , 350 DU) are used in a UVSPEC-derived LUT to obtain a value of UVB irradiance. The algorithm also interpolates for ozone values that lie in between the 10 specific ozone values considered:

$$UVB = a_1 \cdot ozone^2 + a_2 \cdot ozone + a_3 \qquad (4.13)$$

where a_1, a_2 and a_3 are the regression coefficients. Using Equation 4.10, actual values of TOMS ozone are substituted into the equations, and the values of UVB are obtained as a result.

Table 4.4 Data used in UVSPEC routines.

Parameters	Degree of Freedom	Variables
Solar zenith angle	9	0°, 10°, 20°, 30°, 40°, 50°, 60°, 70° and 80°
Cloud fraction	6	0, 20, 40, 60, 80 and 100 %
Surface albedo	2	5% Ocean, 10% Land
Ozone	11	240 – 350 DU
Cloud thickness	1	1 km
Cloud LWC.	5	0.05, 0.15, 0.25, 0.35 and 0.50 g/m^3
Cloud droplet radius	5	2.5, 4.0, 5.5, 7.0 and 8.5 μm

4.3.7 Method for estimating PAR irradiance at the surface

For the estimation of PAR irradiance at the surface, this study uses the Streamer model to provide data pairs of PAR and broadband solar irradiance incorporating a range of solar zenith angles, cloud fraction, surface types and atmospheric conditions. A linear relationship is obtained (Figure 4.26). Using a regression technique, a set of coefficients is derived, allowing PAR irradiance at the surface to be estimated from the relationship:

$$PAR = 0.508 \cdot I_g + 5.19 \qquad (4.14)$$

$$R^2 = 0.999;\ \text{S.E.} = 5.31\ \text{W-m}^2;\ N = 13500$$

where I_g is broadband solar irradiance.

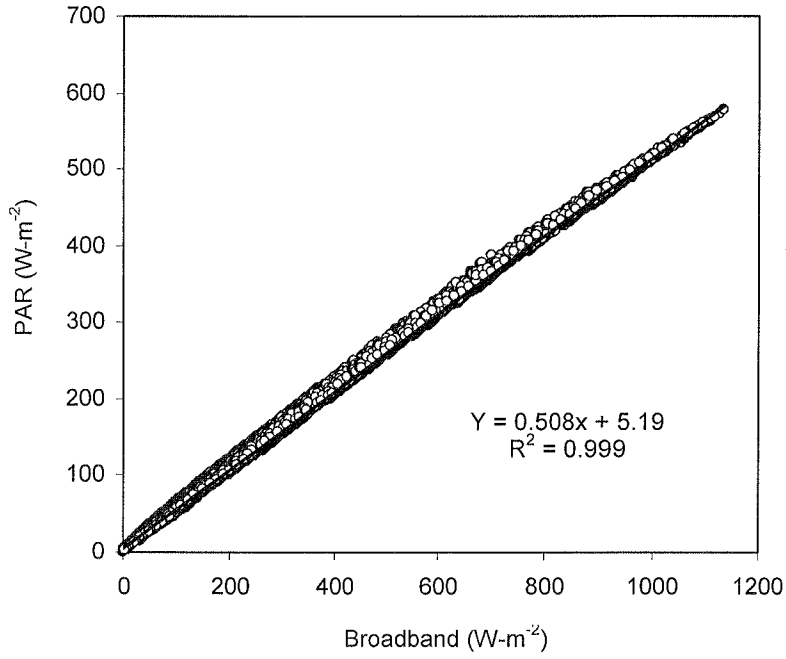

Figure 4.26 Relationship between PAR and broadband irradiance.

4.4 Method for estimating underwater UVB and PAR irradiances

The techniques for mapping solar irradiance underwater using satellite-derived attenuation coefficient (K_d) have been documented since the 1980s (Gordon *et al.*, 1975; Spinrad *et al.*, 1994; Bukata *et al.*, 1995; Roesler and Perry, 1995; Hojerslev, 2004; Liu *et al.*, 2006). Recent studies blended traditional approaches with remotely-sensed data, therefore providing high spatial resolution UVB and PAR irradiance for many oceans across the globe (Bukata *et al.*, 1995; Ershova *et al.*, 2002; Liu *et al.*, 2006).

In the next section, a method for deriving maps of underwater UVB and PAR irradiance for the Great Barrier Reef is discussed. This study uses satellite remote-sensed K_d data, retrieved from SeaWiFS, to characterise PAR and UVB attenuation coefficients. Mapping details are presented in the following sections.

4.4.1 SeaWiFS data

The Coastal Zone Color Scanner (CZCS) project was developed by NASA in response to the growing need for knowledge of ocean optical properties. One notable outcome was the SeaWiFS instrument launched in August 1993. The instrument consists of an optical scanner and an electronic module, capable of providing ocean colour for both global and local area coverage (Figure 4.27). Data retrieved from SeaWiFS provides a series of oceanic measurements including chlorophyll-*a* concentration (mg-m^{-3}), aerosol optical thickness at 865 nm, oceanic diffuse attenuation coefficients (K_d) at 490 nm and seven bands of normalized water-leaving radiance centered at 412 nm, 443 nm, 490 nm, 510 nm, 555 nm, 670 nm and 865 nm (Hooker *et al.*, 1992).

The instrument is on board the SeaStar satellite orbiting the Earth at a low altitude of 705 km providing data at a high spatial resolution of 1.13 km × 1.13 km. The

diffuse attenuation coefficients K_d retrieved from the SeaWiFS instrument apply to the visible band (centered at 490 nm) and encompass a spectral region of 480 - 500 nm (Figure 4.28).

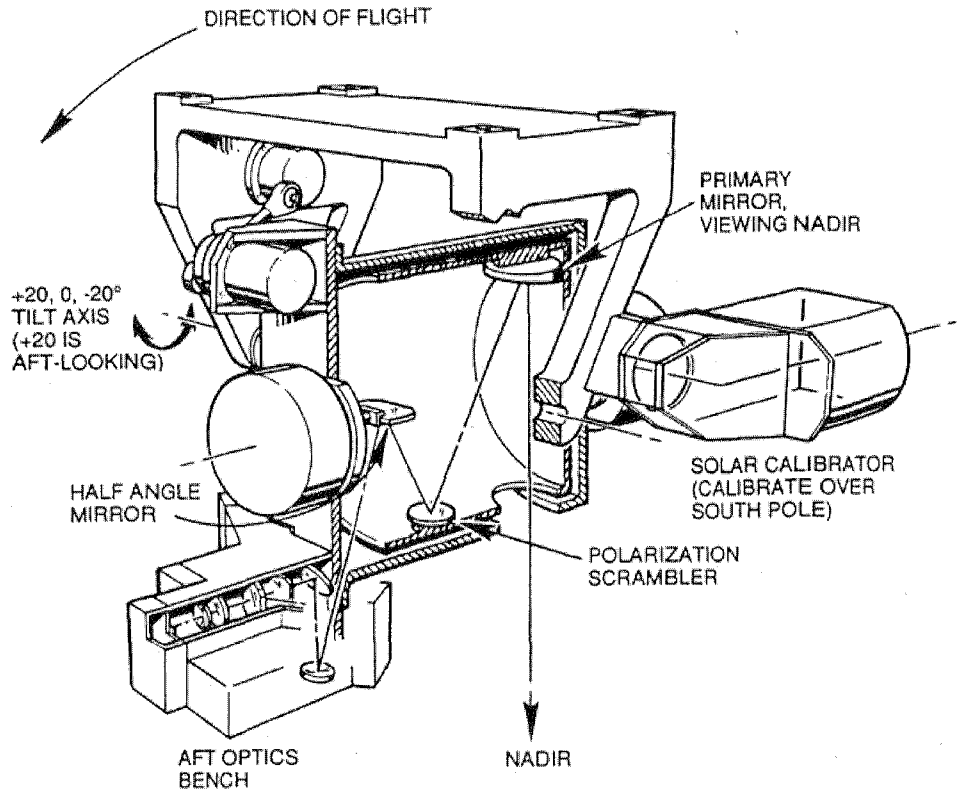

Figure 4.27 Optical configuration of SeaWiFS instrument (Hooker *et al*, 1992).

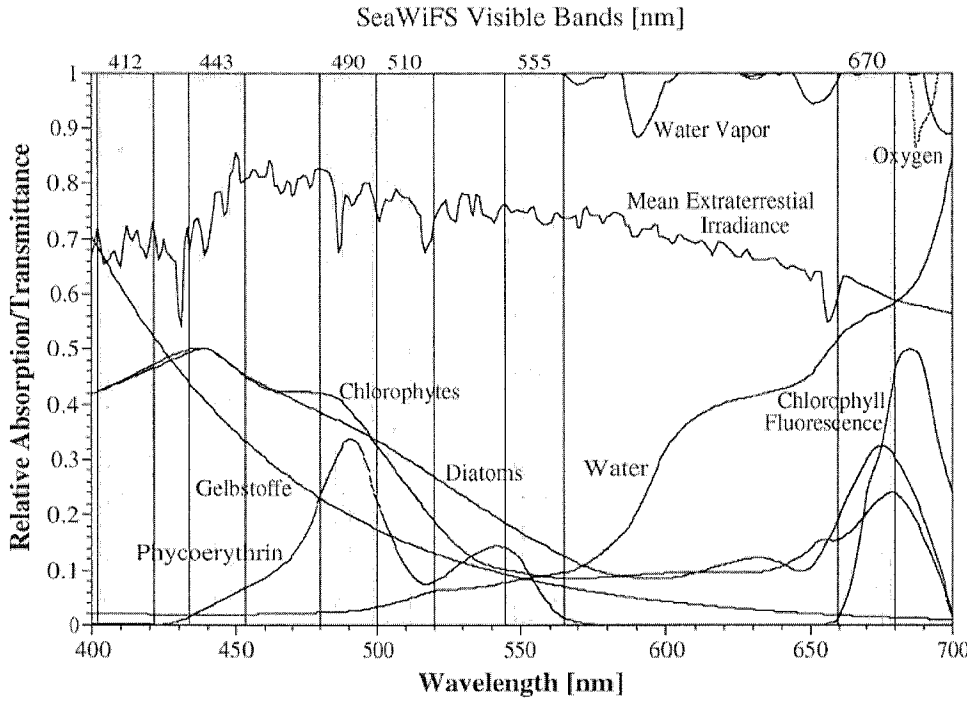

Figure 4.28 Active spectra of the SEAWiFS instrument compared with absorption/transmittance of various substances and the solar irradiance at the top of the atmosphere (Hooker *et al.*, 1992).

This study collected daily, 8-day and monthly Global Area Coverage (GAC) SeaWiFS data from the NASA ftp server (ftp://oceans.gsfc.nasa.gov). Data is available for periods between January 1997 and December 2005. It is already mapped into a cylindrical projection and compressed into Hierarchical Data Format (HDF), which is called *Level 3 mapped* data. The study transforms the raw HDF files into 8-bit arrays featuring image that contains the raw counts over a large array — 4320 pixels × 2160 pixels (Figure 4.29). All images are then sectorised to the GBR region (153 pixels × 195 pixels) and remapped into 600 pixels × 650 pixels to match the geostationary data over the study region (Figure 4.30).

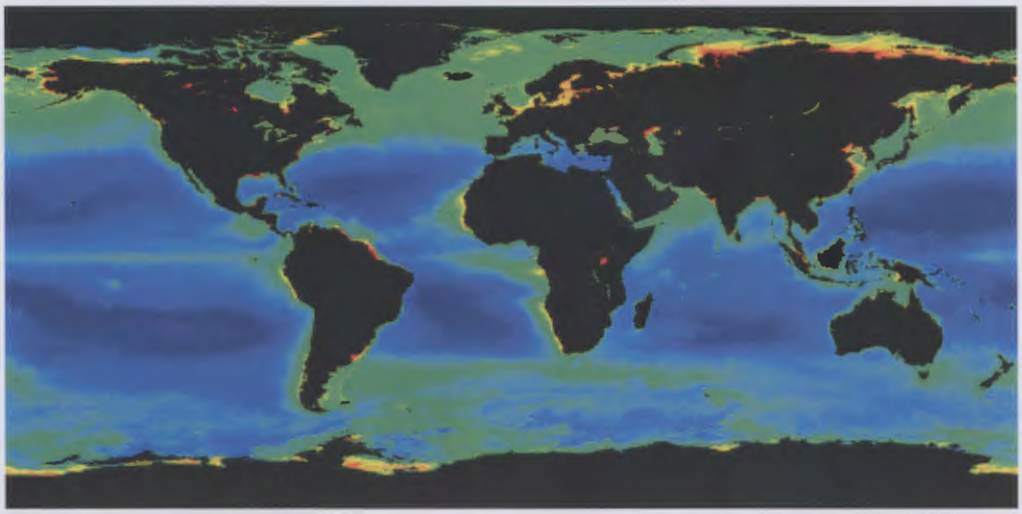

Figure 4.29 A global image of monthly mean diffuse attenuation coefficient at 490 nm retrieved from the SEAWiFS instrument, shown in cylindrical projection (4320 × 2160 pixels).

Figure 4.30 An SeaWiFS image of $K_d(490)$ extracted from HDF data, mapped into a 600 × 650 pixels grid.

To obtain the diffuse attenuation coefficient (K_d), the raw counts (*Count*) which are contained in the SeaWiFS images are converted into $K_d(490)$ by using an equation:

$$K_d(490) = 10^{Slope \cdot Count + y_0} \tag{4.15}$$

where *Slope* and y_0 are defined specifically in each SeaWiFS file. This satellite-derived $K_d(490)$ represents the diffuse attenuation coefficients of ocean waters. However, the data can not be derived over regions that are obstructed by clouds. As a result, the daily images cannot provide a full coverage for the study regions (Figure 4.31). Therefore, monthly rather than daily images are considered in this estimation (Figure 4.32).

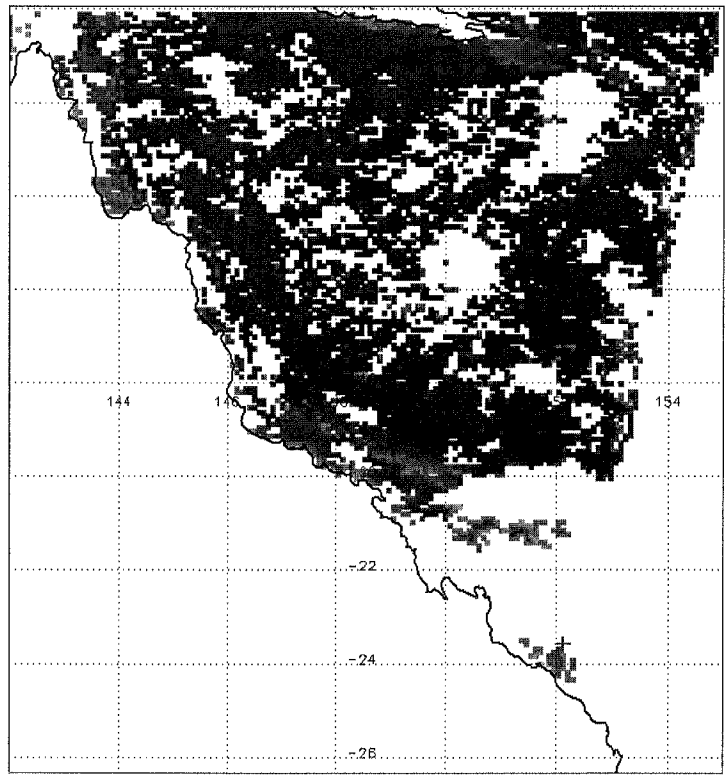

Figure 4.31 A daily image of $K_d(490)$ retrieved from an HDF file.

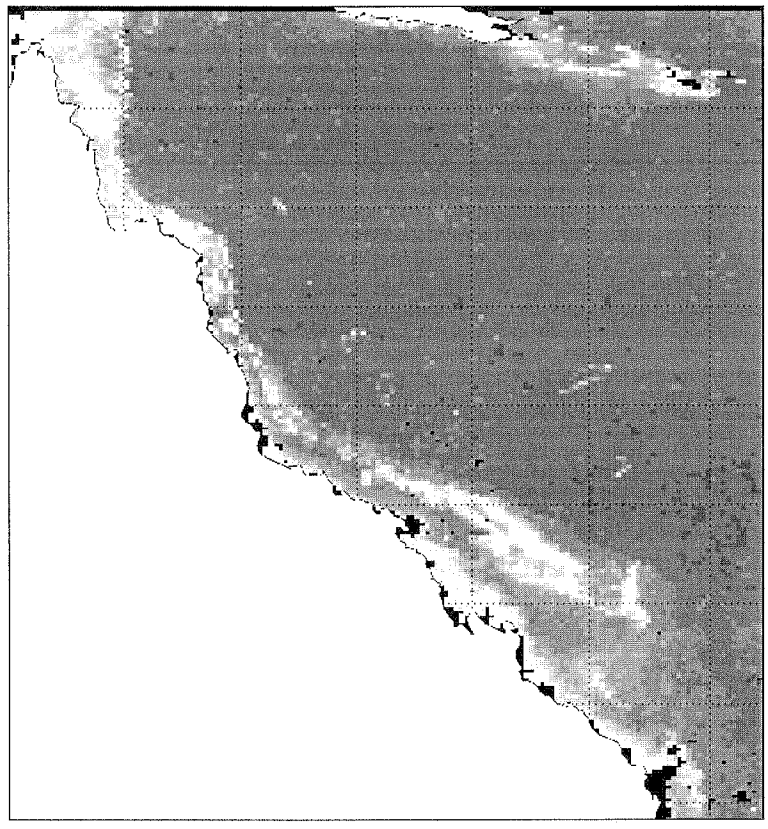

Figure 4.32 A monthly image of K_d(490) retrieved from an HDF file.

It may be noted that K_d (490) over the reef areas are relatively high. This may be interpreted as high turbidity in the water column, although other processes may be operating. Bottom reflectance from shallow depth typical of reef areas may contribute to the upwelling irradiance. Mobley and Sundman (2003) examined this problem using a Monte Carlo model which had two different albedos 0.05 and 0.5. They then estimated the contribution of bottom reflectance to the total upwelling irradiance. For a highly scattering water column and depth of 10 m, approximately 85% of the upwelling irradiance comes from the water column. By contrast, if the bottom reflectance is 50%, only 40% of the upwelling irradiance comes from the water column (Mobley and Sundman, 2003).

Examining the bathymetry of Figure 4.1 and comparing it with Figure 4.32, much of the high K_d (490) signals come from depth that are less than 10 m. As there is no information on bottom albedo, it is not possible to come up with a firm answer.

However, it is a possibility that the high K_d (490) signal is effected by bottom features. Nevertheless, estimates of K_d (490) are needed as the key used in this study to provide the extinction in other wavelengths. Therefore, it is advisable to view the high K_d (490) signal in the reef areas as a combination of turbidity and surface bottom effects.

4.4.2 Ocean surface albedo

Ocean surface albedo α_w is necessary for estimating underwater solar irradiances. Values of ocean surface albedo are available via an online Look-Up Table website (http://snowdog.larc.nasa.gov/jin/albedofind.html). The values of α_w are provided every 0.01 μm for various combinations of solar zenith angles, surface wind speeds, chlorophyll concentrations and aerosol/cloud optical depth at 500 nm.

This study assumes that ocean surface albedo observed in GMS satellite band (0.44-0.99 μm) is equal to the GMS minimum reflectivity, $\alpha'_{EA(\min)}$. The values of α_w were extracted for various of solar zenith angles (0°, 10°, 20°, 30°, 40°, 50° and 60°) and chlorophyll concentrations (0, 0.2, 2.0, 5 and 10 mg-m^{-3}), and then used to create relationships of the spectrally-integrated α_w for three wavebands: UVB (0.28-0.32 μm), PAR (0.4-0.7 μm) and GMS (0.44-0.99 μm). Using regression techniques, empirical relationships of α_w between the GMS and UVB/PAR channels are provided:

$$\alpha_w(PAR) = 1.0139 \cdot \alpha'_{EA(\min)} + 0.0055 \qquad (4.16)$$

$$R^2 = 0.99, \text{ S.E.}=0.00095, \text{ N}=42$$

and

$$\alpha_w(UVB) = -11.55 \cdot \alpha'^2_{EA(\min)} + 1.7139 \cdot \alpha'_{EA(\min)} + 0.015 \qquad (4.17)$$

$$R^2 = 0.83, \text{ S.E.} = 0.00402, \text{ N} = 42$$

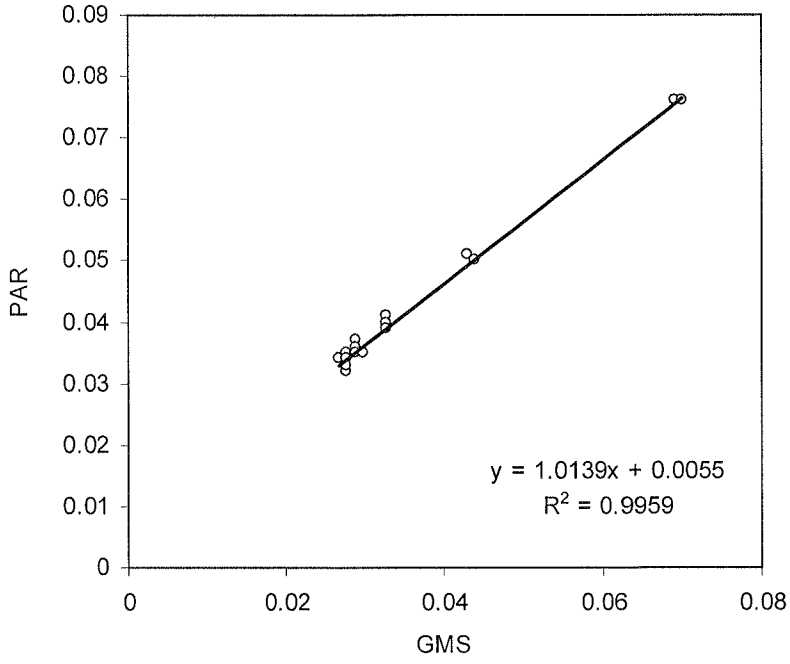

Figure 4.33 Relationship of ocean reflectivity between GMS and PAR.

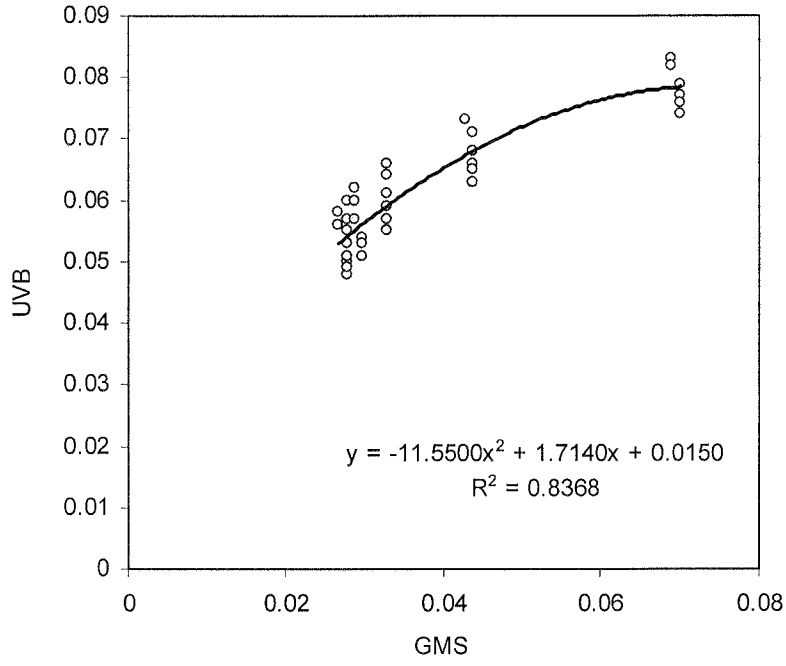

Figure 4.34 Relationship of ocean reflectivity between GMS and UVB, the scatter of points around the UVB axis represents different solar zenith angle, which ranges from 10°-90°.

4.4.3 Model for estimating UVB and PAR underwater irradiances

A technique for deriving the spectral K_d relationships between the SeaWiFS and PAR/UVB channels has been developed. Figure 4.35 summarises the main steps involved in estimating underwater irradiance. Monte Carlo models are used to transform $K_d(490)$ into broadband values for UVB and PAR. Once these estimates are obtained, the underwater irradiances are estimated using the downwelling irradiances from GMS-5. Details of this methodology, including the Monte Carlo models, the spectral relationships and the mapping algorithms, are described in the following sections.

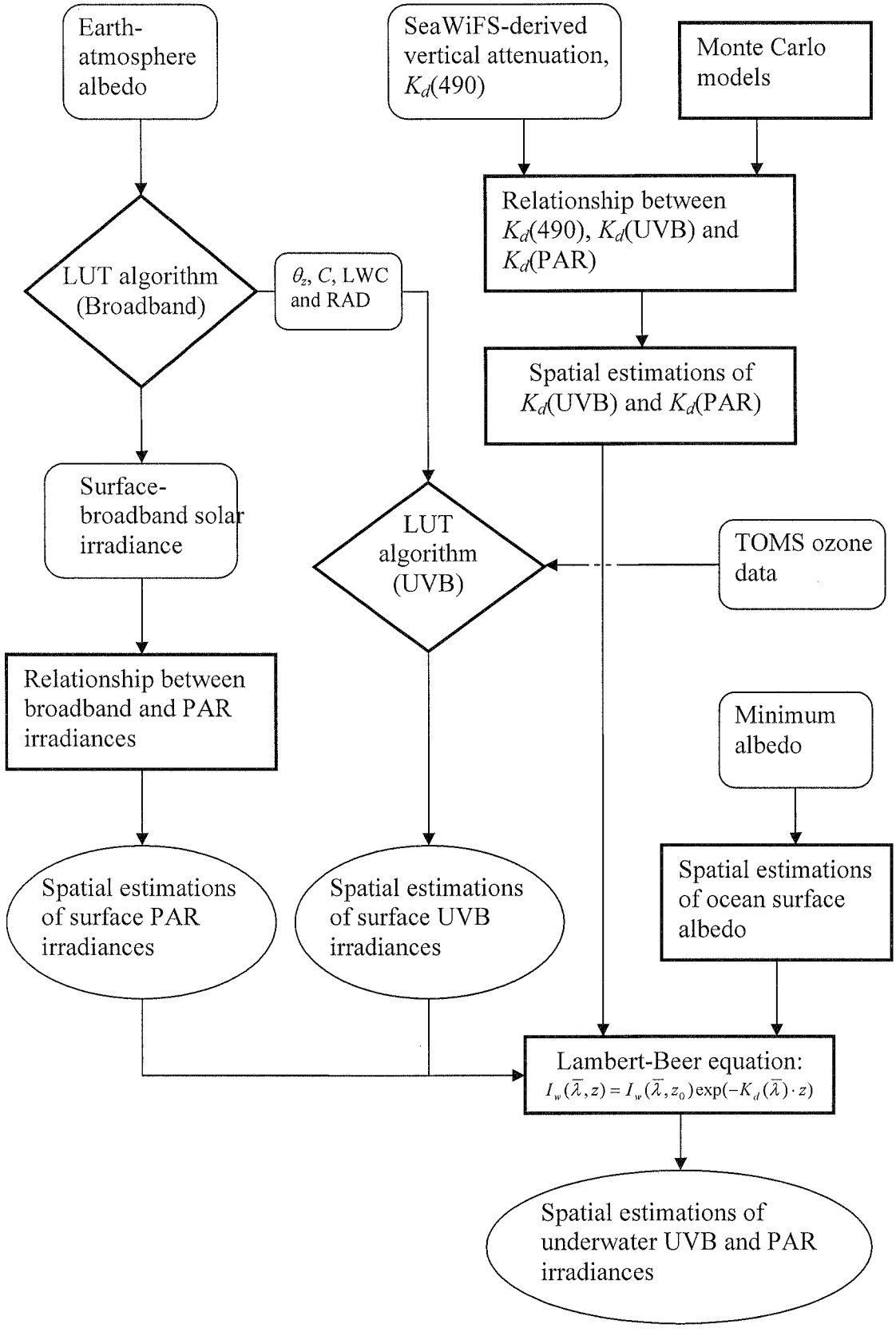

Figure 4.35 Approach used to estimate incident UVB and PAR irradiance at the surface.

4.4.3.1) *Monte Carlo based empirical models*

The total attenuation coefficient of water K_d is essential in estimating the diminishing of solar flux in the aquatic medium (Spinrad, 1994; Bukata *et al.*, 1995). The value of K_d can be empirically derived from Monte Carlo based methods such as those of Gordon *et al.*, (1975), Morel (1991), Kirk (1981) and Ershova *et al.* (2002). Although these studies have different equation forms, their background profiles are based on similar substances, including profiles of absorption and scattering coefficients for pure waters (a_w and b_w) and chlorophyll-*a* absorption (a_c). The spectral distributions of a_w, b_w and a_c are illustrated in Figure 4.36, 4.37 and 4.38, respectively (Prieur and Sathyendranath, 1981; Morel, 1991; Stamnes, 1997; Liu *et al.*, 2006).

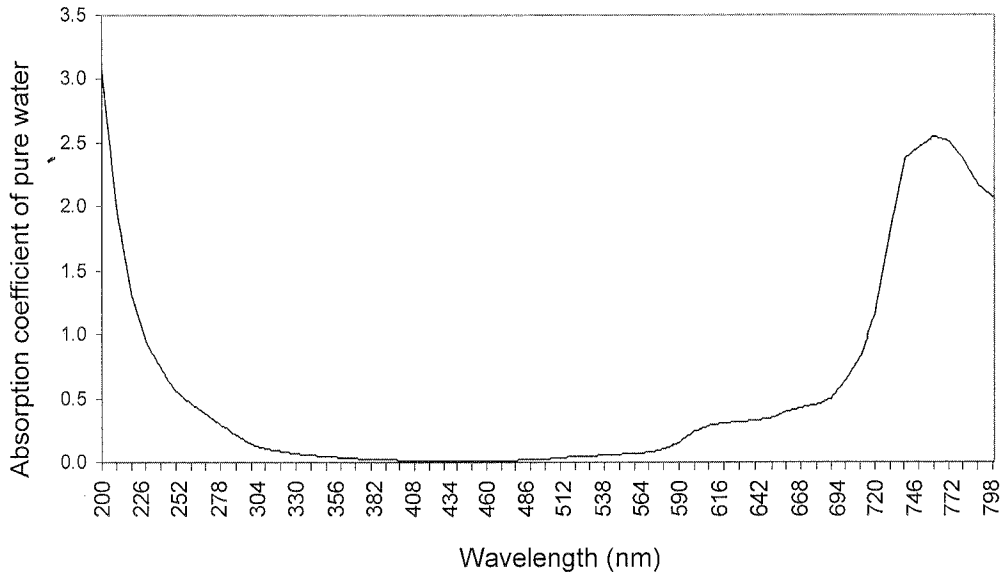

Figure 4.36 Absorption coefficients of pure water a_w plotted against wavelengths (Prieur and Sathyendranath, 1981; Morel, 1991).

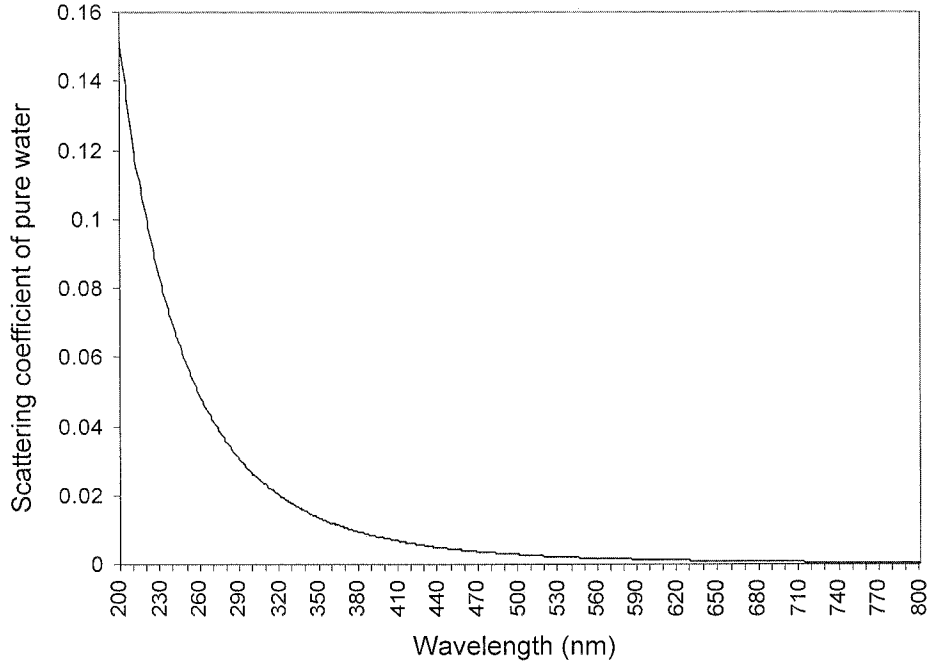

Figure 4.37 Scattering coefficients of pure water b_w plotted against wavelengths (Gordon and Morel, 1983).

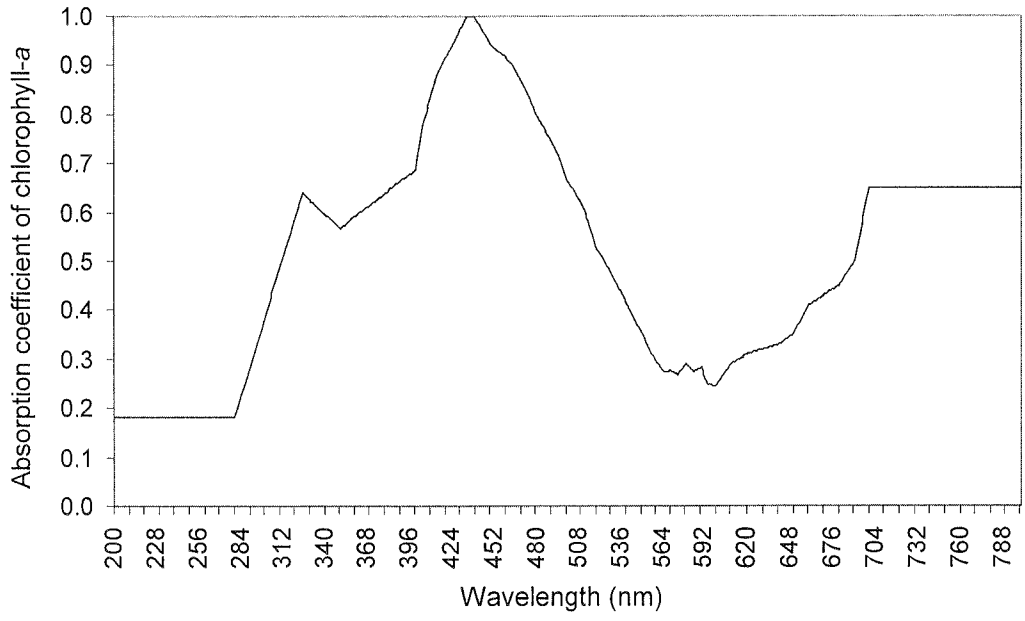

Figure 4.38 Scattering coefficients of chlorophyll-*a*, a_c plotted against wavelengths (Stamnes, 1997).

To derive the total attenuation coefficient in the PAR and UVB regions, the total monochromatic attenuation coefficient $K_d(\lambda)$ is provided as a first step. The estimation of $K_d(\lambda)$ involves the monochromatic profiles of the total absorption and scattering coefficients: $a_w(\lambda)$ and $b_w(\lambda)$ and chlorophyll-*a* concentration, *chlo*. Following Morel (1991) and Prieur and Sathyendranath (1981), the spectral coefficient of total absorption $a_w(\lambda)$ is defined as:

$$a_w(\lambda) = a_{wp}(\lambda) + 0.06a_{wc}(\lambda)chlo^{0.65} + F \cdot 0.06 \cdot a_{wc}(440)chlo^{0.65} \exp(-0.014(\lambda - 440)) \quad (4.18)$$

where $a_{wc}(\lambda)$ is the monochromatic chlorophyll-*a* absorption coefficient, noting that λ is the wavelength in nanometers. Gordon and Morel (1983) derived the total scattering coefficient $b_w(\lambda)$ as a function of chlorophyll-*a* concentration *chlo*. That is:

$$b_w(\lambda) = b_{wp}(\lambda) + 0.30\left(\frac{550}{\lambda}\right)chlo^{0.62} \quad (4.19)$$

As discussed in Section 3.5, there are a number of approaches showing that the monochromatic $K_d(\lambda)$ values can be evaluated from empirical relations (Tilzer *et al.*, 1995; Schanz *et al.*, 1997; Ershova *et al.*, 2002; Liu *et al.*, 2006). This study uses results from three Monte Carlo approximation models as described in Gordon (1989b), Kirk (1981) and Ershova *et al.*, (2002). The parameterisation of $K_d(\lambda)$ considers a wide set of parameters including chlorophyll-*a* concentration, water depth and wavelength (Table 4.5). The various formulations of $K_d(\lambda)$ are as follows:

- Gordon, (1989)

$$K_d(\lambda) = 1.0395 \cdot [a_w(\lambda) + b_w(\lambda)] \quad (4.20)$$

- Kirk (1981)

$$K_d(\lambda) = [a_w^2(\lambda) + 0.256 \cdot a_w(\lambda) \cdot b_w(\lambda)]^{1/2} \quad (4.21)$$

- Ershova *et al.* (2002)

$$K_d(\lambda) = 1.04 D_0 [a_w(\lambda) + b_{wb}(\lambda)] \quad (4.22)$$

where

$$D_0 = (1-p)/\cos\theta_{w-} + 1.197p \quad (4.23)$$

θ_{w-} is the refraction angle of direct solar irradiance and p is the fraction of incident solar radiation at the surface that is diffuse. This study assumes p = 0.2.

Table 4.5 Details of the parameters used in the Monte Carlo examinations.

Variables	Degree of freedom	Ranges	Step size
Wavelength [nm]	601	200 – 800	1.0 nm
Chlorophyll-a concentration [mg-m^{-3}]	101	0.0 – 10.0	0.1 mg-m^{-3}
Depth [m]	20	1.0 – 20.0	1.0 m

Following the output of Monte Carlo models, Equation (4.20) – (4.22), the values of monochromatic attenuation coefficient $K_d(\lambda)$ are routinely computed for every 1-nm step across the 200-800 nm regions. Each step of the 1-nm $K_d(\lambda)$ calculation is repeated for every 0.1 mg-m^{-3} of chlorophyll-*a* concentration, ranging between 0 and 10 mg-m^{-3}. The $K_d(\lambda)$ spectra estimated from the Gordon and Ershova models are similar at high chlorophyll-*a* concentrations (Figures 4.39 and Figure 4.41). By contrast, the $K_d(\lambda)$

values derived from the Kirk model are higher in the PAR (400-700 nm) region (Figure 4.40).

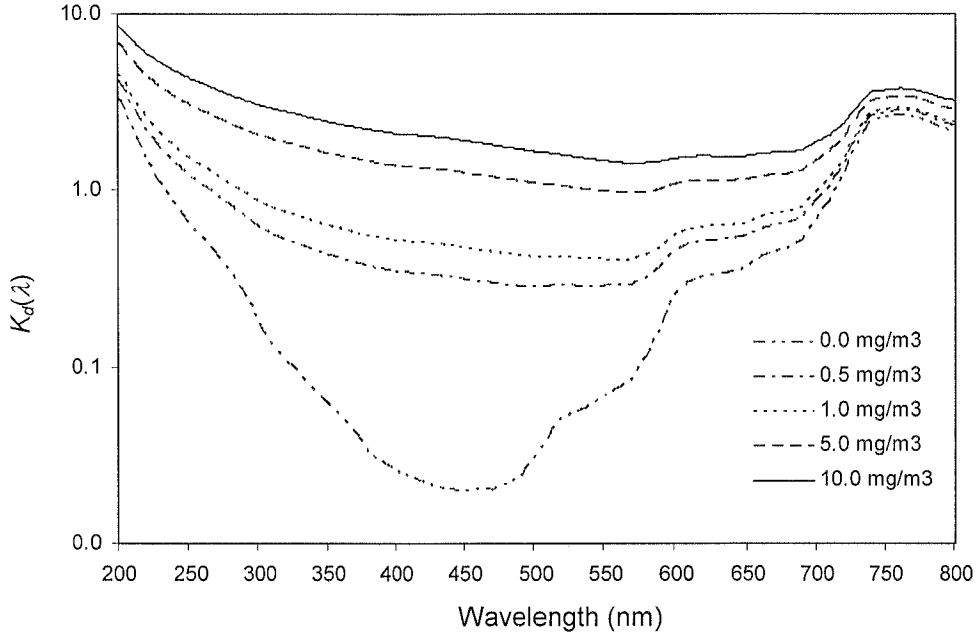

Figure 4.39 The diffuse attenuation coefficient $K_d(\lambda)$ derived from the Gordon Monte Carlo simulation.

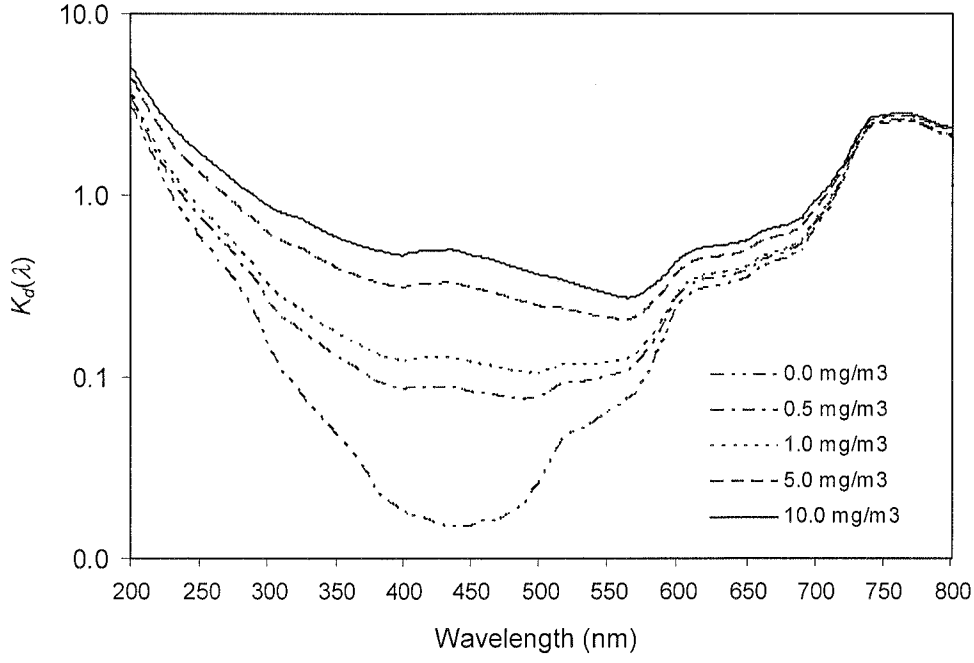

Figure 4.40 The diffuse attenuation coefficient $K_d(\lambda)$ derived from the Kirk Monte Carlo simulation.

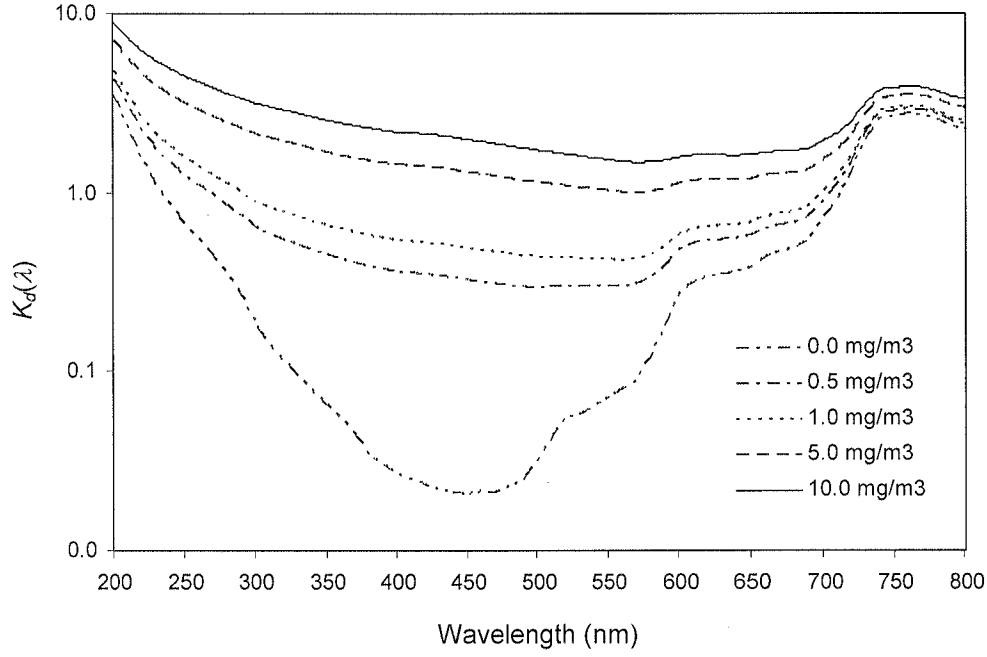

Figure 4.41 The diffuse attenuation coefficient $K_d(\lambda)$ derived from the Ershova Monte Carlo simulation.

4.4.3.2) *Method for deriving the linear relationships of K_d* between *PAR/UVB and SeaWiFS regions*

A further step is to establish the relationships between $K_d(490)$, $K_d(\text{UVB})$ and $K_d(\text{PAR})$. Using the definition of $K_d(\lambda)$, the underwater downwelling solar irradiance for any depth z may be written as:

$$I(\lambda, z_i) = I(\lambda, 0^-) \cdot \exp[-K_d(\lambda) \cdot z_i] \qquad (4.24)$$

It is through Equation (4.24) that any spectrally-averaged value of $K_d(\lambda)$ is linked to the incoming irradiance $I(\lambda,0^-)$, which is not known beforehand. In this study $I(\lambda,0^-)$ was obtained using the Streamer model for 0° degree zenith angle with conditions as defined in Figure 4.25. This allows a series of equations to be formed:

$$I(UVB, z_i) = \int_{\lambda=280}^{\lambda=320} I(\lambda, 0^-) \cdot \exp[-K_d(\lambda) \cdot z_i] d\lambda \cdot E_\lambda d\lambda \tag{4.25}$$

$$I(PAR, z_i) = \int_{\lambda=400}^{\lambda=700} I(\lambda, 0^-) \cdot \exp[-K_d(\lambda) \cdot z_i] d\lambda \tag{4.26}$$

$$I(490, z_i) = \int_{\lambda=480}^{\lambda=500} I(\lambda, 0^-) \cdot \exp[-K_d(\lambda) \cdot z_i] d\lambda \tag{4.27}$$

where each of the above irradiances are estimated for one specific value of chlorophyll concentration *chlo* and depth z_i. E_λ is the erythemal curve. The above equations define three sets of profiles (PAR, UVB and 490) which vary with chlorophyll. For any profile a spectrally-integrated value of $K_d(\lambda)$ may be obtained as:

$$K_d(UVB) = \frac{-1}{z_2 - z_1} \ln \frac{I(UVB, z_2)}{I(UVB, z_1)} \tag{4.28}$$

$$K_d(PAR) = \frac{-1}{z_2 - z_1} \ln \frac{I(PAR, z_2)}{I(PAR, z_1)} \tag{4.29}$$

$$K_d(490) = \frac{-1}{z_2 - z_1} \ln \frac{I(490, z_2)}{I(490, z_1)} \tag{4.30}$$

The Monte Carlo analysis provided 20 depth intervals for each of the above spectral regions, and for each of 100 chlorophyll concentrations. All 20 profiles were grouped together for each spectral interval and chlorophyll concentration. For each spectral interval and chlorophyll concentration, plots for $\ln\left(I(\overline{\lambda}, z_2) / I(\overline{\lambda}, z_1)\right)$ versus depth ($z_2 - z_1$), are constructed. $\overline{\lambda}$ denotes a spectral average wavelengths in the UVB,

PAR and 490 regions. Each of the Equation 4.28-4.30 yields 20 data pairs, with z_1 being constant at 0 m just below the surface, and z_2 varying between 1 and 20 m in 1-m steps. Regression analysis of these two data sets provides $K_d(\lambda)$ as the slope of the statistical relationship:

$$\ln \frac{I(\overline{\lambda}, z_2)}{I(\overline{\lambda}, z_1)} = -K_d \cdot [z_2 - z_1] + c \qquad (4.31)$$

Following these steps for each of the bands, the values of $K_d(490)$, $K_d(\text{UVB})$ and $K_d(\text{PAR})$ are estimated at every 0.1 mg-m^{-3} of chlorophyll-*a* concentration. The relationships between $K_d(490)$, $K_d(\text{UVB})$ and $K_d(\text{PAR})$ are very well defined and independent of chlorophyll concentration:

$$K_d(PAR) = a_2 \cdot K_d^2(490) + a_1 \cdot K_d(490) + a_0 \qquad (4.32)$$

and

$$K_d(UVB) = b_1 \cdot K_d(490) + b_0 \qquad (4.33)$$

where a_0, a_1, a_2, b_0 and b_1 are regression coefficients. Table 4.6 and 4.7 show the coefficients that are used for estimating $K_d(\text{PAR})$ and $K_d(\text{UVB})$, respectively.

Table 4.6 Regression coefficients used for $K_d(\text{PAR})$ estimation.

Model	a_2	a_1	a_0	R^2	S.E.
Gordon (1989b)	-0.0596	0.95701	0.04673	0.9999	0.00338
Kirk (1981)	-0.6887	1.10908	0.02689	0.9999	0.00048
Ershova *et al.* (2002)	-0.0613	0.99243	0.04817	0.9999	0.00361

Table 4.7 Regression coefficients used for $K_d(\text{UVB})$ estimation.

Model	b_1	b_0	R^2	S.E.
Gordon (1989b)	1.64257973	0.1068012	1.0	0.00042051
Kirk (1981)	1.93843797	0.0908820	1.0	0.00012473
Ershova *et al.* (2002)	1.70615351	0.1110850	1.0	0.00048057

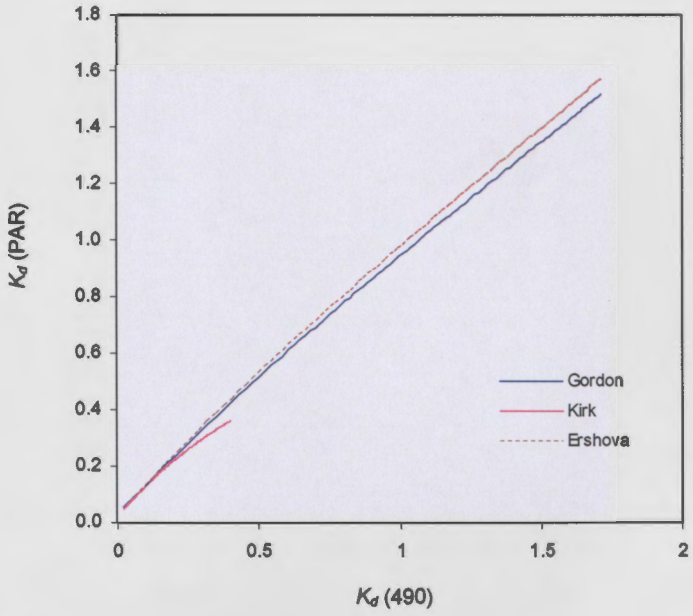

Figure 4.42 Linear relationship of the Monte Carlo-simulated K_d for PAR and the SeaWiFS band.

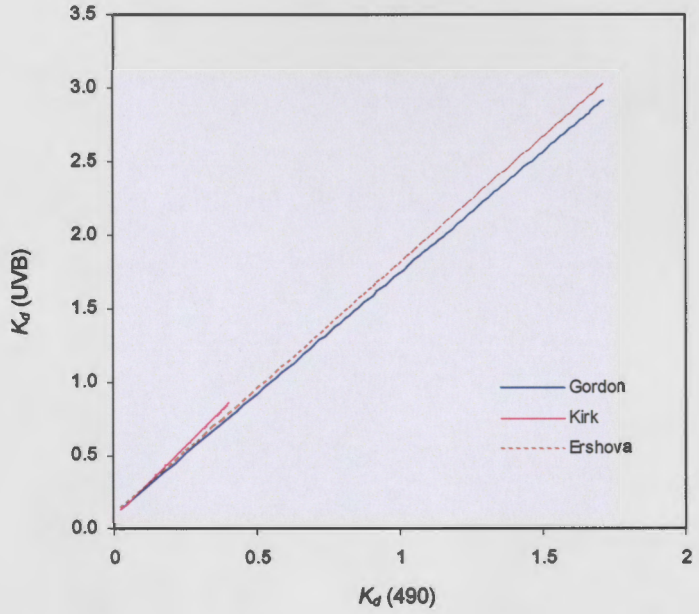

Figure 4.43 Linear relationship of the Monte Carlo-simulated K_d for UVB and the SeaWiFS band.

Using Equations (4.32) and (4.33), the K_d(490) data from the SeaWiFS instrument can be transformed into K_d(PAR) and K_d(UVB), allowing the underwater profiles of PAR and UVB irradiances to be characterised for the study region.

These downwelling PAR/UVB irradiances at various depths are estimated by using the Lambert-Beer equation:

$$I_w(\bar{\lambda}, z) = I_w(\bar{\lambda}, z_0)\exp(-K_d(\bar{\lambda})\cdot z) \tag{4.34}$$

where

$$I_w(\bar{\lambda}, z_0) = I_{w+}(\bar{\lambda})\cdot(1-\alpha_w(\bar{\lambda})) \tag{4.35}$$

and z is the depth. $I_w(\bar{\lambda}, z)$ and $I_w(\bar{\lambda}, z_0)$ are the downwelling irradiance underwater at depth z and just below the water surface, respectively. $I_{w+}(\bar{\lambda})$ is the irradiance just above the water surface, derived from the LUT algorithm at local noon. $K_d(\bar{\lambda})$ is the total attenuation coefficient that was obtained from the conversion algorithms, $\alpha_w(\bar{\lambda})$ is the surface reflectance of water, which is estimated from the GMS minimum albedo, and $\bar{\lambda}$ refers to either the PAR or UVB region.

In conclusion, the method used in this study can derives K_d estimate for PAR and UVB using only the K_d(490) band from SeaWiFS. The technique used the conversion is performed using the best of three Monte Carlo empirical based models. The choice of the best model was determined by how well the model result compared with the measurements of K_d. However, it is important to be aware the SeaWiFS foot print is large and the model does not thoughtful to the other variables such as CDOM and sediments as this study aims to provide a spatial link of above and underwater irradiances. It is likely that the model will become less reliable in locations where these optically-active constituents are in grater abandon. Field program could be established to determine how well these models perform and how important these optically-active constituent can be.

Chapter 5

Validation

5.1 Validation of satellite-derived broadband surface solar radiation

This study employs satellite-derived reflectivity to provide a series of solar radiation maps over the Great Barrier Reef and Coral Sea regions at a spatial resolution of 2.3 × 2.7 km. These maps rely on the use of physically-derived LUTs covering a broad range of atmospheric conditions. However, the spatial resolution is relatively large compared to spot measurements at the ground. Thus, the validation is essential to evaluate the performance of the LUT algorithm.

The validation process compares surface measurements with the satellite-estimated solar radiation. Only two locations were available for such validation: Rockhampton (23.3° S, 150.4° E) and Cairns (16.5° S, 145.3° E). The solar radiation measurements collected at Rockhampton and Cairns were available for 1995-2005 and 1997-2004, respectively. The satellite data was extracted over sub-arrays of 5×5 pixels, centered at Rockhampton and Cairns. The Earth-atmosphere albedo α'_{EA} was derived over both sub-arrays by using the conversion table and converted into a broadband reflectivity α_{EA} using the relationship of Section 4.2. Using α_{EA}, the hourly solar irradiances I_g were estimated through the LUT algorithm for each time when the hourly solar irradiances are collected. The daily total solar radiation was obtained from the sum of the hourly solar irradiance for every daylight hour between 6.30 and 18.30. The comparisons are examined for daily, weekly, monthly, 6-monthly, yearly, 5-yearly and a long-term 11-year basis across the periods that the measurements were available.

Overall, this technique yields very good mean bias errors (model-measurements) of -0.0007 MJ-m^{-2}-day^{-1} for Rockhampton and -0.43 MJ-m^{-2}-day^{-1} for Cairns. The

comparisons between the model estimates and measurements are presented in Table 5.1. Daily comparisons give the highest RMS difference of 2.26 MJ-m^{-2}-day^{-1} (15.7%) and 2.85 MJ-m^{-2}-day^{-1} (20.2%) for Rockhampton and Cairns, respectively (Figure 5.1). The temporal averages of RMS difference are shown in Table 5.1. RMS difference values are expressed as percentages of the mean irradiance over the period of averaging, and the R^2 coefficients are also shown in brackets. The errors decrease for longer averaging periods.

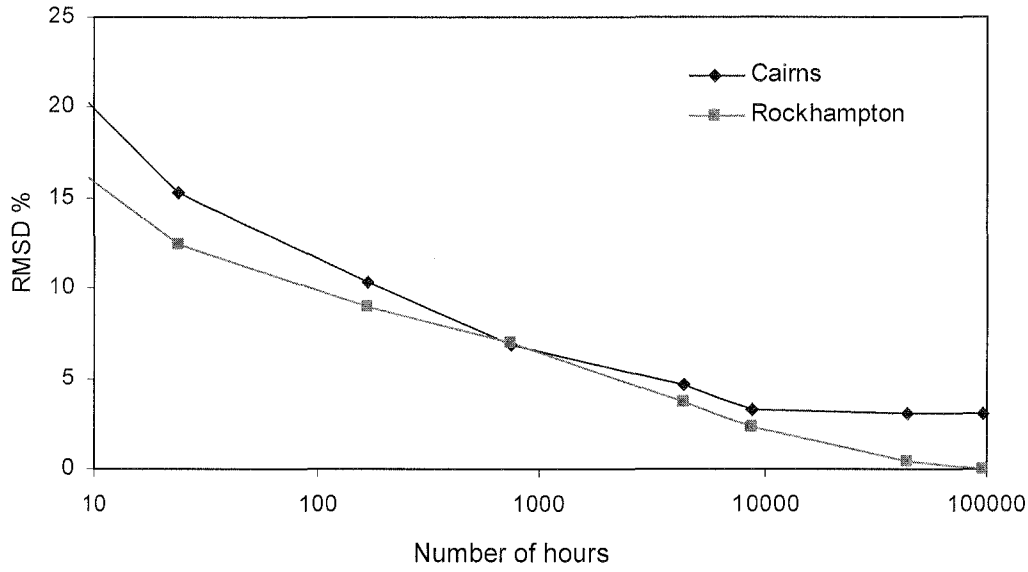

Figure 5.1 RMS difference (percentage of mean) for various temporal comparison scales.

Table 5.1 RMS difference (expressed as percentage of mean) between surface measurement and satellite model as function of temporal averaging, coefficient of variation R^2 is shown in brackets.

Location	hourly	Daily	Weekly	Monthly	6-Monthly	Yearly	5-Yearly	11-Yearly
Cairns	32.16% (0.64)	15.26% (0.70)	10.37% (0.89)	6.88% (0.94)	4.60% (0.97)	3.24% (0.99)	3.07% (1.0)	3.08% (1.0)
Rockhampton	25.03% (0.68)	12.4% (0.85)	8.93% (0.93)	6.97% (0.95)	3.66% (0.98)	2.29% (0.98)	0.42% (1.0)	0.05% (1.0)

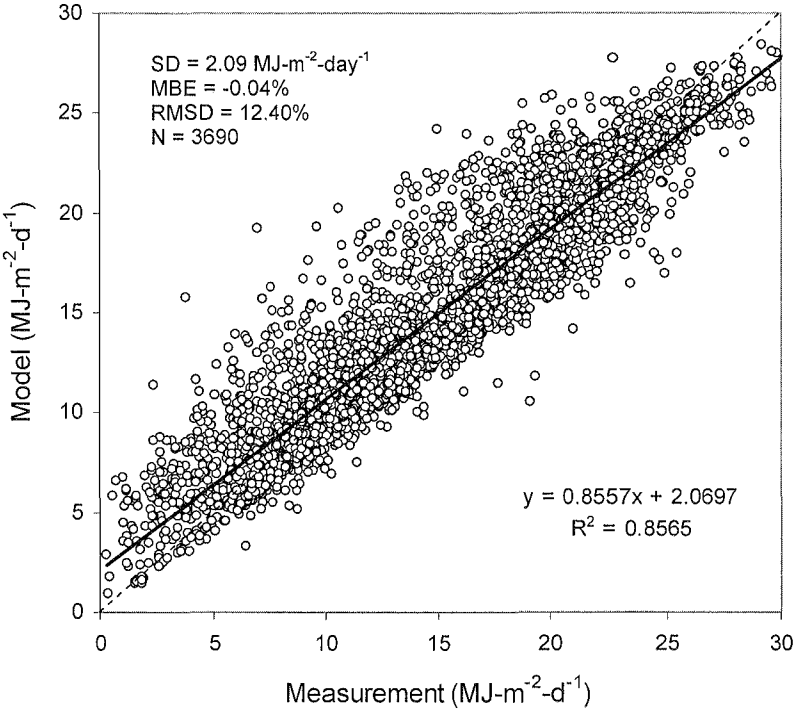

Figure 5.2 The comparison of the daily solar radiation between the satellite prediction and measurement collected at Rockhampton.

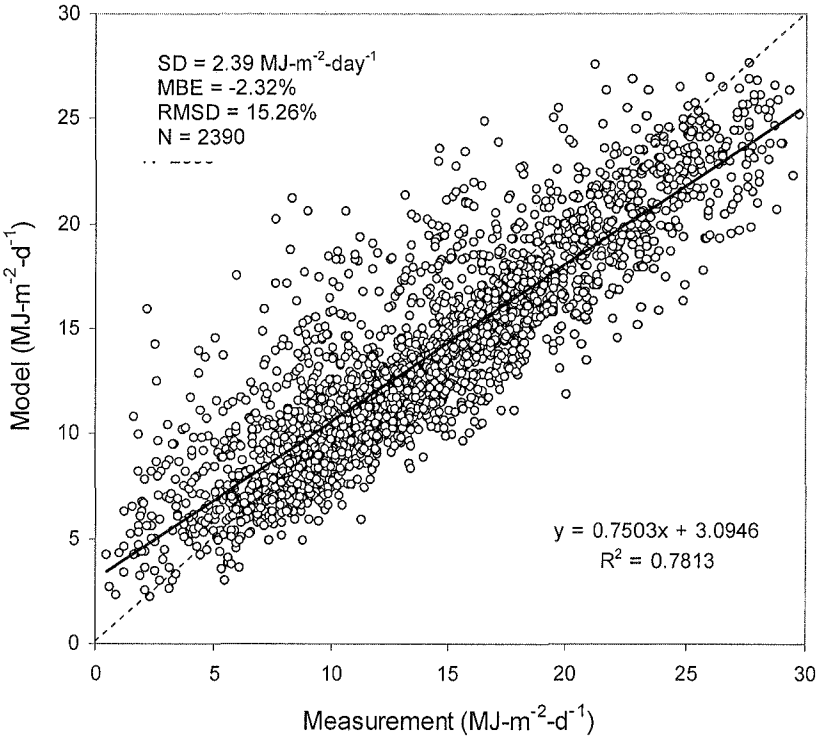

Figure 5.3 The comparison of the daily solar radiation between the satellite prediction and measurement collected at Cairns.

5.2 Validation of satellite-derived surface UVB irradiance

As a first step in calculating underwater UVB irradiance, the values of UVB above the water surface are first estimated from the LUT algorithm. The reliability of the surface UVB estimates is tested by a comparison between these satellite-derived values and erythemal UVB measurements at Townsville (19.35° S, 146.8° E). The data collected for each of the satellite hours were averaged over the months to obtain hourly average UVB irradiances. The values were then compared to the satellite-derived UVB Irradiance values. The comparison (model-measurement) for the whole period shows good agreement, with RMS difference of 17.8 mW-m^{-2}, and mean bias error of 3.9 mW-m^{-2} (Figure 5.4).

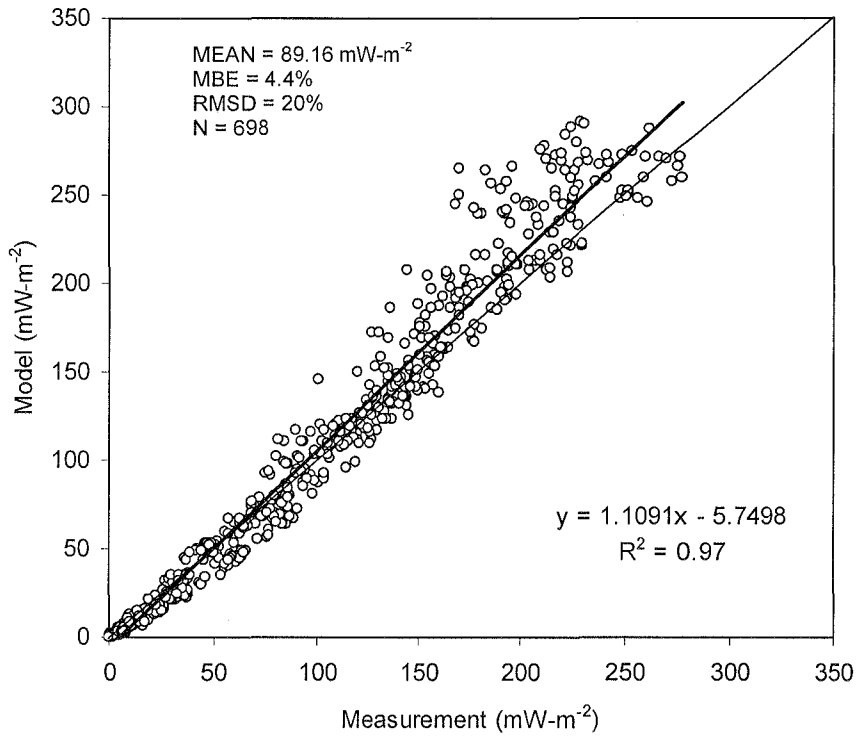

Figure 5.4 The comparison of the hourly average erythemal UVB irradiance between the satellite prediction and measurement collected at Townsville. Data covers a period between January 1997 and December 2001.

5.3 Validation of satellite-derived underwater solar irradiance

In order to estimate underwater solar irradiance there are several factors that must be considered, including sky conditions, atmospheric profiles of water vapour and aerosols and the reflectance at the water surface, which remain unknown for evaluating the SeaWiFS-derived irradiance. However, the estimation of underwater solar irradiance depends strongly on the K_d values, as they are determined by the water properties which play a major role in the attenuation of radiation below the water surface (Kirk 1994). For this reason, the values of the SeaWiFS-estimated total transmission of water are compared to the values that are derived from the PUV measurements.

As explained in Section 4.4.3.2, the regression coefficients derived for the K_d conversion are provided for the PAR (400-700 nm) and UVB (280-320 nm) regions. However, these coefficients cannot be compared directly to the K_d values measured by the PUV instrument as they differ in the wavelength regions that are sampled. As a result, another set of coefficients that are compatible with to the PUV measurements (305 nm, 313 nm, 320 nm, 340 nm, 380 nm, 395 nm and PAR) are created. Following a similar approach to that described in section 4.3, the equations developed by Gordon (1989b), Kirk (1981) and Ershova *et al.* (2002) are examined to provide relationships of the spectrally-integrated K_d between the SeaWiFS (490 nm) and the PUV instrument for all chlorophyll-*a* concentration profiles. A series of linear relationships for each model are therefore obtained for all the PUV wavebands (Figure 5.5). Using regression analysis, a set of coefficients for each Monte Carlo model are obtained from the relationships. The values of $K_d(490)$ from the SeaWiFS images were related to the values at the PUV channels according to these empirical equations:

$$K_d(\bar{\lambda}) = a_1 K_d(490) + a_0 \qquad (5.1)$$

$$K_d(PAR) = a_2 K_d{}^2(490) + a_1 K_d(490) + a_0 \qquad (5.2)$$

where $K_d(490)$ and $K_d(PAR)$ are the total attenuation coefficients centered at the SeaWiFS (480-500 nm) and PAR (400-700 nm) wavebands. $K_d(\overline{\lambda})$ is the total attenuation coefficient at 305 nm, 315 nm, 320 nm, 340 nm, 380 nm, and 395 nm wavebands. a_0, a_1 and a_2 are the regression coefficients obtained from the regression technique (Table 5.2).

Table 5.2 Regression coefficients for estimating PUV K_d values from SeaWiFS K_d data.

Model		305 nm	313 nm	320nm	340 nm	380 nm	395 nm	PAR
Gordon	a_0	0.10601	0.07967	0.06359	0.03339	-0.0024	-0.0065	0.04673
	a_1	1.68232	1.63703	1.60091	1.48052	1.29841	1.24742	0.95701
	a_2	-	-	-	-	-	-	-0.0596
	R^2	0.9999	0.9999	0.9999	0.9999	0.9999	0.9999	0.9999
	S.E.	0.00146	0.00141	0.00137	0.00113	0.00086	0.00081	0.00338
Kirk	a_0	0.09682	0.06972	0.05362	0.02649	-0.0064	-0.0097	0.02689
	a_1	1.97588	1.91203	1.86774	1.61972	1.30902	1.25018	1.10908
	a_2	-	-	-	-	-	-	-0.6887
	R^2	0.9999	0.9999	0.9999	0.9999	0.9999	0.9999	0.9999
	S.E.	0.00029	0.00033	0.00036	0.00030	0.00029	0.00029	0.00048
Ershova	a_0	0.11031	0.08284	0.06612	0.03472	-0.0025	-0.0067	0.04817
	a_1	1.74861	1.70154	1.66399	1.53886	1.34957	1.29657	0.99243
	a_2	-	-	-	-	-	-	-0.0613
	R^2	0.9999	0.9999	0.9999	0.9999	0.9999	0.9999	0.9999
	S.E.	0.00152	0.00146	0.00143	0.00118	0.00089	0.00085	0.00361

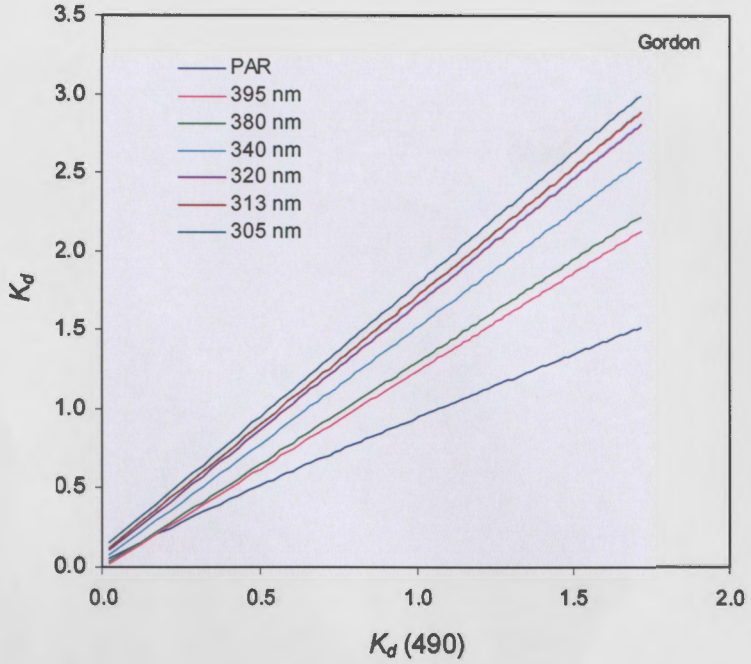

Figure 5.5 (a) The relationships of spectrally-integrated K_d between SeaWiFS and PUV instruments, using the Gordon model (Gordon, 1989).

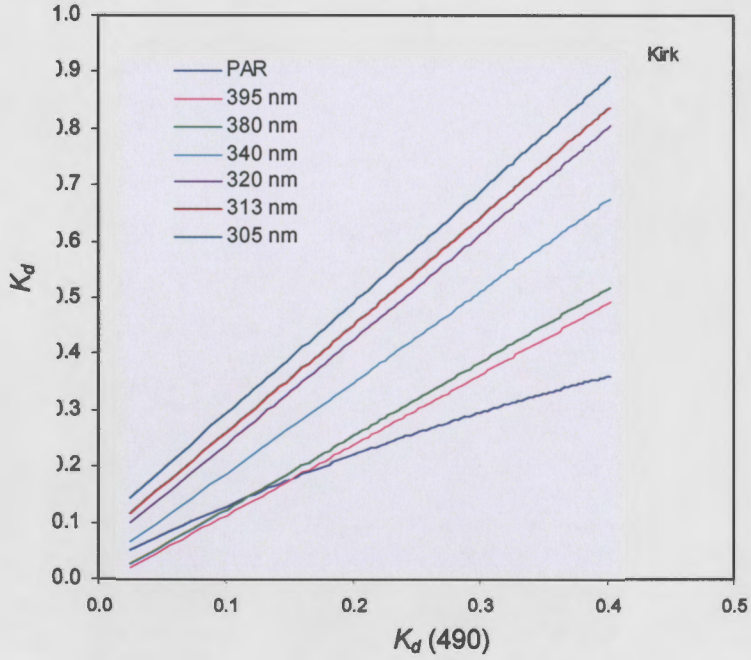

Figure 5.5 (b) The relationships of spectral-integrated K_d between SeaWiFS and PUV instruments, using the Kirk model (Kirk, 1981).

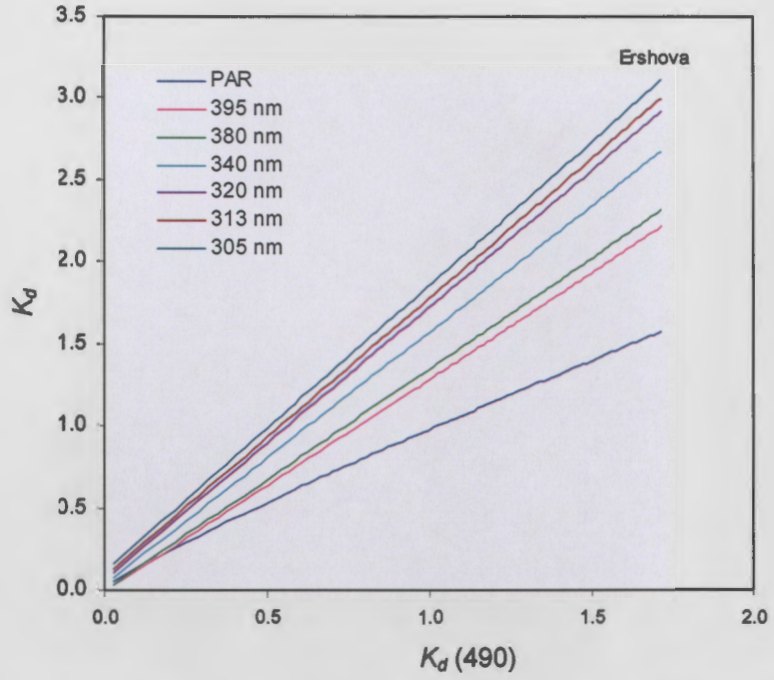

Figure 5.5 (c) The relationships of spectral-integrated K_d between SeaWiFS and PUV instruments, using the Ershova model (Ershova *et al.*, 2002).

As the SeaWiFS instrument scans at local solar noon time, the validations were also performed with PUV data collected as close as possible to local solar noon. It is noted that the spatial resolution of the SeaWiFS-derived K_d data, at 9×9 km, is considerably coarser than the spot measurements on Heron Island. Details of PUV measurements are shown in Section 4.2.3.

In the comparison, this study examines the attenuation profiles of the underwater solar irradiance from the PUV instrument. A series of linear relationships between the normalized-irradiance $\ln\left(\frac{I_w(z_i)}{I_w(0)}\right)$ and the depths $(z_i - z_0)$ are established for estimating the values of K_d for each waveband, where z_i and z_0 are depths i and the surface, respectively. The slopes of the relationships give the values of K_d for each PUV waveband. The spectral shapes of these PUV-measured K_d values, which were collected from different locations, have similar shape but there are differences in offset. The K_d values are high at shorter wavelengths (305 nm, 315 nm, 320 nm and 340 nm), but

decrease in the near visible and PAR regions (Figure 5.6). This figure represents 18 casts with 7 wavebands in each cast.

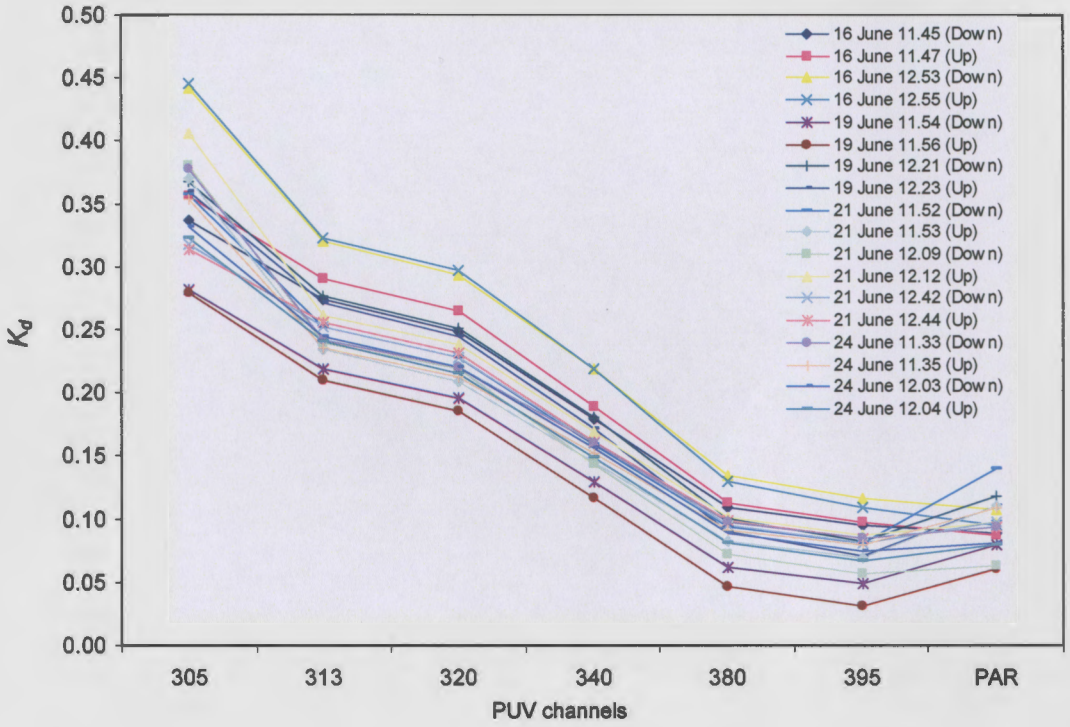

Figure 5.6 The K_d values derived from the PUV measurements. A total of 18 casts were taken (9 up, 9 down in a total of 7 wavebands to make a total of 126 points).

Next, the SeaWiFS-derived K_d values are next compared to the values that were extracted from the PUV measurements at 305 nm, 315 nm, 320 nm, 340 nm, 380 nm, 395 nm and PAR wavebands for those five days. Figure 5.7 illustrates the comparison of the K_d values derived from the SeaWiFS-estimated algorithm with the three different Monte Carlo based empirical models — (a) Gordon (1989b), (b) Kirk (1981) and (c) Ershova *et al.* (2002) — and the measurements. In these comparisons, a large amount of scatter is contributed by the data collected on 13th December 2004. There is a large production of chlorophyll in the lagoon in summer, and as the spatial resolution of SeaWiFS data is coarse it cannot provide fine enough details of water turbidity. Overall,

the models show a similar result with RMS difference (model-measurement) of about 42% (Table 5.3). The Gordon equation yields the lowest MBE at -6.8%. As a result, the Gordon Monte Carlo based empirical model is selected for further estimating underwater irradiance distributions as described in the next chapter.

Table 5.3 The statistics of the K_d comparisons (measurement-model) obtained for each model.

Models	N	Mean (m^{-1})	RMSD (m^{-1})	MBE (m^{-1})	S.E.
Gordon (1989b)	126	0.19582	0.075285 (41.1%)	-0.01267 (-6.81%)	0.07328
Kirk (1981)	126	0.20032	0.077710 (42.4%)	-0.01717 (-9.37%)	0.07197
Ershova (2002)	126	0.20345	0.077578 (42.3%)	-0.02030 (-11.1%)	0.07321

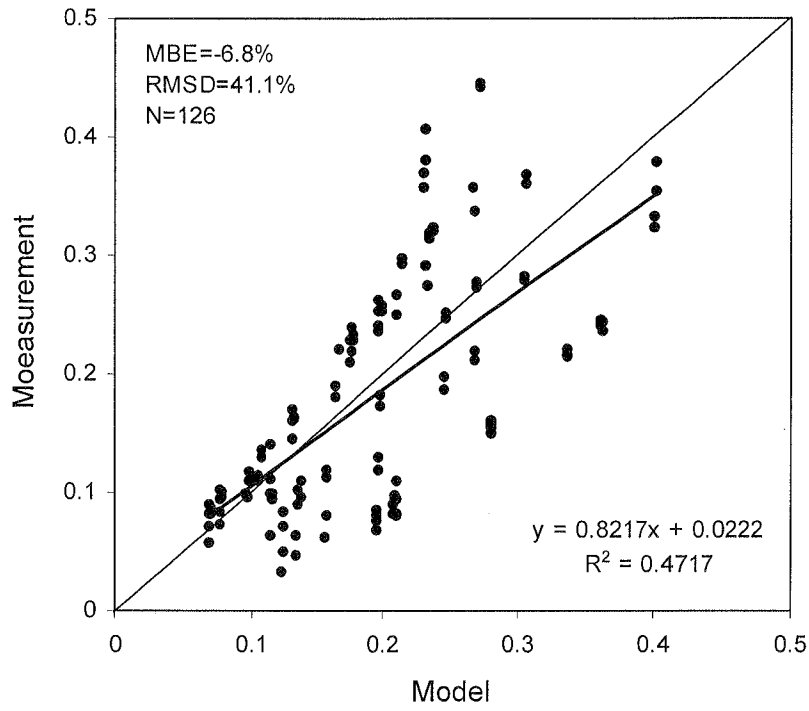

Figure 5.7 (a) The comparison of K_d between the SeaWiFS-derived Gordon model and the PUV measurements.

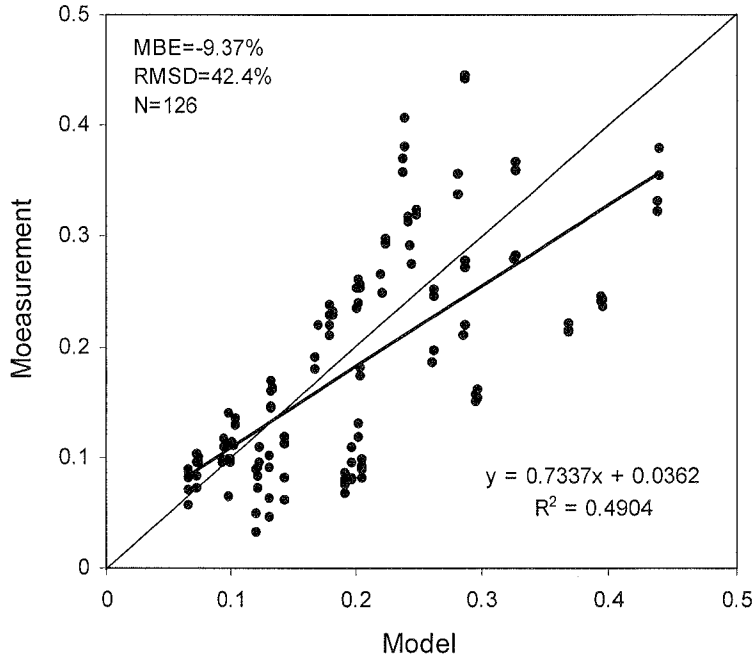

Figure 5.7 (b) The comparison of K_d between the SeaWiFS-derived Kirk model and the PUV measurements.

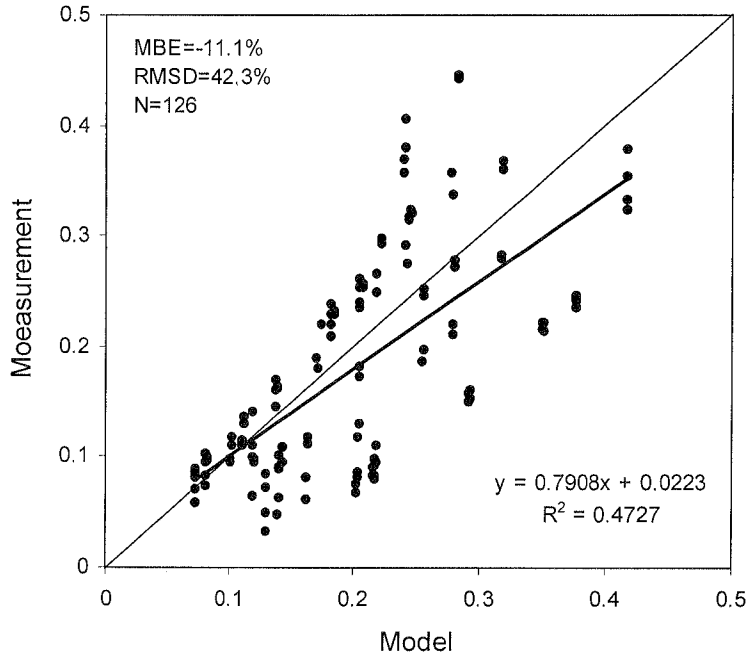

Figure 5.7 (c) The comparison of K_d between the SeaWiFS-derived Ershova model and the PUV measurements.

Chapter 6

Results

6.1 Statistics of surface broadband solar radiation

The LUT technique has been employed to provide maps that show statistics of broadband solar radiation including seasonal variations, annual trends and averages and maximum exposure for the Great Barrier Reef. The satellite data used in the LUT estimation is based on a long-term 11-year record of the geostationary satellite data from 1995 to 2005. In the following sections, spatial maps covering all four seasons and yearly averages are presented, therefore providing solar radiation data that can be used for various marine studies.

6.1.1 Long-term averages and seasonal variations

The 11-year average exhibits a high radiation zone of more than 24 MJ-m^{-2}-day^{-1} at high latitudes between 18° S - 24° S and longitudes 150° E - 154° E (Figure 6.1). Over a large part of the study region, solar radiation fluxes of about 22 MJ-m^{-2}-day^{-1} are obtained. Values of about 20 MJ-m^{-2}-day^{-1} are found in the northern region that borders Papua New Guinea.

The spatial distribution for seasonal periods, which are defined as summer (December-January-February), autumn (March-April-May), winter (June-July-August) and spring (September-October-November), are also examined (Figure 6.2). Overall, the seasonal maps show a strong variation of solar radiation with latitude. In summer, there is a broad area of high solar radiation (more than 30 MJ-m^{-2}-day^{-1}) across the region south of 20° S. The values of solar radiation are lower in autumn, the largest values (more than 24 MJ-m^{-2}-day^{-1}) are seen south of 18° S. Solar radiation is

comparatively low in winter, roughly 16 MJ-m^{-2}-day^{-1} across the whole region, with little variation. In spring, solar radiation values of 20-24 MJ-m^{-2}-day^{-1} are found in most of the region (Figure 6.2).

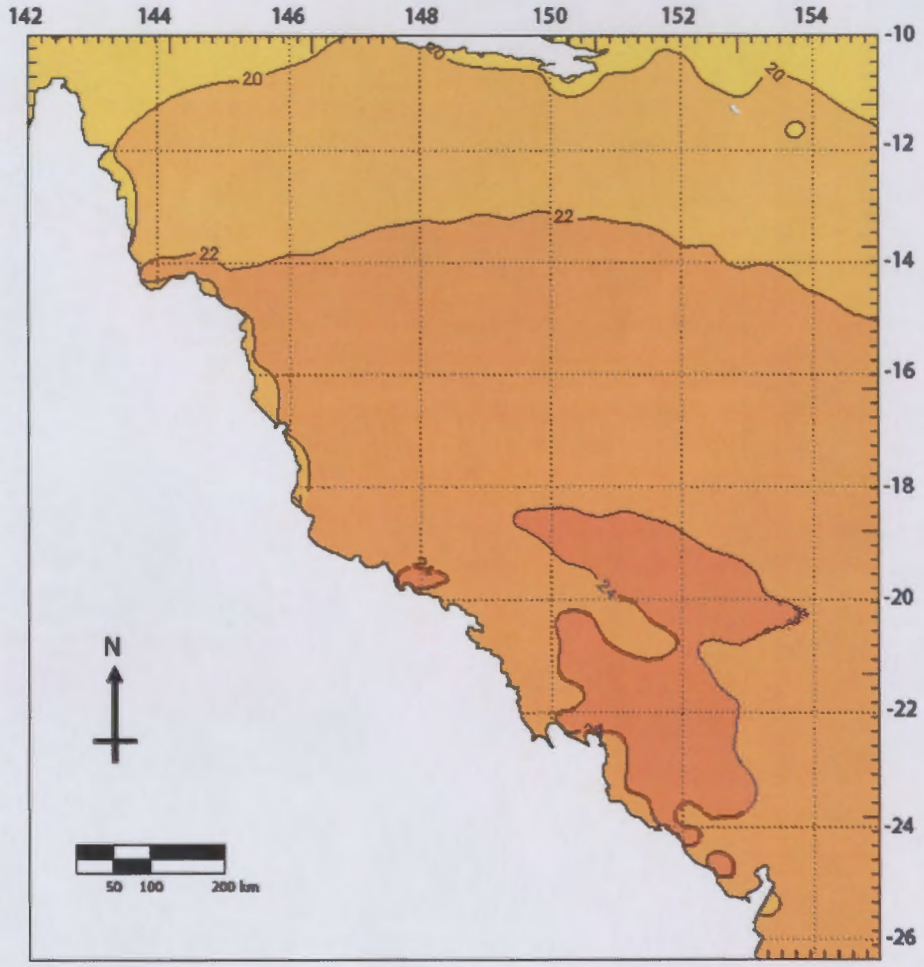

Figure 6.1 Yearly averages of daily solar irradiance (MJ-m^{-2}-day^{-1}) obtained from the 11-year satellite data set.

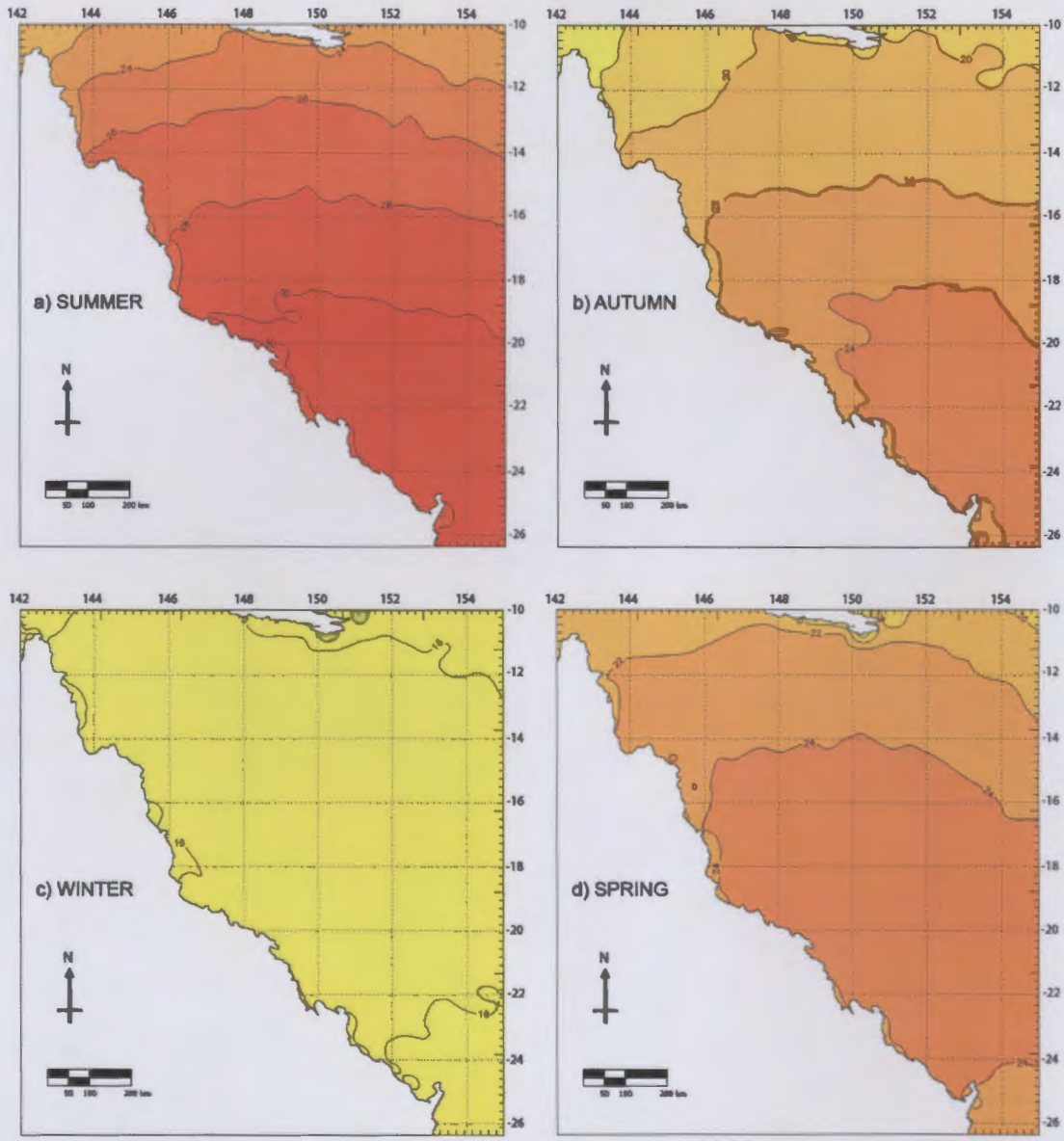

Figure 6.2 Seasonal averages of daily solar irradiance (MJ-m^{-2}-day^{-1}) obtained from the 11-year satellite data set: a) summer, b) autumn, c) winter and d) spring.

6.1.2 Maximum exposure of daily solar radiation

This analysis aims to examine the extreme values of solar radiation in summer months, focusing on the coastline of the GBR. The Great Barrier Reef has a unique geography, with a near coastal shallow lagoon which serves to define two distinctive inner and outer regions. It is therefore interesting to observe the yearly variation of solar radiation during the summer months, a period reported as covering coral bleaching events (Hoegh-Guldberg, 2001). Most of the GBR is found in shallow water up to 200 km from the coastline (Figure 4.1). This study focuses on the distribution of solar radiation within 200 km of the Queensland coastline for the summer months (November, December, January and February) between 1995 and 2005. The satellite-derived monthly solar radiation values were averaged for each pixel to obtain the mean summer values. Following the LUT routines, the parameterization yields the solar radiation distribution for the summer each year (Figure 6.3).

In the summer periods between 1995 and 2001, strong solar radiation values are evident south of 20° S. However, distinctive patterns of anomalously high solar radiation can be seen in the summer of 2001/2002, with irradiances larger than 30 MJ-m^2-day^{-1} evident (Figure 6.3).

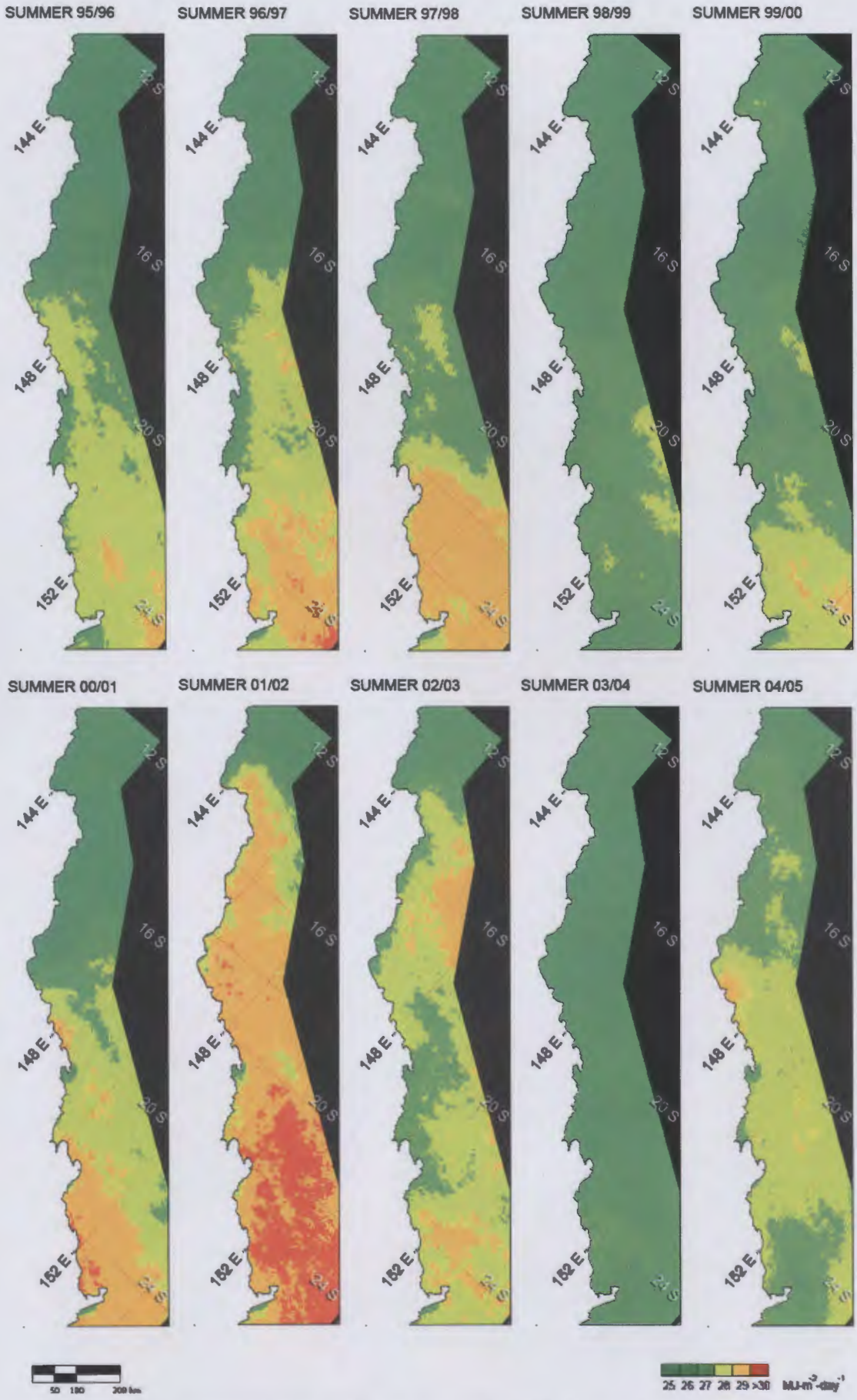

Figure 6.3 Daily average solar irradiance, averaged over the summer months (November to February) for every year of record, over a 200 km strip near the coast.

6.1.3 Yearly averages and long-term trends of daily solar radiation

6.1.3.1) *Yearly averages*

The climatology of solar radiation over the Great Barrier Reef is presented in this section. The yearly averages of daily solar radiation data are examined for the period of 1995-2005 (Figure 6.4). Overall, the results show no significant changes in the northern region (10°-12° S) which consistently receives lower solar radiation of about 18-20 MJ-m^{-2}-day^{-1}. The region between 16° S and 26° S exhibits much higher solar radiation values of more than 22 MJ-m^{-2}-day^{-1} for the whole period (Figure 6.4). This study suggests that there has been a reduction in cloud amount and moisture content of the atmosphere. During 2001 to 2005, values of high solar radiation are evident south of 16° S. A pattern of excessive solar radiation of 24 MJ-m^{-2}-day^{-1} is apparent in 2001–2002. These results are consistent with an increase of the bleaching frequency of the GBR for these recent years.

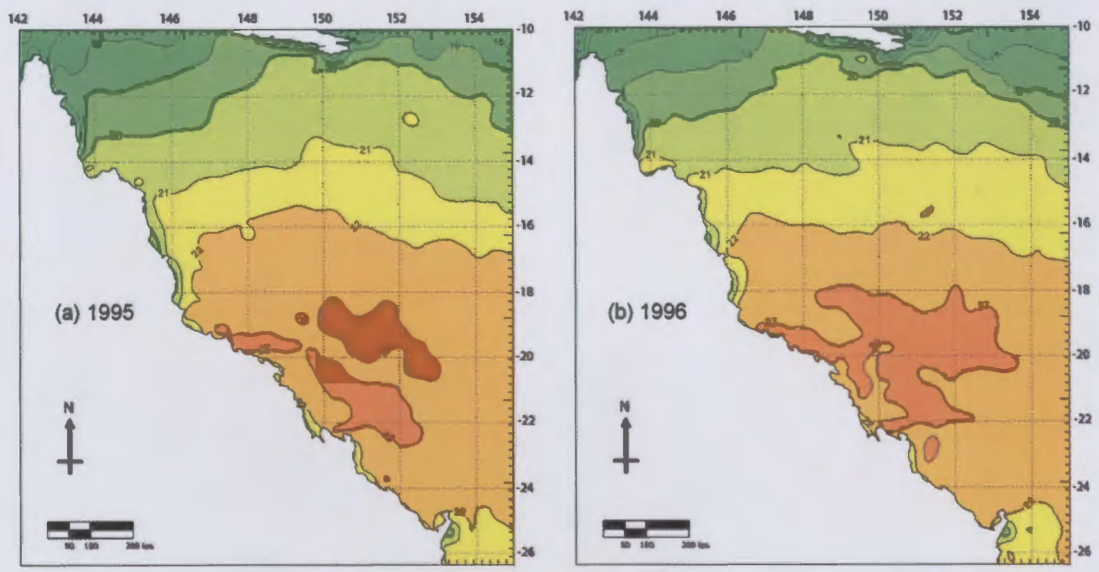

Figure 6.4 Maps of yearly averaged solar radiation (MJ-m^{-2}-day^{-1}) for 1995-2005.

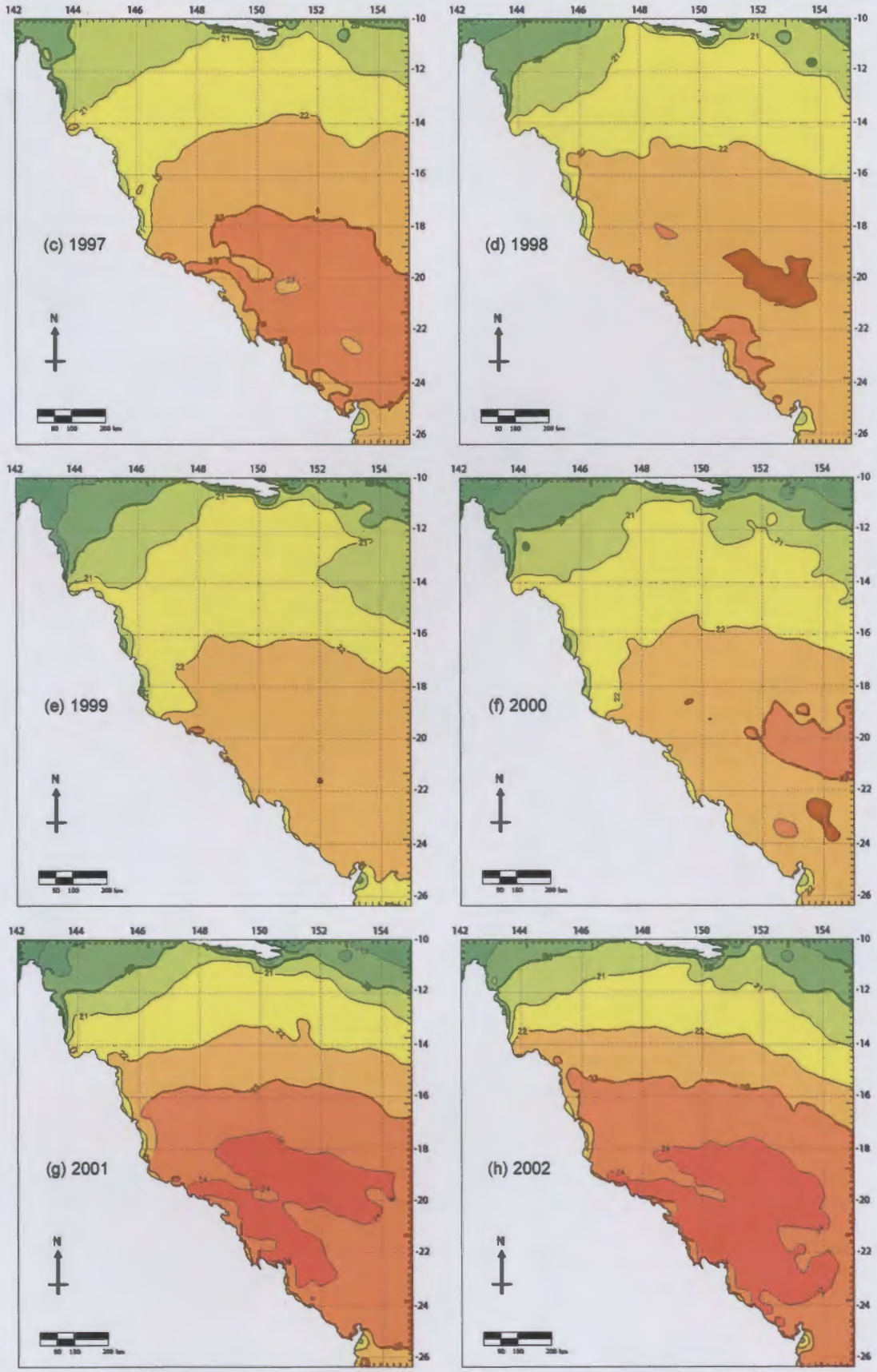

Figure 6.4 Maps of yearly averaged solar radiation (MJ-m^{-2}-day^{-1}) for 1995-2005 (continued).

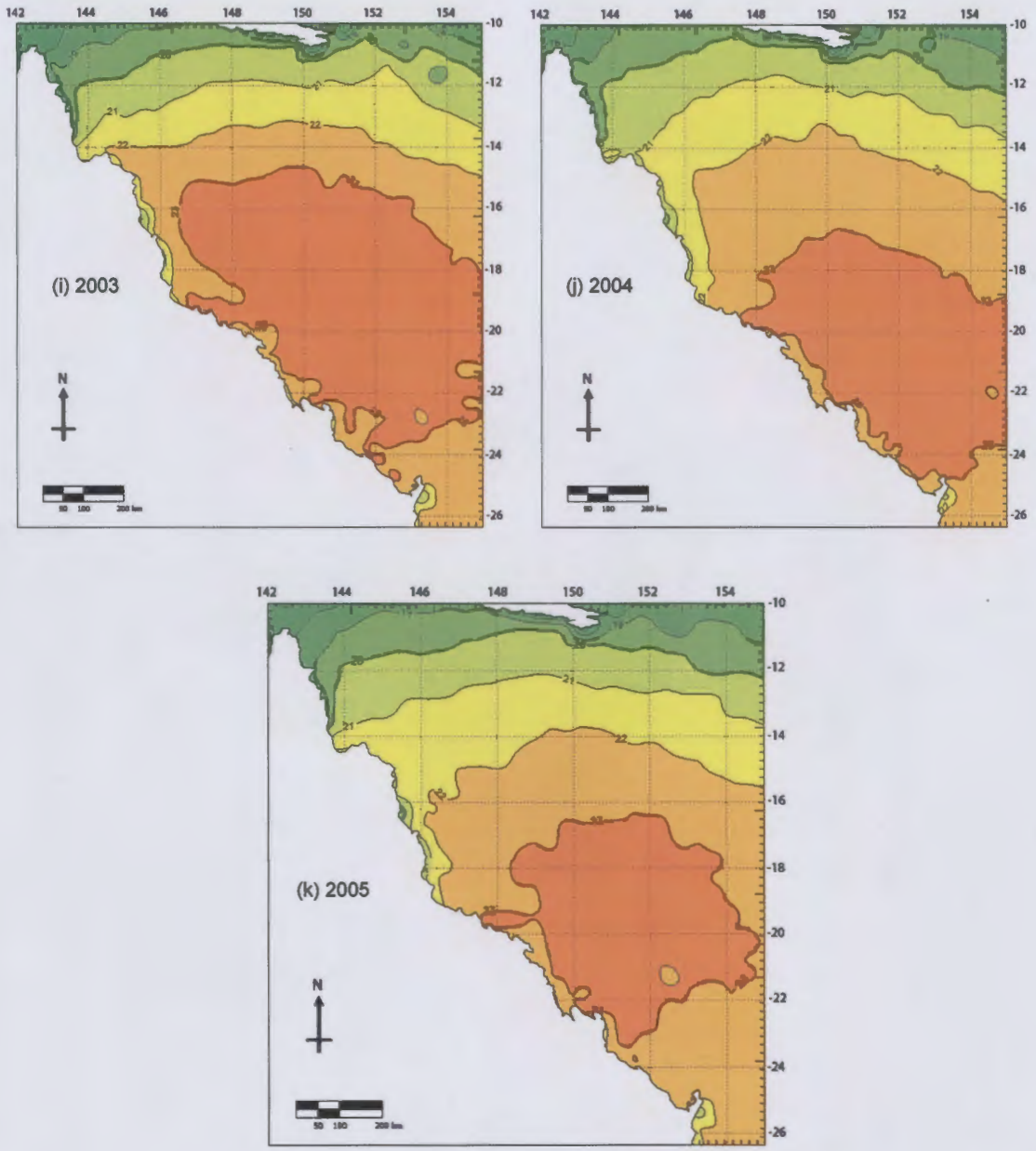

Figure 6.4 Maps of yearly averaged solar radiation (MJ-m^{-2}-day^{-1}) for 1995-2005 (continued).

6.1.3.2) *Long-term trends*

The long-term dataset allows us to examine the trends of solar radiation across the 1995-2005. It also reflects the long-term changes in atmospheric composition and cloudiness over the study region. Using the 11-year dataset, the trends of solar radiation for every pixel across the GBR region were estimated (Figure 6.5). Both negative and positive trends are obtained. To observe the quality of these trends, the statistical significance of 1% and 5% is also indicated. The region with largest positive trends is

located about 200 km from the coastline at latitudes between 12° S and 17° S. Trends are small and less than 0.1% per year. There is no statistical significance of the trends in the reef belt along the coastline of Queensland as the t statistic is larger than 5%, which means that the region exhibits no significant long-term trend in the amount of clouds and moisture.

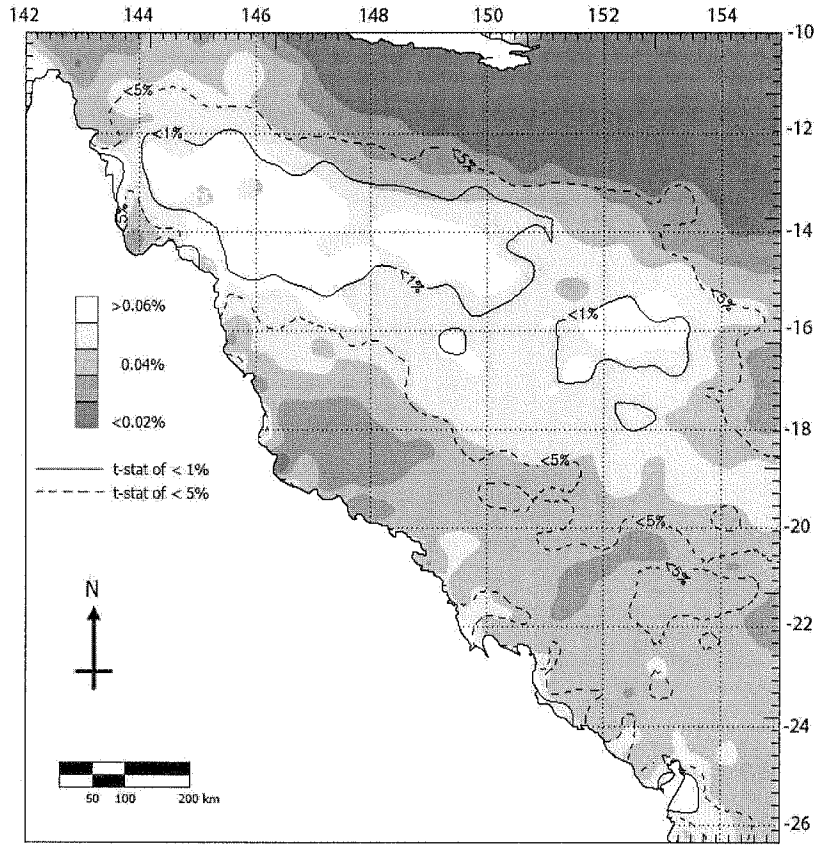

Figure 6.5 Solar irradiance trends for the study area (percent change/decade).

6.1.4 Frequency distribution of daily solar radiation

The frequency distribution of daily solar radiation in the study region is presented in this section. The frequency bins are defined for three intervals, low (< 22 MJ-m^{-2}-day^{-1}), medium (22 - 28 MJ-m^{-2}-day^{-1}) and high (> 28 MJ-m^{-2}-day^{-1}). As the model is most reliable for periods of at least 5 days, all data was pre-processed into weekly means. Therefore every pixel in the study region had 52 weekly averages per year.

The distributions of these low, medium and high regions of solar radiation are shown in Figure 6.6, 6.7 and 6.8. Distinct patterns can be seen in three regions: 10° S-14° S, 14° S-22° S and 22° S-26° S. Overall, the distributions indicate that low solar radiation (less than 22 MJ-m^{-2}-day^{-1}) occurs more than 65% of the time in the far south of the study area. Low values occur about 55% of the time in the middle region, between 14°S and 22°S. In the north of the study region, low values occur less than 45% of the time (Figure 6.6). For the medium range (22-28 MJ-m^{-2}-day^{-1}), the 35% level occupies for almost all the GBR region (Figure 6.7). On the other hand, the distribution of high solar radiation values (>28 MJ-m^{-2}-day^{-1}), shows the values of less than 15% of the time in the northern region (Figure 6.8). These high values are presented more than 25% for the most of the region south of 18° S.

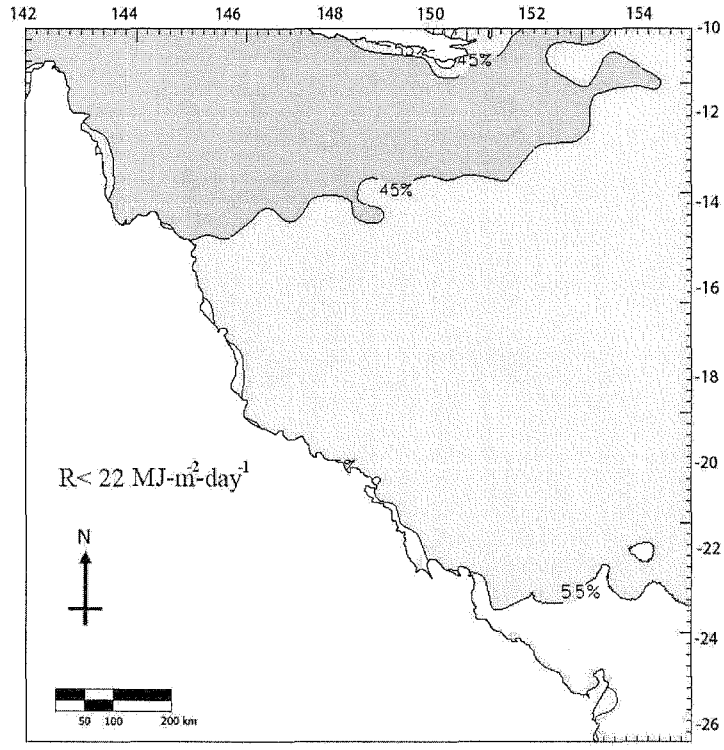

Figure 6.6 The frequency distribution of 'low' values of daily solar radiation (<22 MJ-m^{-2}-day^{-1}).

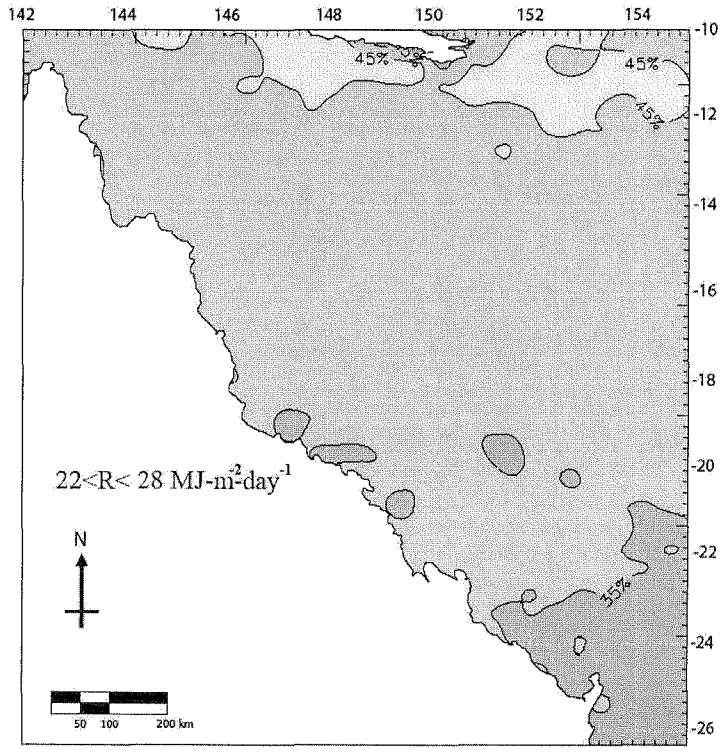

Figure 6.7 The frequency distribution of 'medium' values of daily solar radiation (22-28 MJ-m^{-2}-day^{-1}).

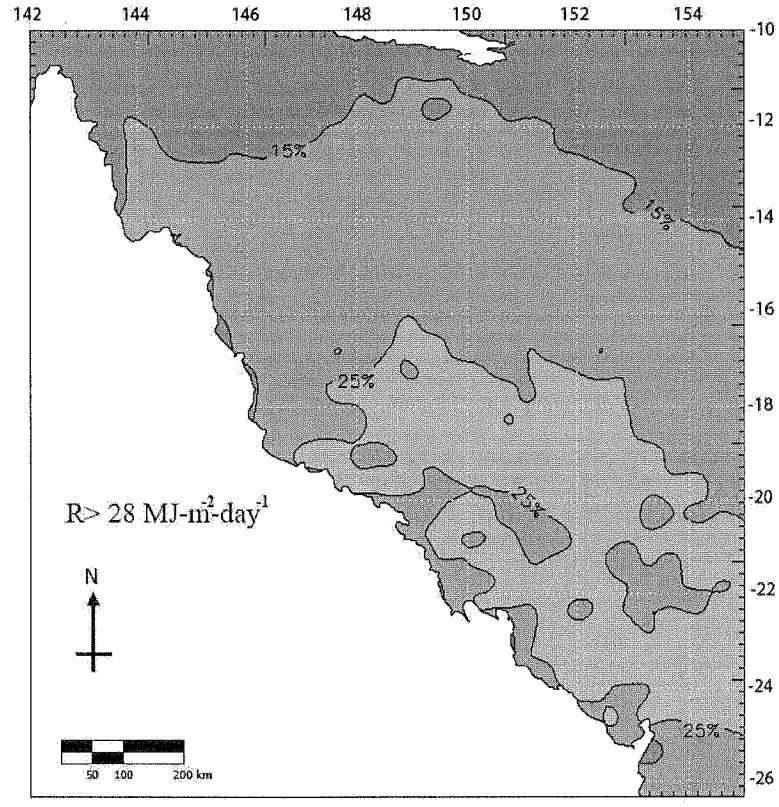

Figure 6.8 The frequency distribution of 'high' values of daily solar radiation (>28 MJ-m^{-2}-day^{-1}).

6.2 Surface broadband solar radiation at Heron Island

6.2.1 Diurnal variation of hourly solar radiation

This section presents feature and statistic of hourly solar radiation for Heron Island (23.44° S, 151.91° E). The island houses a biological station managed by the University of Queensland Centre of Marine Studies. This study represents a contribution to a joint project with the Centre to examine radiation/bleaching influences, and as a result some statistics for the immediate vicinity of Heron Island are presented here.

As a first step, the 11-year satellite data set (1995-2005) was sectorised into a sub-area of 5×5 pixels over Heron Island to provide a time series of Earth-atmosphere reflectivity α'_{EA} for Heron Island. The α'_{EA} data for each satellite hour was then averaged over the month to obtain the monthly value of the Earth-atmosphere

reflectivity for that hour. Using the LUT algorithm, the solar radiation for each satellite hour is estimated for each month, and plotted (Figure 6.9).

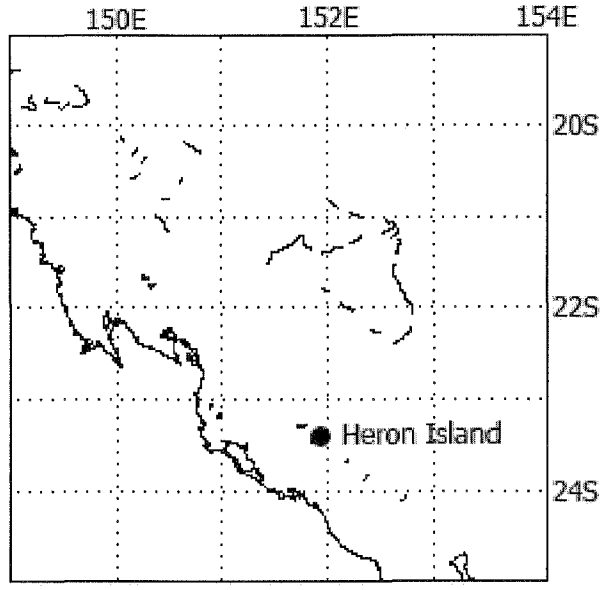

Figure 6.9 Location of Heron Island in the study area.

The monthly diurnal plots illustrate the hourly variations of solar irradiance for the Heron Island region (Figure 6.10). The graphs show that solar radiation at local noontime in the summer months (Nov-Dec-Jan-Feb) is very high, reaching peaks of more than 1000 W-m^{-2}. On the other hand, solar radiation during the winter period is much lower in magnitude, with peak values around 600 W-m^{-2}. The hourly frequency distribution of solar radiation for the 1995-2005 period shows that 500 W-m^{-2} is most common at Heron Island (Figure 6.11). Solar radiation values between 100-300 W-m^{-2} and 400-700 W-m^{-2} represent 25.5% and 53% of the distribution, respectively. Higher solar radiation fluxes, greater than 800 W-m^{-2}, occur 21.5% of the time.

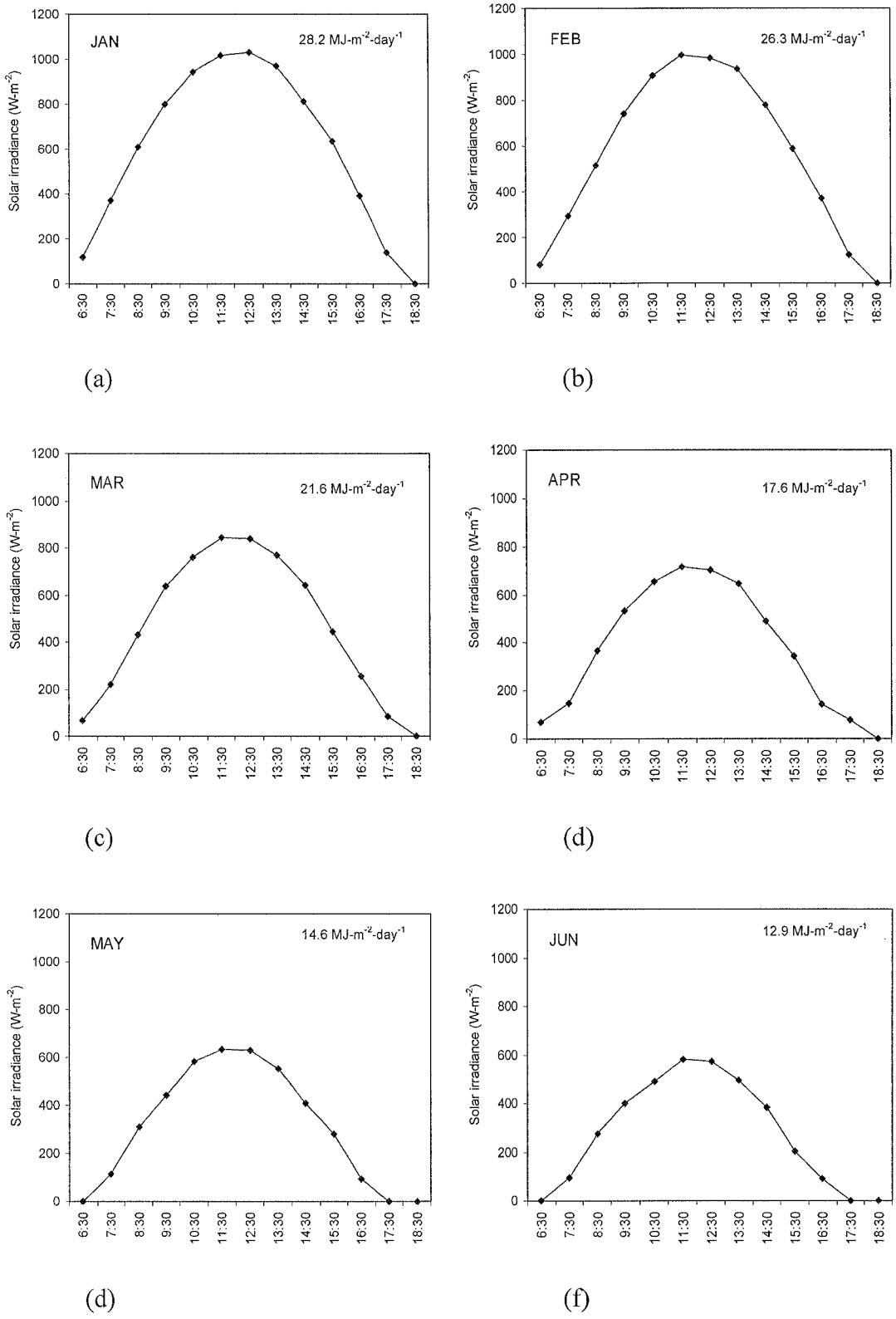

Figure 6.10 Diurnal variation of solar radiation over Heron Island.

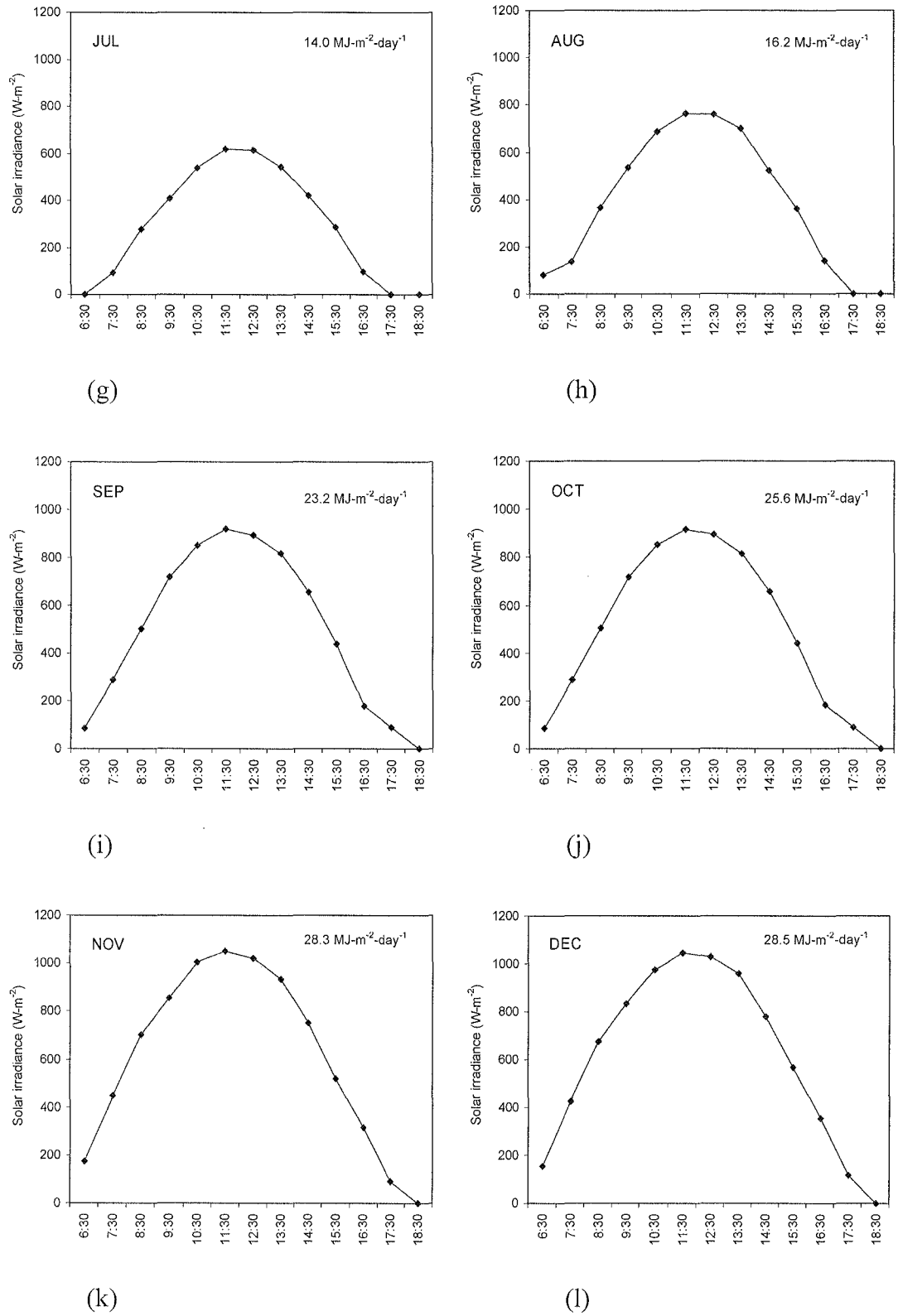

Figure 6.10 Diurnal variation of solar radiation over Heron Island (continued).

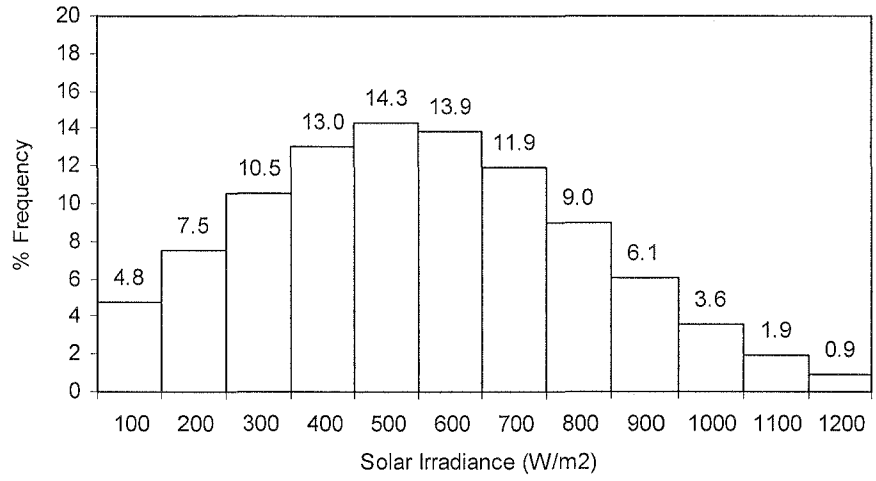

Figure 6.11 Normal distribution of solar irradiance at Heron Island.

6.2.2 Monthly variation of daily solar radiation

The monthly averages of surface daily solar radiation are obtained by integrating the hourly values between 6.30 and 18.30. Figure 6.12 presents the annual variations of solar radiation by comparing monthly average irradiances for each of the 11 years. Overall, the fluctuation of daily solar radiation at Heron Island in each month is less than 2 MJ-m^{-2}-day^{-1} and the monthly averages vary from about 12 MJ-m^{-2}-day^{-1} in winter to over 28 MJ-m^{-2}-day^{-1} in the summer months (Figure 6.13).

The maximum monthly values of solar radiation at Heron Island are mostly observed after the year 2000, as shown in Figure 6.13. In summer, the maximum monthly averages reached often exceed 30 MJ-m^{-2}-day^{-1}. In particular, these extreme values occurred in November 2002, December 2002, January 2001 and February 2002 (Figure 6.12).

It is also interesting to observe how the summer means (Nov-Dec, Jan-Feb) for individual years compare with the long-term means (Figure 6.13). Figure 6.14 presents anomalies for these two pairs of months calculated as a difference from the 11-year means of the period. Strong positive anomalies are evident in Nov-Dec of both 2001 and 2002, and to a lesser extent in Jan-Feb of the same years.

The normal distribution plot illustrates that most daily solar radiation values at Heron Island fell within the 20-24 MJ-m^{-2}-day^{-1} bins (Figure 6.15). The proportions of the high (≥ 28 MJ-m^{-2}-day^{-1}), medium (14-26 MJ-m^{-2}-day^{-1}) and low (≤ 12 MJ-m^{-2}-day^{-1}) daily solar radiation are 8.06%, 73.97% and 17.96%, respectively (Figure 6.15).

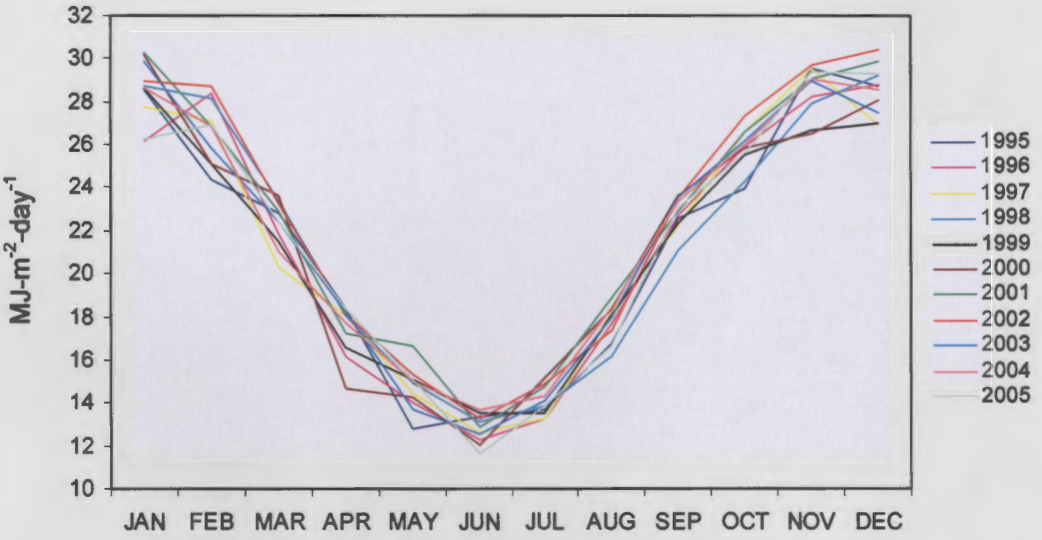

Figure 6.12 Monthly changes of solar radiation at Heron Island for the years between 1995 and 2005.

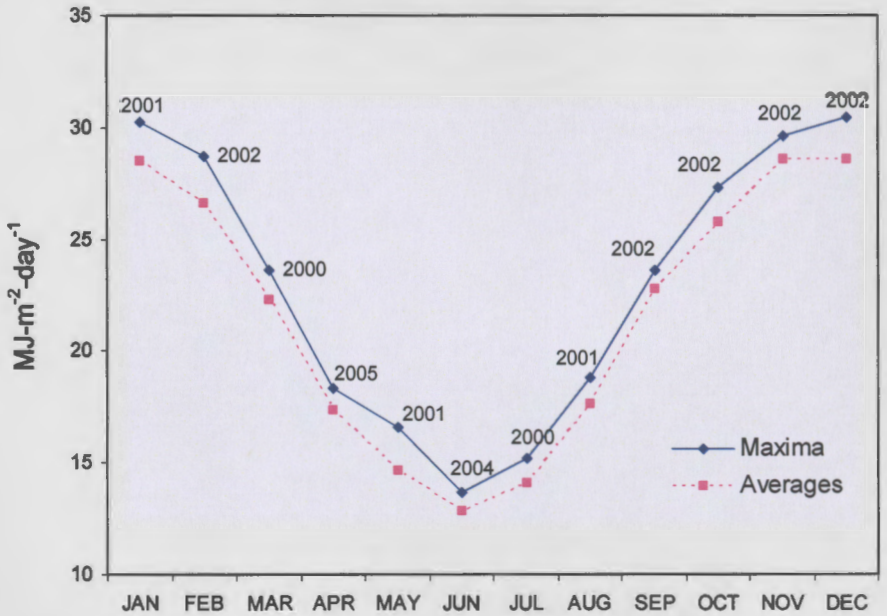

Figure 6.13 Monthly average and maximum monthly values of daily solar radiation at Heron Island.

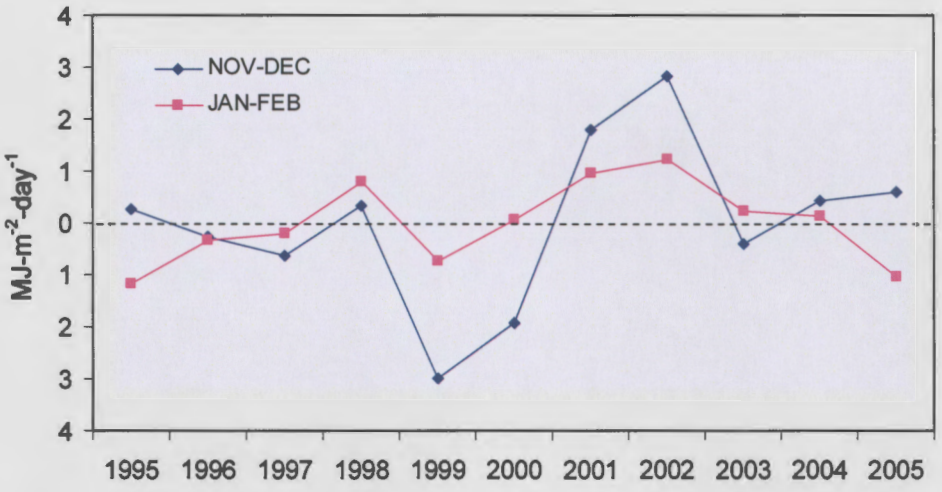

Figure 6.14 Anomaly of monthly solar radiation at Heron Island for the years between 1995 and 2005.

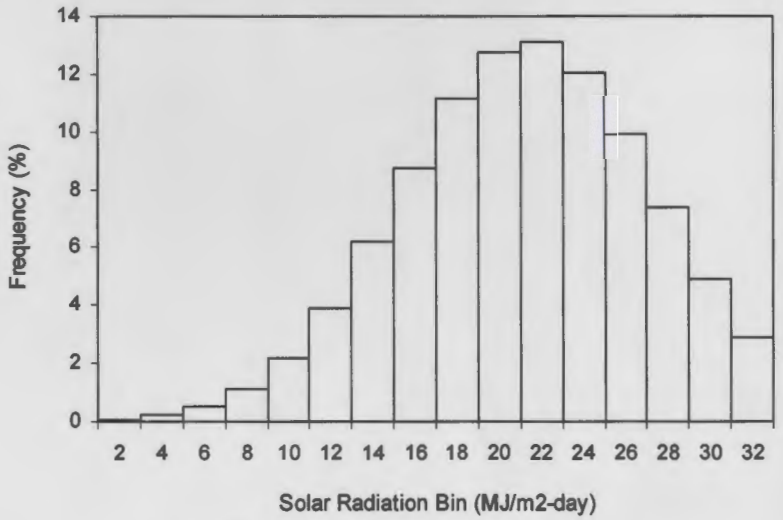

Figure 6.15 Normal distribution of solar radiation at Heron Island.

The statistics of solar radiation at Heron Island have been presented over an 11-year period. These are the first solar radiation data for Heron Island that have been provided in the recent decade. The graphs illustrate the variation of solar radiation at Heron Island, providing information for marine biology. Furthermore, a similar analysis could be performed in other parts of the study region where no surface measurements are available.

6.3 Profiles of PAR and UVB underwater irradiance

Using the set of coefficients derived from the model of Gordon (1975) in Section 4.3, the SeaWiFS-derived total attenuation coefficients at 490 nm, $K_d(490)$, are transformed to estimate the K_d values for the PAR and UVB wavebands. Because of the limitation in the SeaWiFS data as a result of the high number of cloudy pixels in the daily images, this study will utilise the monthly-mapped $K_d(490)$ of the SeaWiFS images. Monthly K_d(PAR) and K_d(UVB) data are estimated from the SeaWiFS K_d data.

6.3.1 Vertical distribution of PAR and UVB underwater

January 1998 averages of PAR and UVB underwater irradiance derived from SeaWiFS data are shown for four depths — 1.0 m, 2.5 m, 5.0 m and 10.0 m (Figure 6.16). Overall, the maps show a decrease in PAR and UVB fluxes between 1 m to 10 m depths. Both PAR and UVB irradiance are very low in magnitude near the coast and in the reef regions where the chlorophyll-*a* concentration is high.

At a shallow depth of 1 m, spatial variations of PAR and UVB irradiances are small in both near-shore and open water. At depths below 2.5 m, the PAR and UVB irradiances show strong vertical gradients in area near the coast. In near-shore regions, PAR irradiance typically decreases from 450 W-m^{-2} at 1 m to below 300 W-m^{-2} at 5 m. Similarly, UVB irradiance decreases from above 200 mW-m^{-2} at 1.0 m to less than 50 mW-m^{-2} at 5 m in near-shore regions. At 10 m depth, PAR and UVB irradiances exhibit values of less than 200 W-m^{-2} and 50 mW-m^{-2}, respectively.

The sum of the low PAR and low UVB irradiances near the reef areas may be an artifact of the method used here. As stated earlier, the bottom effect might influence the upwelling irradiance, so that an artificially high K_d may be a result of turbidity effects as well as a bottom and CDOM effects and others.

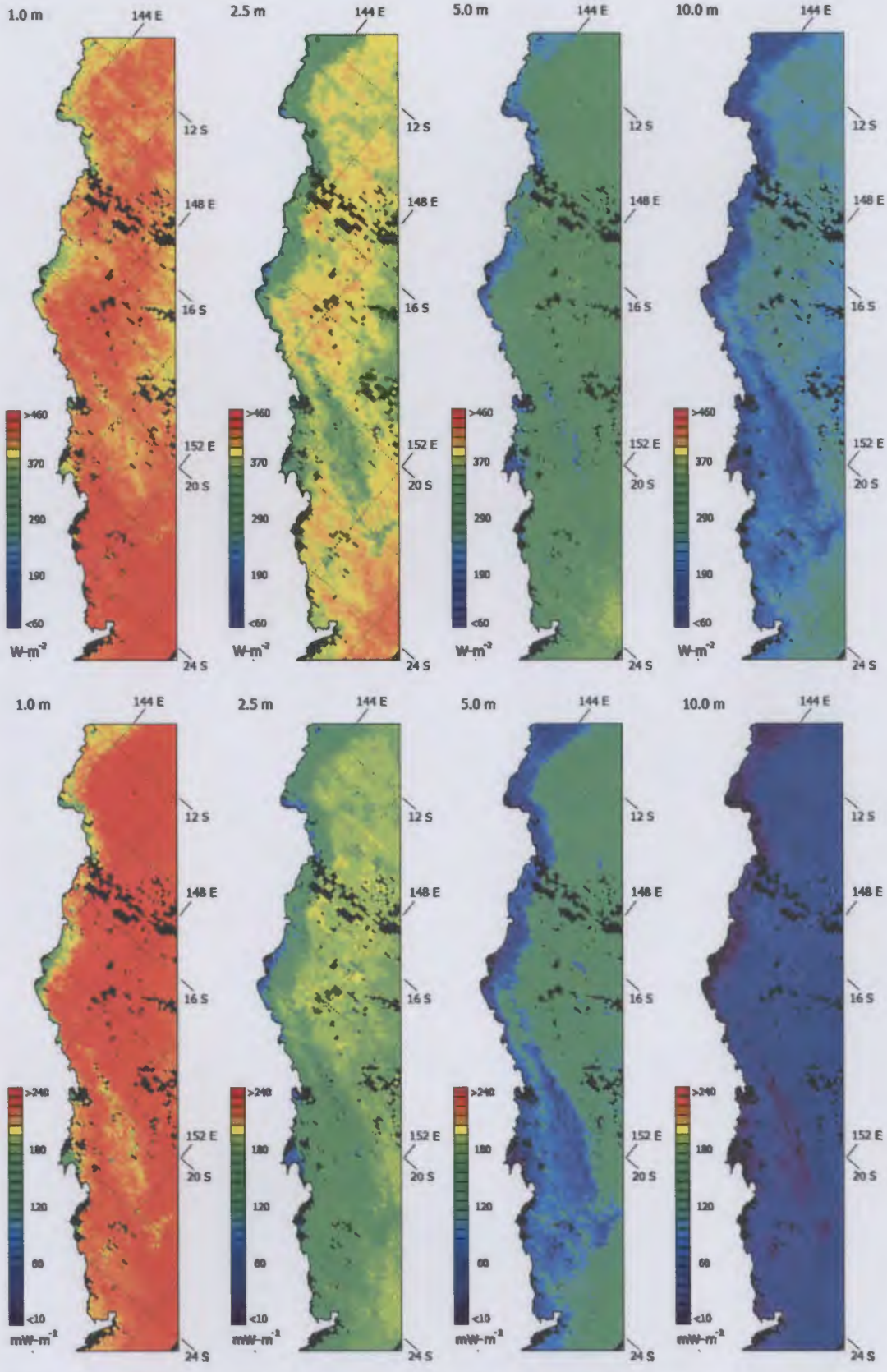

Figure 6.16 The vertical distribution of underwater PAR (top panel) and underwater UVB (bottom panel) irradiances estimated at 1.0, 2.5, 5.0 and 10 m (from left to right, respectively) for January 1998.

6.3.2 Long-term monthly average of PAR irradiance at the 2.5 m depth

This section discusses the large-scale distribution of underwater PAR and UVB irradiances. Living corals colonise in shallow depths and to examine this light environment, PAR and UVB irradiance are estimated at 2.5 m depth. Examination of the data revealed very low values of K_d (~0.05 m^{-1}) in offshore areas with little variation, very likely as a result of low suspended sediments and low chlorophyll-*a* concentrations. In contrast, nearshore areas experience high values of K_d and suspended matter. Maps of underwater PAR and UVB irradiance are examined and illustrated only for a 200-km strip along the GBR, over an 8-year period (1998-2005).

Figure 6.17 presents the monthly average values of PAR irradiance across the GBR region for the years 1998-2005. It is clear that the PAR irradiance is very low in the nearshore regions. Considering the changes along the GBR, the PAR irradiance shows a strong variation in the latitude bands between 20° S and 24° S, dropping from above 400 W-m^2 in summer to below 250 W-m^{-2} in winter. On the other hand, a strong pattern of increasing PAR irradiance extends from September toward March, as seen in most areas of open water and some regions closer to the coast between 18° S and 20° S. In the open water region, PAR irradiance exceeding 200 W-m^{-2} is seen in all months.

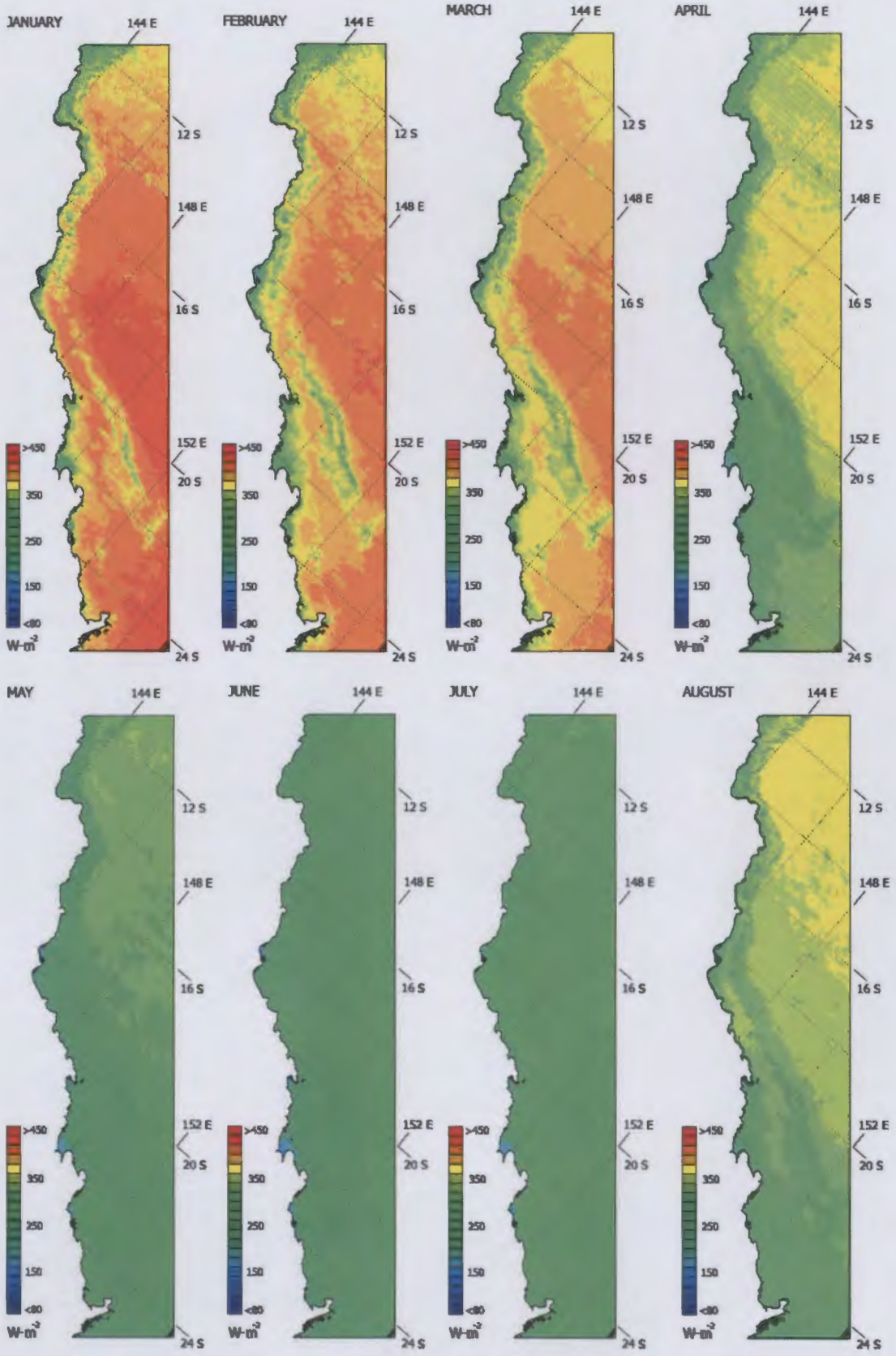

Figure 6.17 Monthly average values (1998-2005) of underwater PAR irradiance at 2.5 m.

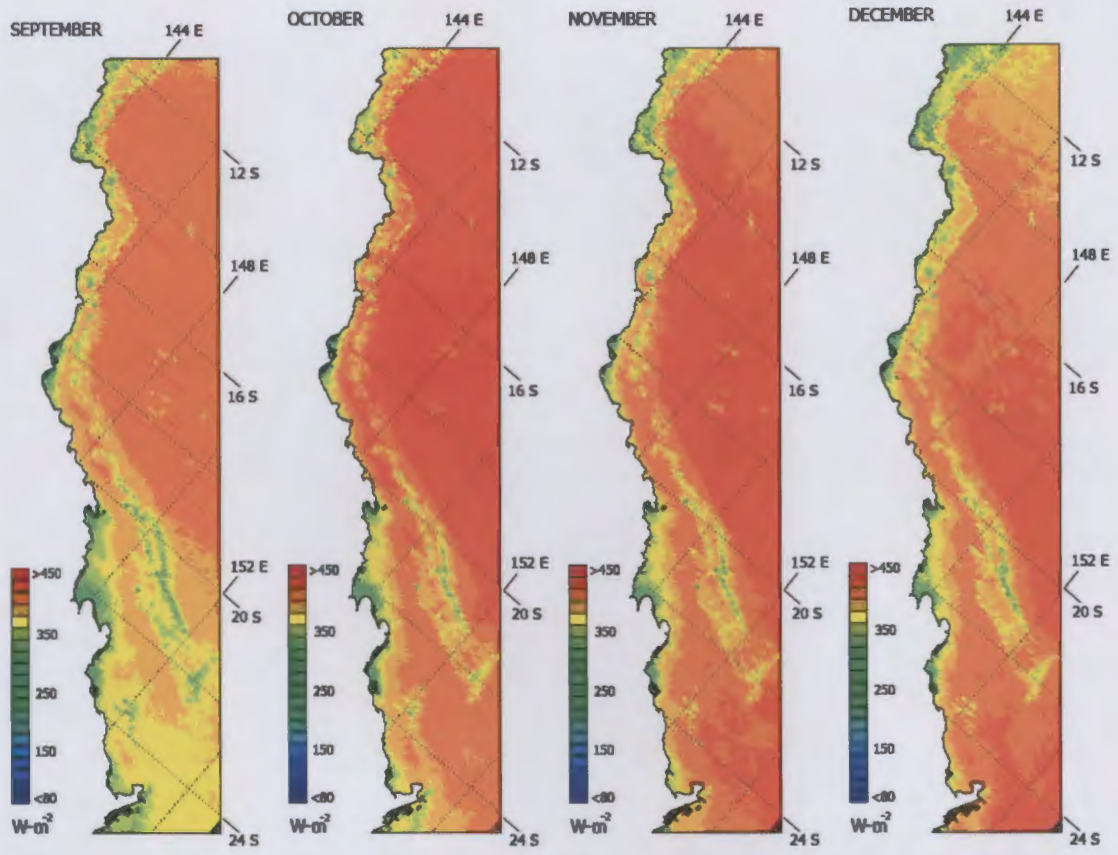

Figure 6.17 Monthly average values (1998-2005) of underwater PAR irradiance at 2.5 m (continued).

6.3.3 Variation of PAR irradiance at 2.5 m during summer periods

This section presents the underwater PAR irradiance at 2.5 m depth averaged across the summer months (Nov-Dec-Jan-Feb) of each year (Figure 6.18). Considering the results for all time periods, high levels of PAR (>400 W-m^{-2}) are mostly seen in open water regions. A strong pattern of PAR irradiance also exists along the coastline in latitude bands between 18° S and 20° S, bordered by low PAR values along the coast and in offshore reef regions.

An increasing trend of high PAR irradiance (>450 W-m^{-2}) in both open water and near-shore regions, occurs during the summers of 2001/2002 and 2002/2003. In both periods, high PAR irradiance also extends over near-shore regions, with values of over 350 W-m^{-2}.

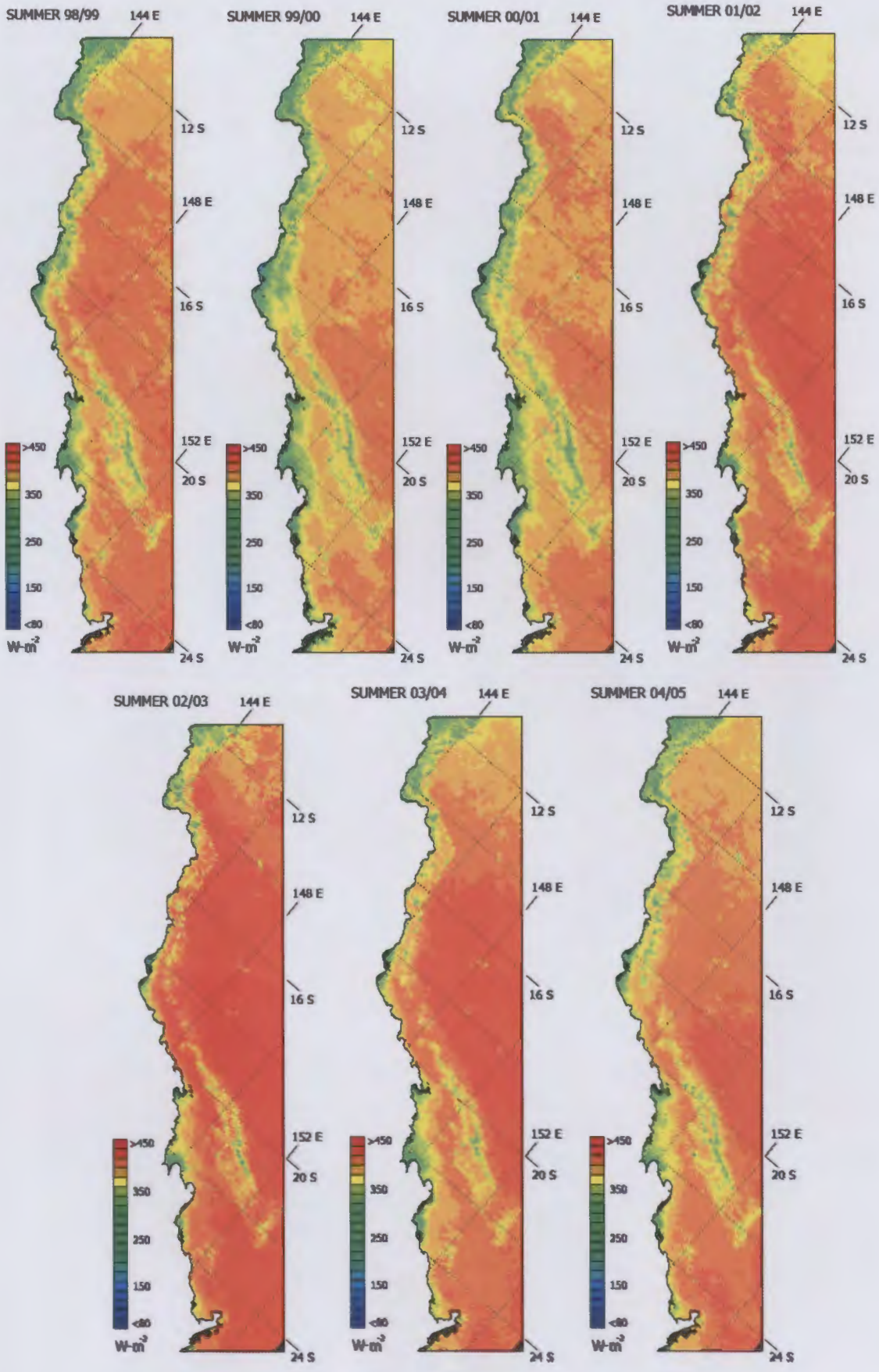

Figure 6.18 Yearly variation of PAR underwater irradiance at 2.5 m depth, estimated for summer months (Nov-Dec-Jan-Feb) from 1998 to 2005.

6.3.4 Long-term monthly average of UVB irradiance at the 2.5 m depth

UVB irradiance is also estimated from the SeaWiFS-derived K_d data across the region. Unlike features of the PAR distribution, the monthly UVB irradiance varies in open water regions east of the outer reefs. During the year, the UVB irradiance is relatively low in the reef regions near-shore, and high UVB irradiance is typically seen in open water. The UVB irradiance estimated for the summer months in open water is largely in excess the values of 180 mW-m^{-2} between 14° and 20° S. By contrast, this region receives little irradiance in May, June and July, especially in near-shore areas south of 20° S (Figure 6.19).

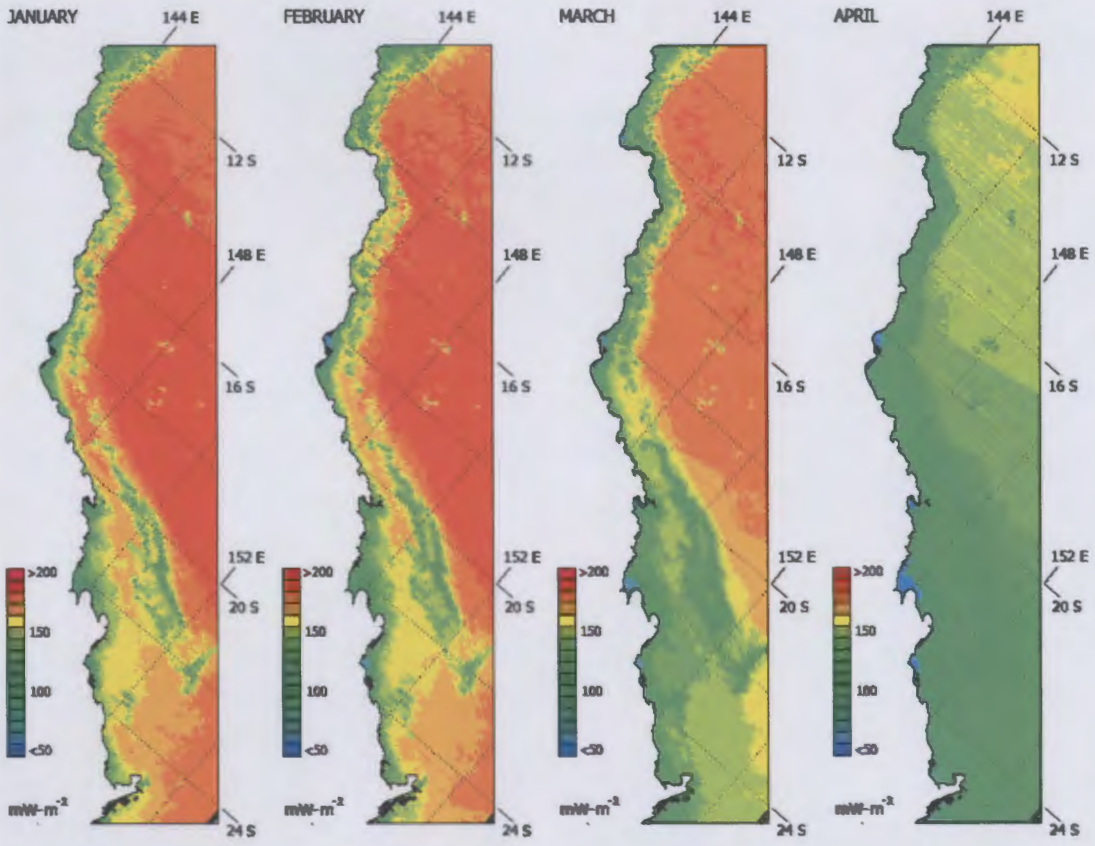

Figure 6.19 Monthly changes of underwater UVB irradiance estimated for 2.5 m depth.

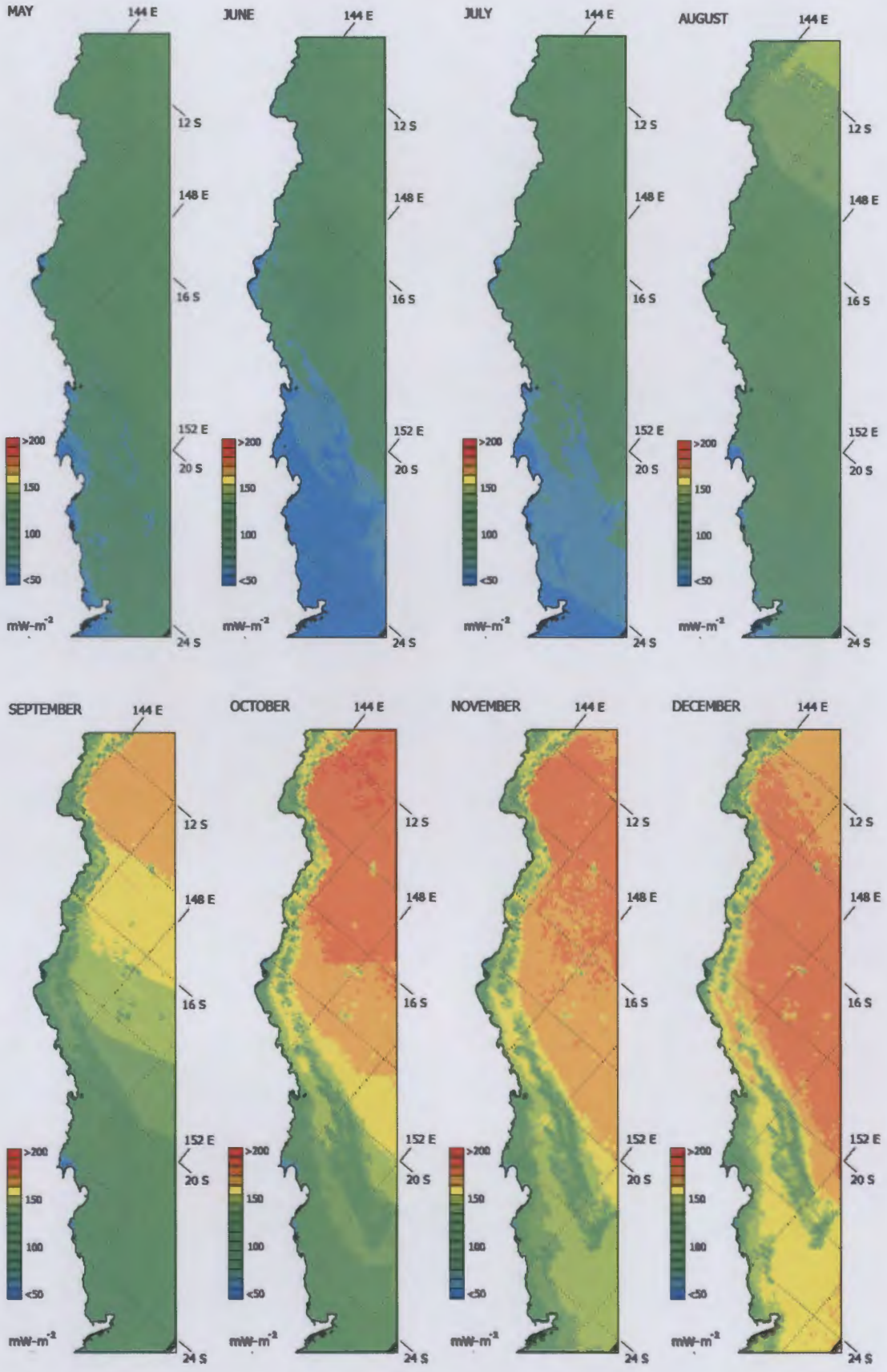

Figure 6.19 Monthly changes of underwater UVB irradiance estimated for 2.5 m depth (continued).

6.3.5 Variation of UVB irradiance during summer periods

A similar approach to that described in Section 6.3.3 is followed to provide values of UVB irradiance for the summer months (Nov-Dec-Jan-Feb) of the 1998-2005 periods (Figure 6.20).

The results in Figure 6.20 show high UVB irradiances of over 180 mW-m^{-2} in the open water. In the reef area, the UVB irradiance at 2.5 m peaks about 120 mW-m^{-2} for both inshore and offshore regions. Most of the near-shore reefs (within 50 km of the coast) experience low UVB irradiances (~100 mW-m^{-2}) in all summers. Over the long-term, high values of UVB irradiance are apparent during the summer of 2001/2002 to 2003/2004.

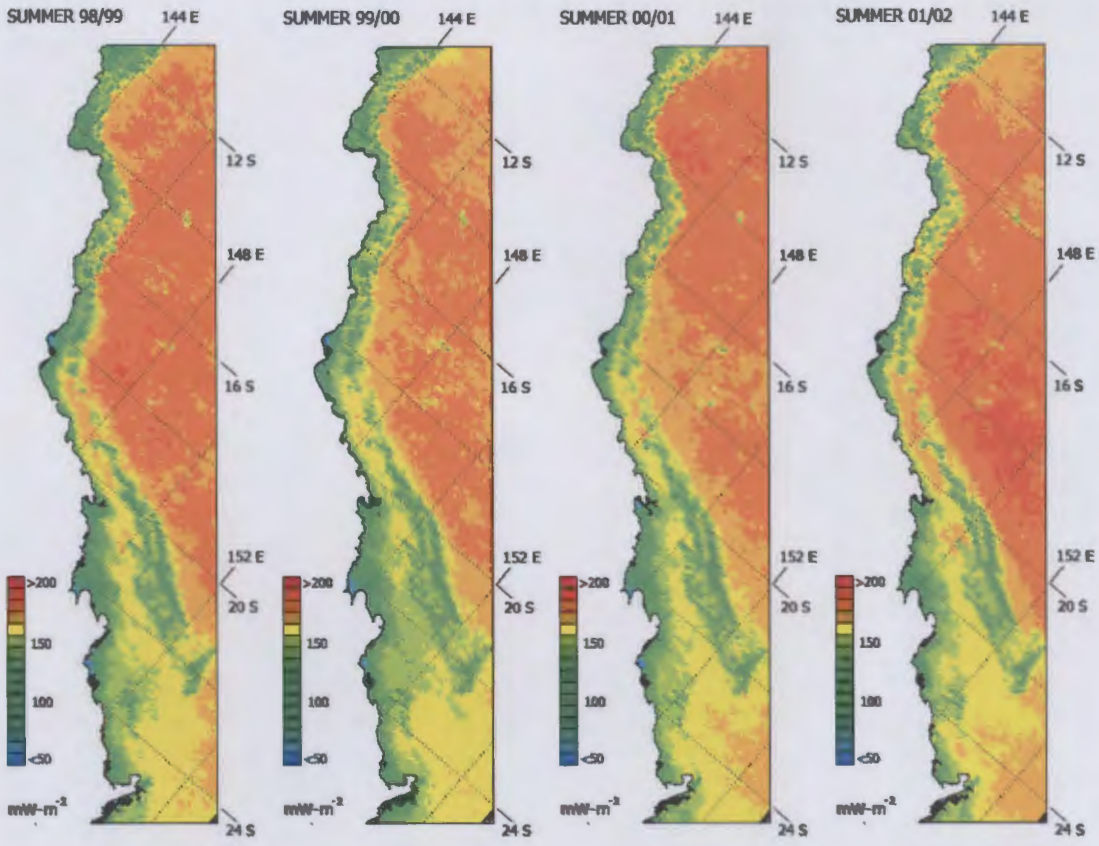

Figure 6.20 The distribution of UVB underwater irradiance at 2.5 m, estimated for summer months (Nov-Dec-Jan-Feb)

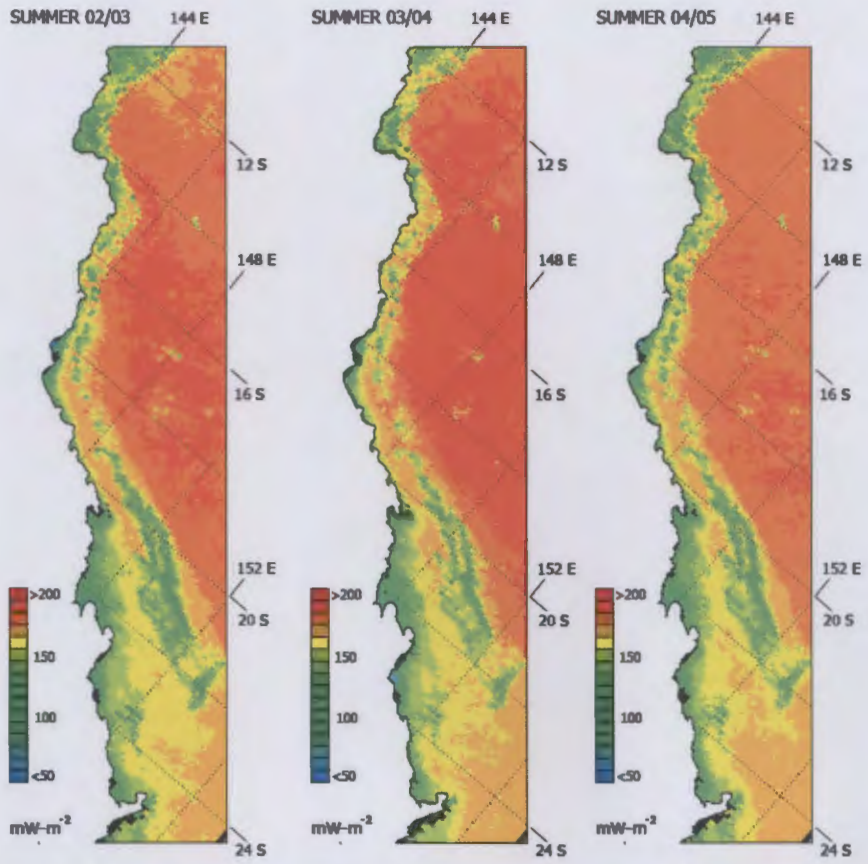

Figure 6.20 The distribution of UVB underwater irradiance at 2.5 m, estimated for summer months (Nov-Dec-Jan-Feb) (continued).

6.3.6 Distribution of UVB and PAR across the lagoon

UVB and PAR irradiances were examined in a transect from roughly 150° - 155° E along the 22° S meridian, covering the coast to regions of open water. Figure 6.21 presents this transect at depths of 1 m, 2.5 m and 5 m.

In near-shore area, values of UVB and PAR are typically low, due to high K_d values associated with reef areas, however the effect may not be real due to bottom topography processes and others. On the other hand, a steep increase of UVB and PAR, by ~40 mW-m^{-2} and ~100 mW-m^{-2} respectively, can be observed at the border between the inshore and offshore reefs.

To examine the variation of PAR and UVB with depth in more detail, the transect is presented as normalised irradiances (Figure 6.22), by dividing the irradiance at depths by the corresponding surface values. It is clear that in general terms the UVB

irradiance is attenuated more swiftly than the PAR irradiances. In the near-shore region, the relative UVB values drop rapidly from ~0.65 at 1 m to ~0.3 at 2.5 m. In comparison, for the same part of the transect, the PAR changes less dramatically, from ~0.8 at 1 m to ~0.5 at 2.5 m. The relative UVB and PAR irradiances increase further east along the transect.

6.3.7 Monthly averages of UVB and PAR at 2.5 m depth: implications for 22° S, 152° E.

A long-term profile of monthly UVB and PAR underwater irradiance is provided in this section. This study has selected a near-shore location at 22° S, 152° E to illustrate the annual variations of PAR and UVB underwater irradiance at 2.5 m depth (Figure 6.23).

Overall, PAR and UVB irradiances are high in summer period (Nov-Dec-Jan-Feb), while in winter they are low (Jun-Jul-Aug). However, it can be seen that high PAR irradiance increases in early months from mid-spring to summer, while high UVB irradiance exhibits only in summer months. On a year-to-year basis, PAR irradiance varies around 400 $W\text{-}m^{-2}$ and decreases to 300 $W\text{-}m^{-2}$ in winter, and UVB irradiance varies between 50-200 $mW\text{-}m^{-2}$. Little temporal change is observed for UVB irradiance, but higher values of PAR are seen from summer 2001 onward.

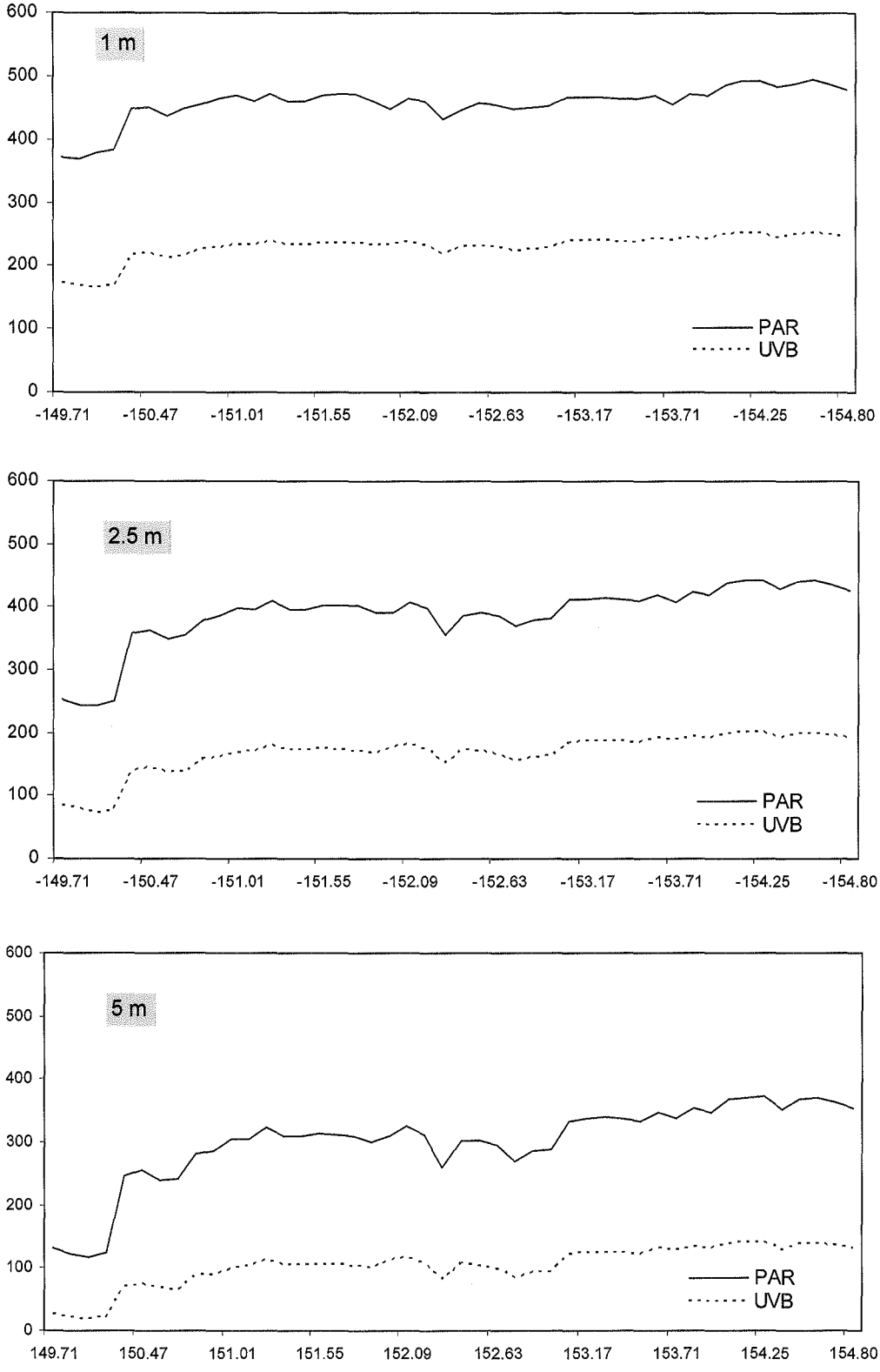

Figure 6.21 UVB and PAR transects at 22° S across longitudes between 149.7° E and 154.6° E, for various depths: (a) 1 m (b) 2.5 m (c) 5.0 m. Note that PAR and UVB are displayed in $W\text{-}m^{-2}$ and $mW\text{-}m^{-2}$, respectively.

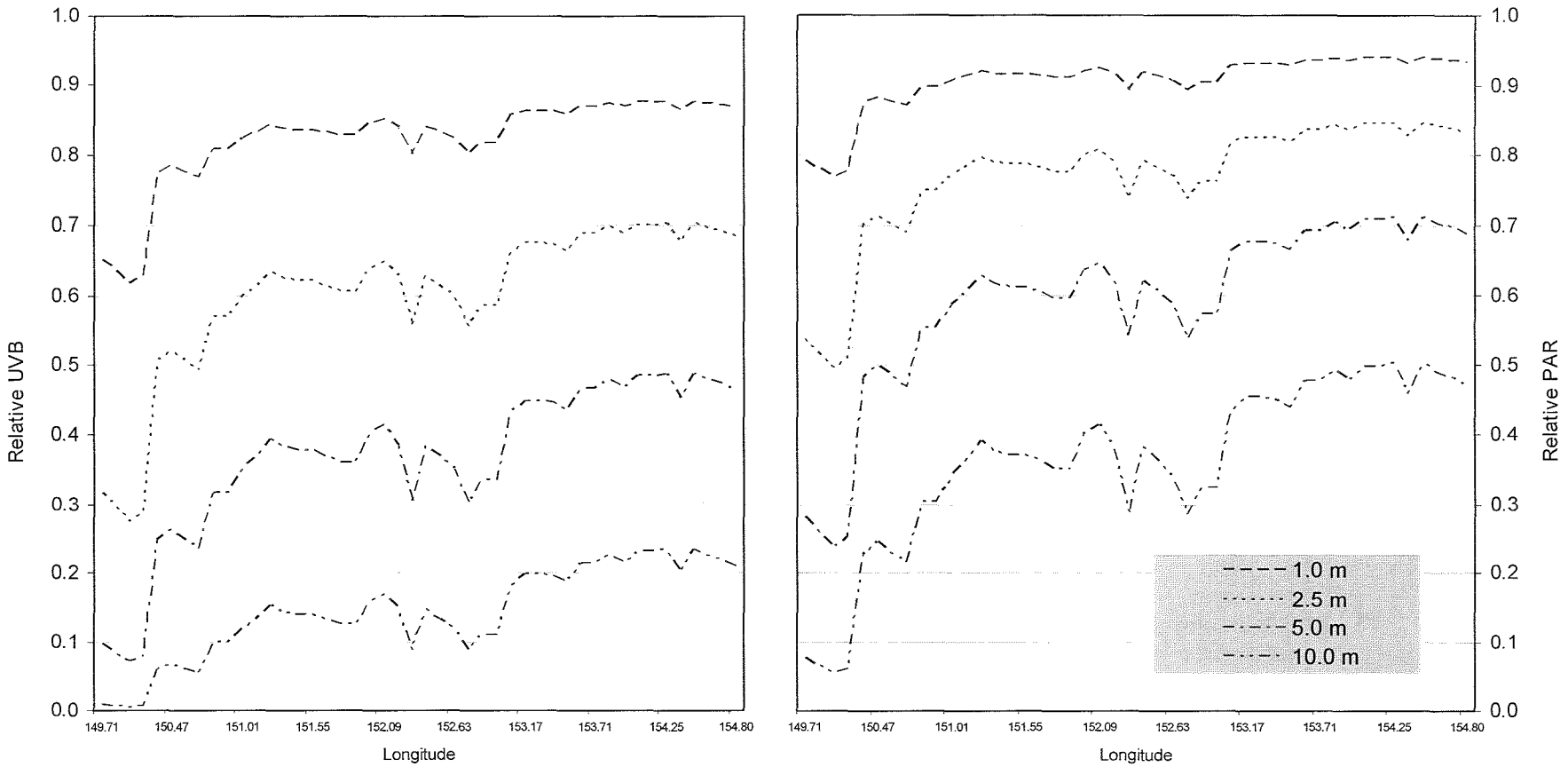

Figure 6.22 UVB and PAR underwater irradiances relative to the surface values, displayed across the transect at 22° S.

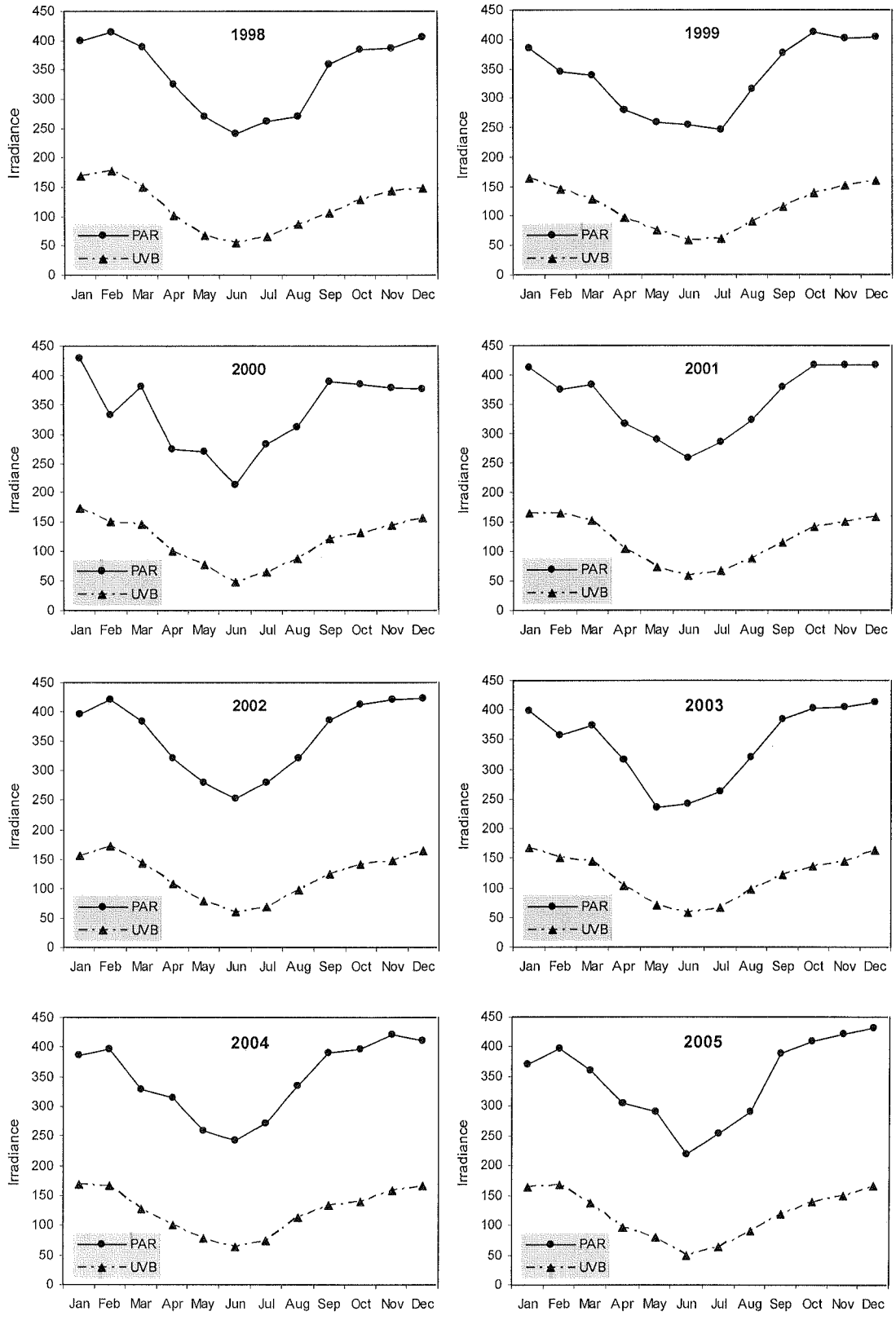

Figure 6.23 Monthly averages of PAR and UVB underwater irradiances, estimated at 2.5 m depth, at 22° S, 152° E. Units of PAR and UVB irradiances are W-m^{-2} and mW-m^{-2}, respectively.

6.4 Discussion

This study has provided both spatial and temporal information of long-term solar radiation for the Great Barrier Reef. First, a climatology of surface broadband solar radiation was provided by using the physically–based LUT algorithm. Next, relationships between spectrally-integrated K_d and various environmental variables were then derived using Monte Carlo models. The estimation of underwater UVB and PAR irradiances was accomplished for various depths across the GBR coastline. Results of the surface broadband solar radiation and UVB irradiance are provided with accuracies within 10-15% and ~20% RMS differences, respectively at the daily scale. For the underwater estimations, this study used SeaWiFS-derived K_d estimates which were evaluated with the measured K_d values, resulting in a RMS error which was 40% of the mean values.

Long-term information and statistics of solar radiation are emphasized in this study, in contrast to a number of satellite-based models which are mainly focused on improving cloud algorithms and model accuracy, but do not provide long-term information (Tarpley, 1979; Gautier, 1980; Diak and Gautier, 1983; Gautier, 1988; Schmetz, 1991; Dedieu *et al.*, 1987; Pinker and Laszlo, 1991; Tovar and Baldasano, 2001; Kandirmaz *et al.*, 2004). In contrast to most studies which estimate underwater irradiance for some specific wavebands and under specific light conditions (Roesler and Perry, 1995; Stambler *et al.*, 1997; Ammenberg, 2002; Aas *et al.*, 2005; Liu *et al.*, 2006), this study has provided a true climatology of both incoming surface and underwater irradiance, in both PAR and UVB bands. This has been accomplished using a methodology by which SeaWiFS-derived K_d is related to K_d for PAR and UVB radiation.

On average, the regions of high levels of surface solar radiation are seen to be located in a distinct zone between 16° and 24° E, which probably is a result of decreasing cloud cover under the influence of the subtropical high (Sturman and Tapper, 2005). In the north of the GBR (10° S – 16° S), low solar radiation prevails throughout the year (Figure

6.2). This feature is typical of monsoonal tropical climates of Papua New Guinea, where low pressures bring heavy rainfall, high humidity, precipitation and cloud (Tapper and Hurry, 1993; Hoinka, 1998; Zeng, 1999; Wang *et al.*, 2000; Dai, 2006). In spring, precipitation over the entire GBR is relatively low compared to the autumn months (Zeng, 1999). As a result, high solar radiation extends in spring time over a large area (14° S – 24° S), while in autumn, high values are seen only in the southern region (20° S – 26° S). In winter, solar radiation is very low due to the effects of solar zenith angle and day length, as the sun moves to the northern hemisphere. There is cloud cover during this dry season, and there is not much regional change throughout the GBR region (Wang *et al.*, 2000).

Along the coast where the high-land areas and the ocean are adjacent, low solar radiation is evident, as cloud forms when the south-westerly trade winds bring moist air over the coastal region (Tapper and Hurry, 1993; Ghan and Shippert, 2006). The weak increases of solar radiation seen in the open water may be linked to a decrease of the relative humidity trend (~0-1% per decade), which has been observed in eastern Australia over the ocean (Dai, 2006). However, the pattern of high solar radiation seen near the coastline of the GBR region in summer 2001/2002 needs further study. It may be argued that these high levels of solar radiation are linked to the ENSO event which prevailed in January/February 2002. However, the higher cloud cover in the eastern and of the study area is unexplained, as is the higher cloud cover obtained for other years which had a more intense ENSO signal (Park and Leovy, 2004; Chen *et al.*, 2007).

Regarding the underwater light climate, this study has found that UVB and PAR underwater irradiances are low in areas between the inshore and offshore reefs. These are areas where chlorophyll production and dissolved organic material (DOM) are high and mixed in the water (Scoffin and Tudhope, 1985; Kirk, 1994; Yentsch *et al.*, 2002). Conversely, high PAR and UVB irradiances are estimated in the open water east of the GBR. Considering the summer season and the 2.5 m depth (Figure 6.16), UVB irradiance

throughout the GBR ranges from 100 mW-m^{-2} near the coast to 180 mW-m^{-2} for open water. This also translates to a transmission of 30% for the coastal regions, as opposed to a higher transmission of 60% in open water. Corresponding features for PAR radiation are 150 W-m^{-2} to 250 W-m^{-2}, and transmission of 50% to 80%.

It is clearly seen that the chlorophyll production which is typically high in near-shore areas plays an important part in the attenuation (Kirk, 1994; Tilzer, 1995; Yentsch; 2002). The vertical profiles of the UVB/PAR ratios show that UVB decreases faster than PAR with increasing depth. It is because K_d is highly absorbed in the UVB to blue regions. In fact, UVB is absorbed best by dissolved organic materials (DOM), while PAR is largely transparent to DOM but can be significantly absorbed by chlorophyll (Smith and Baker, 1981; Kirk, 1994; Tilzer, 1995). This is illustrated by estimates taken in the transect at 22° S (Figure 6.22). At 10 m depth, summer transmissions for offshore areas are typically 10%, while PAR transmissions are twice as high ~20%.

The patterns of high UVB underwater irradiance evident in the northern latitude band (<16° S) corresponds to low column ozone in contrast to higher column ozone measured in the southern region (20° S - 30° S) (Kulkarni, 1980; Corlett and Monks, 2001). In addition UVB levels reach their highest values in October when column ozone is lowest at latitudes less than 16° S (Casiccia *et al.*, 2008). By contrast, PAR did not exhibit maximum values in the northern part of the GBR, nor in the month of October.

In summary, the solar radiation and UVB/PAR underwater irradiances were high in the summer of 2001/2002, 2002/2003 and 2003/2004. These unprecedented events may be a result of global climate changes, manifesting themselves in higher frequency and more intense ENSO events, a continuing depletion of column ozone, and general rise in Southern Hemisphere (SH) temperatures (WMO 2002; Gray *et al.*, 2005; Marchand *et al.*, 2005; Casiccia *et al.*, 2008).

Chapter 7

Solar radiation during coral bleaching events

A mass coral bleaching event was observed in the Great Barrier Reef in 1998, and again in 2002 (Berkelmans *et al.*, 2004). Comparison of bleaching surveys in the Great Barrier Reef conducted in 1998 and 2002 suggested that more than twice the number of offshore reefs were bleached in 2002 than in 1998. Berkelmans *et al.* (2004) derived a relationship between 3-day maximum sea surface temperatures (max3d) and areas of bleaching. Time series of max3d SST indicated that the period from mid-December to early March was particularly prone to bleaching events (Berkelmans *et al.*, 2004).

Considering the conclusion of Berkelmans *et al.* (2004) in terms of the causes of coral bleaching, it is also valuable to examine how solar radiation may have varied over the bleached GBR reefs. Berkelmans *et al.* (2004) used aerial survey data collected during summer of the 1998 and 2002 bleaching events to categorise the degree of bleaching into five bins – extreme (>60%), very high (30-60%), high (10-30%), moderate (1-10%) and no or low (<1%). The bleaching data was grouped based on the proportion of the reef areas that appeared white in colour over the study zones covering the reef crest and upper reef slope (Berkelmans *et al.*, 2004). In the following sections, this study uses the LUT-derived broadband solar radiation to investigate the climatology of solar radiation in the bleached reefs during 2002. The bleached reefs, identified in the aerial survey carried out in 2002 (Berkelmans *et al.*, 2004), are separated into inshore reefs (within 50 km of the coast) and offshore reefs (further than 50 km from the coast). For each of the bleached reefs, the satellite reflectivity data is sectorised for areas of 5 × 5 pixels (equal to 11.5 km (East/West) × 13.5 km (North/South)) and this data is used to

estimate daily broadband solar radiation from the LUT technique. This section seeks to establish the climatology of solar radiation over the GBR during the 2002 coral bleaching episode.

7.1 Climatology of solar radiation during the 2002 coral-bleaching event

In this section, time series of satellite-derived broadband solar radiation over the bleached regions were developed for the bleached reefs on a 7-day timescale. Because the GBR belt is narrow (extending 50-200 km from the coast) and most bleached reefs lie between 11° S and 23° S, the analysis has divided the bleached reefs into three regions: North (10°-16° S), Middle (16°-20° S) and South (20°-26° S). For each region, the time series of broadband solar radiation estimated between November 2001 and March 2002 is compared with the long-term (11-year) averages (Figure 7.1).

Overall, the time series shows that solar radiation over the bleached reefs was very high over the 2001/2002 summer (compared to the mean values) and most of the high solar radiation was received in the Middle and South regions (Figure 7.1). Between November and December 2001, solar radiation in the South and Middle regions was around 31 MJ-m^{-2}-day^{-1}, while the values in the North were lower (~29 MJ-m^{-2}-day^{-1}). In the Middle region, the differences in solar radiation between the 2001/2002 and the 11-year averages were very large from mid-December 2001 to March 2002. Consistent with the study of Berkelmans *et al.* (2004), the time series of solar radiation estimated for the bleached reefs in the Middle region varies in a similar manner to the water temperature measured at Davies Reef and Magnetic Island in 2002 (details are shown in Figure 3 (a) and (b) of Berkelmans *et al.*, (2004), see Appendix IV).

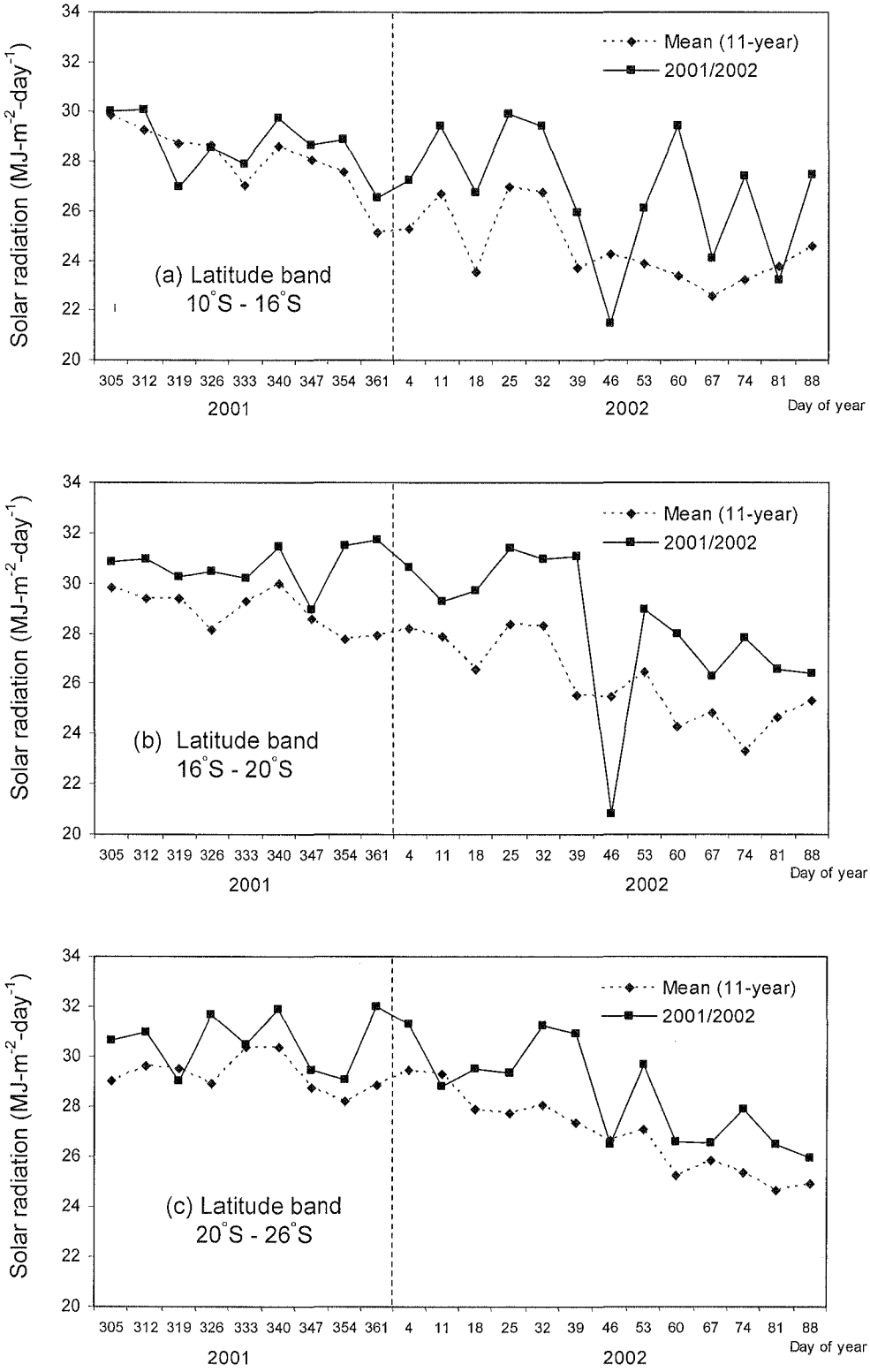

Figure 7.1 Time series of daily solar radiation estimated over the bleached reefs: (a) North (10°-16° S), (b) Middle (16°-20° S) and (c) South (20°-26° S). Radiation values are shown for the 2001/2002 summer, as well as the mean values over the 11 years (1995-2005).

The time series of solar radiation are further separated to cover inshore and offshore reefs (where inshore reefs are within 50 km of the coast). Berkelmans *et al.* (2004) defined the degree of bleaching as: extreme (>60%), very high (30-60%), high (10-30%), moderate (1-10%) and no or low (<1%). The solar radiation estimated over the reefs is then averaged for each of these bleaching indices. The time series of solar radiation for the period November 2001 to March 2002 are presented on a 7-day basis (Figure 7.2).

Overall, the time series shows that solar radiation at both inshore and offshore reefs was generally in the range 26-30 MJ-m^{-2}-day^{-1}. During November and December 2001, high solar radiation was dominant in all regions. A peak of 32 MJ-m^{-2}-day^{-1} can be seen in the first and the fourth weeks of December 2001. During the early months of 2002, solar radiation steadily decreased, approaching values of 26-28 MJ-m^{-2}-day^{-1}.

It can be seen that the bleaching indices from extreme (>60%) to moderate (1-10%) were associated with high values of solar radiation, and this is more pronounced for the inshore reefs. By contrast, the regions with no bleaching (<1%) corresponded to low solar radiation (Figure 7.2 (a)). This pattern is less evident for offshore reefs, indicating that solar radiation may play an important secondary role as a bleaching mechanism, and most of the literatures emphasizes high sea surface temperature (SSTs) as a direct cause of coral bleaching (Fitt *et al.*, 2001; Mumby *et al.*, 2001; Berkelmans *et al.*, 2004; Barton and Casey, 2005).

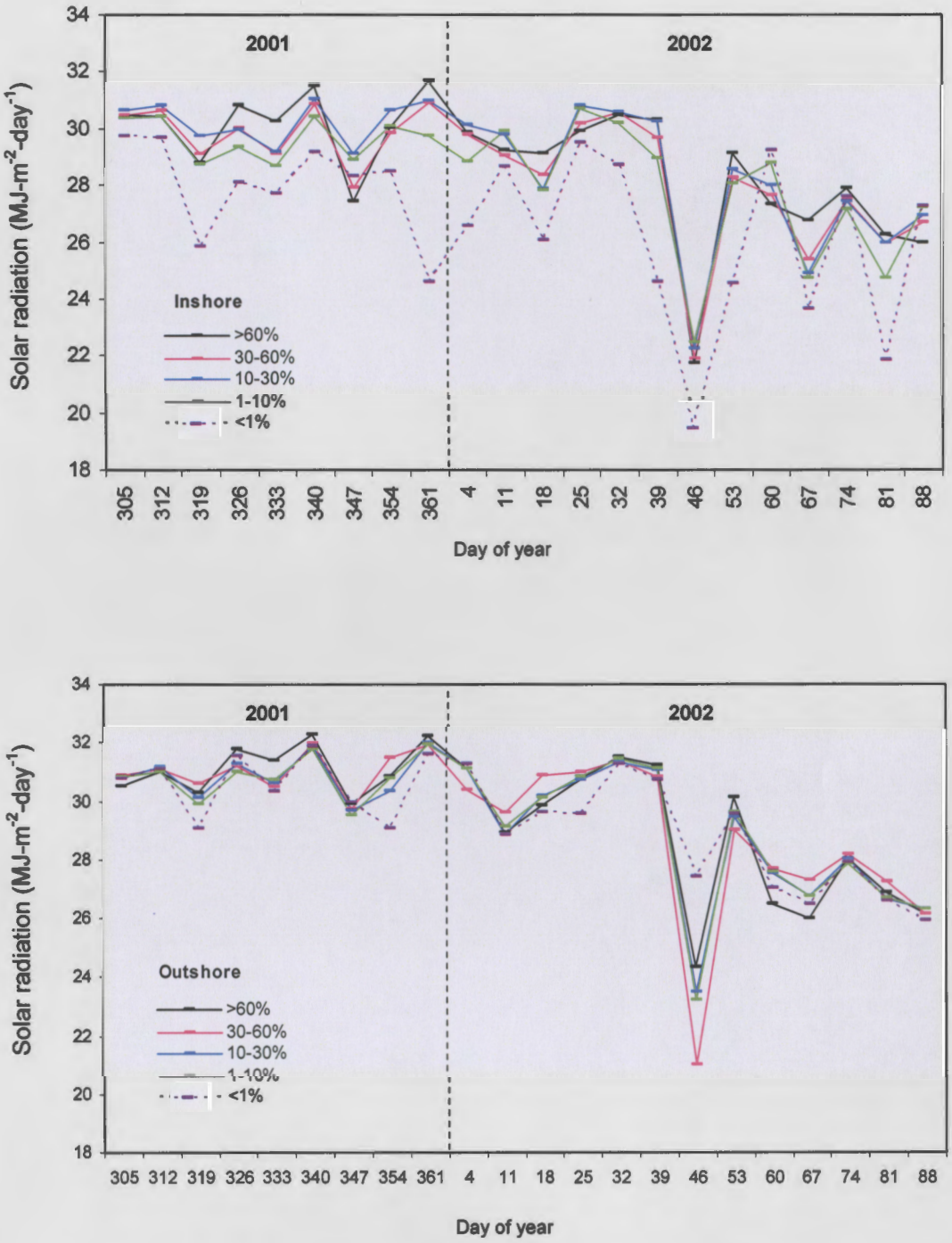

Figure 7.2 The 7-day averages of daily solar radiation over the bleached reefs, grouped according to degree of bleaching: (a) inshore reefs (b) offshore reefs.

Following the method described in Section 4.2, daily solar radiation derived from the LUT technique was estimated as an average over the period from 15 December 2001 to 15 January 2002 (Figure 7.3). The data was then compared with the locations where extreme (>60%) and moderate (1-10%) bleaching occurred in 2002 as reported by Berkelmans *et al.* (2004). However, the figure does not show an obvious agreement between pattern of high solar radiation and the location of the extremely bleached reefs. The map does show that the regions within 200 km of the coastline received high solar radiation of over 30 MJ-m^{-2}-day^{-1} in the latitude bands from 15° to 26° S (Figure 7.3).

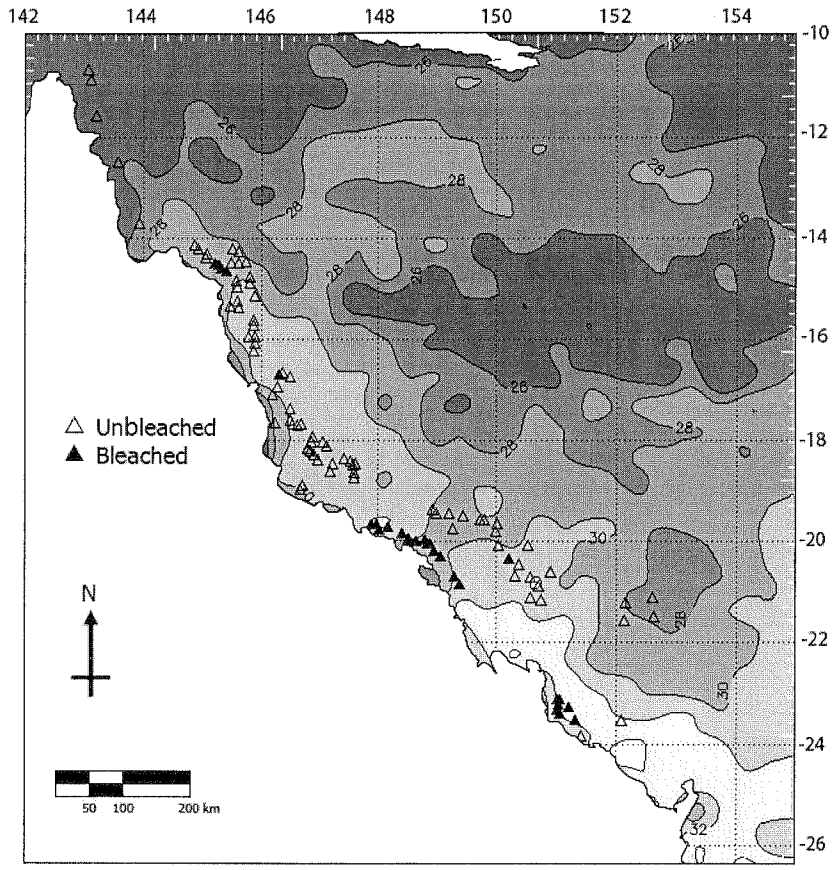

Figure 7.3 Daily average solar irradiance for the period 15 December 2001 to 15 January 2002 (MJ m^{-2} day^{-1}). Also shown are the bleaching sites defined by Berkelmans *et al.* (2004). Open triangles denote less than 10% bleaching, black triangles denote bleaching greater than 60%.

Maximum solar radiation values selected from the days that have the highest solar radiation over the summer 2001/2002 period were examined with the bleaching data of Berkelmans *et al.*, (2004). Figure 7.4 shows the maximum solar radiation experienced by the bleached reefs, sub-divided by the degree of bleaching and whether they are inshore or offshore. The results for the inshore bleached reefs show that the indices of the affected reefs (>1% bleached) were associated with values of maximum daily radiation of over 30 MJ-m^{-2}-day^{-1}. Conversely, the low/no bleached reefs (<1% bleached) experienced maximum daily solar radiation values of ~28 MJ-m^{-2}-day^{-1}. For the offshore reefs, all the bleaching indices are associated with similar levels of maximum daily solar radiation, around 31.5 MJ-m^{-2}-day^{-1}.

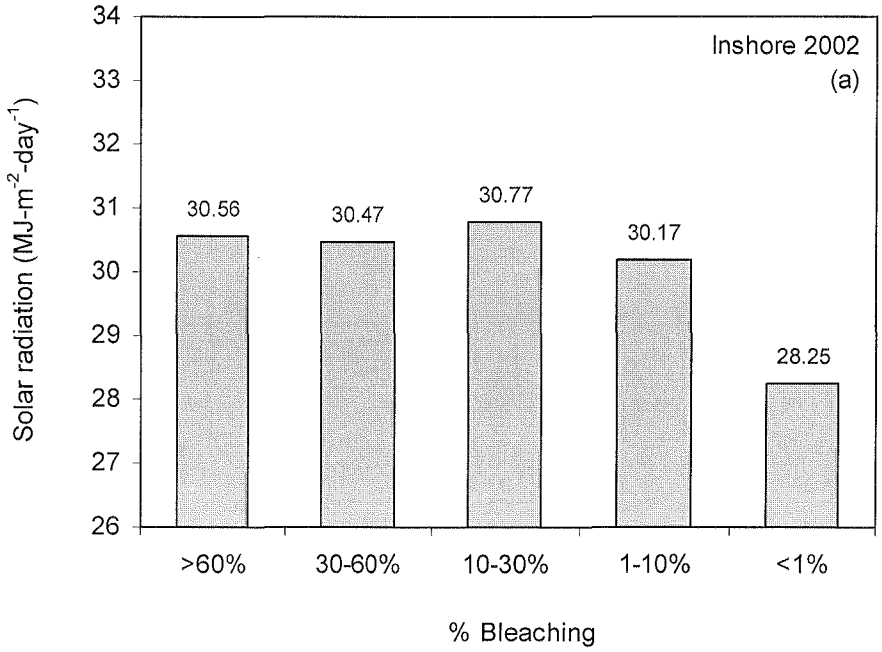

Figure 7.4 Frequency of maximum solar radiation and percentage of bleaching during summer 2001/2002: (a) inshore, (b) offshore.

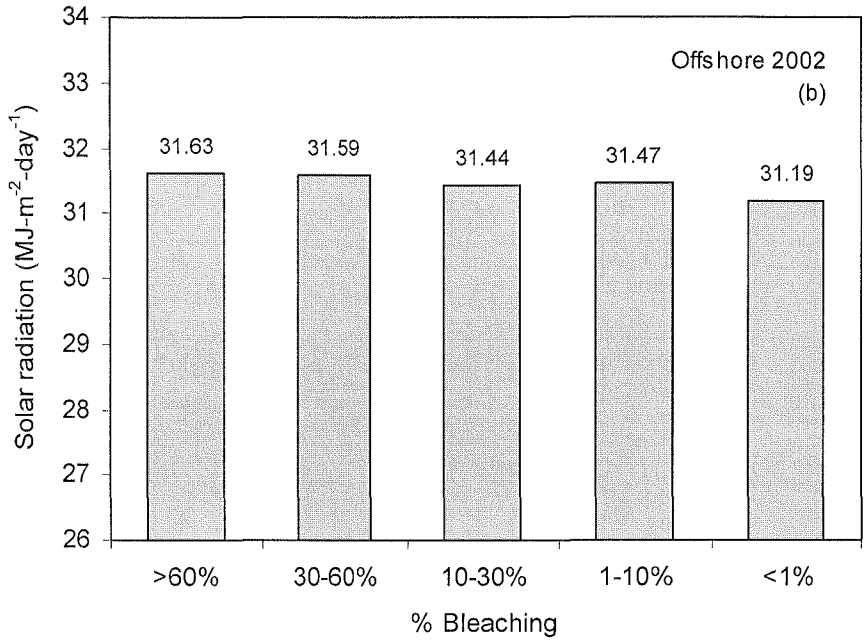

Figure 7.4 Frequency of maximum solar radiation and percentage of bleaching during summer 2001/2002: (a) inshore, (b) offshore (continued).

7.2 The anomaly of maximum solar radiation during the 2002 coral bleaching episode

Differences between maximum daily solar radiation in 2001/2002 and the mean values (over 1995-2005) is next considered. The results in Figure 7.5 show that bleaching at all indices occurs with anomalies larger than 2 MJ-m^{-2}-day^{-1}. For the inshore reefs, the anomaly values have a small decrease toward the low bleaching indices (from 2.74 to 2.64 MJ-m^{-2}-day^{-1}). For the offshore bleached reefs, the four most severe bleaching indices were associated with a similar anomaly values (~3 MJ-m^{-2}-day^{-1}), while the <1% bleached reefs had a much lower anomaly (Figure 7.5).

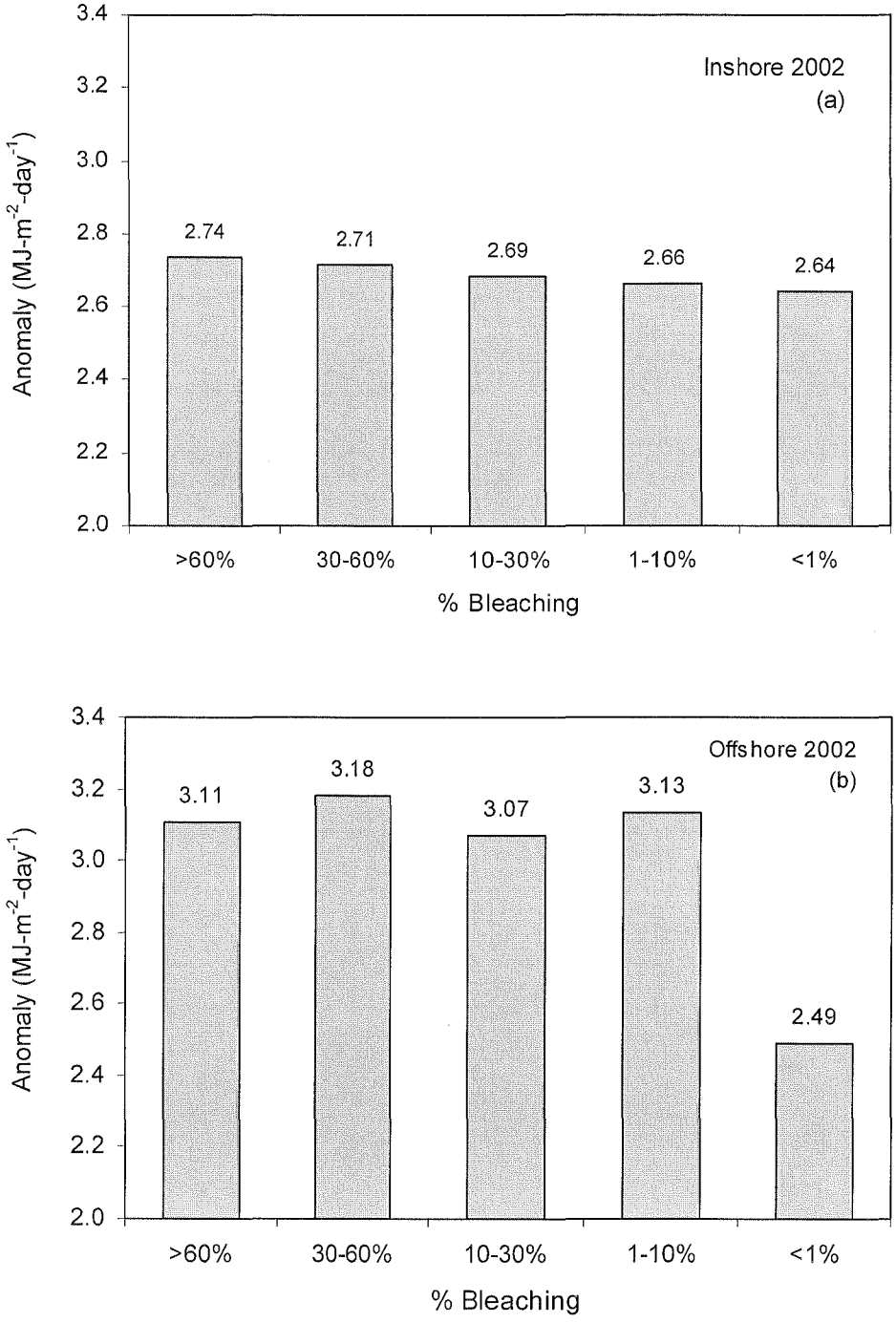

Figure 7.5 Frequency of anomaly solar radiation and percentage of bleaching for the 2001/2002 summer: (a) inshore, (b) offshore.

7.3 Responses of solar radiation and sea surface temperature to coral bleaching

The relationships between solar radiation and bleaching indices shown in the previous sections provide information about solar radiation levels involved in bleaching developments. However, the results were derived for a fixed averaging period of 7 days, and therefore do not contain fine details of bleaching events as a function of time response. Furthermore, sea surface temperature (SST) is always considered as a major effect causing bleaching in corals and, therefore, the damage thresholds of these two variables — SST and solar radiation — must be considered in combination. In order to extend this investigation, this study uses SST data derived from 4-km AVHRR Pathfinder Version 5.0 to analyse the relationships between solar radiation, SST and the 2001/2002 bleaching data. Details of the SST data set are provided in Weller *et al.* (2008).

Plots of SST versus solar radiation for bleached/unbleached reefs are presented for various radiation and temperature averaging periods, consisting of 3/5-day, 1-weekly, 2-weekly and 4-weekly averages. The study gathers the reefs that had extreme to moderate bleaching indices (>60% to 1-10%) into a group called 'bleached reefs', and the reefs which presented low or no bleaching (<1%) are grouped as 'unbleached' reefs. The groups of inshore and offshore reefs are separated on a similar basis. Two-dimensional graphs plotting the relationships between solar radiation and SST over the bleached and unbleached reefs are provided.

Figure 7.6 presents bleaching discriminations between SST and solar radiation for inshore reefs. The graphs show obvious separations along the solar radiation axis, expanding with longer averaging periods. In contrast, discrimination for offshore reefs is mainly along the SST axis (Figure 7.7). Also both inshore and offshore reefs exhibit

the maximum separations at 1-month averaging periods (Figure 7.6 (d) and Figure 7.7 (d)).

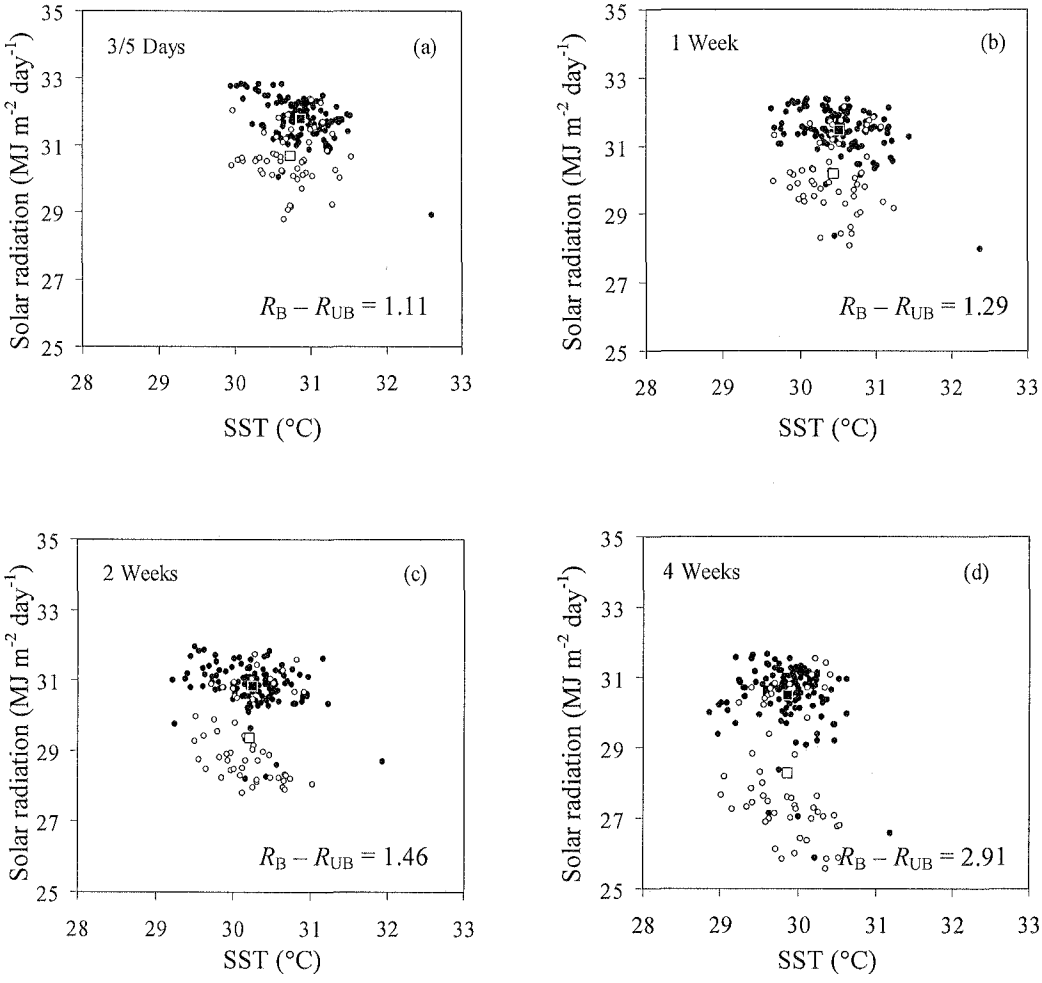

Figure 7.6 Plots of solar radiation vs SST for inshore bleached and unbleached reefs. (a) for maximum 3-day SST and maximum 5-day average solar radiation; (b) maximum 1-week SST and solar radiation; (c) maximum 2-week SST and solar radiation: (d) maximum 4-week SST and solar radiation. Also shown are differences in radiation means for unbleached (R_{UB}) and bleached (R_B) reefs. (black circle = bleached, open circle = unbleached, black square = mean of bleached and open square = mean of unbleached).

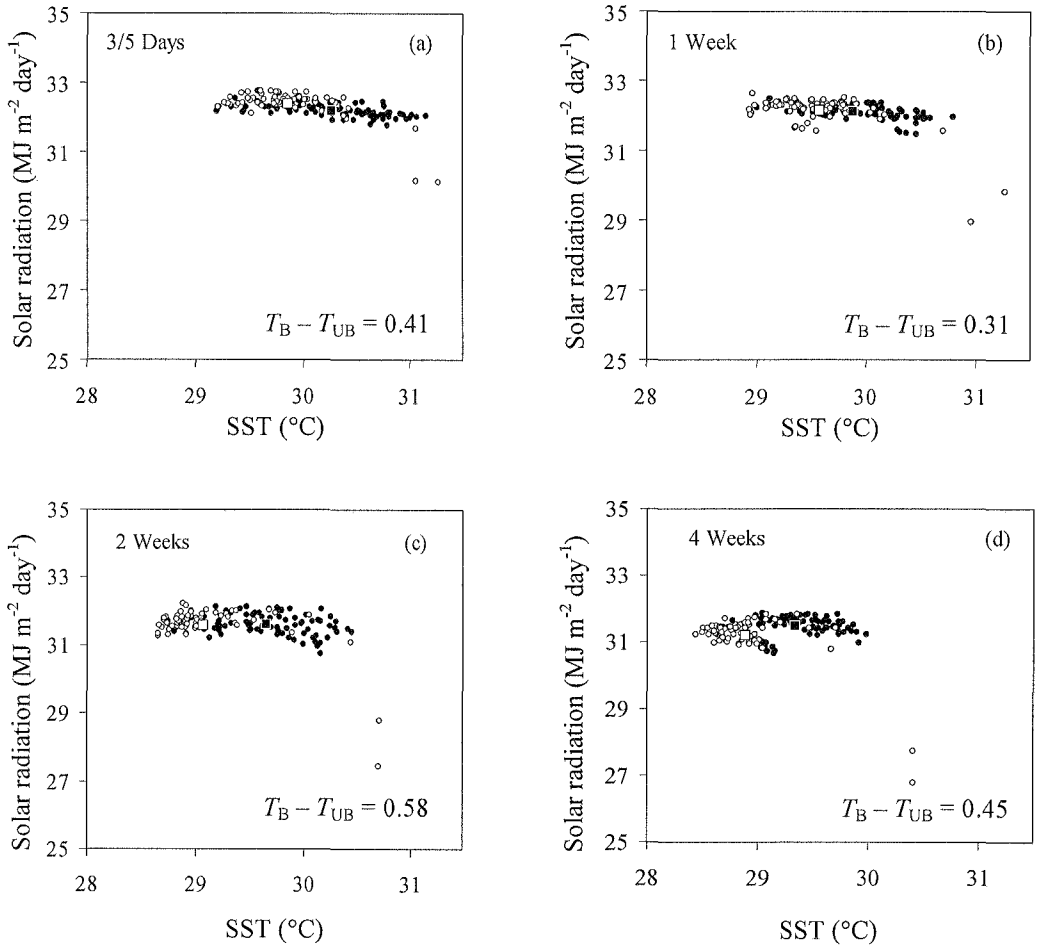

Figure 7.7 Plots of solar radiation vs SST for offshore bleached and unbleached reefs. (a) for maximum 3-day SST and maximum 5-day average solar radiation; (b) maximum 1-week SST and solar radiation; (c) maximum 2-week SST and solar radiation: (d) maximum 4-week SST and solar radiation. Also shown are differences in SST means for unbleached (T_{UB}) and bleached (T_B) reefs. (black circle = bleached, open circle = unbleached, black square = mean of bleached and open square = mean of unbleached).

In order to ensure that the separations between the two groups (bleached and unbleached) are statistically significant and are not obtained from a random sample, *F*-statistic tests were performed on both bleaching groups for all averaging periods. This study uses the two-normal probability distributions described by Sokolnikoff and Sokolnikoff (1941) to examine the separation thresholds of SST and solar radiation. The probability of encountering a value of solar radiation or temperature (x_i) is:

$$P(x_i) = (2/\sqrt{\pi}) \int_0^{x_0} e^{-(x^2/2\sigma)}\, dx \qquad (7.1)$$

where x_i is any element of the series $\{x\}$, $\bar{x}$ is the series mean, x is anomaly at i ($x = x_i - \bar{x}$) and σ is the standard deviation of the series for radiation or SST. In order to define the optimum cutoff points, which differentiate bleached from unbleached reefs, of solar radiation and SST, the threshold (T) is defined as a minimum value of the sum between the two probability curves. That is:

$$T(R) = MIN\left[P_{UB}(\bar{R}_{UB} + \delta R_{UB}) + P_B(\bar{R}_B - \delta R_B)\right] \qquad (7.2)$$

where δR_{UB} and δR_B are differences from the mean of $\bar{R}_B$ and $\bar{R}_{UB}$, respectively. Note that $\bar{R}_B$ is larger than $\bar{R}_{UB}$, so that $(\bar{R}_{UB} + \delta R_{UB})$ and $(\bar{R}_B - \delta R_B)$ are equal.

Table 7.1 presents the results of the *F*-tests, indicating the significances of solar radiation, SST and a combination of both in separating bleached from unbleached reefs. The *P* values shown in Table 7.1 are mostly significant with ($P < 0.01\%$). However, the solar radiation separation for inshore reefs displayed larger *P* values, indicating that the link between solar radiation and bleaching events is stronger. In contrast, SST gave poor

significant levels for discrimination at inshore reefs but it is a good indicator of bleaching events at offshore reefs. The results for the threshold (T) analysis for the monthly timescale (Table 7.2) shows that corals at inshore reefs are likely to suffer bleaching damage at solar radiation in excess of 30.9 MJ-m^{-2}-day^{-1}, with 11% of reefs misclassified as bleached. For offshore reefs, the SST thresholds are dominant, with temperatures in excess of 29 $^{\circ}$C associated with coral bleaching, with a classification error of 24%.

Table 7.1 F ratios and resultant P statistic (in brackets) used as an index of separation between bleached and unbleached sites. Three indices are available, SST, solar radiation and the two combined. Assessment is performed for averaging periods of 3/5 days, and 1, 2 and 4 weeks.

		3/5 days	1 week	2 weeks	4 weeks
SST+RADIATION	Inshore	67.09 (<0.01)	66.01 (<0.01)	73.30 (<0.01)	82.39 (<0.01)
	Offshore	26.25 (<0.01)	10.90 (<0.01)	29.67 (<0.01)	26.45 (<0.01)
	All Reefs	19.80 (<0.01)	17.92 (<0.01)	23.67 (<0.01)	33.52 (<0.01)
RADIATION	Inshore	83.24 (<0.01)	79.43 (<0.01)	86.82 (<0.01)	88.67 (<0.01)
	Offshore	12.57 (<0.01)	0.38 (>0.1)	0.05 (>0.1)	10.24 (<0.01)
	All Reefs	5.85 (0.05>P>0.01)	10.10 (<0.01)	11.30 (<0.01)	21.03 (<0.01)
SST	Inshore	4.91 (0.05>P>0.01)	1.04 (>0.1)	0.47 (>0.1)	0.004 (>0.1)
	Offshore	33.87 (<0.01)	20.10 (<0.01)	69.89 (<0.01)	68.16 (<0.01)
	All Reefs	14.88 (<0.01)	8.75 (<0.01)	15.64 (<0.01)	12.16 (<0.01)

Table 7.2 Statistics for the 2002 bleaching episode using highest monthly average solar radiation and temperature. Numbers in brackets denote the percentage of reefs, bleached or unbleached, misclassified at the threshold value.

	Inshore		Offshore	
	solar radiation (MJ m^{-2} day^{-1})		temperature ($^{\circ}$C)	
	Bleached	Unbleached	Bleached	Unbleached
Threshold	30.9 (11%)	30.9 (28%)	29.1 (24%)	29.1 (24%)
Mean	30.5	28.2	29.3	28.9
Lowest	25.9	25.5	28.6	28.4
Highest	31.6	31.5	30.0	30.4

In summary, the bleaching process is dominated by solar radiation in near-shore areas, while for offshore reefs the bleaching is driven by high water temperature. Inshore reefs are likely to be bleached when solar radiation exceeds 30.9 MJ-m^{-2}-day^{-1}. Conversely, bleaching at offshore reefs would occur at 29.1° C. High currents tend to predominate in outer reefs (Burrage *et al.*, 1996) and this may possibly minimise the impact of warm water temperatures. By contrast, inner reefs receive high solar radiation and low currents. This scenario suggests that both direct and indirect solar radiation effects are affecting the bleaching process in the near-shore reefs (Fitt *et al.*, 2001; Mumby *et al.*, 2001).

This study has linked the spatial distribution of solar radiation and bleaching events which occurred in the GBR near-shore areas. A number of studies have sought to identify the causes of bleaching events using spot measurement or laboratory investigations (Lesser *et al.*, 1990; Kinzie, 1993; Gleason and Wellington, 1993; Brown *et al.*, 1999; Banaszak and Trench, 1995; Warner *et al.*, 1996; Hoegh-Guldberg, 1999; Fitt *et al.*, 2001), but the results were not conclusive due to the general lack of solar radiation measurements over coral reefs. This study uses satellite-derived broadband solar radiation to present a large-scale correlation of bleaching events and solar radiation. Maps presented in this study provide valuable information on spatial patterns of solar irradiance, and should be useful for biologists to have a clear picture of how solar radiation affects bleaching in the region. This study has also established useful background values of solar radiation. Furthermore, the results that are based on the 11-year satellite dataset could be used to forecast the effect of solar radiation on coral reefs in the GBRThe estimations could be developed for near real-time monitoring as long as satellite data is available. The technique could be used as a tool for monitoring bleaching events or any other biological processes over the reefs as well as other NOAA

monitoring programs, such as coral bleaching hotspot, Degree Heating Week (DHW) and Coral Reef Watch (CRW) and Satellite Bleaching Alert (SBA).

Lastly, it is also important to note that the results presented here are linked to a specific geography and time. It is likely that different temperature and light threshold could be obtained in other locations. This technique is suitable for different radiation and temperature thresholds at a variety of locations throughout the world and these data will provide a much more comprehensive picture of the coral bleaching process.

Chapter 8

Conclusion

This study has developed techniques for estimating surface broadband solar radiation and PAR/UVB underwater irradiance. The study area covers the Great Barrier Reef (GBR) region, the north-east coast of Queensland and the Coral Sea (10° S - 26° S, 142° E - 155° E). The satellite-derived Earth-atmosphere reflectivity (α'_{EA}), collected for the period January 1995 to December 2005, was used as input for estimating surface broadband solar radiation. The α'_{EA} data were obtained from three separate satellites — GMS-5, GOES-9 and MTSAT — with a final resolution of approximately 2.3 km (East/West) × 2.7 km (North/South). Underwater UVB and PAR irradiance was estimated using surface irradiance and attenuation coefficients obtained from SeaWiFS. The K_d data, provided at a spatial resolution of 9 km (East/West) × 9 km (North/South), was available for the period January 1998 to December 2005.

Solar radiation was estimated using the Streamer radiative transfer model to create look-up tables (LUT) which contain values of solar irradiance and Earth-atmosphere reflectivity. The configurations set for providing the LUT were based on a tropical atmosphere, with maritime aerosols, cloud height of 2 km and a visibility of 25 km. The values contained in the LUT were created with a wide set of variables including solar zenith angles, cloud fractions, surface albedo, radius of cloud droplets (RAD), liquid water contents (LWC) and thickness (THK) of clouds. At a given pixel, the solar zenith angle, cloud fraction and surface type were determined, and combinations of RAD, LWC and THK that satisfied the satellite-derived α'_{EA} value were deduced. The surface PAR and UVB irradiances were estimated by using a waveband conversion model. This study examined three Monte Carlo models based on studies by

Gordon (1989), Kirk (1991) and Ershova *et al.* (2002) to provide the K_d waveband conversions. The values of K_d obtained from the SeaWiFS instrument were transformed into K_d values for the UVB and PAR spectral regions. Using the Lambert-Beer equation, both UVB and PAR irradiances were able to be estimated at any depth.

Estimates of surface solar radiation were compared to the measurements at Rockhampton, Cairns and Townsville. The daily average comparison gave the highest root-mean square differences of 2.26 MJ-m^{-2}-day^{-1} (12.4%) and 2.85 MJ-m^{-2}-day^{-1} (15.2%) for Rockhampton and Cairns, respectively, and the RMSD values decreased for the longer temporal averages. Comparison of hourly average UVB irradiances collected from the five-year period showed an acceptable agreement with the RMS difference of 17.8 mW-m^{-2} (20%).

Comparisons for underwater solar irradiances were performed on the K_d values. The K_d estimates from SeaWiFS were transformed into values matching the instrumental measurements on Heron Island (305 nm, 315 nm, 320 nm, 340 nm, 380 nm, 395 nm and PAR wavebands). The comparisons between measurement-derived and Monte Carlo-derived K_d showed the best performance with the Gordon model (41.1% RMS difference). The Gordon Monte Carlo model was therefore selected for the underwater estimations.

A long-term climatology and statistics of broadband solar radiation was presented on a spatial and temporal scale over the 11-year period (1995-2005). Overall, a map of solar radiation averaged for the 11 years showed values between 20 MJ-m^{-2}-day^{-1} and 24 MJ-m^{-2}-day^{-1}, with the highest values of solar radiation found in the 18° S - 24° S regions. Highest values of solar radiation were obtained in the southern GBR regions, which showed the highest values of about 30 MJ-m^{-2}-day^{-1} in summer. In contrast, solar radiation was uniformly low in winter, with values around 16 MJ-m^{-2}-day^{-1}. Analysis of inter-annual trends showed small but significant increases in the

regions from 12° S - 18° S. An outstanding feature of solar radiation during summer periods was observed in the 2001/2002 periods, with a large portion of the GBR coastline exhibiting anomalously high values of 29 MJ-m^{-2}-day^{-1}.

Spatial and temporal changes of underwater UVB and PAR irradiances are also presented for the GBR area. The results derived for underwater PAR irradiances at depth of 2.5 m showed high values of PAR for the periods from September to December. At this depth, spatial patterns of the underwater UVB and PAR in near-shore regions exhibit features of very high variations by ~100 mW-m^{-2} and 350 W-m^{-2}, respectively. In open water regions, the underwater UVB and PAR irradiances show a small variation of about 180 mW-m^{-2} and 400 W-m^{-2}, respectively. High UVB and PAR irradiances in excess of 180 mW-m^{-2} and 450 W-m^{-2} are typically seen over a distinct zone between 16° and 24° E in both open water and near-shore regions. It is seen that underwater PAR values were high in early spring before the summer bloom, while high UVB underwater irradiance was occurred between October and March. However, both PAR and UVB irradiances over the reefs were low compared to the lagoons and open water regions. Vertical profiles of both UVB and PAR irradiance show a strong attenuation trend in near-shore regions, while the decreases of the irradiances in open water zones are not progressively substantial. However, the features of these vertical changes can not be presented well in this study as the remote-sensing data used in the estimation is not concerned the vertical turbidity due to CDOM and other suspended organic substances.

In addition to the bleaching events, this study has examined relationships between SST, solar radiation and bleaching events, during the 2002 bleaching episode. For inshore reefs, solar radiation is best at separating bleached from unbleached reefs. In contrast, discrimination in offshore regions is best with SST data. A statistical

analysis yielded optimum thresholds of 30.9 MJ-m^{-2}-day^{-1} and 29.1 $^{\circ}C$ at 4-weekly scales for discriminating bleached from unbleached reefs.

In summary, this study has shown that it is possible to use satellite data to estimate solar radiation both above the water surface and in the water column. The reliability of the techniques used in this thesis were supported with validations against incoming radiation data collected at Rockhampton, Cairns and Townsville, and the water extinction data at Heron Island. The techniques were applied to provide radiation statistics for the region of the Great Barrier Reef. Although solar radiation details can not be provided at the individual reef scale, the technique can be used as a tool for monitoring solar radiation on large temporal and spatial scales, which can help scientists determine the effects of solar radiation on this aquatic ecosystem. It is likely that solar radiation data could provide added accuracy and reliability to bleaching indices such as the one provided by NOAA. However, this study has shown that added bio-geographical factors such as water current, depth and water turbulence could also be important factors affecting the index accuracy. These issues could form important areas for future research.

References

Aas, E., J. Hokedal, and K. Sorensen, Spectral backscattering coefficient in coastal waters, *International Journal of Remote Sensing*, **26** (2), 331-343, 2005.

Ammenberg, P., P. Flink, and T. Lindell, Bio-optical modeling combined with remote sensing to assess water quality, *International Journal of Remote Sensing*, **23** (8), 1621-1638, 2002.

Anderson, D.T., *Invertebrate Zoology*, Oxford University Press, 2001.

Ångström, A., On the atmospheric transmission of sun radiation, *Geografiska Annaler*, **2**, 130-159, 1930.

Atwater, M.A., and P.S. Brown, Numerical computation of the latitudinal variation of solar radiation for an Atmosphere of varying opacity, *Journal of Applied Meteorology*, **13**, 289-297, 1974.

Banas, D., P. Grillas, I. Auby, F. Lescuyer, E. Coulet, J. Moreteau, and B. Millet, Short time scale changes in underwater irradiance in a wind-exposed lagoon (Vaccarès lagoon): efficiency of infrequent field measurements of water turbidity or weather data to predict irradiance in the water column, *Hydrobiologia*, **551,** 3-16, 2005.

Barker, H.W., and J.A. Davies, Surface albedo estimations from Nimbus-7 ERB data and Two-Stream Approximation of the radiative transfer equation, *Journal of Climate*, **2**, 409-418, 1989.

Barton, A.D., K.S. Casey, Climatological context for large-scale coral bleaching, *Coral Reefs*, **24**, 536-554, 2005.

Berkelmans, R., and B.L. Willis, Seasonal and local spatial patterns in the upper thermal limits of corals on the inshore Central Great Barrier Reef, *Coral Reefs*, **18**, 219-228, 1999.

Berkelmans, R., and J.K. Oliver, Large-scale bleaching of corals on the Great Barrier Reef, *Coral Reefs*, **18**, 55-60, 1999.

Berkelmans, R., G. De'ath, S. Kininmouth, and W.J. Skirving, A comparison of the 1998 and 2002 coral bleaching events on the Great Barrier Reef: spatial correlation, pattern, and predictions, *Coral Reefs*, **23**, 74-83, 2004.

Boss, E., J. R. V. Zaneveld, The effect of bottom substrate on inherent optical properties: Evidence of biogeochemical processes, *Limnology and Oceanography*, **48**(1, part 2), 346–354, 2003.

Brown, B.E., and Suharsono, Damage and recovery of coral reefs affected by El Niño related seawater warming in the Thousand Island, Indonesia, *Coral Reefs*, **8**, 163-170, 1990.

Brown, B.E., Coral bleaching: causes and consequences, *Coral Reefs*, **16**, 129-138, 1997.

Brown, B.E., I. Ambarsari, M.E. Warner, W.K. Fitt, R.P. Dunne, S.W. Gibb, and D.G. Cummings, Diurnal changes in photochemical efficiency and xanthophylls concentrations in shallow water reef corals: evidence for photoinhibition and photoprotection, *Coral Reefs*, **18**, 99-105, 1999.

Buiteveld, H., A model for calculation of diffuse light attenuation (PAR) and secchi depth, *Netherlands Journal of Aquatic Ecology*, **29** (1), 55-65, 1995.

Bukata, P., H. Jerome, Ya. Kondratyev, and V. Pozdnyakov., *Optical Properties and Remote Sensing of Inland and Coastal Waters,*CRC Press, 1995.

Call, K.A., J.T. Hardy, and D.O. Wallin, Coral reef habitat discrimination using multivariate spectral analysis and satellite remote sensing, **24**, 2627-2639, 2003.

Cano, D., J.M. Monget, M. Albuisson, H. Gulllard, N. Regas, and L. Wald, A method for the determination of the global solar radiation from meteorological satellite data. *Solar Energy* **37**, 31-39, 1986.

Carder, K. L., C. Liu, Z., Lee, D. C., English, J. Patten, F. R. Chen, J. E. Ivey, and C. O. David, Illumination and turbidity effects on observing faceted bottom elements with uniform Lambertian albedos, *Limnology and Oceanography*, **48**(1, part 2), 355–363, 2003.

Casiccia, C., F. Zamorano, and A. Hernández, Erythemal irradiance at the Magellan's region and Antarctic ozone hole 1999-2005, *Atmósfera,* **21**(1), 1-12, 2008.

Chandrasekhar, S., *Radiative Tracsfer*, Oxford University Press, London, 1950.

Chen, Y., A.D. Del Genno, J. Chen, The Tropical Atmospheric El Niño Signal in Satellite Precipitation Data and a Global Climate Model, *Journal of Climate*, **20**, 3580-3601, 2007.

Conde, D., L. Aubriot, and R. Sommaruga, Changes in UV penetration associated with marine intrusions and freshwater discharge in a shallow coastal lagoon of the southern Atlantic Ocean, *Marine Ecology Progress Series*, **207**, 19–31,2000.

Corlett, G.K., and P.S. Monks, A comparison of total column ozone values derived from the Global Ozone Monitoring Experiment (GOME), the Tiros Operational Vertical Sounder (TOVS), and the Total Ozone Mapping Spectrometer (TOMS), *Journal of Atmospheric Science*, **58**, 1103-1116, 2001.

Crisp, D., The Spectral Mapping Atmospheric Radiative Transfer (SMART) Model, *Geophysical Research Abstracts*, 8, 08209, 2006.

Dai, A., Recent Climatology, Variability, and Trends in Global Surface Humidity, *Journal of Climate*, **19**, 3589-3606, 2006.

Daly, M., D.G. Fautin, and V.A. Cappola, Systematics of the Hexacorallia (Cnidaria: Anthozoa), *Zoological Journal of the Linnean Society*, **139**, 419-437, 2003.

Darnell, W.L., W.F. Staylor, S.K. Gupta, and F.M. Denn, Estimation of surface insolation using Sun-synchronous satellite data, *Journal of Climate*, **1**, 820-835, 1988.

Dedieu, G., P.Y. Deschamps, and Y.H. Kerr, Satellite estimation of solar irradiance at the surface of the Earth and of surface albedo using a physical model applied to Meteosat data, *Journal of Climate and Applied Meteorology*, **26**, 79-87, 1987.

De Gruijl, F.R., Health Effects from Solar UV Radiation, *Radiation Protection Dosimetry*,**72**, 177–196, 1997.

De Gruijl, F.R., Biological action spectra, *Radiation Protection Dosimetry*, **91**, 57–63, 2000.

DeLuisi, J., Atmospheric ultraviolet radiation scattering and absorption, In *Solar Ultraviolet Radiation: Modelling, Measurements and Effects*, Springer-Verlag, New York, 65-83, 1997.

Dewitte, S., D. Crommelynck, S. Mekaoui, and A. Joukoff, Measurement and uncertainty of the long-term total solar irradiance trend, *Solar Physics*, **224**, 209-216, 2004.

Diak, G.R., and C. Gautier, Improvements to a simple physical model for estimating insolation from GOES data, *Journal Climate of Applied Meteorology*, **22**, 505-508, 1983.

DiToro, D.M., Optics of Turbid Estuarine Waters: Approximations and Applications, *Water Research* **12**, 1059-1068, 1978.

Dollar, S.J.. and R.W. Grigg, Impact of a kaolin clay spill on a coral reef in Hawaii. *Marine Biology*, **65**, 269-276, 1981.

Dunne, R.P., and B.E. Brown, Penetration of solar UVB radiation in shallow tropical waters and its potential biological effects on coral reefs; results from the central Indian Ocean and Andaman Sea, *Marine Ecology Progress Series*, **144,** 109-118, 1996.

Dunne, R.P., and B.E. Brown, The influence of solar radiation on bleaching of shallow water reef corals in the Adaman Sea, 1993-1998, *Coral Reefs*, **20**, 201-210, 2001.

Endean, R., *National Library of Australia Cataloguing-in-Publication data*, University of Queensland Press, 1982.

Ershova, S.V., O.V. Kopelevich, S.V. Sheberstov, A method for estimating the penetration of solar radiation into the water of the Arctic Seas using satellite data: the case of a totally overcast sky, *Oceanology*, **42** (1), 17-26, 2002.

Feng, J, and H.G. Leighton, Broadband solar irradiance from visible band measurements: a method based on ScaRaB observation and model simulations, *International Journal of Remote Sensing*, **26** (22), 5125-5148, 2005.

Fitt, W.K., B.E. Brown, M.E. Warner, and R.P. Dunne, Coral bleaching: interpretation of thermal tolerance limits and thermal thresholds in tropical corals, *Coral Reefs*, **20**, 51-65, 2001.

France, S.C., P.E. Rosel, J.E. Agenbroad, L.S. Mullineaux, and T.D. Kocher, DNA sequence variation of mitochondrial large-subunit rRNA provides support for a two subclass organization of the Anthozoa (Cnidaria), *Molecular Marine Biology and Biotechnology*, **5** (1), 15-28, 1996.

Frohlich, C., Observation of irradiance variations, *Space Science Reviews*, **94**, 15-24, 2000.

Frouin, R., D.W. Lingner, and C. Gautier, A simple analytical formula to compute clear sky total and photosynthetically available solar irradiance at the ocean surface, *Journal of Geophysical Research*, **94** (C7), 9731-9742, 1989.

Frouin, R., and B. Chertock, A technique for global monitoring of net solar irradiance at the ocean surface. Part I: model, *Journal of Applied Meteorology*, **31**, 1056-1066, 1992.

Gateno, D., A. Israel, Y. Barki, and B. Rinkevich, Gastrovascular Circulation in an Octocoral: Evidence of Significant Transport of Coral and Symbiont Cells, *The Biological Bulletin*, **194** (2), 178-186, 1998

Gautier, C., A simple physical model to estimate incident solar radiation at the surface from GOES satellite data, *Journal of Applied Meteorology*, **19**, 1005-1012, 1980.

Gautier, C., Surface solar irradiance in the central pacific during tropical heat: comparisons between in situ measurements and satellite estimates, *Journal of Climate*, **1**, 600-608, 1988.

Gjerstad., K. I., J. J. Stamnes, B. Hamre, J. K. Lotsberg, B. Yan, and K. Stamnes, Monte Carlo and Discrete-Ordinate Simulations of Irradiances in the Coupled Atmosphere-Ocean System, *Applied Optics*. **42**, 2609-2622, 2003.

Ghan, S.J., and T. Shippert, physically based global downscaling: climate change projections for a full century, *Journal of Climate*, **19**, 1589-1604, 2006.

Gleason, D.F., and G.M. Wellington, Ultraviolet radiation and coral bleaching, *Nature*, **365**, 836-838, 1993.

Glynn, P.W., and L. D'Croz, Experimental evidence for high temperature stress as the cause of El Niño-coincident coral mortality, *Coral Reefs*, **8**, 181-191, 1990.

Gobron, N., B. Pinty, M. M. Verstraete, A new approach to characterize global land surface, In *Advances in Global Change Research*, Springer Netherlands, 143-150, 2000.

Gordon, H.R., Simple calculation of the diffuse reflectance of the ocean, *Applied Optics*. **12**, 2803-2804, 1973.

Gordon, H.R., O.B. Brown, and M.M. Jacobs, Computed relationships between the inherent and apparent optical properties of a flat homogeneous ocean, *Applied Optics*, **14**, 417-427, 1975.

Gordon, H.R., Radiative transfer in the ocean: A method for determination of absorption and scattering properties, *Applied Optics*, **15**, 261 l-2613, 1976.

Gordon, H.R., and A.Y. Morel, *Remote Assessment of Ocean Color for Interpretation of Satellite Visible Imagery: A Review*, Springer-Verlag, New York, 1983.

Gordon, H.R., O.B. Brown, R.H. Evans, J.W. Brown, R.C. Smith, K.S. Baker, and D.K. Clark, A semianalytic radiance model of ocean color, *Journal of Geophysical Research*, **93**, 10909-10924, 1988.

Gordon, H.R., Can the Lambert-Beers law be applied to the diffuse attenuation coefficient of ocean water?, *Limnology and Oceanography*, **34**, 1389-1409, 1989.

Gordon, H.R., Absorption and Scattering Estimates from Irradiance Measurements: Monte Carlo Simulations, *Limnology and Oceanography*, **36** (4), 769-777, 1991.

Gray, L., W. Norton, C. Pascoe, and A. Charlton, A possible influence of equatorial winds on the september 2002 Southern Hemisphere sudden warming event, *Journal of the Atmospheric Sciences*, **62** (3), 651-665, 2005.

Gregg, W. W., and K. L. Carder, A simple spectral solar irradiance model for cloudless maritime atmospheres, *Limnology and Oceanography*, **35**(8), 1657-1675, 1990.

Hansen, L.B., N. Kamstrup, and B.U. Hansen, Estimation of net short-wave radiation by the use of remote sensing and a digital elevation model — a case study of a high arctic mountainous area, *International Journal of Remote Sensing*, **23** (21), 4699-4718, 2002.

Harriott, V.J., Mortality rates of scleractinian corals before before and during a mass bleaching event, *Marine Ecology*, **21**, 81-88, 1985.

Harrison, A. W., and C. A. Coombes, An opaque cloud cover model of sky short wavelength. radiance, *Solar Engergy*, **41** (4), 387-392, 1988.

Hay, E., The mesoscale distribution of solar radiation at the earth's surface and the ability of the satellite to resolve it. In *Satellite and forecasting of solar radiation*, 76-85, 1981.

Herman, J.R., and P.K. Bhartia, O. Torres, C. Hsu, and C. Seftor, Global distribution of UV-absorbing aerosols from Nimbus 7/TOMS data, *Journal of Geophysical Research*, **102** (D14), 16,911-16,922, 1997.

Hoegh-Guldberg, O., Climate change, coral bleaching and the future of the world's coral reefs. *Marine and Freshwater Research*, **50**, 839-866, 1999.

Hoge, F.E., and P. E. Lyon. Satellite retrieval of inherent optical properties by linear matrix inversion of oceanic radiance models: an analysis of model and radiance measurement errors. *Journal of Geophysical Research*, **101**, 16,631– 16,648, 1996.

Hoge F.E., and P.E. Lyon, Satellite observation of Chromophoric Dissolved Organic Matter (CDOM) variability in the wake of hurricanes and typhoons, *Geophysical Research Letter*, **29** (19), 2002.

Hoinka, K.P., Temperature, Humidity, and Wind at the Global Tropopause, *Monthly Weather Review*, **127**, 2248-2265, 1999.

Højerslev, N.K., Practical sea-water algorithms for fundamental bio-optical and remote sensing quantities, *International Journal of Remote Sensing*, **25** (7-8), 1539-1543, 2004.

Hooker, B., E. Wayne, C. Feldman, W. Gregg, and R. Firestone, *SeaWiFS Technical Report Series*, Vol.1, NASA Goddard Space Flight Center, 1992.

Hopley, D., G. Smithers, and E. Parnell, *The Geomorphology of the Great Barrier Reef*, Cambridge University Press, 2007.

Iqbal, M., *An Introduction to Solar Radiation*, Academic Press, 1982.

Isaksen, I.S.A, Stratospheric ozone depletion and UV-B changes, In *Solar Ultraviolet Radiation: Modelling, Measurements and Effects*, Springer-Verlag, New York, 13-21, 1997.

Islam, R., and R.H.B. Exell, Solar radiation mapping from satellite image using a low cost system, *Solar Energy*, **56** (3), 225-237, 1996.

Jerome, J.H., R.P. Bukata, and J.E. Burton. Utilizing the components of vector irradiance to estimate the scalar irradiance in natural waters. *Applied Optics*, **27**, 4012-4018, 1988.

Jiang, S., K. Stamnes, W. Li, and B. Hamre, Enhanced solar irradiance across the atmosphere-sea ice interface: a quantitative numerical study, *Applied Optics*, **44**, 2613-2625, 2005.

Jin, Z., and K. Stamnes, Radiative transfer in nonuniformly refracting layered media: atmosphere-ocean system, *Applied Optics*, **33**, 431-442, 1994.

Jin, Z., T.P. Charlock, and K. Rutledge, Analysis of broadband solar radiation and albedo over the ocean surface at COVE, *Journal of Atmospheric and Oceanic Technology*, **19**, 1585–1601, 2002.

Jin, Z., T.P. Charlock, W.L. Smith Jr., and K. Rutledge, A parameterization of ocean surface albedo, *Geophysical Research Letters*, **31**, L22301, doi: 10.1029/2004 GL021180.

Jokiel, P.L., and S.L. Coles, Response of Hawaiian and other Indo-Pacific reef corals to elevated reef temperatures, *Coral Reefs*, **8**, 155-162, 1990.

Jones, R.J., O. Hoegh-Guldberg, A.W.D. Larkum, and U. Schreiber, Temperature-induced bleaching of corals begins with impairment of the CO_2 fixation mechanism in zooxanthellae, *Plant, Cell and Environment*, **21**, 1219-1230, 1998.

Jones, R.J., and O. Hoegh-Guldberg, Diurnal changes in the photochemical efficiency of the symbiotic dinoflagellates (Dinophyceae) of corals: photoprotection, photoinactivation and the relationship to coral bleaching, *Plant, Cell and Environment*, **24**, 89-99, 2001.

Kandirmaz, H.M., L. Yegingil, V. Pestemalci, and N. Emrahoglu, Daily global solar radiation mapping of Turkey using Meteosat satellite data, *International Journal of Remote Sensing*, **25** (11), 2159-2168, 2004.

Key, J., and A. J. Schweiger, Tools for atmospheric radiative transfer: Streamer and FluxNet, *Computers and Geosciences*, **24**(5), 443-451, 1998.

Key, J., *Streamer User's Guide*, Cooperative Institute for Meterological Satellite Studies, University of Wisconsin, 2001.

Kirk, J.T.O., A Monte Carlo study of the nature of the underwater light field in, and the relationships between optical properties of, turbid yellow waters. *Australian Journal of Marine and Freshwater Research*, **32**, 517–532, 1981.

Kirk, J.T.O., Attenuation of solar radiation in scattering-absorbing waters: a simplified procedure for its calculation, *Applied Optics*, **23**, 3737-3739, 1984.

Kirk, J.T. O., *Light and Photosynthesis in Aquatic Ecosystems*, Cambridge University Press, 1994.

Koelemeijer, R.B.A., and P. Stammes, Validation of Global Ozone Monitoring Experiment cloud fractions relevant for accurate ozone column retrieval. *Journal of Geophysical Research*, **104D**, 18,801-18,804, 1999.

Kuwahara, V.S., T. Toda, K. Hamasaki, T. Kikuchi, and S. Taguchi, Variability in the Relative Penetration of Ultraviolet Radiation to Photosynthetically Available Radiation in Temperate Coastal Waters, Japan, *Journal of Oceanography*, **56**, 399-408, 2000.

Kyle, H.L., D.V. Hoyt, and J.R. Hickey, A review of the Nimbus-7 ERB solar data set, *Solar Physics*, **152**, 9-12, 1994.

Kylling, A., A.F. Bais, M. Blumthaler, J. Schreder, C.S. Zerefos, and E. Kosmidis, Effect of aerosols on solar UV irradiances during the Photochemical Activity and Solar Ultraviolet Radiation campaign, *Journal of Geophysical Research*, **103** (20), 26051-26060, 1998.

Laine, V., A. Venäläinen, M. Heikinheimo, and O. Hyvärinen, Estimating of surface solar global radiation from NOAA AVHRR data in high latitudes, *Journal of Applied Meteorology*, **38** (12), 1706-1719, 1999.

Leckner, B., The spectral distribution of solar radiation at the Earth's surface-elements of a model, *Solar Energy*, **20**, 143-150, 1978.

Lee, Z. P., K. L. Carder, R. G. Steward, and T. G. Peacock, An empirical algorithm for light absorption by ocean water based on color, *Journal of Geophysical Research*, **103** (C12), 27,967-27,987, 1998.

Lee, Z. P., K. L. Carder, and R. A., Arnone Deriving inherent optical properties from water color: A multi-band quasi-analytical algorithm for optically deep waters, *Applied Optics*, **41**, 5755–5772, 2002.

Lee, Z. P., and J. Sandidge, Ocean-color inversion: a combined approach by analytical solution and neural net. *Ocean Remote Sensing and Imaging*, SPIE5155, 153–161, 2003.

Lenoble, J., *Radiative transfer in scattering and absorbing atmosphere: standard computational procedure*, A. Deepak Publishing, 1985.

Liou, K.N., *An introduction to atmospheric radiation*, Academic Press, 2002.

Liu, C. C., J. D. Woods, and C. D. Mobley, Optical model for use in oceanic ecosystem models, *Applied Optics*, **38**, 4475-4485. 1999.

Liu, C. C., R.L. Miller, K.L. Carder, Z. Lee, E.J. D'Sa, and J.E. Ivey, Estimating the underwater light field from remote sensing of ocean color, *Journal of Oceanography*, **62**, 235-248, 2006.

Lough, J.M., Climate variation and El Niño-Southern Oscillation events, on the Great Barrier Reef: 1958 to 1987, *Coral Reefs*, **13**, 181-195, 1994.

Lough, J.M., Coastal climate of northwest Australia and comparisons with the Great Barrier Reef: 1960 to 1992, *Coral Reefs*, **17**, 351-367, 1998.

Lu, P., H. Zhang, and J. Li, A comparison of two-stream DISORT and Eddington radiative transfer schemes in a real atmospheric profile, *Journal of Quantitative Spectroscopy and Radiative Transfer*, In press, doi:10.1016/j.jqsrt.2008.09.009, 2008.

Marchand, M., S. Bekki, A. Pazmino, F. Lefèvre, and S. Godin-Beekmann, Model simulations of the impact of the 2002 Antarctic ozone hole on the midlatitudes, *Journal of the Atmospheric Sciences*, **62** (3), 871-882, 2005.

Mayer, B., G. Seckmeyer, and A. Kylling, Systematic long-term comparison of spectral UV measurements and UVSPEC modeling results. *Journal of Geophysical Research.* **102** (D7), 8755–8767, 1997.

Madronich, S., and S. Flocke, Theoretical estimation of biologically effective UV radiation at the Earth's surface, In *Solar ultraviolet radiation: modelling, measurements and effects*, Springer-Verlag, New York, **52**, 23-48, 1997.

McKinlay, A., F., and B.L. Diffey, A reference action spectrum for ultra-violet induced erythema in human skin. In *Human Exposure to Ultraviolet Radiation: Risks and Regulations*. W.F. Passchier and B.F.M. Bosnjakovich, eds. International Congress Series. pp. 83-87. 1987.

McKenzie, R., D. Smale, and M. Kotkamp, Relationship between UVB and erythermally weighted radiation, *Photochemical and Photobiological Sciences*, **3**, 252-256, 2004.

Meerkoetter R., B. Wissinger, and G. Seckmeyer, Surface UV from ERS-2/GOME and NOAA/AVHRR Data: A Case Study, *Geophysical Research Letters*, **24** (15), 1939–1942, 1997.

Meteorological Satellite Center, The GMS User's Guide, 1997.

Mobley, C. D., B. Gentili, H. R. Gordon, Z. Jin, G. W. Kattawar, A. Morel, P. Reinersman, K. Stamnes, and R. H. Stavn, Comparison of numerical models for computing underwater light fields, *Applied Optics*, **32**, 7484-7504, 1993.

Mobley, C. D., and D. Stramski, Effect of microbial particles on oceanic optics: Methodology for radiative transfer modeling and example simulation, *Limnological Oceanograhy*, **42** (3), 550-560, 1997.

Mobley, C. D., Estimating of the remote-sensing reflectance from above-surface measurements. *Applied Optics*, **38** (36), 7442-7445, 1999.

Mobley, C. D., Radiative Transfer in the Ocean, In *Encyclopedia of Ocean Science*, Academic Press, 2001.

Mobley, C. D., H. Zhang, and K. J. Voss, Effect of optically shallow bottom on upwelling radiances: Bidirectional reflectance distribution function effects, *Limnological Oceanograhy* , **48**(1, part 2), 337–345, 2003.

Mobley, C. D., and L. K. Sundman, Effects of optically shallow bottoms on upwelling radiances: Inhomogeneous and sloping bottoms, *Limnological Oceanograhy*, **48**(1, part 2), 329–336, 2003.

Morel, A. Light and marine photosynthesis: a spectral model with geochemical and climatological implications. *Progress in Oceanography*, **26**, 263–306, 1991.

Mumby, P.J., J.R.M. Chisholm, A.J. Edwards, S. Andrefouet, and J. Jaubert, Cloudy weather may have saved Society Island reef corals during the 1998 ENSO event, *Marine Ecology Progress Series*, **222**, 209-216, 2001.

Nakajima, T., M. Tsukamoto, Y. Tsushima, A. Numaguti, and T. Kimura, Modeling of the radiative process in an atmospheric general circulation model, *Applied Optics*, **39**, 4869-4878, 2000.

Neale, P.J., R.F. Davis, and J.J. Cullen, Interactive effect of ozone depletion and vertical mixing on photosynthesis of Antarctic phytoplankton, *Nature*, **392**, 585-589, 1998.

Nunez, M., A satellite-based solar energy monitoring system for Tasmania, Australia. *Solar Energy*, **39**, 439–444, 1987.

Nunez, M., Solar energy statistic for Australian capital regions, *Solar Energy*, **44** (6), 343-354, 1990.

Nunez, M., The development of a satellite-based insolation model for the tropical western Pacific Ocean, *International Journal of Climatology*, **13**, 607-627, 1993.

Nunez, M., J.D. Kalma, Satellite Mapping of the Surface Radiation Budget, In *Advances in Bioclimatology*, Springer, Stanhill, G. (ed), Germany, 63-124, 1995.

Nunez, M., K. Michael, D. Turner, M. Wall, and C. Nilsson, A satellite-based climatology of UV-B irradiance for Antarctic coastal regions, *International Journal of Climatology*, **17**, 1029-1054, 1997.

O'Reilly, J.E., S. Maritorena, B.G. Mitchell, D.A. Siegel, K.L. Carder, S.A. Garver, M. Kahru, and C. McClain, Ocean color chlorophyll algorithms for SeaWiFS, *Journal of Geophysical Research*, **103** (C11), 24,937-24,053, 1998.

Paltridge, G.W., and C.M.R., Platt, *Radiative Processes in Meteorology and Climatology*, Elsevier Publishing, 1976.

Park, S. and C. B. Leovy, Marine low-cloud anomalies associated with ENSO, *Journal of Climate*, **17**, 3348-3469, 2004

Pinker, R.T., and J.A. Ewing, Modeling surface solar radiation: model formulation and validation, *Journal of Climate and Applied Meteorology*, **25** (5), 389-401, 1985.

Pinker, R.T., and I. Laszlo, Modeling surface solar irradiance for satellite applications on a global scale, *Journal of Applied Meteorology*, **31**, 194-211, 1992.

Plass, G. N., and G. W. Kattawar, Radiative Transfer in an Atmosphere-Ocean System, *Applied Optics*, **8**, 455-466, 1969.

Plass, G. N., and G. W. Kattawar, Monte Carlo Calculations of Radiative Transfer in the Earth's Atmosphere-Ocean System: I. Flux in the Atmosphere and Ocean, *Journal of Physical Oceanography*, **2**(2), 139–145, 1972.

Potter, G.L., R.D. Cess, P. Minnis, E.F. Harrison, and V. Ramanathan, Diurnal variability of the planetary albedo: an appraisal with satellite measurements and general circulation models, *Journal of Climate*, **1**, 233-239, 1988.

Prieur, L., and A. Morel, Etude théorique du régime assymptotique. Relations entre caractéristqiues optiques et coefficient d'extinction relatif à la pénétration de la lumière du jour. *Cahiers Océanographiques*, **23**, 35-47, 1971.

Prieur, L., and S. Sathyendranath, An optical classification of coastal and oceanic waters based on the specific spectral absorption curves of phytoplankton pigments, dissolved organic matter, and other particulate materials. *Limnological Oceanograhy*, **26**, 671–689, 1981.

Puotinen, M.L., T.J. Done, and W.C. Skelly, *An atlas of tropical cyclones in the Great Barrier Reef regions, 1969-1997*, CRC Reef Research Centre, technical report No. 19., Townsville, 1997.

Roesler, C., and M.J. Perry, In situ phytoplankton absorption, fluorescence emission, and particulate backscattering spectra determined from reflectance, *Journal of Geophysical Research*, **100** (C7), 13,279-13,294, 1995.

Ronald, J., and V. Zaneveld, An asymptotic closure theory for irradiance in the sea and its inversion to obtain the inherent optical properties, *Limnological Oceanograhy*, **34** (8), 1442-1452, 1989.

Schanz, F., P. Zenn, and Z. Dubinsky, Light Absorption by Phytoplankton and the vertical light attenuation: ecological and physiological significance, *Oceanography and Marine Biology: an Annual Review*, **35**, 71-95, 1997.

Schmetz, J., Retrieval of surface radiation fluxes from satellite data, *Dynamics of Atmospheres and Oceans*, **16**, 61-72, 1991.

Schubert, H., S. Sagert, and R.M. Forster, Evaluation of the different levels of variability in the underwater light field of a shallow estuary, *Helgoland Marine Research*, **55**, 12-22, 2001.

Scoffin, T.P., and A.W. Tudhop, Sedimentary environments of the Central Region of the Great Barrier Reef of Australia, *Coral Reefs*, **4**, 81-93, 1985.

Simon, P.C., Extraterrestrial solar irradiance in the near and medium UV ranges, In *Solar Ultraviolet Radiation: Modelling, Measurements and Effects*, Springer-Verlag, New York, 1-12, 1997.

Smith, R.C., and K.S. Baker, Optical properties of the clearest natural waters (200-800nm), *Applied Optics*, **20** (2), 177-184, 1981.

Smith, R.C., C.R. Booth, and J.L. Star, Oceanographic biooptical profiling system, *Applied Optics*, **23** (16), 1984.

Sokolnikoff, I.S., and E.S. Sokolnikoff, *Higher mathematics for engineers and physicists*, McGraw-Hill Book Company, 1941.

Solanki, S.K., and N.A. Krivova, Solar irradiance variations: from current measurements to long-term estimates, *Solar Physics*, **224**, 197-208, 2004.

Spillane, M.C., and D.M. Doyle, Final result for STREX and JASIN photoanalyses with preliminary search for whitecap algorithm. In *Whitecaps and the marine atmosphere, Report 5*, Galway, Ireland: University Collage, 8-27, 1983.

Spinrad, R.W., K.L. Carder, and M.J. Perry, *Ocean Optics*, Oxford University Press, New York, 1994.

Stambler, N., C. Loverngreen, and M.M. Tilzer, The underwater light field in the Bellingshausen and Amundsen Seas (Antarctica), *Hydrobiologia*, **344**, 41-56, 1997.

Stamnes, K., S. Tsay, W. Wiscombe, and K. Jayaweera, Numerically stable algorithm for discrete-ordinate-method radiative transfer in multiple scattering and emitting layered media, *Applied Optics*, **27**, 2502-2509, 1988

Stamnes, K., S.C. Tsay, W.J. Wiscombe, and I. Laszlo, DISORT, A General-Purpose Fortran Program for Discrete-Ordinate-Method Radiative Transfer in Scattering and Emitting Layered Media: Documentation of Methodology, *Report available from ftp://climate.gsfc.nasa.gov/pub/wiscombe/Multiple Scatt/*, 2000.

Stamnes, K., Transfer of ultraviolet light in the atmosphere and ocean: a tutorial review, In *Solar ultraviolet radiation: modelling, measurements and effects*, Springer-Verlag, New York, **52**, 49-64, 1997.

Stix, M., *The Sun: An introduction*, Springer-Verlag Heidelberg, 1989.

Sturman, A.P., and N.J. Tapper, *The weather and climate of Australia and New Zealand*, Oxford University Press, Melbourne, 2006.

Tanre, D., M. Herman, P.Y. Deschamps, and A. de Leffe, Atmospheric modeling for space measurement of ground reflectances, including bidirectional properties, *Applied Optics*, **18** (21), 3587-3594, 1979.

Tanre D., C. Deroo, P. Duhaut, M. Herman, J.J. Morecrette, J. Perbos, and P.Y. Deschamps, Description of a Computer Code to Simulate the Satellite Signal in the Solar Spectrum: 5S code, *International Journal of Remote Sensing*, **11** (4), 659-668, 1990.

Tapper, N., and Hurry, L., *Australian Weather Patterns: an introductory guide*, Dellasta Pty Ltd, 1993.

Tarpley, J.D., Estimating incident solar radiation at the surface from geostationary satellite data, *Journal of Applied Meteorology*, **18**, 1172-1181, 1979.

Taylor, V.R., and Stowe, L.L., Atlas of reflectance patterns for uniform earth and cloud surfaces (NIMBUS-7 ERB - 61 days). *NOAA Technical Report NESDIS*, 10-16, 1984.

Thekaekara, M. P., M. Hersé, P.C. Simon, D. Labs, H. Mandel, D. Gillotay, and T. Foujols, Solar radiation measurement: techniques and instrumentation, *Solar Energy*, **18** (4), 309, 1976.

Thomas, G.E., and K. Stamnes, *Radiative Transfer in the Atmosphere and Ocean*, Cambridge University Press, 1999.

Thullier, G. et al., The solar spectral irradiance from 200 nnm to 2400 nm as measured by the SOLSPEC spectrometer from the ATLAS 1-2-3 and EURECA missions. Solar Physics2003

Tilzer, M.M., N. Stambler, and C. Lovengreen, The role of phytoplankton in determining the underwater light climate in Lake Constance, *Hydrobiologia*, **316**, 161-172, 1995.

Tovar, H.R., and J.M. Baldasano, Solar radiation mapping from NOAA AVHRR data in Catalonia, Spain, *Journal of Applied Meteorology*, **40**, 1821-1834, 2001.

Tozzi, S., O. Schofield, T. Bergmann, M. Moline, and R. Arnone, Variability in measured and modelled remote sensing reflectance for coastal waters at LEO-15, *International Journal of Remote Sensing*, **25**(7-8), 1469-1472, 2004.

VanDuin, E.H.S, G. Blom, F.J. Los, R. Maffione, R. Zimmerman, C.F. Cerco, M. Dortch, and E.P.H Best, Modeling underwater light climate in relation to sedimentation, resuspension, water quality and autotrophic growth, *Hydrobiologia*, **444**, 25-42, 2001.

Veal C.J., *Partitioning of direct and diffuse ultraviolet irradiance in shallow waters at Heron Reef, Queensland*, Thesis B.Sc.(Honours), University of Tasmania, 2006.

Verdebout, J., A method to generate surface UV radiation maps over Europe using GOME, Meteosat, and ancillary geophysical data, *Journal of Geophysical Research*, **105** (D4), 5049-5058, 2000.

Vigroux, E., Contribution áà l'étude expéérimentale de l'absorption de l'ozone, *Ann. Phys.* **8**, 709-762, 1953.

Voss, K. J., C. D. Mobley, L. K. Sundman, J. E. Ivey, and C. H. Mazel, The spectral upwelling radiance distribution in optically shallow waters, *Limnological Oceanograhy,* **48**(1, part 2), 364–373, 2003.

Voss, K. J., and A. Morel, Bidirectional reflectance function for oceanic waters with varying chlorophyll concentrations: Measurements versus predictions, *Limnology and Oceanography*, **50**, 698-705, 2005.

Wang, J., W.B. Rossow, and Y. Zhang, Cloud Vertical Structure and Its Variations from a 20-Yr Global Rawinsonde Dataset, *Journal of Climate*, **13**, 3041-3056, 2000.

Wang, J., K. White, and G.J. Robison, Estimating surface net solar radiation by use of Landsat-5 TM and digital elevation models, *International Journal of Remote Sensing*, **21** (1), 31-43, 2000.

Wang, K., X. Zhou, J. Liu, and M. Sparrow, Estimating surface solar radiation over complex terrain using moderate-resolution satellite sensor data, *International Journal of Remote Sensing*, **26** (1), 47-58, 2005.

Warner, M.E., W.K. Fitt, and G.W. Schmidt, The effects of elevated temperature on the photosynthetic efficiency of zooanthella in hospite from four different species of reef coral, a novel approach, *Plant, Cell and Environment*, **19**, 21-299, 1996.

Wendisch, M., and B. Mayer, Vertical distribution of spectral solar irradiance in the cloudless sky - a case study. *Geophysical Research Letters*, 30: doi: 10.1029/2002 GL016529, 2003.

Wloczyk, C., and R. Richter, Estimation of incident solar radiation on the ground from multispectral satellite sensor imagery, *International Journal of Remote Sensing*, **27** (6), 1253-1259, 2006.

WMO, Scientific assessment of ozone depletion, Rep. 47, 2002

Wolanski, E., and G.L. Pickard, Long-term observations of currents on central Great Barrier Reef continental shelf, *Coral Reefs*, **4**, 47-57, 1985.

Wolanski, E., *Physical oceanography processes of the Great Barrier Reef.* CRC Press, Boca Raton, Florida, 1994.

Wolanski,E., *Oceanographic Processes of Coral Reefs*, CRC Press LLC, 2001.

Yan, B., and K. Stamnes, Fast yet accurate computation of the complete radiance distribution in the coupled atmosphere–ocean system. *Journal of Quantitative Spectroscopy & Radiative Transfer*, **76**, 207–223, 2003

Yentsch, C.S., C.M. Yentsch, J.J. Cullen, B. Lapointe, D.A. Phinney, and S.W. Yentsch, Sunlight and water transparency: cornerstones in coral research, *Journal of Experimental Marine Biology and Ecology*, **268**, 171-183, 2002.

Zacher, K., M.Y. Roleda, D. Hanelt, and C. Wiencke, UV effects on photosynthesis and DNA in propagules of three Antarctic seaweeds (*Adenocystis utricularis, Monostroma hariotii* and *Porphyra endiviifolium*), *Planta*, **225**, 1505-1516, 2007.

Zaneveld, J. R. V., and E. Boss, The influence of bottom morphology on reflectance: Theory and two-dimensional geometry model, *Limnological Oceanograhy*, **48**(1, part 2), 374–379, 2003.

Zerefos, C.S., and A.F. Bais, *Solar Ultraviolet Radiation: Modelling, Measurements and Effects*, Springer-Verlag, New York, 1997.

Zeng, X., The Relationship among precipitation, cloud-top temperature, and precipitable water over the tropics, *Journal of Climate*, **12** (8), 2503–2514, 1999.

Zhang, H., K. J. Voss, R. P. Reid, and E., Louchard, Bidirectional reflectance measurements of sediments in the vicinity of Lee Stocking Island, Bahamas, *Limnology and Oceanography*, **48**(1, part 2), 380-389, 2003.

Zhang, H., and K. J. Voss, Comparisons of bidirectional reflectance distribution function measurements on prepared particulate surfaces and radiative-transfer models, *Apply Optics*, **44**, 597-610, 2005.

Appendix I

GMS Calibration Table

Counts	$\rho'_{EA(GMS)}$	Counts	$\rho'_{EA(GMS)}$	Counts	$\rho'_{EA(GMS)}$
0	0.00000	50	0.03825	100	0.15373
1	0.00000	51	0.03981	101	0.15683
2	0.00000	52	0.04140	102	0.15995
3	0.00000	53	0.04302	103	0.16310
4	0.00000	54	0.04467	104	0.16629
5	0.00000	55	0.04635	105	0.16950
6	0.00000	56	0.04806	106	0.17275
7	0.00028	57	0.04980	107	0.17602
8	0.00052	58	0.05157	108	0.17933
9	0.00079	59	0.05338	109	0.18267
10	0.00109	60	0.05521	110	0.18603
11	0.00142	61	0.05708	111	0.18943
12	0.00178	62	0.05897	112	0.19286
13	0.00217	63	0.06090	113	0.19632
14	0.00259	64	0.06285	114	0.19981
15	0.00305	65	0.06484	115	0.20333
16	0.00353	66	0.06686	116	0.20689
17	0.00405	67	0.06891	117	0.21047
18	0.00459	68	0.07099	118	0.21408
19	0.00517	69	0.07310	119	0.21773
20	0.00578	70	0.07524	120	0.22140
21	0.00641	71	0.07741	121	0.22511
22	0.00708	72	0.07961	122	0.22884
23	0.00778	73	0.08185	123	0.23261
24	0.00851	74	0.08411	124	0.23641
25	0.00927	75	0.08640	125	0.24024
26	0.01006	76	0.08873	126	0.24410
27	0.01088	77	0.09108	127	0.24799
28	0.01174	78	0.09347	128	0.25191
29	0.01262	79	0.09589	129	0.25586
30	0.01353	80	0.09834	130	0.25984
31	0.01448	81	0.10081	131	0.26385
32	0.01545	82	0.10332	132	0.26789
33	0.01646	83	0.10586	133	0.27197
34	0.01749	84	0.10843	134	0.27607
35	0.01856	85	0.11103	135	0.28021
36	0.01966	86	0.11367	136	0.28437
37	0.02079	87	0.11633	137	0.28857
38	0.02195	88	0.11902	138	0.29280
39	0.02314	89	0.12175	139	0.29706
40	0.02436	90	0.12450	140	0.30134
41	0.02561	91	0.12729	141	0.30566
42	0.02689	92	0.13010	142	0.31001
43	0.02820	93	0.13295	143	0.31439
44	0.02955	94	0.13583	144	0.31880
45	0.03092	95	0.13873	145	0.32325
46	0.03232	96	0.14167	146	0.32772
47	0.03376	97	0.14464	147	0.33222
48	0.03523	98	0.14764	148	0.33676
49	0.03672	99	0.15067	149	0.34132

GMS Calibration Table (continued)

Counts	$\rho'_{EA(GMS)}$	Counts	$\rho'_{EA(GMS)}$	Counts	$\rho'_{EA(GMS)}$
150	0.34592	200	0.61480	250	0.96038
151	0.35054	201	0.62096	251	0.96808
152	0.35520	202	0.62715	252	0.97580
153	0.35989	203	0.63337	253	0.98356
154	0.36460	204	0.63962	254	0.99134
155	0.36935	205	0.64591	255	0.99916
156	0.37413	206	0.65222		
157	0.37894	207	0.65856		
158	0.38378	208	0.66494		
159	0.38866	209	0.67134		
160	0.39356	210	0.67778		
161	0.39849	211	0.68425		
162	0.40345	212	0.69075		
163	0.40845	213	0.69727		
164	0.41347	214	0.70383		
165	0.41853	215	0.71042		
166	0.42361	216	0.71704		
167	0.42873	217	0.72369		
168	0.43388	218	0.73037		
169	0.43906	219	0.73709		
170	0.44427	220	0.74383		
171	0.44951	221	0.75060		
172	0.45478	222	0.75741		
173	0.46008	223	0.76424		
174	0.46541	224	0.77111		
175	0.47077	225	0.77800		
176	0.47616	226	0.78493		
177	0.48159	227	0.79189		
178	0.48704	228	0.79888		
179	0.49253	229	0.80590		
180	0.49804	230	0.81295		
181	0.50359	231	0.82003		
182	0.50917	232	0.82714		
183	0.51477	233	0.83428		
184	0.52041	234	0.84145		
185	0.52608	235	0.84866		
186	0.53178	236	0.85589		
187	0.53751	237	0.86315		
188	0.54327	238	0.87045		
189	0.54907	239	0.87777		
190	0.55489	240	0.88513		
191	0.56074	241	0.89252		
192	0.56662	242	0.89994		
193	0.57254	243	0.90738		
194	0.57848	244	0.91486		
195	0.58446	245	0.92237		
196	0.59047	246	0.92991		
197	0.59650	247	0.93749		
198	0.60257	248	0.94509		
199	0.60867	249	0.95272		

Appendix II

Spectral responses of GMS-5 and GOES-9 satellites

1) Spectral response of GMS-5 satellite

Wavelength [μm]	Response
0.319	0.000000
0.337	0.000000
0.355	0.000000
0.374	0.000000
0.394	0.000000
0.415	0.000000
0.437	0.000000
0.459	0.017000
0.477	0.271000
0.487	0.385000
0.496	0.448000
0.506	0.481000
0.511	0.558000
0.521	0.587000
0.531	0.649000
0.542	0.679000
0.552	0.761000
0.563	0.675000
0.574	0.672000
0.585	0.657000
0.596	0.778000
0.607	0.960000
0.619	0.924000
0.631	0.824000
0.643	0.881000
0.655	0.932000
0.668	0.914000
0.680	0.870000
0.693	0.918000
0.706	0.902000
0.720	0.933000
0.733	0.923000
0.747	0.934000
0.762	0.884000
0.776	0.872000
0.791	0.906000
0.806	0.870000
0.821	0.932000
0.837	0.892000
0.853	0.946000
0.869	0.871000
0.886	1.000000
0.903	0.827000
0.920	0.919000
0.938	0.838000
0.956	0.744000
0.975	0.672000
0.994	0.473000
1.013	0.190000
1.043	0.038000
1.096	0.000000
1.152	0.000000

2) Spectral response of GOES-9 satellite

Wavelength [μm]	Response
0.49	0.000000
0.50	0.002890
0.51	0.083880
0.52	0.393160
0.53	0.668750
0.54	0.817820
0.55	0.899710
0.56	0.957380
0.57	0.960200
0.58	0.906390
0.59	0.947680
0.60	1.000000
0.61	0.982490
0.62	0.937340
0.63	0.899440
0.64	0.894950
0.65	0.926080
0.66	0.893970
0.67	0.819790
0.68	0.790560
0.69	0.785190
0.70	0.736590
0.71	0.661450
0.72	0.616890
0.73	0.587760
0.74	0.532760
0.75	0.457690
0.76	0.392580
0.77	0.348490
0.78	0.317790
0.79	0.244500
0.80	0.065550
0.81	0.000000

Appendix III

Look-Up Tables (LUT) and a computer codes to access the values

The Look-Up Tables (LUT) containing arrays of the broadband Earth-atmosphere albedo and solar irradiance are provided in a CD-ROM, which is attached in the cover page of this thesis. The arrays in each file have a dimension of 81×101 (0°-80° solar zenith angles × 0%-100% cloud fractions), which is provided at a certain condition of surface types and cloud properties, including cloud optical thicknesses, droplet radius and liquid water content. The first (above) array contains the values of the Earth-atmosphere albedo and the second (below) contains the values of broadband solar irradiance. Note that the values of solar irradiance are multiplied by 0.0001.

The values of the Earth-atmosphere albedo and solar irradiance contained in the LUT can be accessed by using the following IDL code:

```
;%%%%%%%%%%%%%%%%%%%%%%%%%%%%%%%%%%%%%%%%%%%%%%%%%%%%%%%%%%%%%%%%%%%%%%%%%%%%%%%%%%%
;
; Module: Reading LUTs files.
;
;      by : Itsara Masiri
;
;
; Variables:
;      isurf = surface type: 1=5%, 2=10%
;      ithk = cloud thickness: 1=0.1km, 2=0.6km, 3=1.1km, 4=1.6km, 5=2.1km
;      irad = droplet radius: 1=2.5um, 2=4.0um, 3=5.5um, 4=7.0um, 5=8.5um
;      iwco = cloud liquid water content: 1=0.05g/m3, 2=0.15g/m3, 3=0.25g/m3,
;                                           4=0.35g/m3, 5=0.50g/m3
;      icf = clouf fraction
;      izs = solar zenith angle
;      LUT_glo(isurf,ithk,irad,iwco,izs,icf) = Look-Up Table contains global
;                                                   solar irradiance
;      LUT_aea(isurf,ithk,irad,iwco,izs,icf) = Look-Up Table contains Earth-atmosphere
;                                                   albedo
;
;
;%%%%%%%%%%%%%%%%%%%%%%%%%%%%%%%%%%%%%%%%%%%%%%%%%%%%%%%%%%%%%%%%%%%%%%%%%%%%%%%%%%%

Pro read_LUTs


LUT_glo=fltarr(3,6,6,6,81,105)
LUT_aea=fltarr(3,6,6,6,81,105)

gridlut1=fltarr(81,101)
gridlut2=fltarr(81,101)
head=''

ithk=0
irad=0
```

```
iwco=0

fpath=dialog_pickfile(/read,directory='g:\GBR_Research\LUT_StreamerModel\Broadband\'$

       ,path='g:\GBR_Research\LUT_StreamerModel\Broadband\')

lutload=findfile(fpath+'LUT_*.txt')
numlut=n_elements(lutload)
print,fpath,numlut

if (fpath ne '') and (numlut gt 1) then begin

for n=0,numlut-1  do begin

openr,10,lutload(n),error=err

       if (err eq 0) then begin
              readf,10,head,format='(a5)'
              readf,10,gridlut1,format='(81(f6.4,1x))'
              readf,10,head,format='(a5)'
              readf,10,gridlut2,format='(81(f9.7,1x))'
              close,10

              getclid=str_sep(lutload(n),'_')
              nstr=n_elements(getclid)

              case getclid[nstr-1] of
                     'lwc005.txt' : iwco=1
                     'lwc015.txt' : iwco=2
                     'lwc025.txt' : iwco=3
                     'lwc035.txt' : iwco=4
                     'lwc050.txt' : iwco=5
              endcase

              case getclid[nstr-2] of
                     'rad25' : irad=1
                     'rad40' : irad=2
                     'rad55' : irad=3
                     'rad70' : irad=4
                     'rad85' : irad=5
              endcase

              case getclid[nstr-3] of
                     'thk01' : ithk=1
                     'thk06' : ithk=2
                     'thk11' : ithk=3
                     'thk16' : ithk=4
                     'thk21' : ithk=5
              endcase


              case getclid[nstr-4] of
                     'Land' : isurf=1
                     'Seas' : isurf=2
              endcase


       print,'load LUT library ... ',n+1,'of',numlut,lutload(n),'=',ithk,irad,iwco

       for izs=0,80  do begin
       for icf=0,100 do begin
              LUT_aea(isurf,ithk,irad,iwco,izs,icf)=gridlut1(80-izs,100-icf)
              LUT_glo(isurf,ithk,irad,iwco,izs,icf)=gridlut2(80-izs,100-icf)*10000.0
       endfor
       endfor

endif

endfor

endif

End
```

Appendix IV

SST time series during the 2002 coral bleaching event

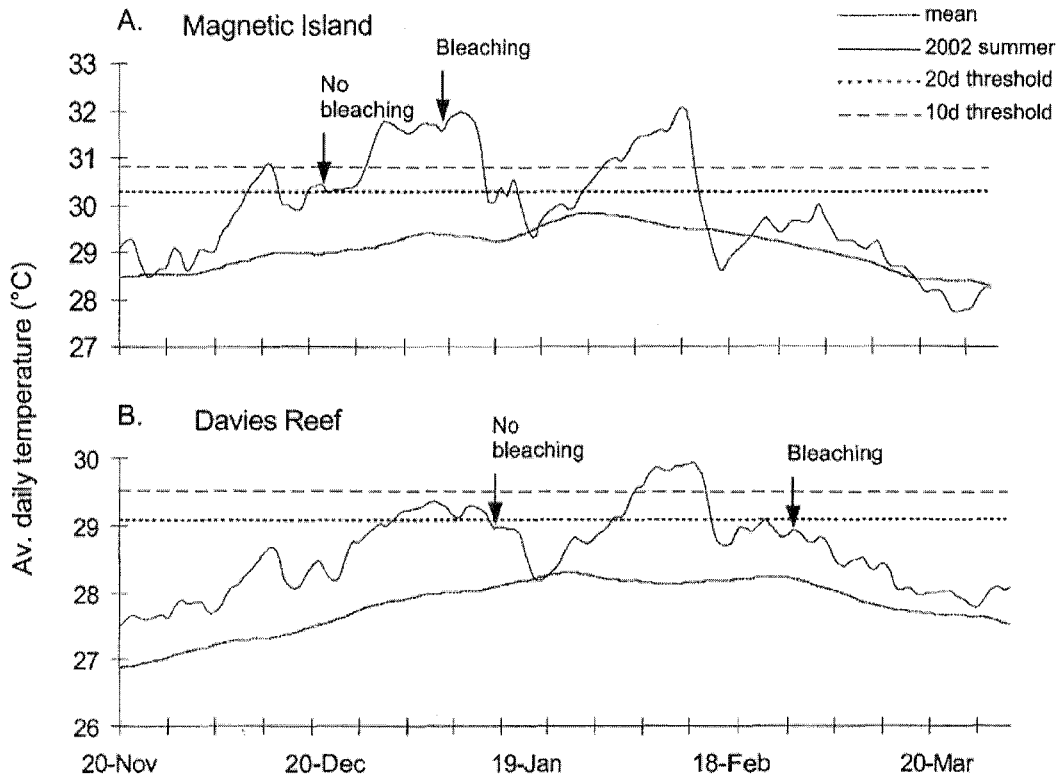

Figure A1 Temperatures and timing of onset of bleaching at a Magnetic Island (Nelly Bay) and b Davies Reef in early 2002. Magnetic Island temperatures measured with an *in situ* temperature logger and the mean calculated over a 10-year period with a 14 day smoothing function applied. Davies Reef temperatures from an automatic weather station and the mean calculated over a 15-year period with a 14-day smoothing function applied (taken from Berkelmans *et al.*, 2004).